UNIVERSITY OF OKLAHOMA

GRADUATE COLLEGE

Tropospheric Polar Vortices and Impacts on Atmospheric Flow from the Arctic to the Mid-Latitudes using a New Global Modeling System

A DISSERTATION

SUBMITTED TO THE GRADUATE FACULTY

in partial fulfillment of the requirements for the

Degree of

DOCTOR OF PHILOSOPHY

By

Christopher Philip Riedel
Norman, Oklahoma
2020

Downloaded from SHAREOK. Persistent Handle URL: https://hdl.handle.net/11244/324334

Tropospheric Polar Vortices and Impacts on Atmospheric Flow from the Arctic to the Mid-Latitudes using a New Global Modeling System

A DISSERTATION APPROVED FOR THE
SCHOOL OF METEOROLOGY

BY THE COMMITTEE CONSISTING OF

Dr. Steven Cavallo, Chair

Dr. David Parsons

Dr. Xuguang Wang

Dr. David Turner

Dr. Ryan Torn

Dr. Henry Neeman

© Copyright by CHRISTOPHER PHILIP RIEDEL 2020
All Rights Reserved.

Dedication

This is dedicated to the memory of my grandparents Arlene and Wayne Thompson and Betty Riedel. Without their support this document would not be possible.

Acknowledgments

14 years. That's how long I have been in some level of higher education since graduating high school. I still can not believe that has been my identity for the last 14 years. While that label will be changing soon, it was not an easy journey arriving to this long, roundabout ending point that is finishing my PhD. I am still used to answering the question of "Are you still in school?" and answering that question with a yes (Grandma Betty was the best at asking this!). Honestly, I would not recommend staying in higher education for 14 years but if you decide to choose this path, I hope you have support from amazing people like I did. I decided to write this acknowledgment section in chronological order to help show how many people helped me along the way.

My love weather started at a young age, or so I am told by my parents. So, I will start here with my parents. Mom (Kala or Karla to annoy her), I am the luckiest kid on earth to call you my mom. You were my superhero as a kid (except for when you were my teacher in 2nd grade, you were my villain that year) and I still look up to you to this day. Grandma and grandpa Thompson, were like a second pair of parents growing up and were always there to support me. Dad, you were always my biggest fan growing up, whether that be sport or school related. I still remember you driving to every game my senior year at Ottawa University to support my last year of basketball. You have no idea how much that meant to me. That same support from you and mom were one of the main factors that help me achieve this point now. Conversations with grandma Betty always brought a smile to my face (even if you were making fun of my hair) and she always supported me in my journey to obtain a PhD. To my sister and Mike, thanks for allowing me to try and be the best uncle to two awesome kids named Berkley and Logan. Stressful days are made better when I am able to see or talk to them. Also, thanks for the support even though I am sure you think I am crazy. To my sisters Haley and Hayden, thank you for keeping me young and smiling. Some of my favorite times at home are spent in the backyard playing some game and just laughing (well sometimes yelling because someone gets mad). Lastly,

I want to thank all other family members (uncles, aunts, cousins) for support throughout this journey and always asking about school at holiday gatherings.

Even though weather was my first love, basketball became one the top of things I loved to do which required me to put my love for weather on the shelf. I was extremely fortunate to receive and accept a scholarship to continue playing at Ottawa University. While at Ottawa University, there were several people that helped shaped my path to achieving my PhD. Nicole Leonhard, thank you for pushing me and never letting me quit in my path to first getting my degree in mathematics but also in my dream of studying weather. I really think you saw something in me that I did not even know I had within me because you always pushed me to do better. Without your guidance, I would have never chosen University of Oklahoma as the school to continue my education and it was a very good advice. To my coach Andy Carrier, while your lessons in practice and games might not have helped me solve complex mathematics or physics problems, those lessons helped prepare me to be a better person in life. The life lessons I learned while being a player under you definitely had an impact on arriving to this point. Friends and teammates at Ottawa University, you always supported me while I was a student and player there.

Having graduated from a small, rural Kansas high school and college, I was pretty nervous starting out at the University of Oklahoma (never told anyone that). However, choosing the University of Oklahoma was probability one the best decisions I have made in my life. Having played basketball, I think hard work and loving a challenge was instilled in me from a young age all the way up to college. To all my undergraduate professors, thank you for challenging me during my time in your classrooms. Also, thanks for always finding time to answer questions and talk, which helped shape me as a student. While being an undergraduate student, I was fortunate to be selected for a student job at the National Severe Storms Lab that is in the building. Thank you, Kevin Manross and Kiel Ortega, for taking a chance on this kid and helping to introduce me to the research side of weather. Without that job and your guidance, I really do not think I would have chosen the path of research

and not applied for graduate school. Once in graduate school at Oklahoma, I had a number of awesome professors which challenged me at next level of education. I am sincere when I say do not stop challenging and pushing young adults in the classroom, while they might be stressed/angry at the moment they will appreciate later, trust me. Lastly, thank you to all my friends I have made while in undergraduate and graduate school. Brandon Wesbury and Casey Peirano, without you guys I would have gone crazy while going through my second bachelor's degree. Zach Wienhoff, Dylan Reif, Kyle Theim, and Jon Labriola (first fundamentals class), thank you for making laugh during long study sessions and making sense of class and code when I am going crazy. I have learned so much from all of you. Josh Geubauer, thanks for always talking through weird stat and coding questions. I hope the Pirates make the post-season because you deserve that being a fan this long. Lastly to our research, AAARG members (Sam Lillo, Nick Szapiro, and Dylan Lusk), thank you for listening to and providing feedback on presentations and research. Furthermore, thank you for always offering up a solution to a coding problem and reading something I had written.

In my time in graduate school, I have made some great friends that were students but also some that were faculty and researchers. I want to thank all of the "Happy Hour" group for keeping things up-beat and listening to an ear full of complaining after a long week. Alan, I have learned so much from you since we first met (mostly about cooking and drink) but were one of my favorite teachers while at OU. To Petra, thank you for always welcoming me, keeping laugher in moments together, and vouching for me when people were unsure about my credentials. Evgeni, you definitely taught the most difficult material-based class I have taken (sorry Steven, fundamentals is a close second) and provided the most critical feedback. Thank You. Also, thank you for always making sarcastic jokes and always smile at happy hours. Louis Wicker, you served on my masters committee and about a year of PhD committee (well you thought you did). Thank you for your guidance and always challenging me with research questions. Also, I know your letter is a big reason I have received the ASP post-doc which means a lot to me. Jeremy, even though you have

arrived during the last year of last part of my PhD, you encouragement and advice has been helpful. Last but not least, Kathryn Gebauer, thank you for always wanting to change the topic from weather and answering stupid grammatical questions. I am still afraid to have you review one of my papers though. . . . . .

I would like to thank my PhD committee members for their guidance, encouragement and answering of any questions I had. My SOM committee members, Dave Parsons and Xuguang Wang, thank you for your time and feedback during my PhD. Non-SOM committee members, Ryan Torn and Dave Turner, thank you for being on my committee even though you were not physically at OU. The time commitment you made for emails and video meetings were important in my progress in obtaining my PhD. Henry Neeman, thank you for your time and commitment for serving as my outside member. Additionally, I would like to thank Jeffrey Anderson for being my host during the NCAR ASP graduate student visitor program. This work would not be possible without your feedback and guidance while I was at NCAR.

People always told me when choosing graduate school, your advisor is the most important item to consider. I chose Steven Cavallo as my advisor after finishing fundamentals in my first semester graduate school. Having taken undergrad synoptic along with fundamentals from Steven, I think always enjoyed him pushing students to challenge themselves in the classroom. It really has been a pleasure to learn and develop into a scientist under his guidance. Steven was great at identifying times when I needed to solve problems myself while also recognizing there are times he needs draw me back in. Furthermore, I like to think a good friendship developed during his time of advising and letting me be a part of Lukas's life. I am very happy for you and Jordan. Speaking of Jordan, happy hour would not be complete without him rolling his eyes at the weather talk but always asking how I am doing. So, I want to say thank you to Steven for allowing me to be his student and for being an awesome advisor.

Choosing Steven as my advisor was very close second to the best decision I have made in my life. Number one would be dressing up at Halloween and working up the courage to talk to my now girlfriend Elizabeth Smith. I was very proud to watch Elizabeth finish her PhD and in such a quick time frame. Elizabeth has been my rock during the time of working towards my PhD. Without her, I would not be in the position I am today to finish my PhD. Thank you for reading my terribly written papers and listening to first go arounds of presentations. I think we both love being challenged academically and that has helped me develop as a person. However, that has led to some heated arguments about research topics, but we always come to some agreement in the end. I love you Elizabeth Smith, and I would do another 14 years of school to meet you at a Halloween party again.

Table of Contents

Dedication iv

Acknowledgments v

List of Tables xii

List of Figures xiii

Abstract xxxv

1 Introduction 1
- 1.1 The Arctic . . . 1
- 1.2 Tropopause Polar Vortices (TPVs) . . . 8
- 1.3 Rossby Waves and Downstream Predictability . . . 11

2 Observations, Numerical Modeling and Data Assimilation 20
- 2.1 Observations . . . 20
  - 2.1.1 The Global Ensemble Forecast System , and ECMWF Re-Analysis Version 5 . . . 20
  - 2.1.2 Conventional Observations . . . 21
  - 2.1.3 Polar Orbiting Wind Observations . . . 23
  - 2.1.4 Atmospheric Infrared Sounder . . . 24
- 2.2 Data Assimilation . . . 25
- 2.3 NWP Model . . . 30
- 2.4 Experiment Details . . . 36

3 Evaluation of MPAS-DART 47
- 3.1 Ensemble Inflation . . . 50
- 3.2 Bias, RMSE, and Total Spread Profiles and Rank Histograms . . . 53
- 3.3 Analysis Increment . . . 58

4 Investigation of Systematic Errors 97
- 4.1 Mean Initial Tendency and Analysis Increment Method . . . 98
  - 4.1.1 Experiment One . . . 100
  - 4.1.2 Experiment Two . . . 105
  - 4.1.3 Summary . . . 107
- 4.2 WRF Single Column Sensitivity Simulations . . . 109
- 4.3 NAWDEX Observations . . . 111

5 TPV and Rossby Wave Initiation Case Study **151**
5.1 Introduction 151
5.2 Methods 153
5.3 RWI Case Study Description 156
5.4 Results from Case Studies 159

6 Conclusions **185**

Reference List **195**

List of Tables

2.1 Physics schemes chosen for MPAS-DART and a general description of their purposes. 35
2.2 Differences between experiment 1 and 2. 38

List of Figures

1.1 Schematic of ways to influence Northern Hemisphere mid-latitude weather. Three major dynamical features for changing Northern Hemisphere mid-latitude weather — changes in the storm tracks, the position and structure of the jet stream, and planetary wave activity — can be altered in several ways. The pathway on the left and highlighted by double boxes is reviewed in this manuscript. Arctic amplification directly (by changing the meridional temperature gradient) and/or indirectly (through feedbacks with changes in the cryosphere) alters tropospheric wave activity and the jet stream in the mid- and high latitudes. Two other causes of changes in the storm tracks, jet stream and wave activity that do not involve Arctic amplification are also presented: (1) natural modes of variability and (2) the direct influence of global climate change (that is, including influences outside the Arctic) on the general circulation. The last two causes together present the current null hypothesis in the state of the science against which the influence of Arctic amplification on mid-latitude weather is tested in both observational and modelling studies. Bidirectional arrows in the figure denote feedbacks (positive or negative) between adjacent elements. Stratospheric polar vortex is represented by 'L' with anticlockwise flow. This figure is from Cohen et al. (2014b) 16

1.2 Illustration of the amplification and spatial growth of forecast errors in a medium-range forecast from the European Centre for Medium-Range Weather Forecasts (ECMWF, polar stereographic projection, forecast initialized at 0000 UTC 12 Nov 2013). The error is depicted in terms of PV (color shading) on the 320-K isentrope intersecting the mid-latitude tropopause. Errors are defined as the difference between the forecast and the verifying analysis. The dynamical tropopause is depicted by the 2-PVU contour (solid for the analysis, dashed for the forecast). Errors with distinct local extrema in amplitude at (a) forecast day 2 develop into error patterns on the scale of RWPs by (b) forecast day 6. This figure is from Wirth et al. (2018) 17

1.3 Time series of ECMWF day-6 forecast anomaly correlation coefficient (ACC) for the mid-latitudes and the Arctic. The calculation of ACC included cosine weighted by latitude. ERA-iterim was used as the climatology for the ACC calculation. Other regions have been compared to the Arctic and mid-latitudes. 18

1.4 Probability of TPV locations (colorfill, %) and location of TPVs associated with RWI events (white contours, %). Red contours of jet streak counts of greater than 70 m s^{-1} windspeed. Yellow triangles denote locations of RWIs where a TPV is within 1000 km. TPV tracks were computed using the ERA-interim dataset and Szapiro and Cavallo (2018) TPV tracking algorithm. The RWI events were from the Röthlisberger et al. (2016) dataset. 18

1.5 Schematic showing MCS (mesoscale convective system), XT (extratropical cyclones), TC (tropical cyclone), and TPV (tropopause polar vortex) features that can act to kick off a RWI event and the downstream propagation of the Rossby wave packet. Figure provided by Sam Lillo and is based in part on Lillo and Parsons (2017) finding of causes linked to dramatic decrease in forecast skill. 19

2.1 Observation locations for valid on 00 UTC 28 September 2016 for (a) convectional observations and (b) convectional observations plus polar orbiting satellite observations. Observations shown are radiosonde (Radiosonde), marine buoy (Marine), geostationary satellite winds (SAT), Meteorological Terminal Aviation Routine Weather Report (METAR), global positioning system (GPSRO), aircraft communications addressing and reporting system (ACARS), automatic weather stations (LAND), AIRS satellite derived profiles (AIRS), and polar orbiting satellite wind observations (MODIS and AVHRR). 39

2.2 Average observations assimilated per cycle for (a) only conventional observations and (b) convectional observations plus polar orbiting satellite observations for experiment one. (c) Differences in averaged observations assimilated per cycle between including polar orbiting satellite observations versus when polar orbiting satellite observations are excluded. 40

2.3 Time series showing the percentage of conventional (red), AIRS (blue), and MODIS/AVHRR (cyan) observations assimilated within MPAS-DART for (a) the Arctic region and (b) the mid-latitudes. 41

2.4 Specified (a) horizontal and (b) vertical localization factor that is applied within MPAS-DART. The black dashed lines represent the half-width of the localization radius. 42

2.5 Climatological Rossby radius of Deformation (in km) computed using ERA5 data. 43
2.6 Three day MPAS simulation of a TPV starting on 00 UTC 15 August 2006 showing the (a) spatial representation and (b) vertical representation with varying horizontal resolutions. 44
2.7 Position of the 60-15 km mesh used in MPAS-DART. 45
2.8 Vertical model levels represented using (a) traditional terrain-following coordinate and (b) hybrid terrain-following coordinate. Figure provided from the MPAS website (https://mpas-dev.github.io) 45
2.9 Spacing between MPAS model levels used in this study. 46

3.1 These are examples of rank histogram types when evaluating temperature: (A) well-calibrated ensemble spread, (B) ensemble spread is to large, (C) ensemble spread is small, (D) ensemble has a warm bias, and (E) ensemble has a cold bias. 63
3.2 This schematic diagram shows the data assimilation and forecast integration aspects of numerical weather prediction. $T_{obs}(t)$ represents an observed time series (e.g. of temperature at some specified location with temperature increasing as you move up the y-axis). For each i, T_i (t_i) represents the model forecast initiated from analysis AN_i. INC_i represents the adjustment added to the forecast from the observations to make the new AN_i. This figure is from Rodwell and Palmer (2007a) 64
3.3 Time series showing maximum inflation for all state variables for experiment 1. Shading shows the range in the max inflation values between the 2.5 and 97.5 percentiles. 65
3.4 Time series showing maximum inflation for all state variables for experiment 2. Shading shows the range in the max inflation values between the 2.5 and 97.5 percentiles. 66

3.5 Time series showing max inflation associated with potential temperature over the Arctic (a,c) and over the mid-latitudes (b,d) for experiment 1 (a,b) and experiment 2 (c,d). Dot colors represent the pressure level the max inflation value is at. 67
3.6 Time series showing max inflation associated with the zonal wind over the Arctic (a,c) and over the mid-latitudes (b,d) for experiment 1 (a,b) and experiment 2 (c,d). Dot colors represent the pressure level the max inflation value is at. 68
3.7 Time series showing max inflation associated with the meridional wind over the Arctic (a,c) and over the mid-latitudes (b,d) for experiment 1 (a,b) and experiment 2 (c,d). Dot colors represent the pressure level the max inflation value is at. 69
3.8 Mean (a) potential temperature, (b) zonal- and (c) meridional-wind inflation calculated over experiment 2 cycling period at 250 hPa. Crosses mark locations of radiosonde launch sites. 70
3.9 Mean (a) potential temperature, (b) zonal- and (c) meridional-wind calculated over the increased inflation period centered on 5 December 2011 in experiment 2 at 250 hPa. Inflation values were averaged over a 2 day window with the center being on 5 December 2011. Crosses mark locations of radiosonde launch sites. 71

3.10 Cycling period averaged vertical profiles of analysis bias (dashed black), 6-hour model forecast bias (black), RMSE (dashed red), and ensemble total spread (dashed blue) when compared to radiosonde temperature observations. Profiles are averaged over the Arctic (a,c) and the mid-latitudes (b,d) for both experiment 1 (a,b) and experiment 2 (c,d). Within all panels, the left profile shows cycling period mean values while the right profile shows total observation counts over the cycling period. Error bars represent the 95% confidence interval from bootstrap resampling. 72

3.11 Cycling period averaged vertical profiles of analysis bias (dashed black), 6-hour model forecast bias (black), RMSE (dashed red), and ensemble total spread (dashed blue) when compared to AIRS temperature observations. Profiles are averaged over the Arctic (a,c) and the mid-latitudes (b,d) for both experiment 1 (a,b) and experiment 2 (c,d). Within all panels, the left profile shows cycling period mean values while the right profile shows total observation counts over the cycling period. Error bars represent the 95% confidence interval from bootstrap resampling. 73

3.12 Cycling period averaged vertical profiles of analysis bias (dashed black), 6-hour model forecast bias (black), RMSE (dashed red), and ensemble total spread (dashed blue) when compared to radiosonde specific humidity observations. Profiles are averaged over the Arctic (a,c) and the mid-latitudes (b,d) for both experiment 1 (a,b) and experiment 2 (c,d). Within all panels, the left profile shows cycling period mean values while the right profile shows total observation counts over the cycling period. Error bars represent the 95% confidence interval from bootstrap resampling. 74

3.13 Cycling period averaged vertical profiles of analysis bias (dashed black), 6-hour model forecast bias (black), RMSE (dashed red), and ensemble total spread (dashed blue) when compared to AIRS specific humidity observations. Profiles are averaged over the Arctic (a,c) and the mid-latitudes (b,d) for both experiment 1 (a,b) and experiment 2 (c,d). Within all panels, the left profile shows cycling period mean values while the right profile shows total observation counts over the cycling period. Error bars represent the 95% confidence interval from bootstrap resampling. 75

3.14 Cycling period averaged vertical profiles of analysis bias (dashed black), 6-hour model forecast bias (black), RMSE (dashed red), and ensemble total spread (dashed blue) when compared to radiosonde zonal-wind observations. Profiles are averaged over the Arctic (a,c) and the mid-latitudes (b,d) for both experiment 1 (a,b) and experiment 2 (c,d). Within all panels, the left profile shows cycling period mean values while the right profile shows total observation counts over the cycling period. Error bars represent the 95% confidence interval from bootstrap resampling. 76

3.15 Cycling period averaged vertical profiles of analysis bias (dashed black), 6-hour model forecast bias (black), RMSE (dashed red), and ensemble total spread (dashed blue) when compared to radiosonde meridional-wind observations. Profiles are averaged over the Arctic (a,c) and the mid-latitudes (b,d) for both experiment 1 (a,b) and experiment 2 (c,d). Within all panels, the left profile shows cycling period mean values while the right profile shows total observation counts over the cycling period. Error bars represent the 95% confidence interval from bootstrap resampling. 77

3.16 Cycling period averaged vertical profiles of analysis bias (dashed black), 6-hour model forecast bias (black), RMSE (dashed red), and ensemble total spread (dashed blue) when compared to geostationary satellite wind observations. Profiles are averaged over the Arctic (a,c) and the mid-latitudes (b,d) for both experiment 1 (a,b) and experiment 2 (c,d). Within all panels, the left profile shows cycling period mean values while the right profile shows total observation counts over the cycling period. Error bars represent the 95% confidence interval from bootstrap resampling. 78

3.17 Cycling period averaged vertical profiles of analysis bias (dashed black), 6-hour model forecast bias (black), RMSE (dashed red), and ensemble total spread (dashed blue) when compared to modis satellite wind observations. Profiles are averaged over the Arctic (a,c) and the mid-latitudes (b,d) for both experiment 1 (a,b) and experiment 2 (c,d). Within all panels, the left profile shows cycling period mean values while the right profile shows total observation counts over the cycling period. Error bars represent the 95% confidence interval from bootstrap resampling. 79

3.18 Rank Histograms of Automatic Weather Stations (AWS) temperature observations. Rank histograms were computed over the Arctic (a,c) and the mid-latitudes (b,d) for both experiment 1 (a,b) and experiment 2 (c,d). Rejection rate is the percent (%) of the observations that were rejected. 80

3.19 Rank histograms of marine buoy temperature observations. Rank histograms are computed over the Arctic (a,c) and the mid-latitudes (b,d) for both experiment 1 (a,b) and experiment 2 (c,d). Rejection rate is the percent (%) of the observations that are rejected. 81

3.20 Rank histograms of Automatic Weather Stations (AWS) specific humidity observations. Rank histograms are computed over the Arctic (a,c) and the mid-latitudes (b,d) for both experiment 1 (a,b) and experiment 2 (c,d). Rejection rate is the percent (%) of the observations that are rejected. 82
3.21 Rank histograms of marine buoy specific humidity observations. Rank histograms are computed over the Arctic (a,c) and the mid-latitudes (b,d) for both experiment 1 (a,b) and experiment 2 (c,d). Rejection rate is the percent (%) of the observations that are rejected. 83
3.22 Rank histograms of Automatic Weather Stations (AWS) zonal-wind observations. Rank histograms are computed over the Arctic (a,c) and the mid-latitudes (b,d) for both experiment 1 (a,b) and experiment 2 (c,d). Rejection rate is the percent (%) of the observations that are rejected. 84
3.23 Rank histograms of marine buoy zonal wind observations. Rank histograms are computed over the Arctic (a,c) and the mid-latitudes (b,d) for both experiment 1 (a,b) and experiment 2 (c,d). Rejection rate is the percent (%) of the observations that are rejected. 85
3.24 Rank histograms of Automatic Weather Stations (AWS) meridional-wind observations. Rank histograms are computed over the Arctic (a,c) and the mid-latitudes (b,d) for both experiment 1 (a,b) and experiment 2 (c,d). Rejection rate is the percent (%) of the observations that are rejected. 86
3.25 Rank histograms of marine buoy meridional wind observations. Rank histograms are computed over the Arctic (a,c) and the mid-latitudes (b,d) for both experiment 1 (a,b) and experiment 2 (c,d). Rejection rate is the percent (%) of the observations that are rejected. 87

3.26 MPAS-DART spacially averaged (poleward of 60°N) potential temperature analysis increments time-height-sections for (a) experiment one and (b) experiment two. Stippling shows statistical significance at the 95% confidence interval using a student's t-test. 88
3.27 MPAS-DART spacially averaged (poleward of 60°N) water vapor analysis increments time-height-sections for (a) experiment one and (b) experiment two. Stippling shows statistical significance at the 95% confidence interval using a student's t-test. 89
3.28 The same as Fig. 3.27 but zoomed into the levels spanning 300 to 50 hPa. . 90
3.29 MPAS-DART spacially averaged (poleward of 60°N) zonal wind analysis increments time-height-sections for (a) experiment one and (b) experiment two. Stippling shows statistical significance at the 95% confidence interval using a student's t-test. 91
3.30 MPAS-DART spacially averaged (poleward of 60°N) meridional wind analysis increments time-height-sections for (a) experiment one and (b) experiment two. Stippling shows statistical significance at the 95% confidence interval using a student's t-test. 92
3.31 Cycling period averaged potential temperature analysis increment at 100 hPa for both (a) experiment one and (b) experiment two. Areas that are below the 20th percentile value of a distribution of the standard deviation values are hatched. Black dashed line represents 60°N latitude. Stars are locations of radiosonde launch sites. 93
3.32 Cycling period averaged zonal analysis increment at 75 hPa for both (a) experiment one and (b) experiment two. Areas that are below the 20th percentile value of a distribution of the standard deviation values are hatched. Black dashed line represents 60°N latitude. Stars are locations of radiosonde launch sites. 94

3.33 Cycling period averaged two-meter temperature analysis increment for both (a) experiment one and (b) experiment two. Areas that are below the 20th percentile value of a distribution of the standard deviation values are hatched. Black dashed line represents 60°N latitude. Stars are locations of land observation sites. 95

3.34 Cycling period averaged two-meter water vapor analysis increment for both (a) experiment one and (b) experiment two. Areas that are below the 20th percentile value of a distribution of the standard deviation values are hatched. Black dashed line represents 60°N latitude. Stars are locations of land observation site. 96

4.1 Experiment one spatially averaged profiles of MITA increment method for (a) potential temperature, (b) water vapor, (c) zonal wind, and (d) meridional wind over the Arctic. Each colored line represents a different term in equation 4.1. The black line is the residual which is the difference between the RHS and LHS in equation 4.1. Error bars are included on the total accumulated average model tendency profiles only at points where the 70% confidence intervals (Cavallo et al. 2016) do not cross zero, indicating the profile values are statistically different from zero. 120

4.2 Experiment one spatially averaged profiles of MITA increment method for potential temperature (a) over the Arctic, (b) over land in the Arctic, (c) over ocean in the Arctic, and (d) over seaice in the Arctic. Each colored line represents a different term in equation 4.1. The black line is the residual which is the difference between the RHS and LHS in equation 4.1. Error bars are included on the total accumulated average model tendency profiles only at points where the 70% confidence intervals (Cavallo et al. 2016) do not cross zero, indicating the profile values are statistically different from zero. 121

4.3 Experiment one spatially averaged accumulated model tendencies for potential temperature (a) over the Arctic, (b) over land in the Arctic, (c) over ocean in the Arctic, and (d) over seaice in the Arctic. Each colored line represents a different physics tendency representing potential temperature. . 122

4.4 Experiment one spatially averaged profiles of MITA increment method for water vapor (a) over the Arctic, (b) over land in the Arctic, (c) over ocean in the Arctic, and (d) over seaice in the Arctic. Each colored line represents a different term in equation 4.1. The black line is the residual which is the difference between the RHS and LHS in equation 4.1. Error bars are included on the total accumulated average model tendency profiles only at points where the 70% confidence intervals (Cavallo et al. 2016) do not cross zero, indicating the profile values are statistically different from zero. 123

4.5 Experiment one spatially averaged accumulated model tendencies for water vapor (a) over the Arctic, (b) over land in the Arctic, (c) over ocean in the Arctic, and (d) over seaice in the Arctic. Each colored line represents a different physics tendency representing qv. 124

4.6 Arctic averaged water vapor profiles (a,b) averaged over the cycling period and (c,d) at initialization time for experiment one. MPAS ensemble average (solid red line), MPAS member 70 (dashed red line), and control member GEFS (solid blue line) are compared to ERA5 (solid black line). 125

4.7 (a) GEFS Water vapor profiles comparing computed water vapor from relative humidity when the WPS subroutine fix is applied (dashed red line) versus when the relative humidity fix is not applied (solid red line). The solid black is the water vapor profile provided from the GEFS data. (b) Water vapor bias profiles comparing when the relative humidity fix is applied versus when the fix is not applied. 126

4.8 Schematic illustrating the radiative cooling linked back to the increase in moisture. The red line represents the moisture profile found in MPAS-DART member 70. The black wiggly lines represent longwave (LW) radiation being absorbed and reemitted from the layer with increased moisture. The moisture gradient in shown by the black dashed lines. The longwave wave cooling profile from MPAS-DART member 70 is shown with by the blue line. 127
4.9 Sea ice concentration provided from (a) NCEP GFS, (b) ERA5, and (c) passive microwave satellite from National Snow and Ice Data Center (NSIDC) that are valid on 8 October 2016 at 00 UTC. 128
4.10 Accumulated model tendency profiles for simulations initialized using sea ice concentration data from (a,b) GEFS and (c,d) ERA5. Figures (a,c) represent total accumulated averaged model tendency while figures (b,d) are the decomposed model tendencies. 129
4.11 Experiment two spatially averaged profiles of MITA increment method for (a) potential temperature, (b) water vapor, (c) zonal wind, and (d) meridional wind over the Arctic. Each colored line represents a different term in equation 4.1. The black line is the residual which is the difference between the RHS and LHS in equation 4.1. Error bars are included on the total accumulated average model tendency profiles only at points where the 70% confidence intervals (Cavallo et al. 2016) do not cross zero, indicating the profile values are statistically different from zero. 130
4.12 Arctic averaged water vapor profiles (a,b) averaged over the cycling period for experiment two. MPAS ensemble average (solid red line), MPAS member 70 (dashed red line), and control member GEFS (solid blue line) are compared to ERA5 (solid black line). 131

4.13 Experiment two spatially averaged profiles of MITA increment method for potential temperature (a) over the Arctic, (b) over land in the Arctic, (c) over ocean in the Arctic, and (d) over seaice in the Arctic. Each colored line represents a different term in equation 4.1. The black line is the residual which is the difference between the RHS and LHS in equation 4.1. Error bars are included on the total accumulated average model tendency profiles only at points where the 70% confidence intervals (Cavallo et al. 2016) do not cross zero, indicating the profile values are statistically different from zero. 132

4.14 Experiment two spatially averaged accumulated model tendencies for potential temperature (a) over the Arctic, (b) over land in the Arctic, (c) over ocean in the Arctic, and (d) over seaice in the Arctic. Each colored line represents a different physics tendency representing potential temperature. . 133

4.15 Experiment two spatially averaged profiles of MITA increment method for water vapor (a) over the Arctic, (b) over land in the Arctic, (c) over ocean in the Arctic, and (d) over seaice in the Arctic. Each colored line represents a different term in equation 4.1. The black line is the residual which is the difference between the RHS and LHS in equation 4.1. Error bars are included on the total accumulated average model tendency profiles only at points where the 70% confidence intervals (Cavallo et al. 2016) do not cross zero, indicating the profile values are statistically different from zero. 134

4.16 Experiment two spatially averaged accumulated model tendencies for water vapor (a) over the Arctic, (b) over land in the Arctic, (c) over ocean in the Arctic, and (d) over seaice in the Arctic. Each colored line represents a different physics tendency representing qv. 135

4.17 Arctic spatially averaged (a,c) MITA increment method and (b,d) accumulated model tendencies for zonal wind for (a,b) experiment one and (c,d) experiment two. (a,c) Each colored line represents a different term in equation 4.1. The black line is the residual which is the difference between the RHS and LHS in equation 4.1. Error bars are included on the total accumulated average model tendency profiles only at points where the 70% confidence intervals (Cavallo et al. 2016) do not cross zero, indicating the profile values are statistically different from zero. (b,d) Each colored line represents a different physics tendency representing the zonal wind. 136

4.18 Water vapor profiles used to initialize WRF single column simulations. (a) Represents an increase in water vapor while (b) represents a decrease in water vapor. Shading represents distribution of water vapor within the profiles. 137

4.19 WRF single column model (a) accumulated total tendencies and (b) accumulated longwave radiation tendency averaged over 105 sea ice grid points spanning experiment one cycling period. Shading represents 95% of the adjusted water vapor distribution. The solid lines represent the mean of the adjusted water vapor distribution. 138

4.20 (a) Black line with dots represents the flight path through TPV of interest. Red line with dots represents the dropsonde profiles used to time-height cross-sections. (b) Time-height cross-section showing dropsonde potential temperature (colorfill), ERA5 2 PVU surface (thick black line), and dropsonde wind speed (white contours). (c) Time-height cross-section showing dropsonde potential temperature (colorfill), ERA5 2 PVU surface (thick black line), and dropsonde relative humidityy (white contours). 139

4.21 Schematics showing MPAS-DART cycling procedures for (a) without NAWDEX observations assimilated and (b) when NAWDEX observations are assimilated. The black lines correspond to MPAS forecasts while the red lines are the data assimilation step. The shaded boxes represent the observation window. 140
4.22 Analysis increment associated only from NAWDEX dropsonde (a) temperature, (b) water vapor, (c) zonal-wind, and (d) meridional wind. 141
4.23 TPV composite cross-section differences between experiments with NAWDEX dropsondes versus without NAWDEX dropsonde observations for (a) potential temperature, (b) Ertel's potential vorticity (EPV), (c) water vapor, and (d) normal component of wind (positive values correspond to wind coming out of page). 142
4.24 Eigenvalue spectrum's for (a) spatial EOF analysis and (b) NAWDEX TPV Multivariate EOF (MVEOF) analysis. The calculation of the eigenvalue spectrum follows the equations in North et al. (1982). 143
4.25 EOFs (a) 1 and (b) 2 of the 2 PVU potential temperature analysis field for the NAWDEX TPV for both experiments with NAWDEX dropsondes assimilated and without NAWDEX dropsonde assimilated. Proability density functions (PDF) are computed for each experiments PCs. 144
4.26 Multivariate EOF 1 that contains cross-section analysis potential temperature, normal component wind speed, and water vapor for both experiments with NAWDEX dropsondes assimilated and without NAWDEX dropsonde assimilated. 145

4.27 2 PVU potential temperature differences between experiments with NAWDEX observations assimilated vesus without NAWDEX observations assimilated valid at forecast hour (a) 0, (b) 12, (c) 24, (d) 36, (e) 48, and (f) 60. Hatching represents significant differences at the 95% confidence level. Significance testing was calculated using a student t-test. The grey contours are ensemble mean 2 PVU potential temperature from the experiment where NAWDEX observations were assimilated. 146
4.28 TPV counts (colorfill), median track position (black line), and median minimum potential temperature associated with tpv (colored dots) for the 96 realization of the NAWDEX TPV for experiments (a) with NAWDEX dropsondes assimilated and (b) without NAWDEX dropsondes assimilated. . . . 147
4.29 Potential temperature distribution throughtout the forecast for the NAWDEX TPV for experiments with NAWDEX dropsondes assimilated (red) and without NAWDEX dropsondes assimilated (black). The shading shows the range of 95% of the potential temperature distribution and the dotted line is the median of the potential temperature distribution. 148
4.30 MPAS-DART member 70 and ERA5 TPV characteristics for TPV tracks spanning the entire cycling period for (a) experiment one and (b) experiment two. Time series shows median TPV potential temperature (lines with dots), spread in the potential temperature associated with TPVs (shading), and number of TPVs that last some lifetime (dot-dashed line, values on the y-axis). MPAS-DART member 70 TPV tracks were computed using 6-hour forecasts while ERA5 TPV tracks were computed using analyses. . . 149

4.31 MPAS-DART member 70 and ERA5 TPV characteristics for TPV tracks spanning the entire cycling period for (a) experiment one and (b) experiment two. Box and whisker plot shows minimum potential temperature for each TPV that last longer that two days. MPAS-DART member 70 TPV tracks were computed using 6-hour forecasts while ERA5 TPV tracks were computed using analyses. 150

5.1 Diagram showing a TPV (blue circle) and mid-latitude interaction. Times -5 to 0 are analysis representative of a TPV moving out of the Arctic and interacting with a jet streak (red). Times 0 to +7 are forecast representative of the height field (black contours) propagating downstream. The different black contours represent the uncertainty associated with the forecast height field. 166

5.2 Seasonal climatology of gridded RWI segments (frequency is per month and per 1° by 1° grid box) for (a) DJF, (b) MAM, (c) JJA, and (d) SON. The value of 0.1 is highlighted by the black contour. Figure is from from Röthlisberger et al. (2016) 167

5.3 RWI event centered composites of 2 PVU potential temperature anomalies (colorfill, K) and windspeed anomalies (contours, knots) for (a) 15th percentile ((within less than 1000 km) and (b) 85th percentile (more than 2500 km) concerning TPV RWI distance. Anomalies were calculated from a ERA5 climatology spanning 1980 to 2010. 168

5.4 ERA5 analysis of 2 PVU potential temperature (colorfill, K), 2 PVU wind (barbs, knots), and mean sea level pressure (black contours, hPa) for (a) 12 hours prior to RWI, (b) time of RWI, (c) 12 hours after, (d) 24 hours after, (e) 36 hours after, (f) 48 hours after, (g) 60 hours after and (h) 72 hours after the RWI event occurred. The gold star represents the location of the identified RWI event. Analysis cross-section through TPV of interest is denoted by the white line. 169

5.5 MPAS-DART analysis and forecasts ensemble mean of 2 PVU potential temperature (colorfill, K), 2 PVU wind (barbs, knots), and mean sea level pressure (black contours, hPa) for (a) 12 hours prior to RWI, (b) time of RWI, (c) 12 hours after, (d) 24 hours after, (e) 36 hours after, (f) 48 hours after, (g) 60 hours after and (h) 72 hours after the RWI event occurred. The gold star represents the location of the identified RWI event. Analysis cross-section through TPV of interest is denoted by the white line. 170

5.6 North-south cross-section through TPV of interest showing potential vorticity (colorfill, PVU), potential temperature (black contours, K) and zonal windspeed (white contours, knots) for (a) ERA5 and (b) MPAS-DART ensemble mean analysis. 171

5.7 MPAS-DART ensemble average 2 PVU potential temperature (colorfill, K), 2 PVU wind (barbs, knots), and mean sea level pressure (black contours, hPa) for (a) at the time of the RWI event and (b) 72 hours after initial RWI event. Black boxes denote the area that minimum sea level pressures were computed for each ensemble member. 172

5.8 Histograms showing analysis (a) minimum potential temperature and (b) distance to the jet stream for the TPV. 173

5.9 Sensitivity (Eq. 5.2) of 250 hPa windspeed to analysis minimum potential temperature associated with TPV of interest for forecast hours (a) 0, (b) 6, (c) 12, and (d) 18. Black contours are the ensemble mean 250 hPa geopotential heights (m) surface. Black stars indicate relative position of TPV of interest. RWI occurred on 31 December 2011 at 00z. 174

5.10 Sensitivity (Eq. 5.2) of 250 hPa windspeed to the distance from the jet stream to TPV in the analysis for forecast hours (a) 0, (b) 6, (c) 12, and (d) 18. Black contours are the ensemble mean 250 hPa geopotential heights (m) surface. Black stars indicate relative position of TPV of interest. RWI occurred on 31 December 2011 at 00z. 175

5.11 Sensitivity (Eq. 5.2) of 250 hPa windspeed to analysis minimum potential temperature associated with TPV of interest for forecast hours (a) 0, (b) 6, (c) 12, and (d) 18. Black contours are the ensemble mean 250 hPa geopotential heights (m) surface. Black stars indicate relative position of TPV of interest. RWI occurred on 31 December 2011 at 00z. 176

5.12 Sensitivity (Eq. 5.2) of 250 hPa windspeed to the distance from the jet stream to TPV in the analysis for forecast hours (a) 0, (b) 6, (c) 12, and (d) 18. Black contours are the ensemble mean 250 hPa geopotential heights (m) surface. Black stars indicate relative position of TPV of interest. RWI occurred on 31 December 2011 at 00z. 177

5.13 Sensitivity (Eq. 5.2) of precipitable water (Kg m^{-2}) to the distance from the jet stream to TPV in the analysis for forecast hours (a) 6, (b) 12, (c) 18, and (d) 24. Black contours are the ensemble mean precipitable water. Black dashed contours are the ensemble mean 250 hPa geopotential heights (m) surface. Black stars indicate relative position of TPV of interest. RWI occurred on 31 December 2011 at 00z. 178

5.14 Sensitivity (Eq. 5.2) of poleward moisture flux (cm s^{-1}) to the distance from the jet stream to TPV in the analysis for forecast hours (a) 6, (b) 12, (c) 18, and (d) 24. Black contours are the ensemble mean poleward moisture flux. Black dashed contours are the ensemble mean 250 hPa geopotential heights (m) surface. Black stars indicate relative position of TPV of interest. RWI occurred on 31 December 2011 at 00z. 179

5.15 Histogram of minimum sea level pressures from each ensemble member within the sensitivity box. 180

5.16 Sensitivity (Eq. 5.2) of mean sea level pressure to potential vorticity on 320 Kelvin surface for forecast hours (a) 12, (b) 24, (c) 36, and (d) 48. Black contours are the ensemble mean potential vorticity (PVU) on the 320 Kelvin potential temperature surface. The black box represents the sensitivity box where minimum surface pressures where computed for each ensemble member. Black stars indicate relative position of TPV of interest. Black circle is relative position of surface cyclone. RWI occurred on 31 December 2011 at 00z. 181

5.17 Sensitivity (Eq. 5.2) of mean sea level pressure to wind speeds on the 320 Kelvin surface for forecast hours (a) 12, (b) 24, (c) 36, and (d) 48. Black contours are the ensemble mean potential vorticity (PVU) on the 320 Kelvin potential temperature surface. The black box represents the sensitivity box where minimum surface pressures where computed for each ensemble member. Black stars indicate relative position of TPV of interest. Black circle is relative position of surface cyclone. RWI occurred on 31 December 2011 at 00z. 182

5.18 Sensitivity (Eq. 5.2) of mean sea level pressure to precipitable water (Kg m^{-2}) for forecast hours (a) 12, (b) 24, (c) 36, and (d) 48. Black contours are the ensemble mean precipitable water. Black dashed contours show the ensemble mean 2, 3, and 6 potential vorticity (PVU) contours on 320 Kelvin potential temperature surface. The black box represents the sensitivity box where minimum surface pressures where computed for each ensemble member. Black stars indicate relative position of TPV of interest. Black circle is relative position of surface cyclone. RWI occurred on 31 December 2011 at 00z. 183

5.19 Sensitivity (Eq. 5.2) of mean sea level pressure to poleward moisture flux (cm s^{-1}) for forecast hours (a) 12, (b) 24, (c) 36, and (d) 48. Black contours are the ensemble mean poleward moisture flux. Black dashed contours show the ensemble mean 2, 3, and 6 potential vorticity (PVU) contours on 320 Kelvin potential temperature surface. The black box represents the sensitivity box where minimum surface pressures where computed for each ensemble member. Black stars indicate relative position of TPV of interest. Black circle is relative position of surface cyclone. RWI occurred on 31 December 2011 at 00z. 184

Abstract

The observed rapid changes in the Arctic are important to quantify not only for understanding the region, but also for understanding how processes between the Arctic and lower latitudes can interact to culminate in high-impact weather events. The tropopause polar vortex (TPV) is an Arctic feature that can interact with mid-latitude atmospheric flow, in which the maintenance and intensification of TPVs depends on diabatic processes. Improved knowledge and a better representation of TPV-mid-latitude interactions in numerical prediction models could extend forecast skill beyond the present-day barrier of 7-10 days.

This study investigates TPVs in the Arctic and their interactions with mid-latitude atmospheric flow using a newly developed global modeling system. This modeling system couples an ensemble Kalman filter (EnKF) data assimilation software (DART) with the Model for Prediction Across Scales (MPAS) global model called MPAS-DART. This system utilizes a newly developed non-hydrostatic global model that allows for smooth transitions from coarse to fine mesh resolutions. The EnKF data assimilation technique allows for flow-dependent background error covariances within MPAS-DART, which is especially important in data sparse regions like the Arctic.

Evaluation of MPAS-DART over the Arctic shows reasonable consistency between the model and observations, however, there are some notable points for improvement. There is a cold bias in the upper-troposphere and lower-stratosphere levels where TPVs are often found, which is a result of too much cooling from the model's longwave radiation scheme. This overactive longwave cooling is associated with a moisture bias found in the same layer. Assimilating special dropsonde observations from a field campaign flight mission through a TPV mitigates the moisture bias, especially in analyses. Implementing an improved moisture initialization procedure is able to alleviate the moisture bias, even in the absence of special observations. The moisture bias and associated longwave cooling in MPAS-DART results in less intense TPVs later in their lifetimes compared to ERA-5.

After quantifying the bias patterns in MPAS-DART, an interaction of TPVs with mid-latitude flow is investigated through the hypothesis that TPVs can initiate Rossby wave packets. Referred to as Rossby wave initiation (RWI), flow patterns relevant to RWI development are more sensitive to TPV position relative to the jet stream than to TPV intensity. The moisture field, a well-documented source of RWI, is not found to be sensitive to TPV characteristics. A surface cyclone that develops downstream of the RWI is sensitive to the position and magnitude of potential vorticity and windspeed in the upper levels. Lastly, it is found that surface cyclone strength is sensitive to moisture with stronger cyclones associated with increased moisture.

This study is one of the first to demonstrate the utility of a state-of-the-art global modeling system in the Arctic for process studies. While room remains for improvement, the tool enabled valuable scientific exploration of a recently documented Arctic feature, TPVs. Using tools such as this one allow for improved understanding of complex atmospheric processes, their evolution, and the the potential feedbacks between processes, which is particularly powerful in a remote and data-sparse region like the Arctic.

Chapter 1

Introduction

In the last coupled decades, it has been observed that the Arctic is undergoing rapid changes when compared to other locations on the globe (Richter-Menge and M. Jeffries 2019). There are still uncertainties on how processes in the Arctic can influence the weather that is occurring in the mid-latitudes (Barnes 2013). The knowledge gained on physical interactions are critical to understanding climate change. In order to increase our knowledge, an improved understanding of the processes in the Arctic are required along with how these processes can influence mid-latitude weather (Jung et al. 2014). This requires an integration of knowledge on time-scales ranging from climate to synoptic time-scales. Due to the sparse number of conventional observations in the Arctic, previous studies heavily rely on NWP models to study Arctic processes. However, NWP errors are larger over the Arctic (Fig. 1.3) so this implies some of the key processes are missing in the model's physical representation of the atmosphere (Jung et al. 2016). This study used a global NWP model coupled with data assimilation to investigate the impacts an Arctic based feature can have on mid-latitude weather.

1.1 The Arctic

The Arctic generally includes the region around the Earth's North Pole, which is mostly composed of the Arctic Ocean. Sea ice is a common feature in this region, and the surface area and thickness of sea ice has a seasonal cycle (Parkinson and Cavalieri 1989). Different land masses border the Arctic Ocean, adding to the surface complexity already present in this region. The most common specific definition of the Arctic is the region north of the Arctic circle, or the 66° degree north latitude band (Serreze and Barry 2014). The Arctic Circle is the latitude above which the sun does not set on the summer solstice,

and does not rise on the winter solstice (Little 1968). Beyond this common definition, scientists have described the spatial coverage of the Arctic in various ways. Some studies have used the area north of the Arctic tree line, while other studies have used a defined temperature as the boundary for the Arctic (Armstrong et al. 1978; Smithson et al. 2013). In this work the Arctic will be defined as the area north of the 60° degree latitude band. This choice provides more spatial coverage of the region where important Arctic processes are commonly observed for comparison and evaluation of our modeling system.

The Arctic cryosphere is an important component of the Earth-system climate which has experienced unprecedented changes over the last couple of decades. These changes have led the National Science Foundation (NSF) to promote the goal of Navigating the New Arctic to one of the agency's "10 Big Ideas for Future Investments." The impacts these unprecedented changes will have on the earth system remain poorly understood. September sea ice extent has declined at a rate of 12.4% per decade since 1979 (Stroeve et al. 2011), and the decreasing trend in sea ice extent has continued through fall of 2019. Along with a decrease in ice extent, there has been a 40% decrease in winter sea ice thickness (Kwok and Rothrock 2009) and around 80% loss in volume (Overland et al. 2014). While sea ice has received the most attention from researchers, snow cover has also seen a decline in recent years. Snow cover during the summer months has decreased at a rate double of the decrease in sea ice extent during September (Derksen and Brown 2012). The decrease in snow cover during the spring months has led to an increase in Northern Hemisphere surface temperatures over landmasses and has contributed to the decrease in summer Arctic sea ice (Matsumura et al. 2014). The combination of sea ice and snow cover loss in the spring and summer months can help explain the increase in Arctic surface temperatures. Furthermore, the increase in the land-sea temperature gradient has resulted in an increase Arctic cyclone activity and intensity (Day and Hodges 2018). This increase in Arctic surface temperatures has been referred to as "Arctic amplification".

The Arctic is undergoing rapid changes in surface temperatures at more than double the global rate (Blunden and Arndt 2013). The rapid warming found in the Arctic as compared to lower latitudes is referred to as Arctic amplification (Serreze and Francis 2006). This warming is most pronounced during the winter season (Screen et al. 2013) during the sea ice re-freeze. Furthermore, observations are not only showing a consistent signal of Arctic amplification, climate model simulations forced with increased greenhouse gas concentrations also project increased surface temperatures in the Arctic (Holland and Bitz 2003). There are several proposed theories that are hypothesized to contribute to Arctic amplification, including local drivers from greenhouse gas forcing (Gillett et al. 2008), changes in snow- and ice-albedo feedbacks due to the decrease in snow and sea ice coverage (Winton 2006; Screen et al. 2012), aerosol concentration changes (Shindell and Faluvegi 2009), and changes in Arctic cloud cover and water vapor (Francis and Hunter 2006; Graversen and Wang 2009). While the local drivers in the Arctic might be most impactful, one can not rule out senstivities of Arctic temperature changes to the poleward transport of heat and moisture from the mid-latitude weather systems into the high latitudes (Graversen et al. 2008).

A decrease in Arctic sea ice is concurrent with a rapid increase in Arctic atmospheric surface temperatures temperatures (Screen and Simmonds 2010a). Arctic sea ice strongly controls near-surface conditions in the Arctic, when thus can influence regional – and possibly remote – climates. Quite unlike sea ice, open ocean water has a low albedo leading to much more absorption of incoming solar radiation in areas where sea ice has receded. Due to more open ocean in that last decade, more energy has been absorbed leading to a $\sim 4^{\circ}$ C increase in sea surface temperature anomalies in regions presently free of ice (Wood et al. 2013). During the fall, air temperatures become cooler than the ocean surface. This excess heat is then transferred from the ocean to the atmosphere via radiative and turbulent fluxes, warming at least the lower portion of the Arctic atmosphere. Furthermore, the additional heat absorbed by the ocean will slow the growth of sea ice in the winter, both in extent and

thickness (Steele et al. 2008; Inoue and Hori 2011). Due to an increase of warmer open ocean water during the winter, warmer, more moist air masses have been generated over the Arctic ocean and over nearby landmasses which in turn will weaken the meridional temperature gradient (Serreze and Barry 2011; Screen and Simmonds 2010b; Cohen et al. 2014b). These feedbacks imply that Arctic sea ice loss is both a response to and a driver of Arctic amplification. Furthermore, this further shows how complex the Arctic environment is and the importance of better understanding how these coupled Earth-system components interact.

Over the past decade, there has been an increase in extreme heat and rainfall events reported, especially over the northern mid-latitudes (Min et al. 2011; Coumou and Rahmstorf 2012; Westra et al. 2013). Cohen et al. (2014b) showed that several standard extreme temperature and precipitation indices have rapidly increased in both frequency and intensity over in the last couple of decades over mid-latitude land areas (20° - 50°). For example, Cohen et al. (2014b) showed the amount of precipitation on very wet days (exceeded the 95th percentile) increased from 160 to 185 mm and the percentage of warm days (exceeding the 90th percentile) increased by 16%. Along with increased extremes in warm temperature and precipitation, should also include cold extremes in temperature. In general, winter temperatures have had a warming trend since the 1960s and there has been a decrease in frequency of anomalously cold winter days over both the mid- and high-latitudes, but primarily north of 50° N (Cohen et al. 2014b). However, over the past decade, with the lowest minimum September sea ice extents since satellite observations began, several winters following low sea ice minima have been unusually cold across Northern mid-latitude landmasses (Cohen et al. 2012; Liu et al. 2012). While global warming can be linked with increased warm temperatures and precipitation, linkages to cold events are less direct. Coupled climate models under greenhouse-gas forcing project winter temperature amplification over the Northern Hemisphere landmasses would warm faster in winter as compared

to other seasons (Holland and Bitz 2003). This might help illustrate that there is still unknown processes attributing to the cold events during the winter that we do not understand yet.

To further understand the impact Arctic amplification is having on mid-latitude weather, we must determine how warming temperatures are impacting the high latitudes. Most studies agree that the first order impact sea ice melting and warmer temperatures will be to modify the atmospheric boundary layer over the Arctic (Screen and Simmonds 2010b; Serreze and Barry 2011). How that energy travels out of the Arctic and into the mid-latitudes is still not understood. Cohen et al. (2014b) offer up three dynamical pathway frameworks on how Arctic amplification can effect the mid-latitudes (Fig. 1.1): 1) changing storm tracks in the North Atlantic, 2) modified jet stream characteristics, and 3) anomalous planetary wave configurations.

The first dynamical pathway that will be discussed is how Arctic amplification can effect storms tracks (Cohen et al. 2014b). Large-scale variability in the extratropical atmosphere is dominated by shifts in storm tracks, often expressed as changes in atmospheric modes (Woollings and Blackburn 2012). Changes in storm tracks associated with the North American oscillation (NAO) and Arctic oscillation (AO) have a strong influence on temperature and precipitation variability over the North Atlantic sector (Bader et al. 2011). When the NAO/AO is in a positive phase, winters over Northern Hemisphere extratropical continents are mild and with cold temperatures in the Arctic while storm tracks shift towards the pole. When the NAO/AO is in a negative phase, winters are more severe over the Northern Hemisphere extratropical continents and are climatologically mild in Arctic with the storm tracks shifted more towards the equator. Recent observations of wintertime temperatures project strongly on the negative phase of the AO (warm Arctic–cold continents), which reflects the negative trend in the AO over the past couple decades (Cohen et al. 2012). Furthermore, when climate models are forced with latitudinal and regionally variations in heating they are accompanied by changes in NAO/AO (Wu et al. 2007; Bader

et al. 2011). The link between Arctic amplification and the NAO/AO remain unclear and requires more investigation into how much the changes in NAO/AO can be contributed to Arctic amplification and not variability in sea ice and snow coverage. Lastly, there have been some discrepancies between studies on how the NAO/AO will respond to Arctic amplification however there are two general outcomes: 1) there are studies that show a shift to a negative NAO/AO than to a positive NAO/AO (Screen et al. 2013; Tanaka and Seki 2013) and 2) simulations show that the response of NAO/AO to sea ice loss is smaller than natural variability (Magnusdottir et al. 2004; Liu et al. 2012; Cohen et al. 2014b).

The second dynamical pathway discussed is the effect of Arctic amplification on the polar jet stream (Cohen et al. 2014b). The meridional temperature gradient between the Arctic and the mid-latitudes is the fundamental driver for the polar jet stream (Wallace and Hobbs 2006), meaning a weakening in the gradient from Arctic amplification would result in a weaker jet (Haarsma et al. 2013; Francis and Vavrus 2015). A weaker jet results in slower eastward movement of planetary waves due to larger meanders and slower momentum in the jet stream, which could lead to more persistent weather patterns (Francis and Vavrus 2012). Furthermore, an increase in temperature, as a result of Arctic amplification, would result in increased thickness over the Arctic, which would allow ridge peaks to extend farther into the Arctic, increasing north-south flow (Francis and Vavrus 2012). However, a more recent study has shown there is not a positive tend in elongated meridionally planetary waves as a result to Arctic amplification so further investigation is required (Barnes 2013). Persistent weather, a result of the increased meridional flow, has been linked to the frequency of extreme weather events over the Northern Hemisphere landmasses (Petoukhov et al. 2013; Screen and Simmonds 2014). There are still challenges in linking Arctic amplification to a change in jet speed and location. Other factors need to be included such as feedbacks from synoptic-scale weather systems and the upper-level north-south temperature gradient (Cohen et al. 2014b; Lee et al. 2019). Observational support for the impacts of the theory related to a weakening zonal jet component is lacking, mainly in whether Arctic

amplification leads to larger amplified waves along with slower moving weather patterns (Allen and Sherwood 2008). The need for additional support is not surprising given that Arctic amplification is a relatively new idea and the large natural variability.

The third proposed dynamical pathway linking Arctic amplification to mid-latitude weather is modifications to large-scale Rossby waves from changes in sea ice and snow cover (Cohen et al. 2014b). Extensive snow cover over Eurasia can lead to higher sea level pressure, induced by radiative cooling, which may lead to larger Rossby wave (wave numbers 1-3) that increase vertical propagation of energy into the stratosphere (Fletcher et al. 2009; Allen and Zender 2011). Cohen et al. (2014a) proposed that the atmospheric response lags the changes to Eurasia snow cover by a month due to the feedback timescales associated with energy traveling from the surface to the stratosphsere then feedback into the tropopshere. Other studies have linked the reduction of fall-winter sea ice, especially over the Barent and Kara seas, to greater mid-tropopsheric geopotential heights over the Arctic with a trough over Eurasia (Honda et al. 2009; Petoukhov and Semenov 2010). The mid-tropospheric response to the snow cover and/or the reduction in sea ice provides a pathway to transfer information on what is occurring at the surface to the upper-troposphere/lower-stratosphere, which ultimately plays a role in mid-latitude weather through teleconnections. However, like most studies, there are shortcomings to the proposed ideas above which includes disagreement between observations and climate model simulated wave responses to snow cover (Cohen et al. 2014a; Hardiman et al. 2008) and reduced statistical significance linking sea ice and atmospheric responses due to the short sea ice datasets (Cohen et al. 2013).

The complexity and remoteness of the Arctic makes it a challenging region to study. Due to limited convectional observation coverage, studies have relied on using numerical weather models when trying to understand Arctic processes and how theses Arctic processes impact the mid-latitude weather. Due to the different types of surface characteristics and connections between them means each Earth-system component's processes needs to

be represented correctly if progress is to be made. In order to make progress in model representation of complex Arctic processes, each component of the Earth system (including the atmosphere) and their respective interconnections needs to be represented in a modeling system. Furthermore, the rapid changes happening in the Arctic have been shown to have an impact on the mid-latitude weather. Better understanding of the Arctic impact on mid-latitude weather is still needed not only on the climate time-scale but also on synoptic time-scale. The ideas discussed above further supports the idea of better understanding of how the Arctic or Arctic base features can impact mid-latitude weather.

In this study, the ability of a newly developed global numerical weather model to predict the Arctic is evaluate but on synoptic timescales compared to climate timescales mentioned above. Better understanding of Arctic weather on these shorter time scales would help in our prediction of the Arctic climate. One particular Arctic feature will be discussed in this work is call the tropopause polar vortex or TPV.

1.2 Tropopause Polar Vortices (TPVs)

TPVs are a common dynamic feature in the Arctic and their role in Arctic-middle latitude interactions remains relatively unaddressed. From a predictability standpoint, correctly forecasting TPVs is important due their links to cyclogenesis in the mid-latitudes (Kleinschmidt 1950; Bosart et al. 1996a) and to initiation of rossby waves when interacting with the jet stream (Röthlisberger et al. 2016). TPVs are long-lived, coherent vortices that are defined by material closed contours on the dynamic tropopause which is represented by potential vorticity (PV) (Cavallo and Hakim 2009). In the absence of diabatic and frictional effects, PV is conserved, which is convenient when tracking these features. TPVs on the dynamic tropopause are associated with closed contours of potential temperature assuming adiabatic conditions (Cavallo and Hakim 2009). When observing the dynamic tropopause, cold-core TPVs are observed as cyclonic circulations with a lower tropopause and warm-core TPVs are observed as anti-cyclonic circulations with a higher tropopause (Cavallo

and Hakim 2009). Cold-core cyclonic TPVs are associated with anomalously warm (cold) temperatures above (below) the tropopause, positive PV anomalies above the tropopause, and anomalously low (high) moisture above (below) the tropopause (Cavallo and Hakim 2010). Characteristics of TPVs include radii of around 500 km and potential temperature amplitudes of about 8 K (Hakim 2000). Furthermore, TPVs have preferred locations in the Arctic and can have life spans that last up to a month or more (Hakim and Canavan 2005a). Due to the fact that TPVs reside mainly in the Arctic away from the jet stream, it is believed that diabatic effects are important to TPV maintenance and intensification (Cavallo and Hakim 2010).

To understand how the diabatic effects can modify TPVs, we first look at Ertel's Potential Vorticity (Pedlosky 1992) as it describes TPV amplitude

$$\Pi = \frac{1}{\rho}\omega_a \cdot \nabla\theta, \tag{1.1}$$

where ρ is the density, ω_a is the absolute vorticity, and U and θ are 3D fields of wind and potential temperature. Applying the time rate of change derivative to Eq. 1.1 provides a way to predict intensity change and neglecting the effects of frictional processes since they are small at the tropopause, we arrive at an equation to quantify TPV intensity changes due to diabatic effects:

$$\frac{D\Pi}{Dt} \simeq \frac{\omega_a}{\rho} \cdot \nabla \frac{D\theta}{Dt}. \tag{1.2}$$

The diabatic effect is contained within the $\frac{D\theta}{Dt}$ term which can be expanded to represent each diabatic effect represented in the numerical model.

$$\frac{D\theta}{Dt} = (\dot{\theta}_{radiation} + \dot{\theta}_{latent\ \ heating} + \dot{\theta}_{pbl} + \dot{\theta}_{convective} + \dot{\theta}_{mixing}). \tag{1.3}$$

The above diabatic tendency terms ($\dot{\theta}_{radiation}, \dot{\theta}_{latentheating}, \dot{\theta}_{pbl}, \dot{\theta}_{convective}, \dot{\theta}_{mixing}$) come from physics parameterization schemes that represent model tendencies from radiation, latent heating, boundary layer processes, non-resolved convection, and numerical disspation. Furthermore, the Arctic is characterized by low temperatures and widespread cloudiness, which implies that diabatic effects from radiative processes and latent heating will be the

largest in equation 1.3 (Curry et al. 1996). Ignoring the other small diabatic terms and only considering the vertical component of vorticity, we arrive at

$$\frac{D\Pi}{Dt} \simeq \frac{\zeta_a}{\rho}\frac{\partial}{\partial z}(\dot{\theta}_{longwave\ \ radiation} + \dot{\theta}_{shortwave\ \ radiation} + \dot{\theta}_{latent\ \ heating}), \tag{1.4}$$

where ζ_a is the vertical component of absolute vorticity. Equation 1.4 describes how EPV will change in time due to diabatic processes represented in the NWP model.

Studies have found that intensity changes are likely due to local factors surrounding the TPV, such as radiative cooling and latent heating Cavallo and Hakim (2009, 2010) . Studies have shown that cloud-top radiative cooling had the most influence on increasing EPV while latent heating acted to destroy EPV, but on a much smaller magnitude (Cavallo and Hakim 2009, 2010). In further investigation of the radiative effects, Cavallo and Hakim (2013) found maximum TPV intensification was occurring when clouds contributed to the longwave cooling. In the absence of clouds TPV intensification was primary due to an enhanced vertical water vapor gradient near the tropopause. The representation of the vertical gradient in moisture is important when trying to accurately forecast TPV characteristics, especially during the cloudless times during the winter (Shupe 2011). Due to lack of high-quality observations present over the Arctic, it can be hard to correctly represent this gradient near the tropopause, perhaps degrading forecasts.

TPVs are most frequent in the Arctic regardless of the season (Fig. 1.4). There are two preferred pathways where TPVs exit the Arctic and move into the mid-latitudes: 1) North Pacific and 2) west of Greenland. These two pathways are more pronounced during the wintertime while not as defined in the summertime (Fig. 1.4). Furthermore, jet streak counts greater than 70 m s^{-1} are overall greater in the winter, implying TPVs could be having a dynamical impact on the jet streaks that are located in this region.

For this study, evaluation of the representation of the vertical gradient in moisture within the ensemble assimilation cycling system will be performed along with verification to observations. Since the ensemble contains multiple forecasts, investigation into TPV intensity forecast sensitivities associated with the vertical gradient in moisture are also considered.

1.3 Rossby Waves and Downstream Predictability

Predictability is used here to quantify how well we are able to predict some atmospheric feature. Predictability can be split into two categories: 1) practical predictability and 2) intrinsic predictability (Sun and Zhang 2016). Practical predictability is described as the ability to predict some feature based on current data assimilation techniques to obtain the optimal initial state while using the best forecast model available (Lorenz 1982). Intrinsic predictability is described as the extent to which prediction is possible if a nearly perfect initial state is known while using a nearly perfect forecast model (Lorenz 1969). Practical predictability can be limited by uncertainties found in the observations, data assimilation techniques and the forecast model (Zhang et al. 2007). Intrinsic predictability suggests that there will be a limit of predictability for atmospheric features even if the initial condition and forecast model are nearly perfect (Melhauser and Zhang 2012). This study will focus on the practical predictability aspects since our initial states and forecast models are not considered to be perfect. Furthermore, this study aims to investigate the downstream predictability, or how differences in the initial state impact the forecasts.

Rossby waves, represented by undulations in zonal flow which are diagnosed by meridional wind , v, are an atmospheric feature important to large-scale meteorological processes (Rossby 1939). Rossby waves owe their existence to gradients in potential vorticity from a poleward gradient in the Coriolis force (Hoskins et al. 1985). Rossby waves are able to transfer energy, heat and moisture across large distances, which allows there to be covariability in atmospheric properties between remote places (Wallace and Gutzler 1981; Branstator 2002). Usually Rossby waves predominately travel downstream in packs or wave trains referred to as Rossby wave packets (RWPs) (Chang 2000). One can represent the speed of the RWPs using the dispersion relation computing phase speed and group velocity (Holton 2004). The phase speed represents the speed of individual troughs and ridges, while the group velocity describes the speed of propagation of the entire RWP

(Wirth et al. 2018). In the most general case, the phase speed differs from that of group velocity, which gives Rossby waves their dispersive nature (Rossby 1945; Hovmöller 1949). Due to the positive change in planetary vorticity with increasing latitude, the group velocity is greater than the phase velocity which means that Rossby wave envelope moves eastward faster than the individual troughs and ridges. Since Rossby waves are dispersive and flow is west to east, this implies that an initial wave packet, that is limited in zonal extent initially, will gradually extend downstream over a larger region as time passes.

The generation of a Rossby wave would first start with a single occurrence of a ridge or trough in a undisturbed zonal flow. Early work using idealized numerical modeling investigated the generation of Rossby waves or RWPs by applying perturbations to a initially unperturbed jet (Simmons and Hoskins 1979; Schwierz et al. 2004a). In the real atmosphere, there are a wide range of potential processes and dynamical features that can play the role of the initial perturbation, including recurving tropical cyclones (Jones et al. 2003), mesoscale convective systems (Rodwell et al. 2013), warm conveyor belt outflows associated with extratropical cyclones (Madonna et al. 2014), and TPVs (Röthlisberger et al. 2018), which are a focus in this work. Additionally, wave breaking, which usually marks to the end of one RWP, can excite new Rossby wave or RWP growth (Martius et al. 2010). Most of the early work on Rossby wave or RWP dynamics is based on dry balanced flow. Most of the features discussed above have diabatic processes associated with them leaving open questions about the role of diabiatic processes. It has been established that moist processes amplify surface cyclones (Danard 1964; Sanders and Gyakum 1980; Bosart 1981; Gyakum 1983; Thorpe and Emanuel 1985; Emanuel et al. 1987; Davis and Emanuel 1991; Davis et al. 1993). Furthermore, latent heat release modifies the tropopause locally, which in turn modifies the jet structure (Kleinschmidt 1950; Hoskins and Berrisford 1988; Davis et al. 1993; Wernli and Davies 1997; Bosart 1999). More recent studies investigating the impacts of latent heat release on RWP modifications include warm conveyor belts (Grams

et al. 2011), organized convection (Rodwell et al. 2013), deep monsoon convection (Stensrud 2013), and tropical cyclones recurving into the mid-latitudes (Quinting and Jones 2016). The impacts of latent heat on RWPs can be thought of as both a direct and indirect process (Wirth et al. 2018). The direct impact of diabatic processes is to generate a negative PV anomaly in upper-troposphere, which than modifies the ridge and may induce downstream effects (Ahmadi-Givi et al. 2004; Chagnon et al. 2013; Chagnon and Gray 2015). The indirect impact is from the upper-tropspheric divergent outflow associated with latent heat release below, which can modify the ridge (Davis et al. 1996; Riemer and Jones 2010; Teubler and Riemer 2016). It has been discussed that the indirect impact – from the divergent outflow – can modifiy the propagation speed and characteristics of troughs (Riemer and Jones 2014). Lastly, the influence of longwave radiation on Rossby waves or RWPs is thought to occur by sharpening the tropopause due to the large vertical gradient in moisture near the tropopause (Zierl and Wirth 1997). Furthermore, the longwave wave cooling can substantially modifiy the PV disturbution near the tropopause within Rossby waves (Chagnon et al. 2013; Teubler and Riemer 2016). Radiative processes can have an impact on the propagation speed of the Rossby waves (Chagnon and Gray 2015; Harvey et al. 2016), however, fundamental questions still remain in fully understanding the impacts.

RWPs can be simulated in forecasts when the RWP is already within the initial analysis (Glatt and Wirth 2014), however, there are documented issues within operational systems at misrepresentation of the RWPs (Gray et al. 2014; Giannakaki and Martius 2016). Studies have shown that information regarding differences in analyses, impact of observations, and forecast errors propagate in the zonal direction at speeds faster than individual troughs and ridges (Hollingsworth et al. 1985; Barwell and Lorenc 1985; Langland et al. 2002), usually at group velocity speeds (Hakim 2005; Anwender et al. 2008; Zheng et al. 2013). The predictability of Rossby wave initiation or RWPs is linked back to the representation of upscale growth of errors associated with diabatic processes to synoptic-scales (Zhang et al.

2003). Errors associated at convective-scales then grow upscale to those related to large-scale balanced motions and displacement of PV gradients by divergent flow, while finally the large-scale components of the errors grow with the background baroclinic instability (Zhang et al. 2007; Hohenegger and Schar 2007; Bierdel et al. 2018; Baumgart et al. 2018). Some studies have suggested that the diabatic process errors are not scale transfered but instead it is coupling of errors from convective scale up to large-scale (Wernli et al. 2002; Parsons et al. 2019). The error growth related to diabatic processes is illustrated in Figure 1.2 where the large PV errors are locally maximized near the mid-latitude jet stream at forecast day 2 (Fig. 1.2a). At forecast day 6 (Fig. 1.2b), the location of the larger PV errors are in the trough and ridges associated with Rossby waves. Lastly, there are other proposed mechanisms for upscale growth in forecast errors that are not associated with baroclinic instability (Snyder 1999; Davies and Didone 2013).

The predictability of the Arctic is important in this study since TPVs spend the majority of their lifetimes in the Arctic. The average forecast skill over the Arctic region is comparable to that over the mid-latitudes, however, there is more variability in the daily forecast skill in the Arctic (Fig. 1.3). The large forecast skill variability could be related to large analysis uncertainty and the sub-optimal use of the limited conventional observations that are found over the Arctic region (Jung et al. 2016). Correct representation of the coupled processes between sea ice and the atmosphere could be leading to forecast errors as well (Jung and Matsueda 2016). When the Arctic region is nudged towards reanalyses, it is shown to increase forecast skill in the mid-latitudes at long forecast leads, hinting there is flow of information coming out of the Arctic (Jung et al. 2014). The reduction in forecast error when nudging the Arctic further emphasizes the need to improve an understanding of polar processes in order to extend the forecast barrier that is currently around a week.

As discussed above, the initiation of Rossby waves can either be from an initial perturbation on the jet stream or through diabatic process associated with convection. Different types of atmospheric features were discussed that could act as the driver to perturbation or

the latent release (Fig. 1.5), including the TPV – a feature of interest in this work. Röthlisberger et al. (2016) identified a local maximum in Rossby wave initiation (RWI) over the North Pacific, which is co-located with the highest probability of a TPV being in that area (Fig. 1.4). Furthermore, pathways for information leaving the Arctic and influencing the mid-latitudes have been shown through an increase in forecast skill while nudging Arctic forecasts towards reanalyses (Semmler et al. 2018). Semmler et al. (2018) found the biggest reduction in wintertime forecast errors over the North Pacific, which is co-located with the maximum in RWIs and the highest probability of TPVs during the winter. The co-location of highest frequency of RWIs and TPVs being over the North Pacific further motivates the need to understand if TPVs can initiate Rossby waves that later in time develop into RWPs. Lastly, this study will investigate the sensitivities in Rossby wave development and the downstream growth to the TPV characteristics, which include position and intensity.

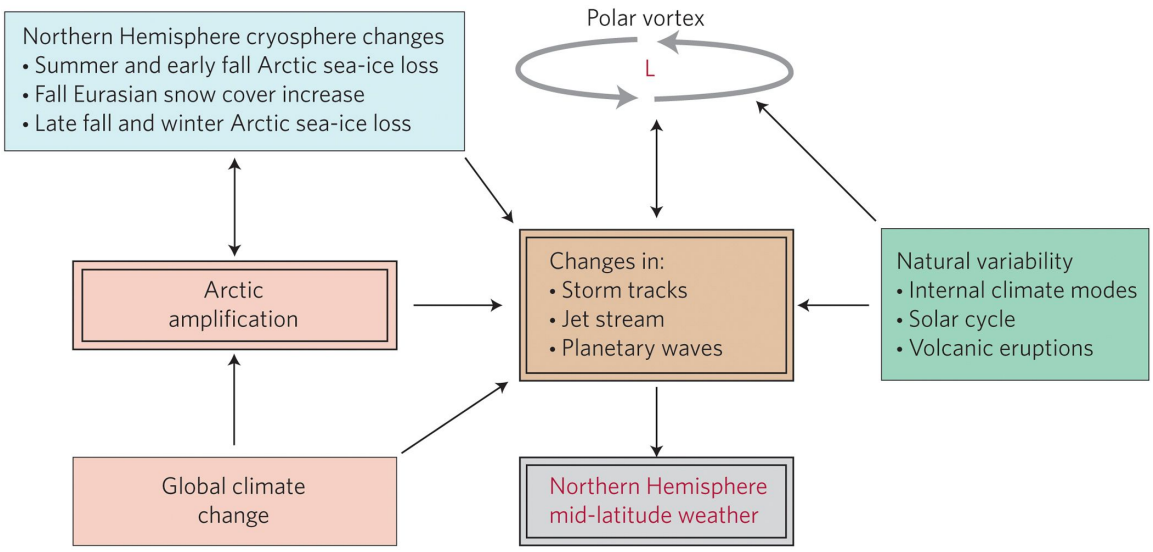

Figure 1.1: Schematic of ways to influence Northern Hemisphere mid-latitude weather. Three major dynamical features for changing Northern Hemisphere mid-latitude weather — changes in the storm tracks, the position and structure of the jet stream, and planetary wave activity — can be altered in several ways. The pathway on the left and highlighted by double boxes is reviewed in this manuscript. Arctic amplification directly (by changing the meridional temperature gradient) and/or indirectly (through feedbacks with changes in the cryosphere) alters tropospheric wave activity and the jet stream in the mid- and high latitudes. Two other causes of changes in the storm tracks, jet stream and wave activity that do not involve Arctic amplification are also presented: (1) natural modes of variability and (2) the direct influence of global climate change (that is, including influences outside the Arctic) on the general circulation. The last two causes together present the current null hypothesis in the state of the science against which the influence of Arctic amplification on mid-latitude weather is tested in both observational and modelling studies. Bidirectional arrows in the figure denote feedbacks (positive or negative) between adjacent elements. Stratospheric polar vortex is represented by 'L' with anticlockwise flow. This figure is from Cohen et al. (2014b)

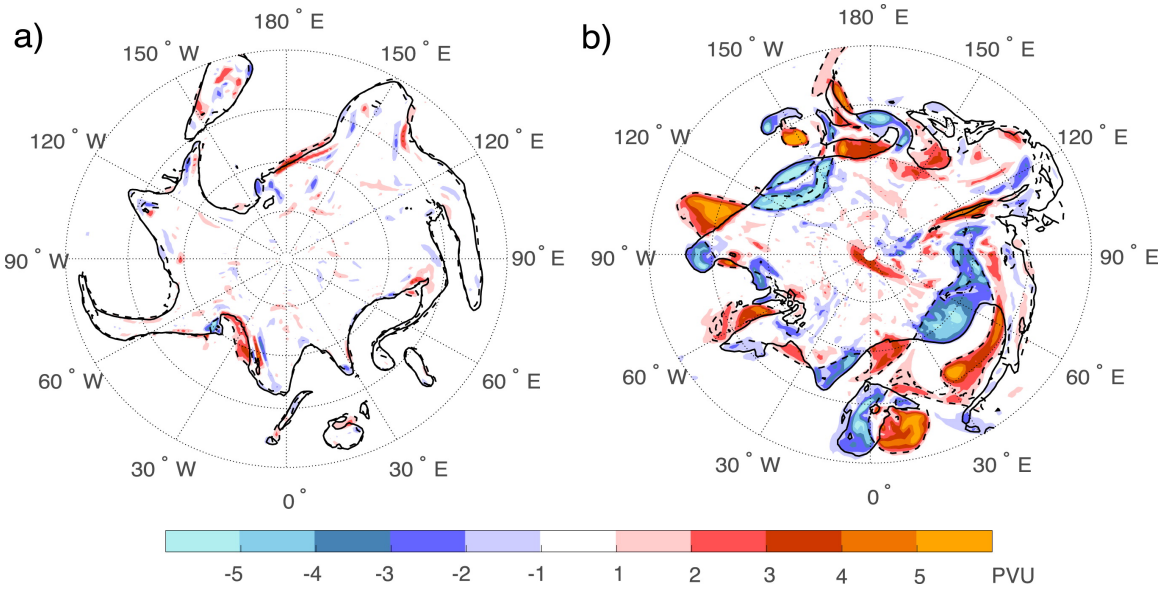

Figure 1.2: Illustration of the amplification and spatial growth of forecast errors in a medium-range forecast from the European Centre for Medium-Range Weather Forecasts (ECMWF, polar stereographic projection, forecast initialized at 0000 UTC 12 Nov 2013). The error is depicted in terms of PV (color shading) on the 320-K isentrope intersecting the mid-latitude tropopause. Errors are defined as the difference between the forecast and the verifying analysis. The dynamical tropopause is depicted by the 2-PVU contour (solid for the analysis, dashed for the forecast). Errors with distinct local extrema in amplitude at (a) forecast day 2 develop into error patterns on the scale of RWPs by (b) forecast day 6. This figure is from Wirth et al. (2018)

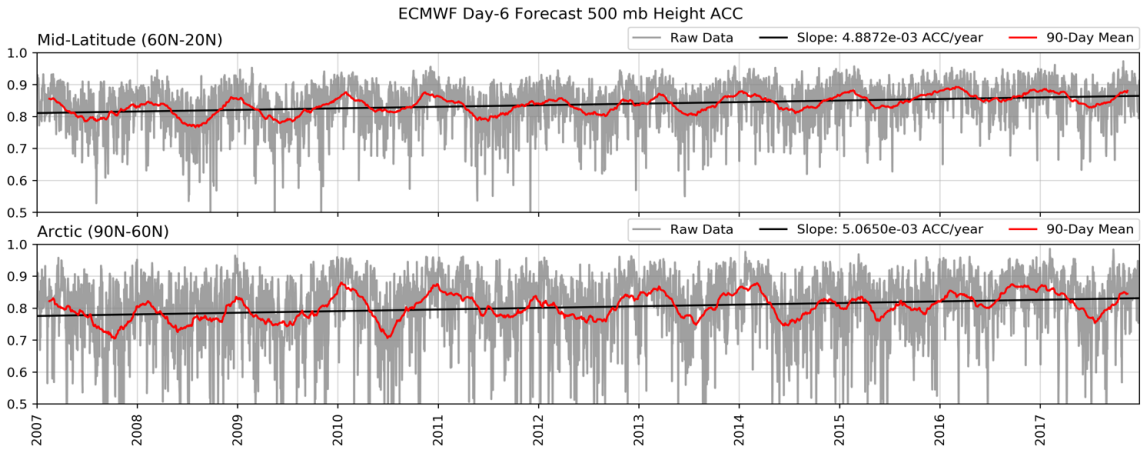

Figure 1.3: Time series of ECMWF day-6 forecast anomaly correlation coefficient (ACC) for the mid-latitudes and the Arctic. The calculation of ACC included cosine weighted by latitude. ERA-iterim was used as the climatology for the ACC calculation. Other regions have been compared to the Arctic and mid-latitudes.

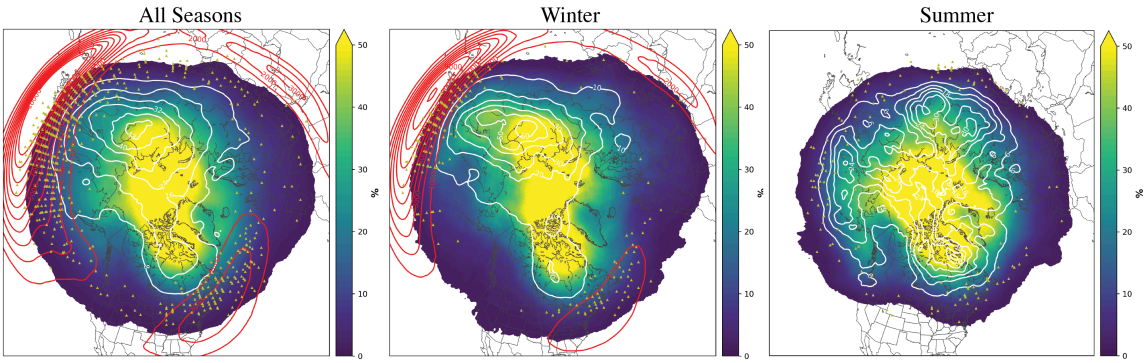

Figure 1.4: Probability of TPV locations (colorfill, %) and location of TPVs associated with RWI events (white contours, %). Red contours of jet streak counts of greater than 70 m s^{-1} windspeed. Yellow triangles denote locations of RWIs where a TPV is within 1000 km. TPV tracks were computed using the ERA-interim dataset and Szapiro and Cavallo (2018) TPV tracking algorithm. The RWI events were from the Röthlisberger et al. (2016) dataset.

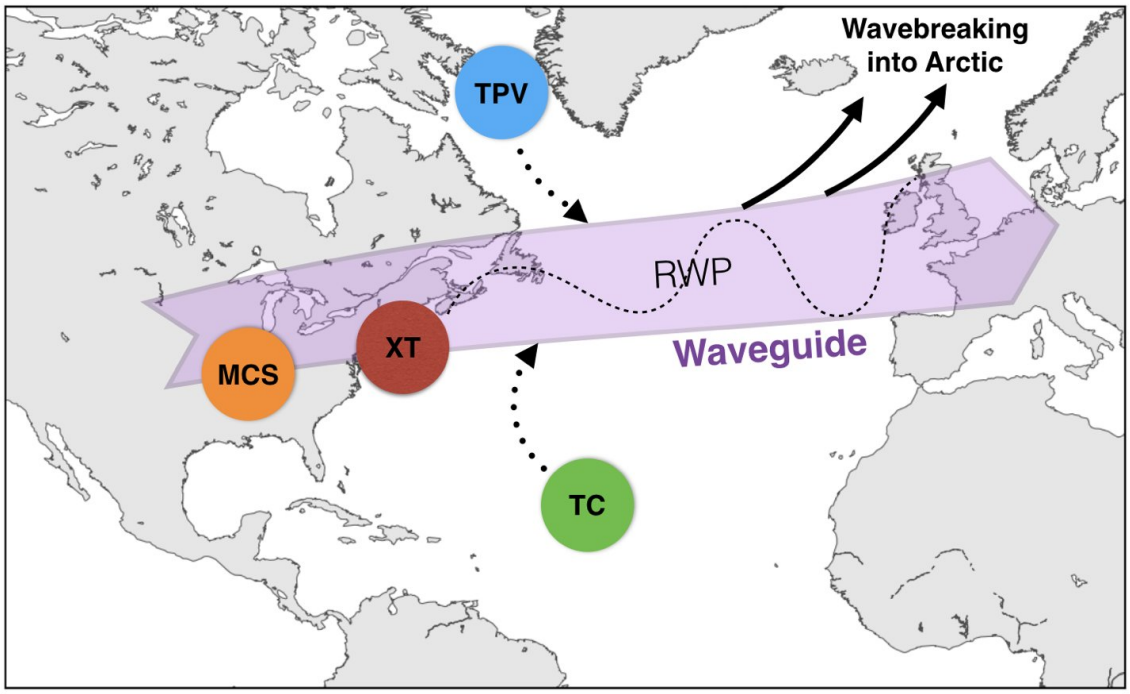

Figure 1.5: Schematic showing MCS (mesoscale convective system), XT (extratropical cyclones), TC (tropical cyclone), and TPV (tropopause polar vortex) features that can act to kick off a RWI event and the downstream propagation of the Rossby wave packet. Figure provided by Sam Lillo and is based in part on Lillo and Parsons (2017) finding of causes linked to dramatic decrease in forecast skill.

Chapter 2

Observations, Numerical Modeling and Data Assimilation

This chapter describes the observations, data assimilation, and NWP model used in this study. The modeling system is composed of two components: (1) a data assimilation system and (2) a NWP model. These two components were developed at National Center for Atmospheric Research (NCAR); the NWP model is the Model for Prediction Across Scales (MPAS) and we use data assimilation software developed by the Data Assimilation Reseach Test (DART) group. MPAS-DART's setup and procedures follow closely to those found in Cavallo et al. (2013), except this study will use a global rather than a regional NWP model.

2.1 Observations

This section discusses the different global NWP models and reanalysis products that were used for initializing and evaluating our modeling system produced analyses and forecasts. Also, a brief explanation will be provided of the observations used in the data assimilation step when producing analyses and when evaluating our model.

2.1.1 The Global Ensemble Forecast System , and ECMWF Re-Analysis Version 5

The Global Ensemble Forecast System (GEFS) is the National Centers for Environmental Prediction (NCEP) global ensemble that is run 4 times daily. The GEFS data used in this study have horizontal spacing of 1.0° x 1.0° and are used to initialize this ensemble. GEFS has 21 ensemble members, however, more members are desirable to help reduce sampling errors (Houtekamer and Zhang 2016), and allow for stronger statistical information to be calculated from the ensemble. Since there are only 21 GEFS ensemble members, the lagged forecast technique (Kumar and Hoerling 2000) is used to build up the number of ensemble

members specified in this study. The initialization process starts by obtaining GEFS 48-,54-,60-,66-,and 72-hour forecasts valid 12 hours prior to initialization time to get 96 ensemble members. Spin-up of the perturbations is completed by running MPAS 12-hours prior to the first cycling period. Using the lagged forecasts initialization technique reduces the amount of time required to spin-up initial perturbations compared to the time required to spin-up initial random perturbations. More documentation on GEFS model setup and forecast run times can be found at the NCEP website (https://www.ncep.noaa.gov).

For comparisons against other modeling systems, the reanalysis product used in this study is the European Center for Medium Range Weather Forecasting (ECMWF) ReAnalysis 5 (ERA5) data set. This reanalysis product spans back to 1979 and utilizes newly developed data assimilation and model physics at higher spatial resolution to produce a more accurate analysis than older reanalysis products. The ECMWF integrated forecast system (IFS) released in 2016 combines atmosphere, land and ocean wave models and is used to create the ERA5 reanalyses (Hersbach et al. 2019). Furthermore, the ERA5 uses all conventional and other observations that are available at that analysis time including radiances from satellites. ERA5's horizontal resolution of approximately 30-km is finer resolution than that of the GEFS, which is approximately 50-km resolution. More information regarding the ECMWF's ERA5 data set can be found in Hersbach et al. (2019).

2.1.2 Conventional Observations

In contrast to most operational systems where satellite radiances are the largest portion of observations, conventional observations account for the majority of the observations types that are assimilated in this study. Satellite radiances carry uncertainties associated with their radiance derived products, which can be particularly impactful when satellite radiances make up a large portion of the total assimilated observation dataset. Additionally, assimilating millions of satellite radiances comes with a large computational cost. With these limitations in mind, the present system assimilates mostly conventional observations.

In particular PREPBUFR files, which contains the majority of processed conventional observations used to create various NCEP analysis, are obtained from NCEP and are the same as those used in the NCEP's NWP Global Data Assimilation System (GDAS) (NCEP 2020). The PREPBUFR files are stored on NCAR's Computational and Informational Systems Laboratory data archive. The available conventional observations for our study were radiosonde data, marine buoy data, METAR data, Aircraft Communications Addressing and Reporting System data (ACARS), and Automatic Weather Stations (AWS) (Figure 2.1). Although Global Positioning System (GPS) data are included in Figure 2.1, they are not a part of the PREFPBUFR files but are used and will be discussed later. The observation errors for all conventional observations are included in the PREPBUFR files and no additional changes were employed. Note that observations are not perfect, and therefore contain some degree of bias. For example, the ACARS root mean square error for temperature is largest between the layer of 300-200 hPa but no explanation has been given for the large error in this layer (Benjamin et al. 1999). Lastly, geostationary satellite wind observations and ACARS can be concentrated in spatial coverage leading to a breakdown in the assumption that observation errors are uncorrelated. Thinning of the data, "super-obing," is performed by setting a specified radius inside which observations are combined into one "super" observation. For example, the horizontal radius is 100 km and the vertical radius is 25 hPa for geostationary satellite wind observations. More information on super-obing can be found in Purser et al. (2000).

Some of the issues with conventional observations over the Arctic region are illustrated in Figure 2.1a. First, there is dense conventional observation coverage over the mid-latitudes, comprising all conventional observation types. As latitude increases towards the North pole, the conventional observational coverage rapidly decrease. North of 60° N, the only observations that primarily remain are a few upper-air radiosonde sites, and mainly surface observations (METAR, marine buoy and AWS sites). Around 360,000 observations are assimilated per cycle when only conventional observations are included. When

confined to only over the Arctic, around 15,000 conventional observations are assimilated per cycle, which is around 4% of the total conventional observations assimilated. (Fig. 2.2a and Fig. 2.3). Unlike in the mid-latitudes, a lower percentage of conventional observations are assimilated in the Arctic. Most operational global models are assimilating satellite radiances increasing the total number of observations into the millions. Thus, global models utilize special satellite observations that not only increase the number of overall observations assimilated but fill in regions that have infrequent observations.

GPS profiles (or radio occultation profiles) are included in the conventional observation group and are assimilated in this study. GPS soundings are created by measuring how much a radio wave is bent, or refracted, while traveling through the atmosphere (Hardy et al. 1992). Since atmospheric refractivity is a function of pressure, temperature, and water vapor, profiles of atmospheric refractivity can provide potentially useful information that can help NWP (Ware et al. 1996). Ware et al. (1996) shows that in portions of the atmosphere where moisture is negligible, temperature can be estimated directly from the refractivity profiles. The GPS observations account for one of the smallest number of observations assimilated, but their quasi-vertical profiles are well distributed spatially to help in some observationally sparse areas (Figure 2.1a). Improvements in forecast were found in the upper-atmosphere over polar regions when GPS observations were assimilated (Healy et al. 2005; Cucurull et al. 2007; Healy 2008). Positive impacts of the GPS observations discussed in the literature provide a basis for them to be included in this study.

2.1.3 Polar Orbiting Wind Observations

Polar orbiting satellite wind observations can be used to help fill in the observationally sparse area over the Arctic region. The polar orbiting satellites used in this study are the MODerate-resolution Imaging Spectroradiometer (MODIS) and Advanced Very High Resolution Radiometer (AVHRR) satellites. MODIS and AVHRR generate upper-level wind observations by tracking, with multiple satellite passes, cloud and water vapor features in

the inferred band and the water vapor windows (Key et al. 2003). Comparing Figure 2.1b and Figure 2.1a, the MODIS and AVHRR wind observations help fill in the observation gap towards higher latitudes. Furthermore, $\sim$18,000 additional observations per cycle are available with the inclusion of the polar orbiting winds (Fig. 2.2b and Fig. 2.3). Polar orbiting wind observations account for the largest percentage of observations assimilated in the Arctic region. Lower level winds observed by polar orbiting satellites are often of poor quality due to height assignment issues over complex topography and ice. Restrictions are applied to different satellite channels and observation altitude based on the surface over which the measurement is taken (Key et al. 2003). The filtering criteria Key et al. (2003) applied is as follows: over land, both infrared (IR) and water vapor (WV) channel data above 400 hPa are used, while IR data above 700 hPa and WV data above 550 hPa are used over the ocean. Bormann and Thépaut (2004) found a positive impact on medium-range forecasts over polar regions when assimilating MODIS winds. Additionally, Key et al. (2003) discusses significant improvements in the geopotential height field over the Arctic region when assimilating polar orbiting observations. The literature supports the positive impact that polar orbiting wind observations can have on analyses and forecasts in over the Arctic.

2.1.4 Atmospheric Infrared Sounder

The Atmospheric Infrared Sounder (AIRS) was launched in 2002 aboard the Aqua satellite. The infrared instrument and two multi-channel microwave instruments aboard Aqua allow AIRS to sample 2,378 wavelengths while prior satellites could only sample 15 wavelengths. Each infrared wavelength is sensitive to a temperature or water vapor value over a range of heights. This enables AIRS to use thousands of different wavelength channels to retrieve an atmospheric profile. Aqua's mirror rotates along the center axis of the satellite creating "swaths" that are roughly 800 km wide. DART does not directly assimilate AIRS measured radiance, rather AIRS derived temperature and moisture profiles are used instead. These

AIRS temperature profiles have a vertical resolution of 1 km, are accurate to 1 K for every 1 km in the troposphere, and are accurate to 1 K for every 4 km in the stratosphere (Olsen et al. 2013). AIRS moisture profiles have an upper limit which coincides with the level where atmospheric mixing ratio values fall to 10-15 ppmv; where sensitivities in measured mixing ratio begins to degrade the profiles around 300 hPa. AIRS moisture profiles have a vertical resolution of 2 km (Olsen et al. 2013). Figure 2.1b shows the spatial distribution of the AIRS observations for one cycle period. The addition of the AIRS observations adds $\sim$9,000 observations per cycle that are assimilated and fills observationally sparse areas (Fig. 2.2b and Fig. 2.3). The AIRS profiles are thinned by retaining every 4th profile in the satellite swath. This method was used instead of super-obing due to the computation time it would take to complete. Chou et al. (2009) found that including AIRS profiles produced an analysis closer to in-situ observations while improving forecast temperature and geopotential height biases. Jones and Stensrud (2012) discuss the impacts of assimilating AIRS profiles in convective-scale forecasts. They found AIRS mixing ratio profiles assimilated over the contiguous United States (CONUS) to be valuable since they are providing otherwise rare unique information during assimilation time. Furthermore, Jones and Stensrud (2012) found a reduction in ensemble spread and forecast uncertainty. Even though the impact of assimilating AIRS profiles is still being investigated, they provide additional coverage in sparse areas over the Antarctic region.

2.2 Data Assimilation

Two common types of data assimilation are the variational, which can be 3-dimensional (3DVAR) or 4-dimensional (4DVAR), and the ensemble approach (Bannister 2017). Many global modeling centers use the 4-dimensional variational data assimilation methods (Bonavita et al. 2016) while some use a hybrid method that combines the variational approach with the ensemble approach (Clayton et al. 2013; Kuhl et al. 2013; Wang et al. 2013b). Hamill and Snyder (2000) showed that with a hybrid ensemble kalman Filter 3DVAR analysis scheme,

applying more weight to the flow-dependent background error covariance produces more accurate analyses and improves forecast lead time by one day as compared to a 3DVAR system. Since the background error covariance is nearly constant when observations are dense, the flow-dependent background error covariance is most important when observations are limited. The importance in the flow-dependent background error covariance in data sparse areas has been shown in previous studies (Whitaker et al. 2004; Jung and Leutbecher 2007; Whitaker et al. 2009). Since the Arctic is a data sparse region compared to the mid-latitudes, the use of a flow-dependent background error covariance provided from an ensemble approach will be used in this study.

Advancements in data assimilation in the past decades have helped provide a more accurate representation of the atmospheric state, which in turn leads to better forecasts (Carrassi et al. 2018). Section 2.1 discussed the aspect of weak observation coverage in the absence of satellite observations around the Arctic region. Furthermore, an ensemble of forecasts provides additional statistical information which can be used to test for significance or evaluate forecast sensitivities.

The data assimilation technique used in this study will be the ensemble Kalman filter (EnKF) technique, which is a modified version of the Kalman filter (Kalman 1960). The Kalman filter equations use the following assumptions: (1) both the observations and background field are unbiased, (2) errors from observations and the model are not temporally correlated with themselves and (3) the errors from the observations and model are not correlated with each other. The basic equations for the Kalman filter are given by:

$$\boldsymbol{X^a} = \boldsymbol{X^b} + \boldsymbol{K}(\boldsymbol{X^o} - H(\boldsymbol{X^b})) \tag{2.1}$$

$$\boldsymbol{K} = \boldsymbol{P^b H^T}(\boldsymbol{H P^b H^T} + \boldsymbol{R})^{-1} \tag{2.2}$$

$$\boldsymbol{P^a} = (\boldsymbol{I} - \boldsymbol{K H})\boldsymbol{P^b} \tag{2.3}$$

where $\boldsymbol{X^a}$ and $\boldsymbol{X^b}$ are the model atmospheric state vectors for the analysis and background, respectively, $\boldsymbol{X^o}$ is the observation vector, $\boldsymbol{I}$ is the identity matrix, and $\boldsymbol{H}$ is a

linear forward operator that acts to interpolate the data to observation locations along with transforming the model background state variables to match those of the observations. The difference between $\boldsymbol{X^o}$ and $\boldsymbol{H}(\boldsymbol{X^b})$ found in equation 2.1 is the weighted adjustment that is applied to the background field, the innovation. In equation 2.2, $\boldsymbol{P^b}$ and $\boldsymbol{R}$ are error covariance matrices that represent the errors for the background model state and the observations, respectively. The observation errors are assumed to be known while the background error covariances are the analysis error covariances from the previous time step projected forward in time by a linear model. The error covaiances combine in equation 2.2 to make the Kalman Gain, $\boldsymbol{K}$. The Kalman Gain is an optimal weight matrix derived by minimizing the total analysis error variance. This optimal weight matrix determines how much of an adjustment is applied to the background model state. For example, if the background error covariance is large, there will be more weight on the observations. Likewise, if the observation error is large, there will be less weight on the observations. Lastly, equation 2.3 represents the analysis error covariance or $\boldsymbol{P^a}$. If the assumptions listed above are maintained, then from equation 2.3, the analysis error covariance should be less than that of the background error covariance.

Modifications have since been made to the Kalman filter equations. The two most common modifications are the extended Kalman filter (EKF) and the ensemble Kalman filter (EnKF). The extended Kalman filter applies the same equations but allows for a non-linear model for advancing the analysis forward in time, and the forward operator. The EnKF also uses a non-linear model for advancing the analysis forward in time and an ensemble of forecasts to compute the background error covariances. There is a computational advantage to using the EnKF over the EKF because there is no need for a model to project the analysis error covariance forward in time. A version of the EnKF will be applied in this study. There are two main types of EnKF approaches: deterministic and stochastic. The deterministic approach requires that the updated analysis perturbations satisfy the Kalman filter analysis

error covariance equation whereas the stochastic method adds random noise to observations so that the Kalman filter analysis error covariance equation is satisfied (Tippett et al. 2003). There are several different types of deterministic formulas including the ensemble transform Kalman filter (Bishop et al. 2001), local ensemble transform Kalman filter (Hunt et al. 2007), and serial ensemble square root Kalman filter (Whitaker and Hamill 2002). The version used in this study is the ensemble adjustment Kalman filter (EAKF) provided within DART (Anderson et al. 2009; Anderson 2001). In the EAKF, the analysis error covariance will converge to the Kalman filter optimal analysis error covariance that is represented by equation 2.3. Tippett et al. (2003) showed that the EAKF is largely a modification of the ensemble square root filter, and the equations are similar.

Like the equations for the Kalman filter, the EAKF has equations for both a forecast and data assimilation step. Starting with the forecast step, the equations used are given by:

$$\boldsymbol{X}_k^{\boldsymbol{b}}(t) = M(t-1)(\boldsymbol{X}_{\boldsymbol{k}}^{\boldsymbol{a}}(t-1)) \tag{2.4}$$

$$\boldsymbol{P}^{\boldsymbol{b}}(t) = \frac{1}{K-1}\sum_{k=1}^{K}(\boldsymbol{X}_{\boldsymbol{k}}^{\boldsymbol{b}}(t) - \bar{\boldsymbol{X}}^{\boldsymbol{b}}(t))(\boldsymbol{X}_{\boldsymbol{k}}^{\boldsymbol{b}}(t) - \bar{\boldsymbol{X}}^{\boldsymbol{b}}(t))^T \tag{2.5}$$

where M represents the non-linear model used to project the analysis forward in time, K is the number of ensemble members, k is the kth ensemble member, and $\bar{\boldsymbol{X}}^{\boldsymbol{b}}$(t) is the ensemble mean of the background field. Unlike in the Kalman filter and EKF formulas, the background error covariance is calculated from a ensemble of forecasts produced by the non-linear model. The calculation of $\boldsymbol{P}^{\boldsymbol{b}}$ in this manner allows for a flow-dependent background error covariance which is different than the static background error covariances found in variational methods. At the end of each forecast cycle, a new analysis is calculated from a new background forecast and a new set of observations. Following the EnKF equations found in Anderson (2001):

$$\bar{\boldsymbol{X}}^{\boldsymbol{a}}(t) = \sum u(\sum{}^{-1}\bar{\boldsymbol{X}}^{\boldsymbol{b}}(t) + \boldsymbol{H}^{\boldsymbol{T}}\boldsymbol{R}^{-1}\boldsymbol{X}^{\boldsymbol{o}}) \tag{2.6}$$

$$\boldsymbol{X}_{\boldsymbol{k}}^{\boldsymbol{a}}(t) = \bar{\boldsymbol{X}}^{\boldsymbol{a}}(t) + \boldsymbol{A}^{\boldsymbol{T}}(X_k^b(t) - \bar{\boldsymbol{X}}^{\boldsymbol{b}}(t)) \tag{2.7}$$

where $\sum$ is the background error covariance, $\sum u$ is the updated covariance, and $\boldsymbol{A^T}$ is a weight that dictates the adjustment made to $\bar{\boldsymbol{X}}^{\boldsymbol{a}}$. The formulation for the updated covariance can be performed on an identity and diagonal matrix which helps to speed up computational time. Equation 2.6 states that the mean of the analysis is updated by applying a combination of updated error covariances ($\sum u$), background error covariances, and observation error covariances on both the mean background field and observations. In equation 2.7, the final analysis is a combination of the mean background field adjusted through a weighted difference between the background field and the mean background field. Equation 2.7 makes the adjustments necessary for the analysis error covariances to converge to those calculated with Kalman filter equations.

Problems can arise when using the ensemble Kalman filter technique for a data assimilation system. One of the most common problems is filter divergence, which can be caused by sampling error or model error. The computational cost of integrating a numerical model forward in time can impose restrictions on the ensemble sizes, which ultimately can cause sampling error. The sampling error causes the background error covariances to be rank deficient, and the correlation between distant grid points is overestimated (Poterjoy et al. 2014). Covariance localization is applied to mitigate sampling error. Covariance inflation is the process of inflating ensemble background perturbation fields by some factor to increase the model error. For this study, the covariance localization technique applied is the Gaspari-Cohn 5th order polynomial (Gaspari and Cohn 1999). This localization technique is applied to the ensemble created background covariance matrix where it is multiplied point-by-point with a correlation function that is 1.0 at the observation location then decreases monotonically to zero after twice the cutoff radius. The equation is given by:

$$\boldsymbol{K} = (\rho \circ \boldsymbol{P^b H^T})(\boldsymbol{H P^b H^T} + \boldsymbol{R})^{-1} \tag{2.8}$$

where ρ denotes the multiplication factor applied to $\boldsymbol{P^b}$ and $\circ$ represents the Schur product. The system here uses a cut off radius of 0.16, correlations between grid points stop in the horizontal at 2,000 km and 2 km in the vertical (Fig. 2.4). The number of degrees

of freedom in the background error covariance is also limited by the ensemble size, but by applying the covariance localization, one can increase the number of degrees of freedom realized in the background error covariance. Another data assimilation issue that can cause filter divergence is poor representation of model errors. Poor representation of model errors can develop from inadequate specification of model grid spacing, errors in model's physics parameterizations, and inaccuracy in the initial and boundary conditions. There are various treatments for model error issues, but most commonly, covariance inflation is used. Unrealistic confidence in the background field estimates can lead to insufficient weighting of the observations. When this occurs, the analysis produced is influenced only by the background field. An equation applying inflation is given by:

$$\boldsymbol{X}_{\boldsymbol{k}}^{\boldsymbol{b}} = \gamma(\boldsymbol{X}_{\boldsymbol{k}}^{\boldsymbol{b}} - \bar{\boldsymbol{X}}^{\boldsymbol{b}}) + \bar{\boldsymbol{X}}^{\boldsymbol{b}} \tag{2.9}$$

where γ is the inflation factor that is applied to the background ensemble perturbations. The covariance inflation applied in this study is an adaptive technique, where the prior ensemble estimate, the observation, and the observation error variance is used to estimate whether γ is too big or small (Anderson 2007). Anderson (2007) shows that the only changes to the distribution of γ are due to the observations. Applying our choice of EnKF technique along with these treatments for filter divergence allows this study to have a more confident and accurate ensemble system.

2.3 NWP Model

The second part of modeling system is the numerical model that is used to advance the ensemble of analyses forward in time. Since the aim of this study is to examine in interactions between the Arctic and mid-latitudes, a global NWP model is chosen. Historically, less attention has been paid to identification of issues over the Arctic region in global models. Jung (2005) found that during seasonal climate integrations, the ECMWF under predicted synoptic activity in the high-latitudes. The under prediction was speculated to be connected

to the model being too dissipative at small scales, which can degrade forecasts as low pressure systems are smaller in scale over the poles as compared to mid-latitudes. Additionally, increased forecast skill was found when an increase in horizontal resolution was applied (Jung and Leutbecher 2007). The increase in forecast skill suggests there may be significance in resolving finer scale features of the Arctic during forecasts. Furthermore, there are large analysis uncertainties in the Arctic compared to mid-latitudes based on the different analysis generation procedures used at varying global modeling centers, which can inhibit forecast performance (Jung and Matsueda 2016). Lastly, accurate representation of the stable boundary layer, a common feature in the Arctic region, is limited due to boundary layer parameterization used in operational global models often maintaining stronger mixing in stable conditions (Sandu et al. 2013).

Many modeling studies focused over the Arctic use regional research NWP models such as Weather Research and Forecasting (WRF; Skamarock et al. 2005) model. Arctic studies using the WRF model highlight the struggles the model has at representing mixed-phase clouds. Mixed-phase clouds are unique since supercooled liquid is present at cold temperatures (Shupe et al. 2006). Processes involved in the formation of mixed-phase clouds have been investigated but an improved knowledge is still needed (Curry 1983; Morrison et al. 2012; Devasthale et al. 2020). The implications mixed-phase clouds have on radiative processes makes the ability to correctly represent them in NWP models crucially important (Shupe and Intrieri 2004; Curry et al. 1996; Hines et al. 2011; Porter et al. 2011; Hines and Bromwich 2017). Furthermore, mixed-phase clouds can also impact how well the boundary layer is represented in NWP models (Pinto 1998). Difficulties arise representing mixed-phase clouds because supercooled liquid water's existence is unstable as liquid water's saturation vapor pressure is higher than that of ice leading to vapor deposition to ice more readily than to liquid (Kalesse et al. 2016). The higher saturation vapor pressure leads to liquid water evaporating since ice deposition is more favorable than liquid condensation via the Wegener-–Bergeron-–Findeisen (WBF) process (Wegener 1911; Bergeron

1935; Findeisen 1938). Single moment bulk microphysics schemes, which only predict mixing ratios for different cloud/precipitation hydrometers, struggle to accurately represent mixed-phase cloud properties (Curry et al. 2000; Morrison et al. 2003). The ice crystal concentration is important in mixed phase clouds since it determines the time scale of the uptake of water vapor by deposition growth of ice (Morrison and Pinto 2005). High ice concentrations lead to short water vapor up take time scales, which enhances the WBF process. Double moment microphysics schemes, which in addition to predicting mixing ratios of hydrometeor species in single-moment schemes, additionally predicts number concentration, and, have shown improvement in representation of mixed phase clouds (Girard and Curry 2001; Morrison et al. 2005). Systematic model biases found in surface radiative properties were reduced due to modifications made to microphysics schemes to better represent mixed-phased clouds in polar regions (Hines and Bromwich 2017; Listowski and Lachlan-Cope 2017).

The NWP model used in this study to integrate the ensemble of analyses forward in time is MPAS, which is developed at NCAR (Skamarock et al. 2012). The atmospheric component of MPAS is a global model that solves the fully compressible nonhydrostatic equations using finite-volume numerics discretized on centroidal Voronoi (Du et al. 1999) meshes using C-grid staggering of the prognostic variables (Ringler et al. 2008; Thuburn et al. 2009). The use of the unstructured Voronoi mesh, instead of a more commoon latitude-longitude grid, eliminates the singularity that develops near the poles when using a latitude-longitude grid. Since MPAS is a global model, this eliminates any dependence on boundary conditions, which are needed in a regional model like WRF. MPAS offers variable mesh resolutions which gradually smooth down to finer resolutions unlike nested domains within WRF. Park et al. (2014) found smoother transitions and better representation of atmospheric features from the coarser to finer resolutions in the MPAS variable mesh simulations as compared to nested WRF simulations. The use of the variable mesh allows for finer resolutions

in the particular region of interested while keeping computational costs lower than would otherwise be incurred with a global model of the same resolution.

There have been few studies evaluating MPAS, especially concerning the Arctic. Judt (2020) used MPAS to investigate the predictability of different regions at convective scales and found that polar regions had shorter predictability than the tropics. Several studies that used MPAS to investigate different tropical cyclone topics (Pilon et al. 2016; Davis et al. 2016; Huang et al. 2017; Judt 2018) along with extreme precipitation (Wong and Skamarock 2016; Zhao et al. 2019) found good performance by the model. There is one study investigating MPAS coupled with DART, which found that the model cycled successfully for an entire month (Ha et al. 2017). In this work, technical settings enabling DART to work with MPAS follow those found most successful in Ha et al. (2017).

MPAS will be cycled using the EAKF approach, an initialization approach referred to as "warm starting", where the same model used for the data assimilation is used to create forecasts. Six-hourly forecasts are then used in the data assimilation to create new analyses. The 6-hourly cycling allows for the model's climatology to be retained in the MPAS-DART's cycled data. During the first few days of forecasts, the model error can be influenced by the differences between the analysis and model physics which is referred to as the "initial shock" (Klocke and Rodwell 2014). By initializing the model with warm starts, "initial shock" is reduced since the model has had time to adjust to its climatology.

Atmospheric features are inherently smaller in the polar regions due to the Earth's rotation decreasing the Rossby radius, which implies that higher resolution is needed over the Arctic to represent a similar feature in low latitudes (Fig. 2.5). Furthermore, the non-hydrostatic core within MPAS will allow for better representation of mesoscale processes that would be associated with small features. Using MPAS will allow for the placement of increased grid resolution over the Arctic while relaxing back to coarser resolution else where on the globe. Additionally, increased resolution over the Arctic will resolve some of

the smaller scale processes associated with TPVs (Fig. 2.6). Representation of the finer-scale structures in the environment around the vicinity of a TPV is apparent in the spatial representation (Fig. 2.6a) and in the vertical representation (Fig. 2.6b). Due to the reasons above, this study uses a variable mesh with a 15 km mesh spacing over the Arctic, while relaxing to 60 km over the rest of the globe (Fig. 2.7).

The model time step is 90 seconds to ensure numerical stability with the chosen mesh specifications. The MPAS model top is set at 30 km with a gravity wave absorbing layer starting at 22 km extending to the top (Klemp et al. 2008). MPAS uses a modified version of the traditional terrain-following height coordinate, where at the lower levels the height surfaces are terrain following and relax to a more constant surface at the upper boundary (Klemp 2011). An example is provided in Fig. 2.8 showing how, in the hybrid height coordinate, levels become smoother at larger heights. The hybrid height coordinate is especially beneficial since MPAS is a global NWP model which means there are a wide ranges of terrain heights to represent. The model top height is set to 30 km to focus on the upper tropospheric and lower stratospheric processes that are expected to be important in this study. MPAS is set to use 55 vertical height levels spanning the surface to the model top. The vertical distribution of the height levels is depicted in Figure 2.9. The height levels are spaced closer together in the atmospheric boundary layer, as recommended in numerous previous studies in order to better represent boundary layer processes (McInnes and Curry 1995; Mirocha et al. 2014; Smith et al. 2018).

The physics package used in MPAS-DART is listed in Table 2.1. The Thompson microphysics scheme (Thompson et al. 2008) is a double moment scheme with the intent of more accurately capturing ice phase processes and mixed phase clouds. Since MPAS-DART's resolution is not convective-resolving, the Tiedtke cumulus scheme (Zhang et al. 2011) is applied to account for sub-grid effects from latent heating due to deep and shallow clouds. The Rapid Radiative Transfer Model for global circulation models (RRTMG) (Iacono et al. 2008) are used to resolve both longwave and shortwave radiative processes that need to

Parameterization	Scheme
Longwave (radiative processes in the longwave)	**RRTMG** (Iacono et al. 2008)
Shortwave (radiative processes in the shortwave)	**RRTMG** (Iacono et al. 2008)
Boundary Layer (subgrid boundary layer processes including eddies)	**Yonsei University (YSU)** (Hong et al. 2006)
Surface Layer (connects land surface to the boundary layer parameterization in the shallow surface layer)	**Monin-Obukhov (Janjic Eta)** (Janjić 2002)
Land Surface (land use, sub-surface properties, and surface fluxes)	**Unified Noah LSM** (Chen and Dudhia 2001)
Microphysics (cloud and moisture processes)	**Thompson** (non-aerosol aware) (Thompson et al. 2008)
Cumulus (subgrid cloud processes)	**Tiedtke** (Zhang et al. 2011)

Table 2.1: Physics schemes chosen for MPAS-DART and a general description of their purposes.

parameterized. For the representation of boundary layer and surface processes, the Yonsei Unviersity (YSU) (Hong and Lim 2006) and Monin-Obukhov (Janjic eta) surface (Janjić 2002) schemes are employed. The Noah land surface model (Chen and Dudhia 2001) provides fluxes to the boundary layer scheme thereby acting as a lower boundary condition for vertical transport in the boundary layer. Lastly, sea ice and sea surface temperatures are updated every cycling period with daily data. Depending on the experiment, sea ice data is from either NCEP global forecasting system (GFS) analysis files or from the National Snow and Ice Data Center (NSICD; Nolin et al. 1998). Both datasets enable fractional sea ice to be used in the land surface model to help represent over sea ice. Sea surface temperature (SST) data are obtained from the National Centers for Environmental Prediction/Marine Modeling and Analysis Branch (NCEP / MMAB) 1/12th degree resolution archive dataset (Gemmill et al. 2007). The high resolution SST data ensures the modeling system represents gradients in SST gradients properly during model integration.

2.4 Experiment Details

Two different cycling experiments were successfully run using MPAS-DART. Both experiments use the same observation types during the data assimilation step with small differences in the amount of observations assimilated per cycle between the two experiments. Additionally, both experiments use the same MPAS mesh and physics parameterization schemes that were described in section 2.3. There are some differences between the experiments which will be discussed below. Unlike a traditionally designed set of experiments, where one experiment acts as a control or baseline, differences between experiments 1 and 2 were implemented in response to identified issues in experiment 1. Experiment 2 includes solutions to those issues in an effort to obtain the best possible results. While comparison of the two experiments was not the main goal of this study, there is useful information on the impacts of the changes between the experiments.

Experiment 1 (which is the 'control' experiment for comparison purposes) cycled for $\sim$17 days starting on 00 UTC 28 September 2016 and finishing on 12 UTC 15 October 2016. This cycling time period is chosen for experiment 1 so special dropsonde observations that were collected during the North Atlantic Waveguide and Downstream Impact Experiment (NAWDEX) could be assimiated in MPAS-DART (Schäfler et al. 2018). Sea ice dataset employed in experiment 1 was from NCEP GFS analyses. Furthermore, initialization of the ensemble from GEFS forecast used default settings in the WRF preprocessing system (WPS) software when correcting relative humidity values.

Experiment 2 was cycled for 31 days, which is longer than experiment 1. The cycling period for experiment 2 is run from 00 UTC 1 December 2011 - 00 UTC 1 January 2012. Experiment 2 cycled for all of December whereas experiment 1 was cycled during the end of September into October. The sea ice dataset employed in experiment 2 is from NSICD, which had to be interpolated to the MPAS mesh. Furthermore, initialization of the ensemble from GEFS forecasts used a modified version of the WPS software that allowed a relative humidity fix to be applied to the moisture profiles. The flag was set to work with GEFS data for experiment 2 whereas the flag was not modified to work for experiment 2. Lastly due to numerical instabilities, the time step had to be reduced from 90 seconds to 60 seconds in experiment 2 after a couple days of cycling.

As mentioned above, comparison of experiments was not the main goal of this study, and thus experimental design does not reflect that. However, useful information can still be gained by comparing the two experiments. Even though the cycling length and time periods are different, comparisons and evaluations between experiments will still be completed. The different time periods will allow this study to determine if biases found are systematic or related to the period that MPAS-DART was cycled over. Furthermore, differences between experiments will be investigated to determine the impacts of the different sea ice datasets used and the impacts the different moisture initialization had on model results.

Experiment	**Cycling Period**	**Sea Ice Concentration Dataset**	**WPS Relative Humidity Fix Flag**	**Model Time Step**
1 (Control)	28 September 2016 - 15 October 2016	NCEP GFS analyses	Off	90s
2	1 December 2011 - 1 January 2012	Passive microwave satellite dataset (NSICD)	On	90s switched to 60s several days into cycling

Table 2.2: Differences between experiment 1 and 2.

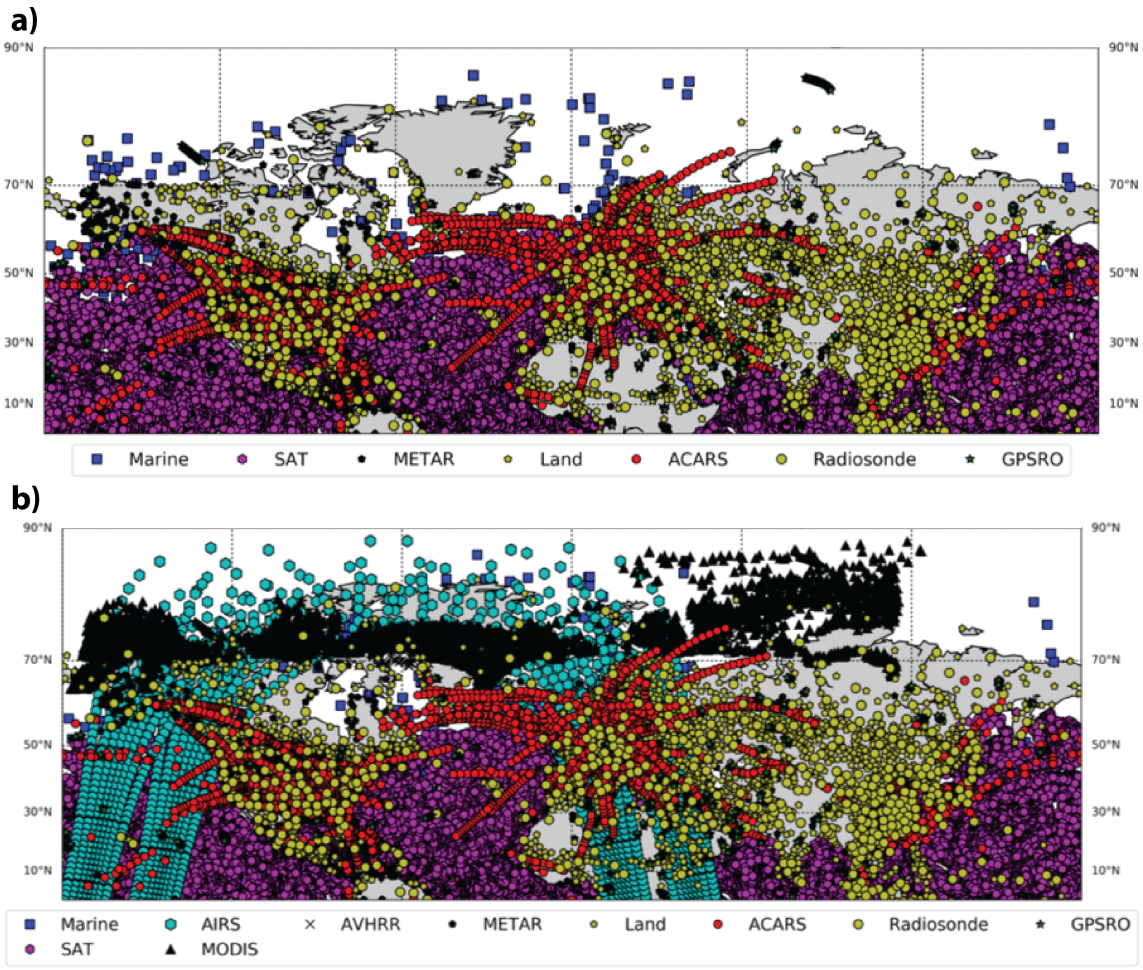

Figure 2.1: Observation locations for valid on 00 UTC 28 September 2016 for (a) convectional observations and (b) convectional observations plus polar orbiting satellite observations. Observations shown are radiosonde (Radiosonde), marine buoy (Marine), geostationary satellite winds (SAT), Meteorological Terminal Aviation Routine Weather Report (METAR), global positioning system (GPSRO), aircraft communications addressing and reporting system (ACARS), automatic weather stations (LAND), AIRS satellite derived profiles (AIRS), and polar orbiting satellite wind observations (MODIS and AVHRR).

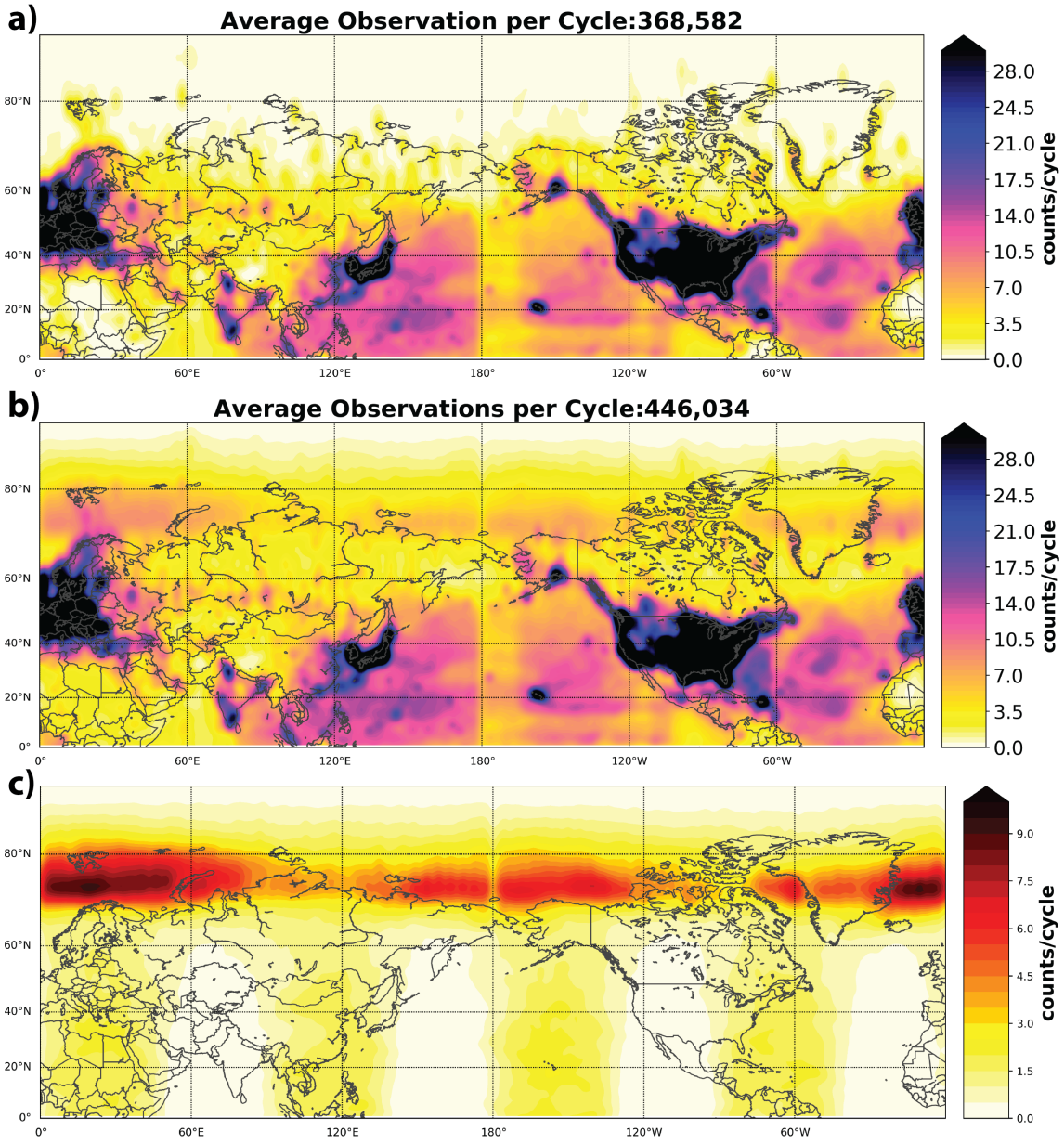

Figure 2.2: Average observations assimilated per cycle for (a) only conventional observations and (b) convectional observations plus polar orbiting satellite observations for experiment one. (c) Differences in averaged observations assimilated per cycle between including polar orbiting satellite observations versus when polar orbiting satellite observations are excluded.

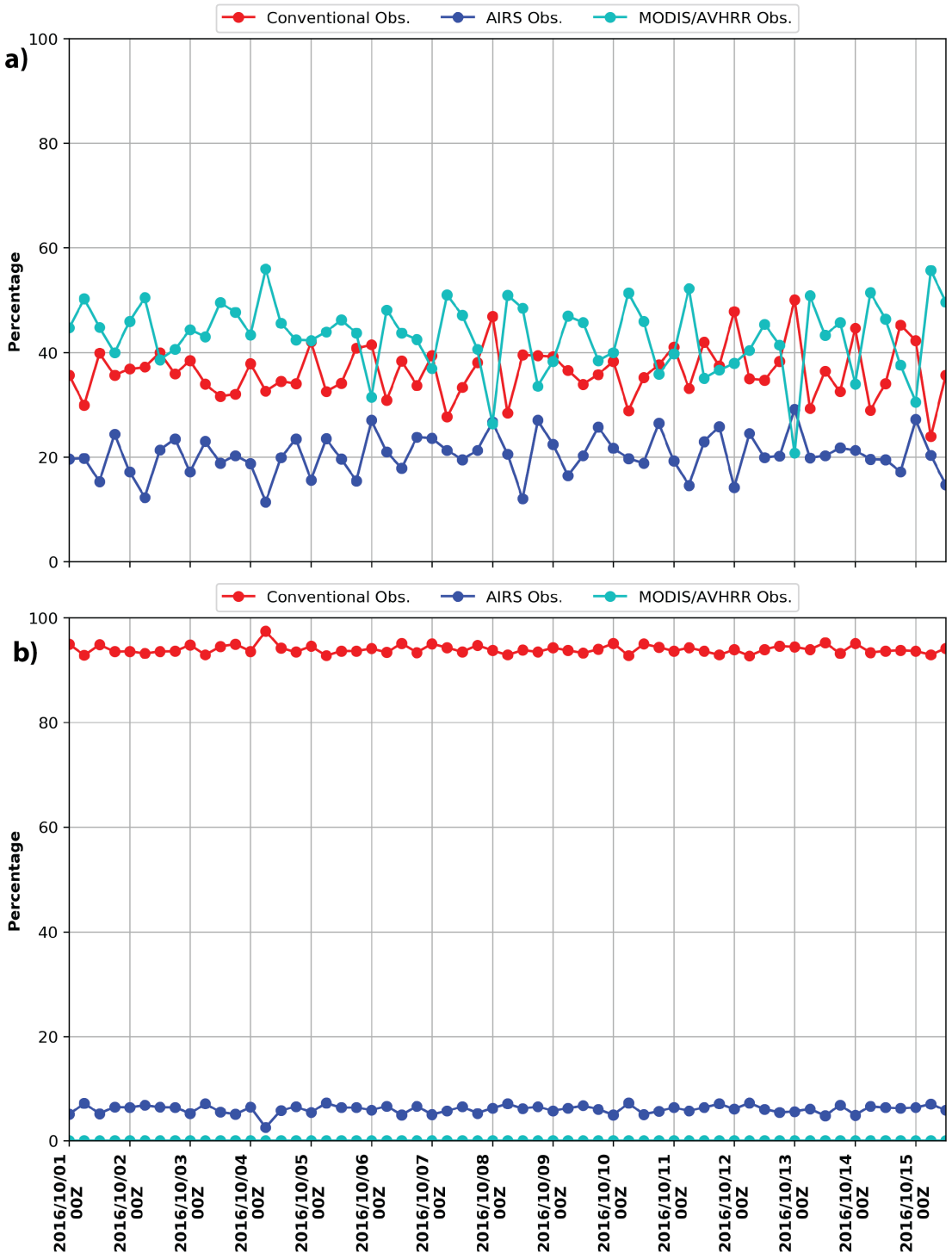

Figure 2.3: Time series showing the percentage of conventional (red), AIRS (blue), and MODIS/AVHRR (cyan) observations assimilated within MPAS-DART for (a) the Arctic region and (b) the mid-latitudes.

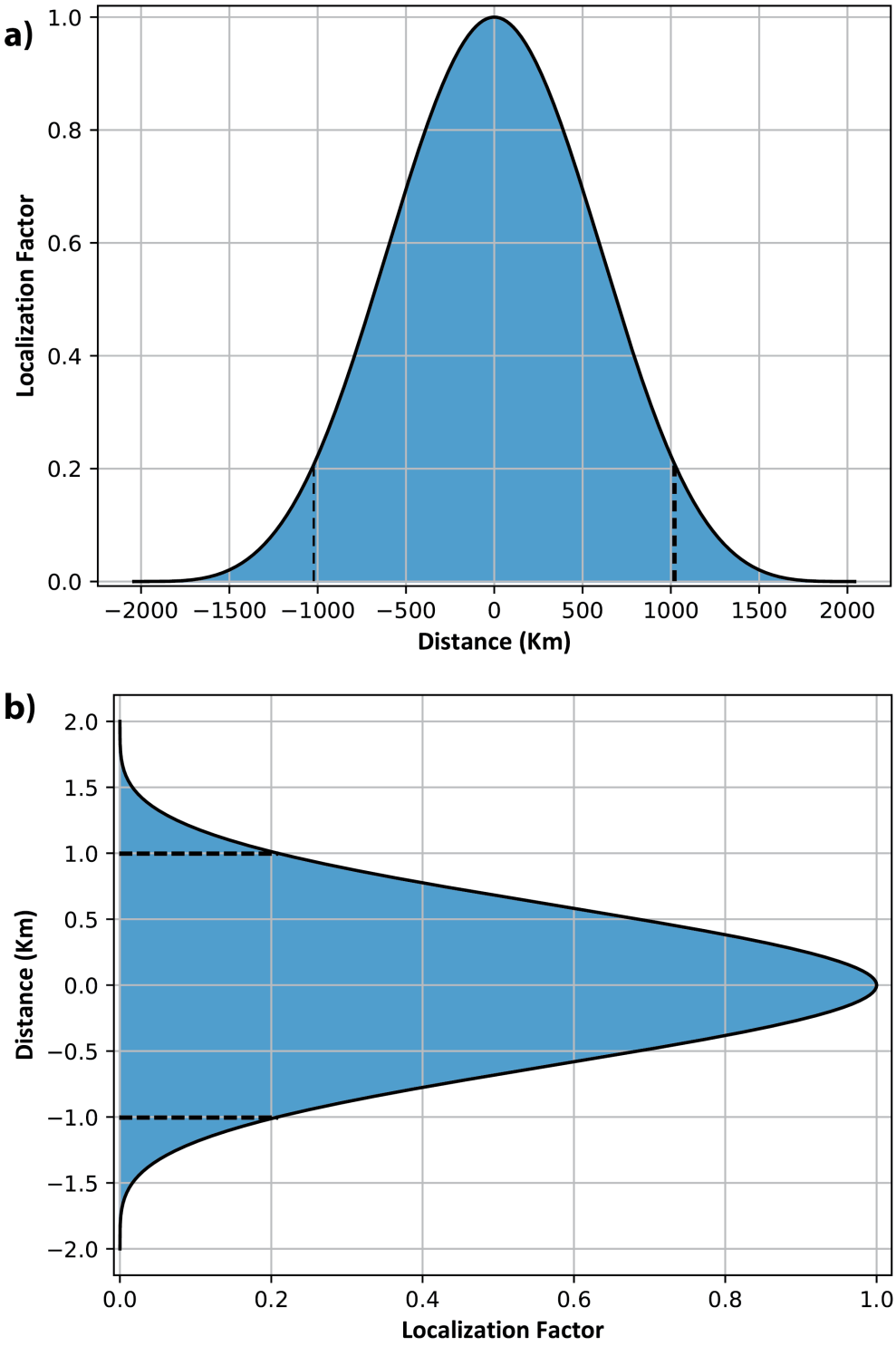

Figure 2.4: Specified (a) horizontal and (b) vertical localization factor that is applied within MPAS-DART. The black dashed lines represent the half-width of the localization radius.

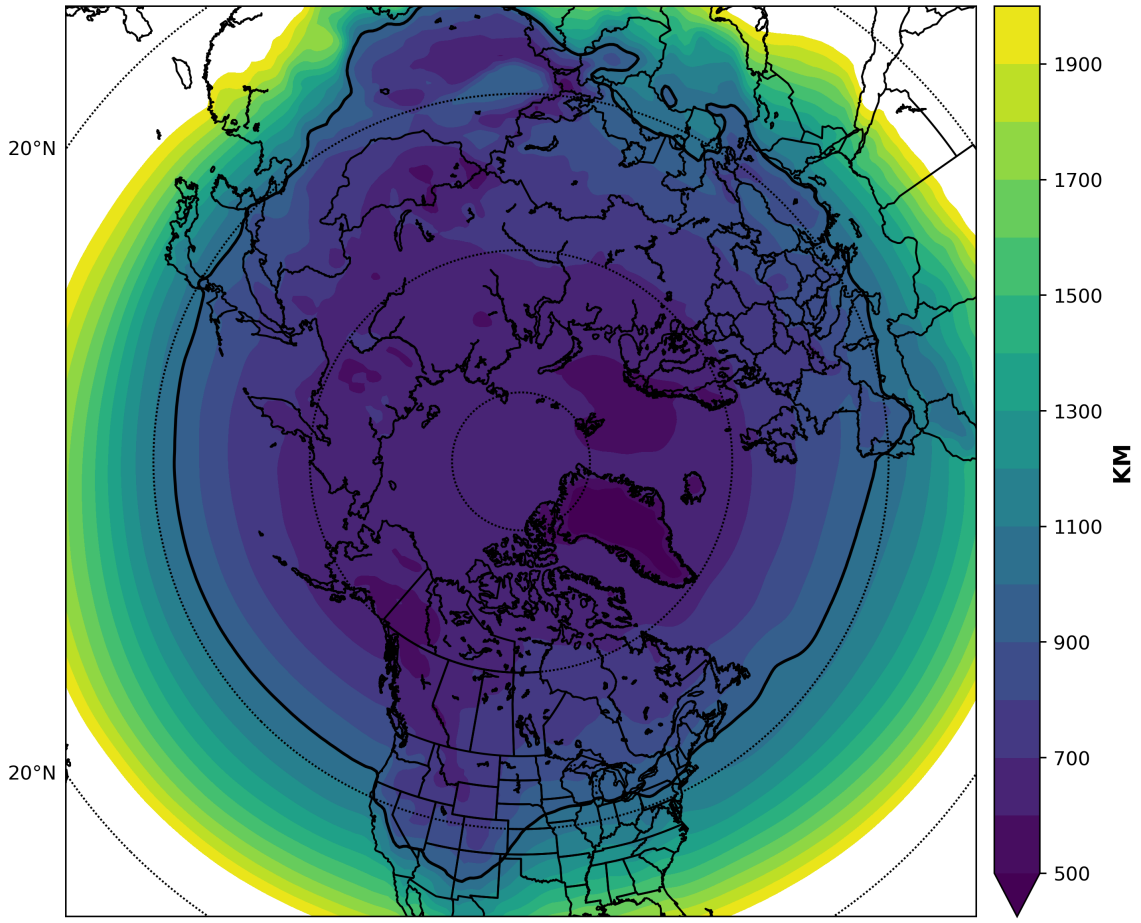

Figure 2.5: Climatological Rossby radius of Deformation (in km) computed using ERA5 data.

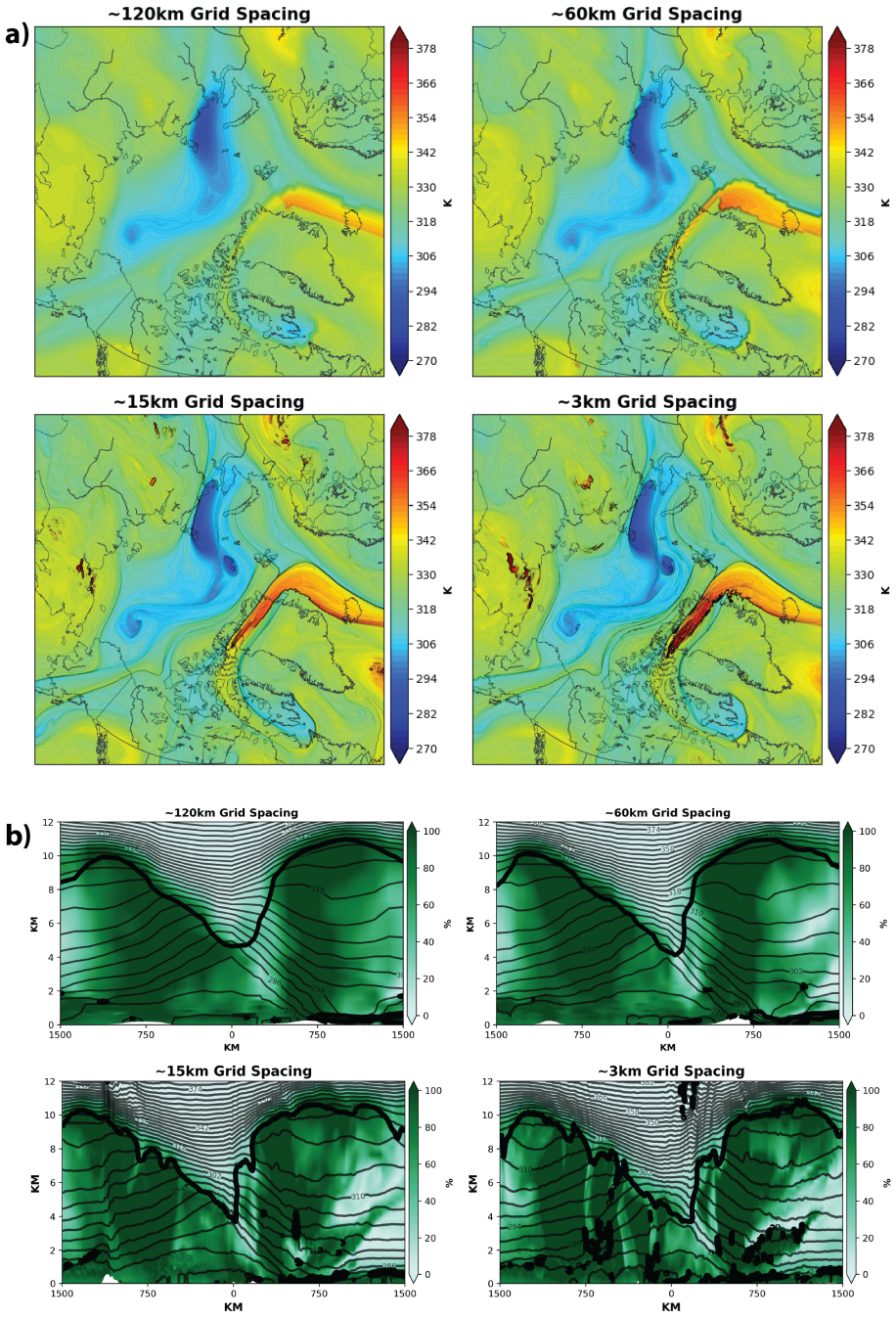

Figure 2.6: Three day MPAS simulation of a TPV starting on 00 UTC 15 August 2006 showing the (a) spatial representation and (b) vertical representation with varying horizontal resolutions.

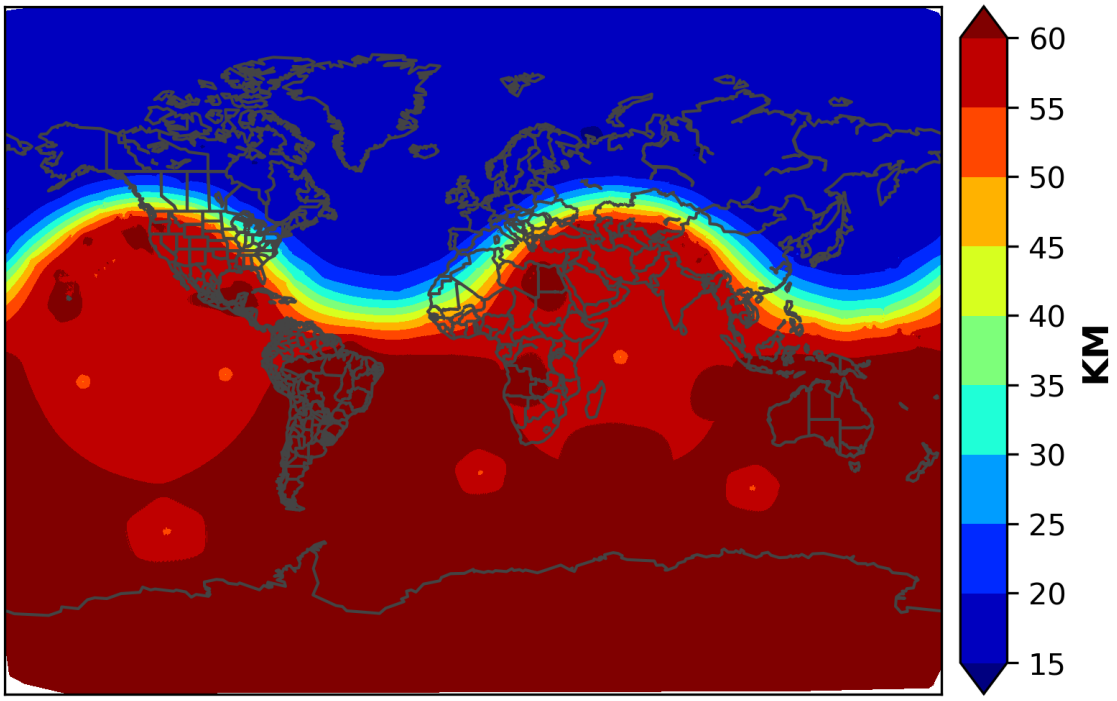

Figure 2.7: Position of the 60-15 km mesh used in MPAS-DART.

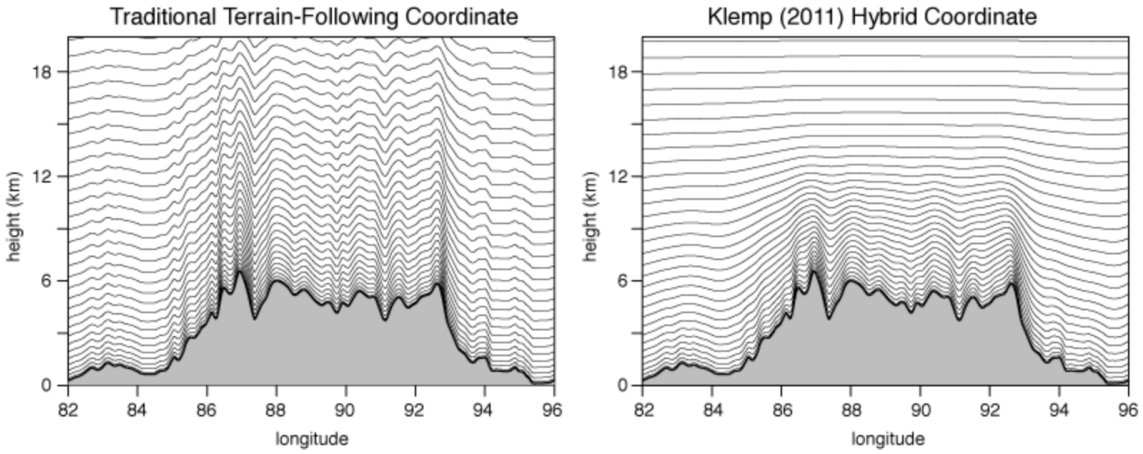

Figure 2.8: Vertical model levels represented using (a) traditional terrain-following coordinate and (b) hybrid terrain-following coordinate. Figure provided from the MPAS website (https://mpas-dev.github.io)

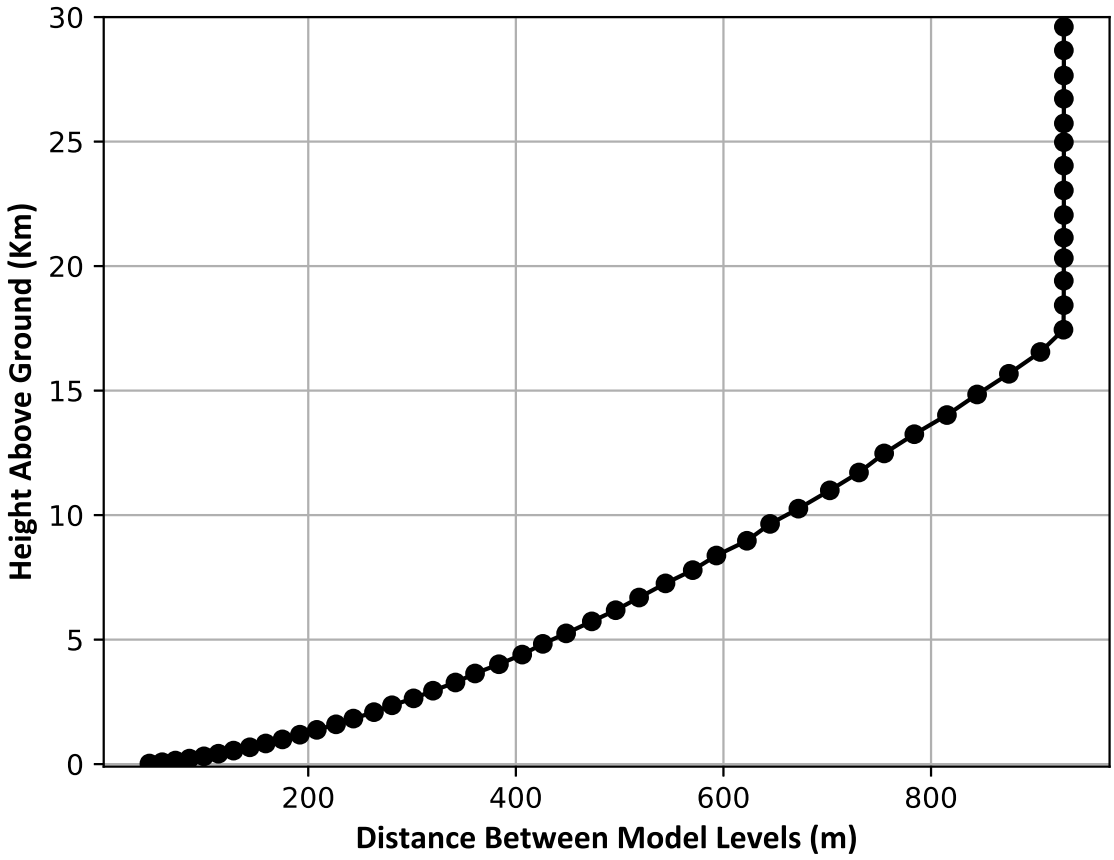

Figure 2.9: Spacing between MPAS model levels used in this study.

Chapter 3

Evaluation of MPAS-DART

This chapter evaluates the performance of MPAS-DART using several different statistical approaches. The first three statistics that are applied to evaluate the performance of MPAS-DART are (1) bias, (2) root mean square error (RMSE), and (3) total spread. The bias is given by:

$$Bias = \frac{1}{n}\sum_{i=1}^{n} M_i - O_i \tag{3.1}$$

where M is model data, O is observational data and i is the index of data over all observations. Since observations are considered the best representation of the true atmospheric state, bias can be used to diagnose deficiencies in the model. Confidence intervals (95%) are computed for vertical profiles of model bias after bootstrapping the bias 10,000 times. Next, the RMSE is given by:

$$RMSE = \sqrt{\frac{1}{n}\sum_{i=1}^{n}(M_i - O_i)^2} \tag{3.2}$$

where the notation is the same as in (3.1). The RMSE is a reasonable measure of model error when examining a particular variable but can be highly sensitive to outliers in the dataset (Pontius et al. 2008). Lastly, the total spread is given by:

$$Total\ Spread = \sqrt{\sum_{i=1}^{n}(\sigma_i^{2\ model} + \sigma_i^{2\ observation\ errors})} \tag{3.3}$$

where $\sigma_i^{2\ model}$ is the ensemble model variance, $\sigma_i^{2\ observation\ error}$ is the error variance associated with the observations and n is the total number of observations. Note that the total spread includes the error variance of the observations in addition to model forecast variance. This formulation provides the expected value of the difference between the model ensemble mean and the observed value (Raeder et al. 2012). When there is large uncertainty in the forecast, the spread should be large enough to capture the uncertainty. Likewise, if

there is small uncertainty in the forecast the spread should be small. Comparing RMSE to total spread is one method to determine whether the ensemble system is calibrated. Thus, if a specific event has large uncertainty the spread will be higher, and since the event is less predictable the RMSE should also be higher. This relation is often called the "spread-skill relation" and is discussed in detail by Fortin et al. (2014).

Rank histograms are another diagnostic approach utilized to evaluate MPAS-DART against surface observations. The concept of utilizing rank histograms was first presented by Anderson (1996). The theory states: for a probability to be reliable, as desired from an ensemble, the set of ensemble member forecast values at a given point and the true state should be considered random samples from the same probability distribution (Hamill 2001). Hamill (2001) shows that if an n-member ensemble and the true state are brought together and sorted from lowest to highest then there is equally likely chance that the verification will occur in each of the n+1 possible ranks. A rank histogram is created by repeatedly counting how often the true state or the observation falls in a certain bin for our sorted ensemble members.

The reliability of an ensemble can be determined by the shapes of the rank histograms. Figure 3.1 displays some of the more common shapes that can be found when using rank histograms. For a well-calibrated ensemble, there would be a uniform distribution of counts across all bins in the rank histogram (Fig. 3.1 A). However, care must be taken to determine if the flat rank histogram is indeed indicative of the reliability in the ensemble (Hamill 2001). One issue that can develop in an ensemble is the spread being too large or too small. If the spread is too large, the observation will always fall in the middle bins of the sorted ensemble. This leads to the upside down U-shape (Fig. 3.1 B). If the spread is too small, the observation will always fall in the outside bins of the sorted ensemble. This leads to upright U-shape seen in Fig. 3.1 C. Furthermore, model bias can be diagnosed with rank histograms since the ensemble members are sorted from lowest to highest. If the ensemble members are continually biased in a consistent way compared to the observations, then

peaks will skewed to one side, representing that the observation keeps falling in outside bins on one side of the distribution. Such peaks displayed in Fig 3.1 panels D and E, where D represents a warm model bias and E represents a cold model bias.

Knowledge of how the observations affect the analysis can provide useful information about the ensemble system. Analysis increment is the difference between the new analysis after data assimilation (posterior state) and the background state (prior state):

$$INC = X^a - X^b = K(X^o - H(X^b)) \tag{3.4}$$

where *INC* represents the adjustment made by the observations. A diagram depicting the data assimilation process is given in Figure 3.2. In this example a temperature forecast is initialized from an analysis (noted as AN_0), and runs until the next cycling period (noted as $T_0(n)$). During this period, the forecast temperature ($T_0(n)$) is drifting away fron the observed temperature ($T_{obs}(t)$). At $T_0(n)$, data assimilation is performed to create a new analysis AN_1. The new temperature analysis at each point where data assimilation occurs falls somewhere between the forecasted and observed temperature at that time. The increment (INC) quantifies how much the temperature observation has adjusted the forecasted temperature towards it's own value. The analysis increment can tell us the degree to which observations are pushing or pulling our forecasted field. If the analysis increment, or the left-hand side of (3.4), is equal to zero, then the observation and the forecasts are equal and no adjustment is needed. If the right-hand side of (3.4) is not equal to zero, than the observation is adjusting the forecast. If observations are unbiased, then, with a perfect model, the mean analysis increment (averaged over many data assimilation cycles) should be zero (Rodwell and Palmer 2007a). While analysis increment will be one method used to evaluate the cycling system, there are some assumptions made that need to be addressed. First, the density of the observations over the region you are evaluate can have an effect on the analysis increment. Over the mid-latitudes, where there is dense and diverse observations, the analysis increment provides a reliable estimate of how different observations

are impacting the background forecast. Over the Arctic, where observations are more limited to satellite observations, the analysis increment may only provide an estimate of how only one type of observation is impacting your background forecast which could lead to an incorrect evaluation. The second assumption is the observations are the truth and have no inherent biases themselves. This assumption can be invalid if some observations are you assimilating have inherent biases that are impacting your analyses. Due to this coupled assumptions, care must be taken when using analysis increment to determine if there are biases within your cycling system.

These different verification approaches will be used to help evaluate the reliability of MPAS-DART. Comparisons between different experiments will allow for the evaluation of changes that were applied between the experiments and determine their impacts on the cycling system. Additionally, comparisons between the Arctic and the mid-latitudes will help determine if any issues within the MPAS-DART are regional or more widespread.

3.1 Ensemble Inflation

The covariance inflation approach is used to mitigate errors associated with imperfect forecast models by inflating the background state to apply more weight to the observations. A damping coefficient of 0.9 is chosen for the adaptive covariance inflation algorithm to maintain model stability (This is the recommended value for the DART software). In previous work, setting the damping coefficient to 0.9 was shown to produce good results in a regional cycling modeling system developed for the Southern Hemisphere (Riedel et al. 2019). During the cycling, if the model is being pulled closer to observations, then the maximum inflation for all variables should reduce over time (Figs. 3.3 and 3.4). For experiment 1 over the Arctic, the mean of the maximum value of inflation for all model state variables is highest at the first cycling time which, eventually reduces and settles in at value around 2 (Fig. 3.3a). There is a similar evolution of the mean in the maximum inflation in the mid-latitudes as in the Arctic in experiment 1 (Figure 3.3b). For experiment 2, the mean

of the maximum inflation does eventually reduce down to a smaller value for both regions, but not before a slight increase around cycling time 18 (Figures 3.4). The increase in the mean of the maximum inflation is most pronounced in the Arctic region (Compare Fig. 3.4a to Fig. 3.4b). The slight increase in the mean of the maximum inflation occurs in near temporal proximity to when the time step had to be decreased from 90 to 60 seconds for numerical stability relating to the very high lower-stratospheric windspeeds. The numerical stability could explain the slight increase in inflation during this time period. Regardless, the mean of the maximum inflation values for all state model variables eventually settles in on values comparable to experiment 1. For both experiments and regions, the mean in the maximum inflation values for model state variables asymptote around 2, however, there can be slight increases in the covariance inflation depending different factors (weather regime, availability of observations, cycling time period, etc).

To gain a better understanding of how the adaptive inflation is evolving with different state variables, time series of the maximum inflation associated with potential temperature, zonal- and meridional wind is compared for different regions and experiments (Figs. 3.5, 3.6, and 3.7). For potential temperature, cycling period maximum inflation values are similar for both regions and experiments (Fig. 3.5). There is a slight increase in the potential temperature maximum inflation around 5 December 2011 in experiment 2 over the Arctic which is consistent with the adjustment of the time step (Fig. 3.5c). For the zonal wind, the maximum inflation time series is different for the mid-latitudes in experiment 1 compared to the rest of the regions and experiments (Fig. 3.6b to Fig. 3.6a,c,d). Experiment 1 maximum inflation values occur at varying pressure levels relative to experiment 2, where the maximum value starts at lower levels then transitions to upper levels towards the end of cycling (Fig. 3.6a,b compared to Fig. 3.6c,d). Furthermore, the slight increase in the maximum inflation just after 5 days of cycling shows up in the zonal wind, similar to the potential temperature inflation values (Fig. 3.6c compared to Fig. 3.5c). Lastly, maximum inflation associated with the meridional wind is similar to those found for the zonal wind

(Fig. 3.7 compared with Fig. 3.6). Most maximum inflation values asymptote to around a value of 2 towards the end of the cycling period (Fig. 3.7). The slight increase in the maximum inflation around day 5 is the largest for the zonal wind and potential temperature (Fig. 3.7c compared to Fig. 3.6c and Fig. 3.5c). Regardless of the slight increase in maximum inflation early in cycling, the values eventually decrease to those commonly found in geophysical numerical models (Anderson 2009; Anderson et al. 2009). The decrease in maximum inflation over time indicates that the cycling system is working properly and is stable during the cycling period.

To gain a better understanding of the increase in inflation during experiment 2, a spatial visualization of inflation is examined. The time series of maximum inflation (Fig. 3.5, 3.6, and 3.7) shows the increase in the maximum inflation is occurring is around the 250 hPa level. Thus, mean inflation values at 250 hPa will be analyzed during experiment 2's cycling period (Fig. 3.8). There are minimal differences in mean inflation across different variables. The zone of maximum inflation (value near 1.5) is located over the North Pacific for potential temperature, zonal- and meridional-wind. Over the Arctic, the mean inflation is less than that over the mid-latitudes for all variables, and has an average value of around 1.2. Since there is a more consistent, dense network of observations over the mid-latitudes as compared to the Arctic (Fig. 2.2), it is not surprising to see higher inflation values over the mid-latitudes. On average, inflation values stay relatively low for all areas around the globe over the cycling period in experiment 2. However, where there are dense observation networks is co-located with larger values of ensemble inflation. Lastly, weather patterns that are difficult for NWP models to predict would lead to higher ensemble inflation values because both errors and spread issues.

To investigate the period of a slight increase in inflation, 5-day mean inflation is shown centered on the period of interest (Fig. 3.9). For potential temperature, zonal- and meridional-wind, there are larger values of inflation during this time period as compared to mean inflation values for the entire experiment 2 cycling period (compare Fig. 3.9 to Fig. 3.8).

There is a slight increase in inflation over the North Pacific compared to other locations in the mid-latitudes. Over the Arctic, there is a maximum of large inflation values centered over the pole for both potential temperature and meridional-wind, while the zonal-wind inflation is slightly lower (compare Fig. 3.9a,c to Fig. 3.9b). There are small pockets of increased inflation in both the Arctic and the mid-latitudes, which are most likely related to weather features occurring at that time. The increase in ensemble inflation over the Arctic may be related to the model representation of the polar vortex while increased inflation values over the mid-latitudes may be linked back to model representation of weather systems. One would expect to see these when averaging only over several days compared to over a month. Higher values of mean potential temperature ensemble inflation centered over the Arctic could indicate a disagreement in the representation of the tropospheric polar vortex between the model and the observations. Furthermore, the large magnitude, blotchy patterns over the mid-latitudes may be related to misrepresentation (displacement and magnitude errors) of weather systems such as troughs, ridges, surface cyclones, and similar features. Overall, the cycling period mean ensemble inflation values are relatively low over both experiments cycling periods which indicates that our cycling system is stable.

3.2 Bias, RMSE, and Total Spread Profiles and Rank Histograms

Comparison of MPAS-DART to various observations that are assimilated into the cycling system allows for the identification of potential issues. This evaluation is limited to the prognostic state variables within MPAS: temperature, water vapor and wind components. The 6-hour forecast bias will be used to diagnose whether the model is drifting away from the observations. Furthermore, comparison of the spread and skill (RMSE) will help to identify calibration issues within the cycling ensemble system.

MPAS-DART compared to radiosonde temperatures show similar 6-hour forecast bias profiles for both the Arctic and the mid-latitudes for both experiments (Fig. 3.10). There is a cold temperature bias in the middle troposphere for both experiments in the Arctic and

mid-latitudes. The bias is stronger in the Arctic compared to the mid-latitudes. There are disagreements between MPAS-DART and observations in the upper levels (300 hPa and above), which is present in both regions and experiments. The spread and skill profiles for MPAS-DART compared to radiosonde temperature are close to each other for both experiments and regions, except near the surface and above 300 hPa (Fig. 3.10). There are far fewer radiosonde observations over the central Arctic, so to investigate MPAS-DART's performance over the Arctic in more detail, AIRS observations will be examined for comparison (Fig. 3.11). Over both the Arctic and mid-latitudes, the bias values are relatively small at most levels. The surface has larger values in bias, but there are fewer AIRs observations at the surface (spread in the bias is large).

There are larger differences between the experiments when MPAS-DART is compared to AIRS observations than when compared to radiosondes. Over the Arctic, the bias in the upper levels is quite small in the first experiment versus the second experiment (compare Fig. 3.11a to Fig. 3.11c). There are similar biases when examining upper level bias over the mid-latitudes (compare Fig. 3.11b to Fig. 3.11d). Since these experiments are valid for different time periods, early October versus December, this could be representing different bias patterns that may occur during different seasons (Rodwell and Jung 2008). Since AIRS satellite temperature observations are retrievals and radiosonde observations are in-situ observations, comparing their bias profiles could provide helpful insight on how these observations are effecting MPAS-DART. There are lower bias values for both experiments over the Arctic when comparing MPAS-DART to AIRS versus radiosonde observations (compare Fig. 3.11a,c to Fig. 3.10a,c). Additionally, upper-level bias values over the mid-latitudes are larger when compared to radiosonde versus AIRS observations (compare Fig. 3.11b,d to Fig. 3.10b,d). There are far more AIRS observations assimilated versus radiosonde observations for both regions, thus this could mean the MPAS-DART system is over fitting to the AIRS observations. The process of thinning the AIRS observations

(super-obing) might need to be increased, which needs to be investigated more in future studies.

AIRS and radiosonde specific humidity observations are the only two moisture observations that are assimilated above the surface. Comparing MPAS-DART to radiosonde specific humidity observations shows a low moisture bias in the lower troposphere over the Arctic for both experiments (compare Fig. 3.12a,c). Over the mid-latitudes, the bias is reduced, but has reversed signs to mainly positive in the lower troposphere (compare Fig. 3.12b,d). Additionally, there is large separation between ensemble spread and RMSE for both regions and experiments indicating there could be calibration issues with regard to moisture within MPAS-DART.

Since AIRS specific humidity observations account for the bulk of the moisture observations assimilated in the Arctic, comparisons of MPAS-DART to these observations can provide important information on whether there are systematic issues over the Arctic regarding moisture (Fig. 3.13). There is a positive moisture bias over the Arctic throughout the troposphere in experiment 1, but is the bias is reduced in experiment 2 (compare Fig. 3.13a to Fig. 3.13c). The bias over the mid-latitudes is nearly zero throughout the profile except near the surface, where there is a positive bias (compare Fig. 3.13b to Fig. 3.13d). In agreement with radiosonde specific humidity observations, there is an increase in the separation between the ensemble spread and RMSE for both regions and experiments (compare Fig. 3.12 to Fig. 3.13). Comparing the profiles between radiosonde and AIRS specific humidity, radiosondes show a negative bias where the AIRS profiles show a positive bias (compare Fig. 3.12a,c to Fig. 3.13a,c). The bias profiles are similar in magnitude and sign between observation types over the mid-latitudes (compare Fig. 3.12b,d to Fig. 3.13d,d). Due to the radiosonde locations being located around the outer portion of the Arctic, this could suggest that the AIRS observations are sampling more of the inner-portion of the Arctic. This could be an explanation for the differences in bias profiles over the Arctic and similarities over the mid-latitudes.

There are three different types of wind observations that are assimilated in MPAS-DART: radiosonde winds, polar orbiting winds (MODIS) and geostationary satellite winds. Comparing MPAS-DART to radiosonde zonal winds shows bias profiles near zero for both regions and experiments, except near the surface (Fig. 3.14). The bias profiles are similar when MPAS-DART is compared to radiosonde meridional winds, except near the surface and over the Arctic in experiment 2 where there is a slight negative bias (Fig. 3.15). Near surface wind biases will be examined later with rank histograms. Geostationary satellite wind observations are mainly located in mid-latitudes, so they can provide information on MPAS-DART wind performance in that location. For experiment 1, the bias profiles are very close to zero for both zonal and meridional winds, except the the zonal wind bias near 700 hPa (Fig. 3.16a,b). For experiment 2, there is a positive bias present in the zonal winds throughout the profiles whereas there is a slight negative meridional wind bias above 300 hPa were there are few observations (Fig. 3.16c,d). Since the peak in the zonal wind bias near 700 hPa is present in both experiments, this could indicate that MPAS-DART has systematic errors in representing the zonal wind at this level. This differing in zonal wind bias between experiments could be related to the different time periods represented, late fall in experiment 1 versus December in experiment 2.

The last wind observations dataset assimilated is polar orbiting satellite or MODIS winds (Fig. 3.17). These observations are only assimilated in the polar regions, so they can provide information on MPAS-DART performance over the Arctic. Similar to radiosonde wind observations, the bias is nearly zero throughout the column for experiment 1 (Fig. 3.17a,b). For experiment 2, there is a negative bias for both zonal and meridional wind components around 250 hPa over the Arctic (Fig. 3.17c,d). This is similar to the results found when comparing MPAS-DART to geostationary satellite observations that are over the mid-latitudes (compare Fig. 3.16 to Fig. 3.17). Since large biases are found over the Arctic in upper-levels for both polar orbiting and radiosonde wind observations in experiment 2, this could point to poor representation of the jet stream or the tropospheric

polar vortex in experiment 2. Lastly, the ensemble spread and RMSE is relatively close to each for all wind observation types, meaning MPAS-DART seems to be relatively well-calibrated in terms of wind.

To examine and evaluate MPAS-DART performance at the surface, rank histograms are analyzed for AWS and marine buoy surface observations. These temperature comparisons share a common theme: too much spread, represented by the inverted "U" shape (Fig. 3.18 and Fig. 3.19). AWS rank histograms have a peak in counts on the left side for both experiments and regions meaning MPAS-DART has a warm bias compared to the observations (Fig. 3.18). When comparing MPAS-DART to marine buoy temperature observations, there are peaks in counts on both the right (cold bias) and left (warm bias) side in the experiment 1 over the Arctic and a peak on the right side (cold bias) for experiment 2 over the Arctic (Fig. 3.19a,c). Once again there is too much ensemble spread when comparing MPAS-DART to AWS and marine buoy specific humidity observations (Fig. 3.20 and Fig. 3.21). There is evidence of a positive moisture bias when evaluating against AWS observations, indicated by the peak on the left side, in experiment two over both the Arctic and the mid-latitudes which is not present in experiment 1 (Fig. 3.20). However, there does not appear to be a bias in moisture when compared to marine buoy specific humidity observations (Fig. 3.21). With regard to the different wind components in MPAS-DART, there does not appear to be a ensemble spread issue when compared to AWS wind observations versus marine buoy observations (compare Figs. 3.23 and 3.25 to Figs. 3.22 and 3.24). The disagree in spread issues for surface wind components could be highlighting difficulties in model representation of wind near the surface over land as compared to over the ocean, where in most cases flow is relatively uniform. In terms of biases, there is a slight bias associated with the zonal wind component in experiment 2 over both regions (Fig. 3.22c,d) and a slight bias over the Arctic associated with the meridional wind component when compared to AWS observations (Fig. 3.24c). MPAS-DART appears to have both low and high wind speed biases for both wind components when compared to marine buoy

wind observations (Figs. 3.23 and 3.25). Overall, there tends to be too much ensemble spread within MPAS-DART at the surface for most variables. As mentioned above, this suggests the model has difficulty representing the surface over both regions. Lastly, the rejection rate is higher for the AWS observations in the mid-latitudes but greater for marine buoy observations over the Arctic (compare Figs. 3.18, 3.20, 3.22, and 3.24 to Figs. 3.19, 3.21, 3.23 and 3.25). The higher rejection rate could be a result of greater density of AWS observations over the mid-latitudes, which provides more opportunity to reject observations for multiple reasons. Similarly, there are more marine buoy observations over the Arctic which provides more opportunities for observations to be rejected.

3.3 Analysis Increment

To this point, MPAS-DART has been evaluated with average profiles of different metrics and rank histograms for near surface observations. These evaluation techniques provide a temporally and spatially averaged view of the different metrics, but offer little information about regional variability in performance. A bias-blind data assimilation system, only designed to correct random errors, will have a biased analysis if biases are present in the background fields or in the observations (Dee 2005). If the NWP model is being cycled with a data assimilation system, evaluation of analysis increment (AI; analysis minus background forecast) can determine systematic model biases (negative of AI is model bias). AI was introduced at the beginning of Ch. 3. Recall, non-zero values indicate that observations are adjusting the background fields. AIs can provide spatial information about the evaluation of MPAS-DART. Since this study focuses on the performance of MPAS-DART over the Arctic, evaluation of AI will accordingly focus over this region.

There are differences in spatially averaged potential temperature AI over the Arctic between experiments (Fig. 3.26). There are significant positive AIs located in the layers between 150 hPa and 50 hPa in experiment 1, meaning MPAS-DART is colder compared to observations (Fig. 3.26a). Comparing AI in experiment 1 to experiment 2 in the early

cycling times, there are positive significant AIs (cold bias) in the layers spanning 200 hPa to 100 hPa and negative significant AIs (warm bias) in the layers between 100 hPa and 50 hPa (Fig. 3.26b). Later in experiment cycling time, there is a transition to mainly negative significant AIs (warm bias) spanning the layer from 200 hPa up to 50 hPa (Fig. 3.26b). In the middle troposphere, there are significant AIs early in the cycling period, but after a few days of cycling, they disappear and AIs appear more random (Fig. 3.26). For both experiments, there are positive AIs confined close to the 1000 hPa (Fig. 3.26).

The magnitude of water vapor AIs are largest in the middle troposphere, where profiles of moisture observations are found from AIRS or radiosondes (Fig. 3.27). There are more periods of significant negative AI in experiment 1 versus in experiment 2 (compare Fig. 3.27a to Fig. 3.27b). This reduction in AIs could be due to the different initialization process that was used for experiment 2, as discussed in Section 2.4. Furthermore, there are positive AI values near 1000 hPa in both experiments, which is different from the negative AI values found in the middle troposphere (Fig. 3.27). There are very small, but significant negative AIs located above 200 hPa in both experiments (Fig. 3.27). However, water vapor decreases exponentially with height, so smaller AIs can still have significant physical implications. Since increment values are very small in this layer, time-height water vapor analysis increment figure are examined spanning 300 hPa up to 50 hPa for both experiments (Fig. 3.28). For both experiments, there are significant negative AIs located in this layer with experiment 1 having much lower AIs compared to experiment 2 (compare Fig. 3.28a to Fig. 3.28b). Once again, this could be due to the different moisture initialization process used.

Lastly, the AIs associated with MPAS-DART wind components have fewer periods of significant values and values are more random over the cycling period (Fig. 3.29 and Fig. 3.30). For the zonal wind component, there is a short period in experiment 1 where there are significant negative AIs (high zonal wind bias) around 300 hPa (Fig. 3.29a), but in experiment 2 above 100 hPa there are significant positive AIs over the last half of

the cycling period (Fig. 3.29b). For both experiments, the meridional wind AIs are low, random and have few periods where significant increments appear (Fig. 3.30). Overall, the spatially averaged AIs over the Arctic are relatively small for the different variables. Further investigation is needed for the significant AIs found in the upper levels for potential temperature, and the zonal wind component, and near the surface for water vapor.

In order to further evaluate the spatial distribution of AIs, mean AIs over the cycling period are computed for both experiments. Furthermore, cycling period AI standard deviations are computed, which provides a quantification of the spread of the increments. Areas that are below the 20th percentile value of a distribution of the standard deviation values are hatched to show regions where AI values are not temporally varying. To further investigate the significant potential temperature increments found in the upper levels, cycling period averaged 100 hPa potential temperature AIs are computed for the different experiments (Fig. 3.31). For experiment 1, positive AIs are found throughout most the Arctic region with some areas having low standard deviations values (Fig. 3.31a). For experiment 2, there are strong negative AIs situated over Alaska and Northern Canada (Fig. 3.31b). However, the standard deviation values in this region are relatively large (no stippling), meaning the strong AIs are not continually present throughout the cycling period. Furthermore, there are strong positive AI values over Northern Russia with some areas having low standard deviations (Fig. 3.31b). The 100 hPa level marks the transition from the tropospheric polar vortex to the stratospheric polar vortex (Waugh et al. 2017). Since 100 hPa potential temperature analysis increments are within that transition level, these increments could represent a location error in the lower levels of the stratospheric vortex or errors associated with the coupling of the two large-scale vortices.

An increase in significant zonal AIs at 75 hPa is found in experiment 2 when averaged over the entire cycling period. To investigate these significant increments further, cycling period averaged 75 hPa zonal wind AIs are compared for the two experiments (Fig. 3.32). There is an enhanced area of positive AIs over Alaska and extending into the North Pacific

in the mean zonal AIs for experiment 2 (Fig. 3.32b). Since there is no hatching over this area, which could mean there are very high AI values for only a short period during cycling, while the rest of the period had very small AI values. Furthermore, the negative AIs over Resolute and Eureka could be related to the two radiosondes sites in this area. Comparing to experiment 1, the AI patterns are more random and at a lower magnitude, especially over Alaska (Fig. 3.32b). The area of increased zonal wind, denoted by the positive AIs, over Alaska is co-located with the region where there is an increase in the 100 hPa potential temperature gradient from temperature observations (compare Fig. 3.32b to Fig. 3.31b). Even though the zonal wind and potential temperature AIs are at different levels, this could be a balance response to observations lowering potential temperature over the Beaufort sea and Canadian Archipelago, thus increasing the zonal wind around 60° N. This further supports the idea that the wind speeds associated with lower levels of the stratospheric vortex are being misrepresented.

There is a pattern of positive AIs near the surface in both potential temperature and water vapor when averaged over the Arctic (Figs. 3.26 and 3.27). Rank histograms are generally consistent with the AIs for potential temperature and water vapor near the surface (Figs. 3.18, 3.19, 3.20, 3.21). Two-meter temperature AIs for experiment 1 reveal two areas where there are higher values, one over sea ice and the other over land (Fig. 3.33a). Conversely, there are large AI values over sea ice in experiment 2, while over land there are similar magnitudes but opposing signs compared to experiment 1 (compare Fig. 3.33a to Fig. 3.33b). The positive AIs are co-located with surface observations for both experiments (Fig. 3.33). Even though there are varying signs associated with the AIs over land, they are located in the same areas for both experiments. Since they are located in the same area could mean that the various mountain ranges with large magnitudes of AI located in the Arctic are not well-represented. Jung and Matsueda (2016) found high analysis uncertainties near the surface in the Arctic compared to the mid-latitudes near the surface, especially

over snow-covered and ice-covered surfaces. This highlights the difficulties weather models have representing near-surface variables over the Arctic. For two-meter water vapor, there are similar areas with a large magnitude in AI values as found for to two-meter temperature (compare Fig. 3.33 to Fig. 3.34). Over sea ice for both experiments, there are larger water vapor AI values that are co-located with surface observations (Fig. 3.34). One area that is different across the experiments is Northern Russia, where there are smaller magnitude AI values in experiment 2 than in experiment 1 (compare Fig. 3.34b to Fig. 3.34a).

Overall, MPAS-DART has successfully cycled two different experiments with varying time spans. Maximum ensemble prior inflation decreased with time for both experiments and in all regions, which indicated our cycling system was stable. There were similar magnitudes and signs for biases associated with MPAS-DART for both the Arctic and mid-latitudes. The use of AI averaged over the Arctic identified some potential issues for both experiments. These issues included: 1) significant positive potential temperature AIs in the upper levels for experiment 1, (2) significant positive zonal wind AIs in upper levels for experiment 2, and (3) positive temperature and water vapor AIs near the surface for both experiments. These potential issues will be further investigated in subsequent chapters by applying a novel evaluation technique within MPAS-DART. The novel evaluation technique will aid in a better understanding of the physical processes connect to the issues that were identified in this chapter.

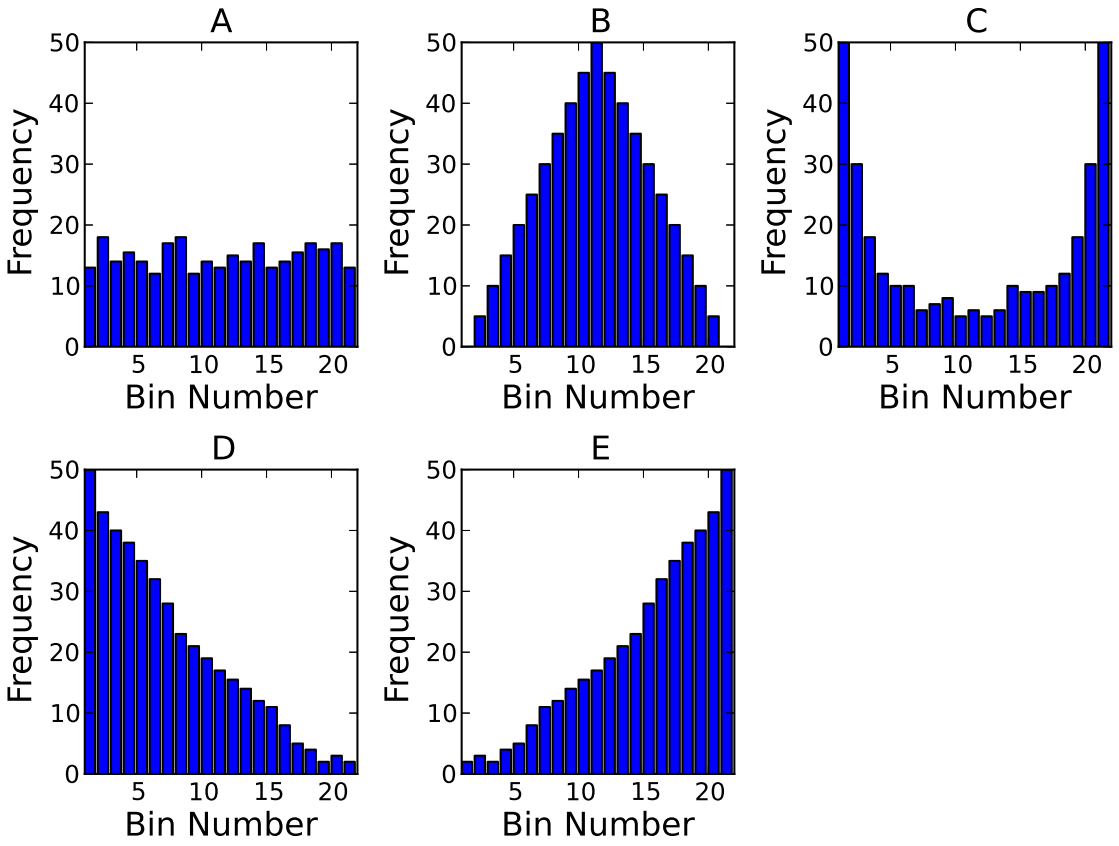

Figure 3.1: These are examples of rank histogram types when evaluating temperature: (A) well-calibrated ensemble spread, (B) ensemble spread is to large, (C) ensemble spread is small, (D) ensemble has a warm bias, and (E) ensemble has a cold bias.

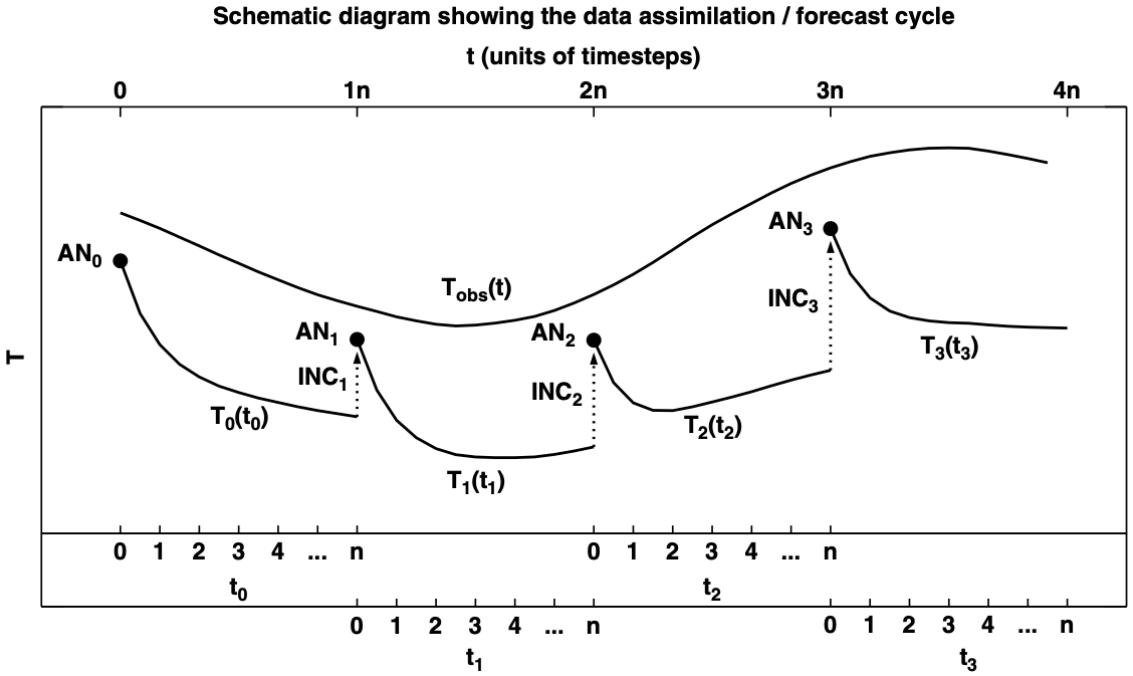

Figure 3.2: This schematic diagram shows the data assimilation and forecast integration aspects of numerical weather prediction. $T_{obs}(t)$ represents an observed time series (e.g. of temperature at some specified location with temperature increasing as you move up the y-axis). For each i, T_i (t_i) represents the model forecast initiated from analysis AN_i. INC_i represents the adjustment added to the forecast from the observations to make the new AN_i. This figure is from Rodwell and Palmer (2007a)

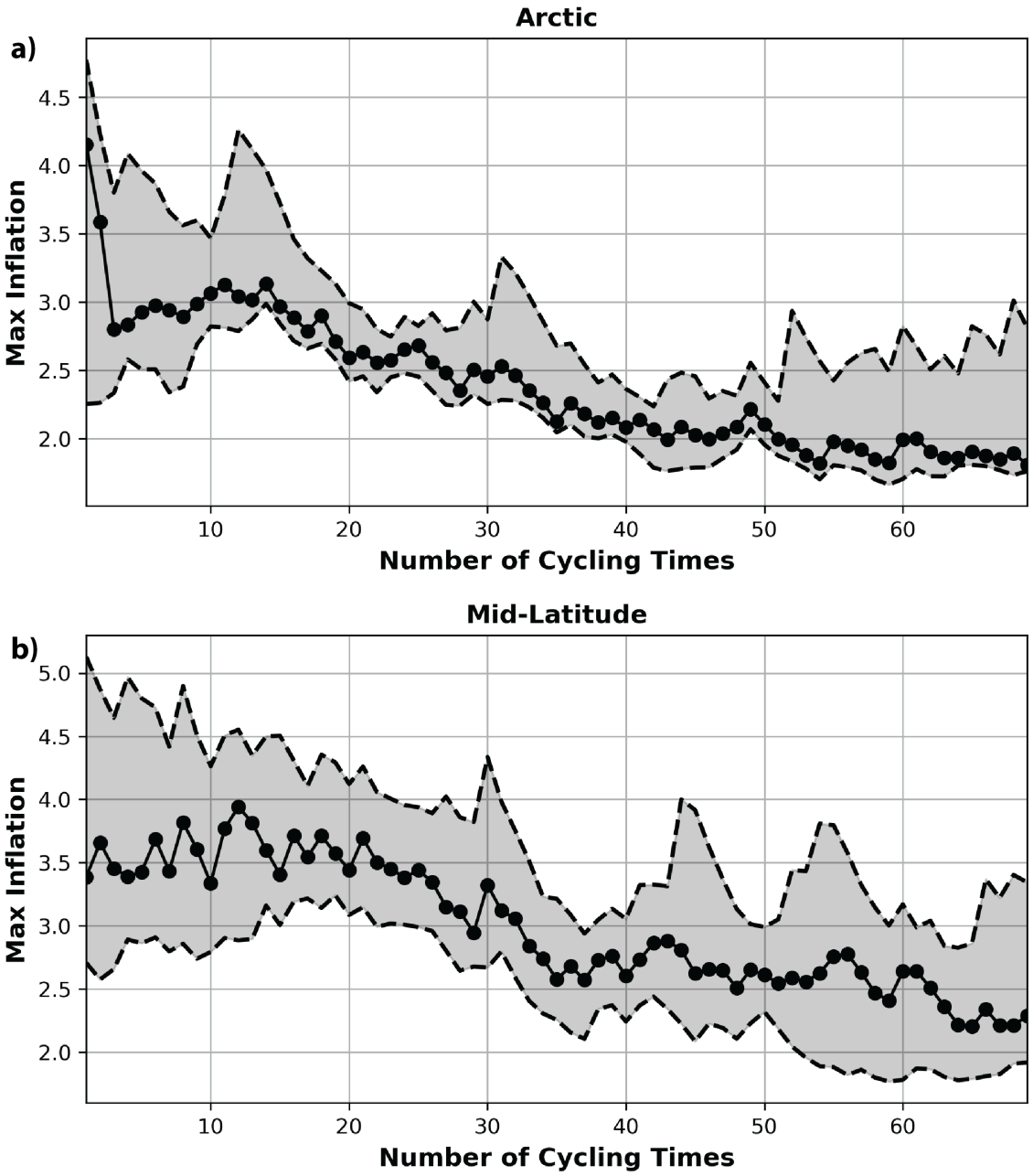

Figure 3.3: Time series showing maximum inflation for all state variables for experiment 1. Shading shows the range in the max inflation values between the 2.5 and 97.5 percentiles.

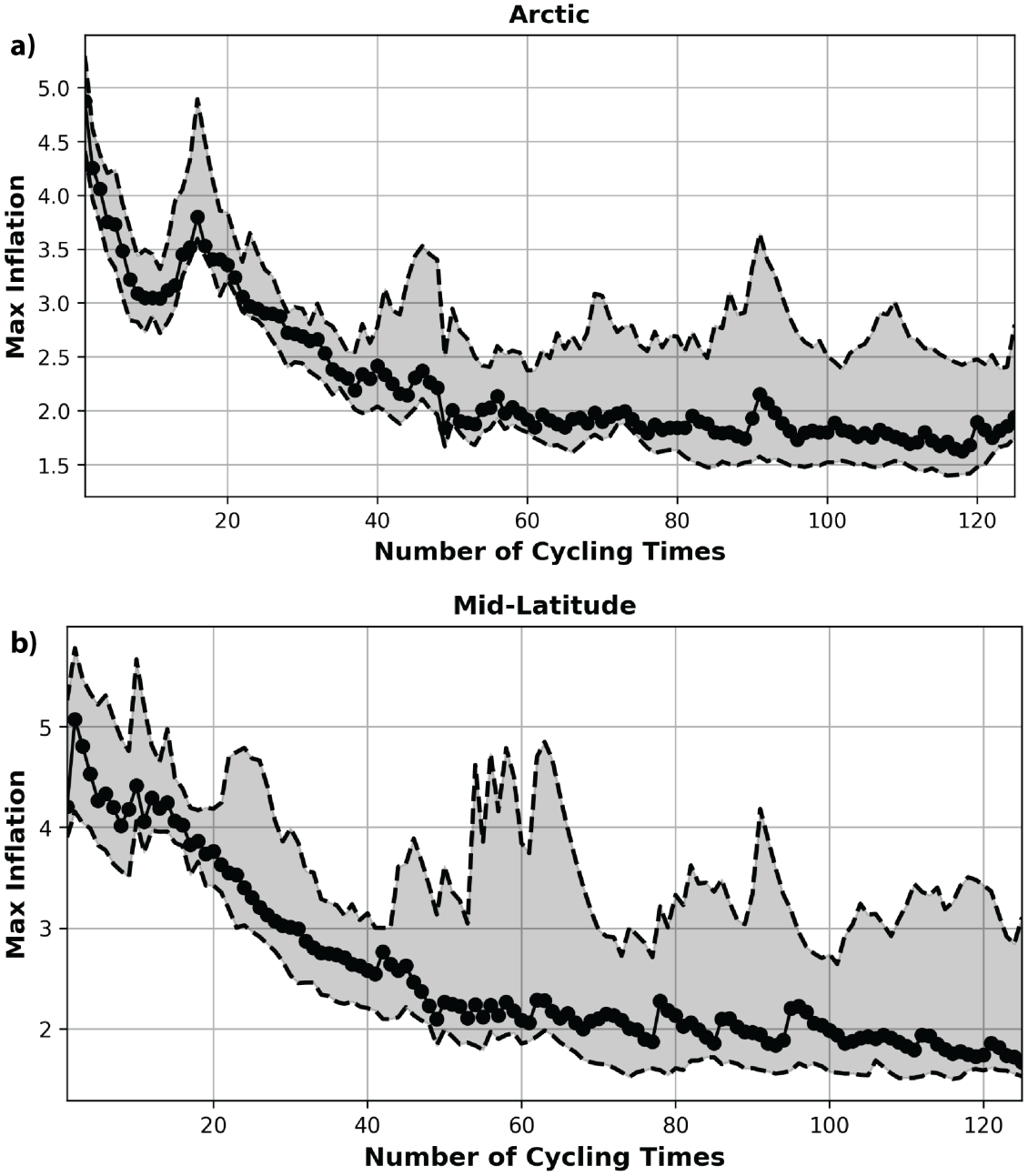

Figure 3.4: Time series showing maximum inflation for all state variables for experiment 2. Shading shows the range in the max inflation values between the 2.5 and 97.5 percentiles.

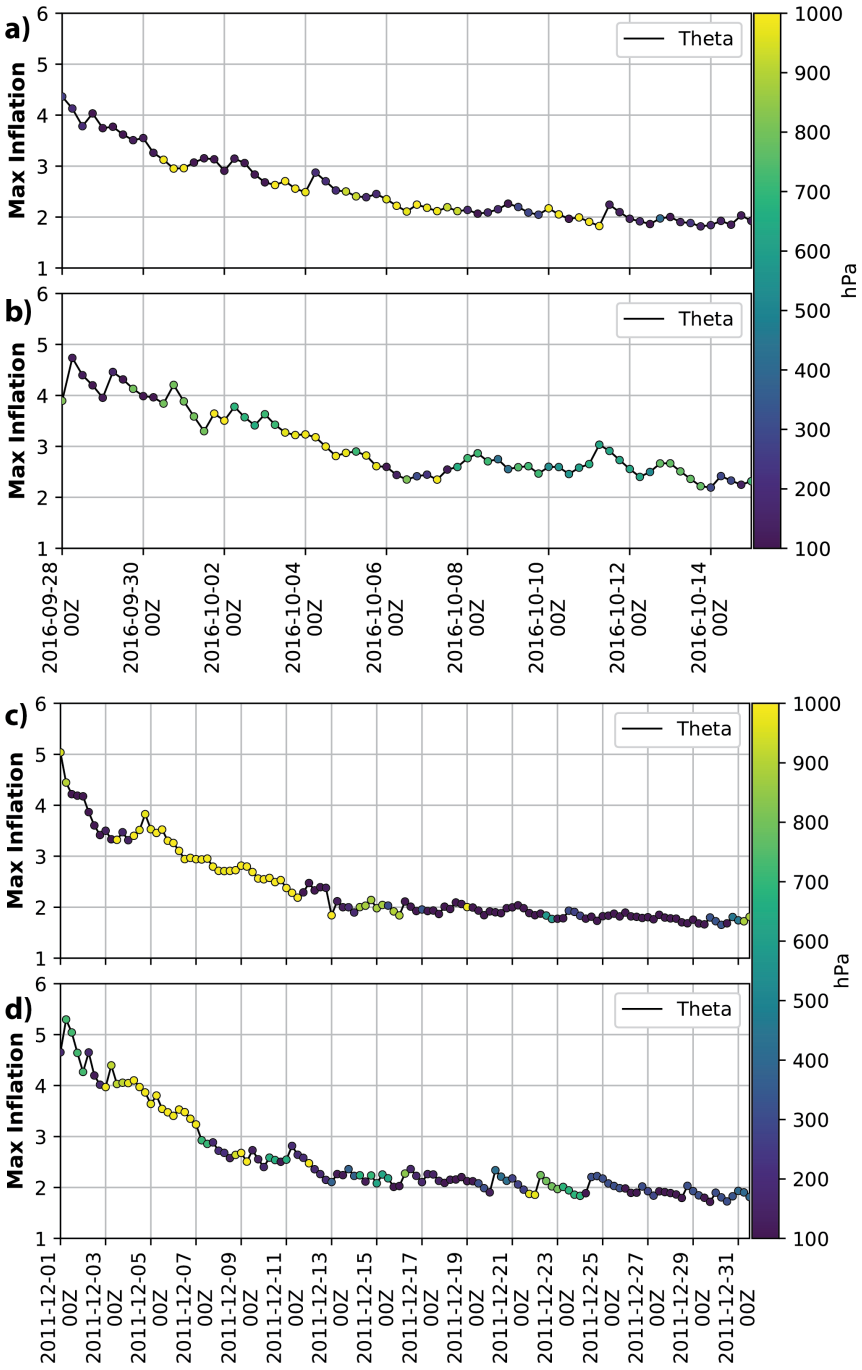

Figure 3.5: Time series showing max inflation associated with potential temperature over the Arctic (a,c) and over the mid-latitudes (b,d) for experiment 1 (a,b) and experiment 2 (c,d). Dot colors represent the pressure level the max inflation value is at.

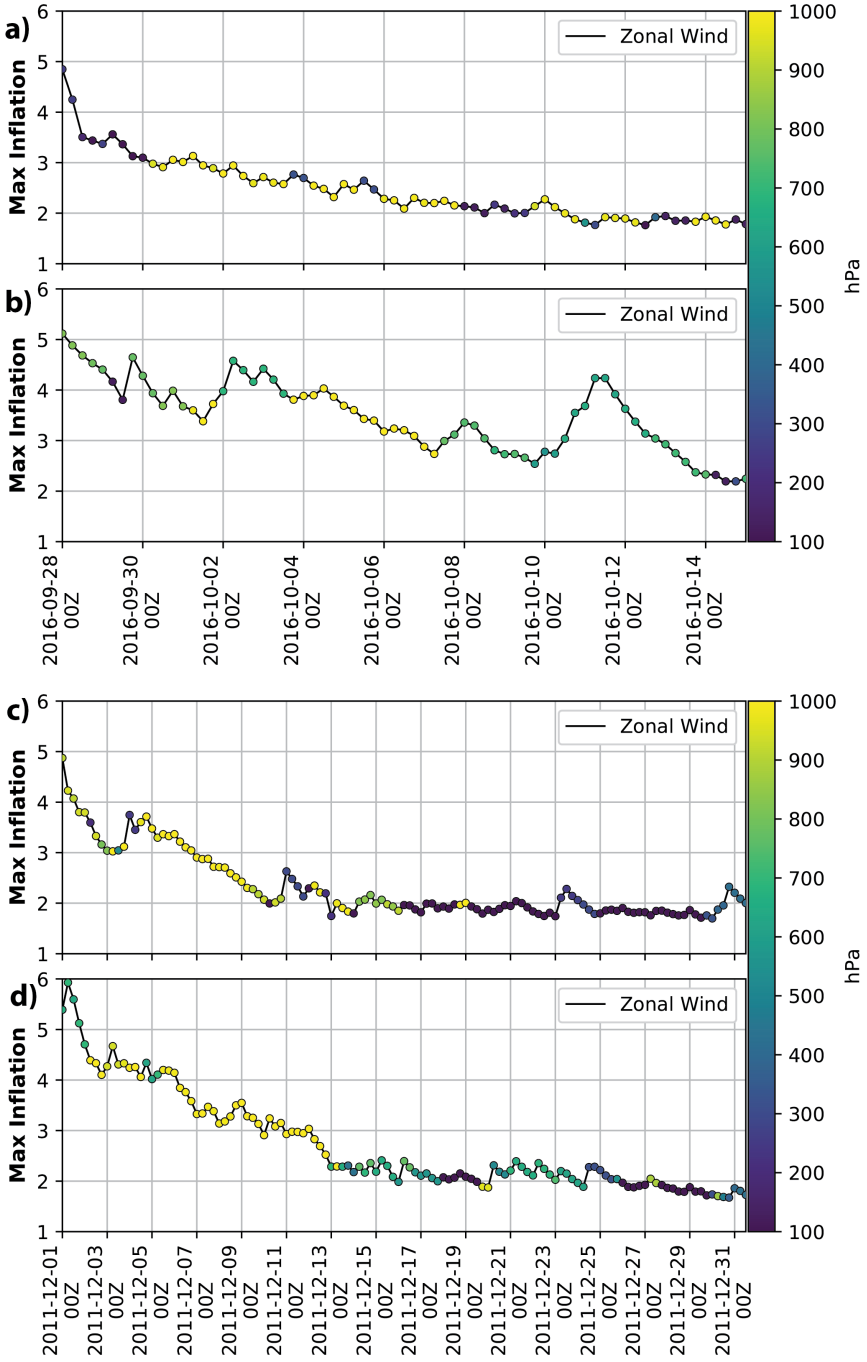

Figure 3.6: Time series showing max inflation associated with the zonal wind over the Arctic (a,c) and over the mid-latitudes (b,d) for experiment 1 (a,b) and experiment 2 (c,d). Dot colors represent the pressure level the max inflation value is at.

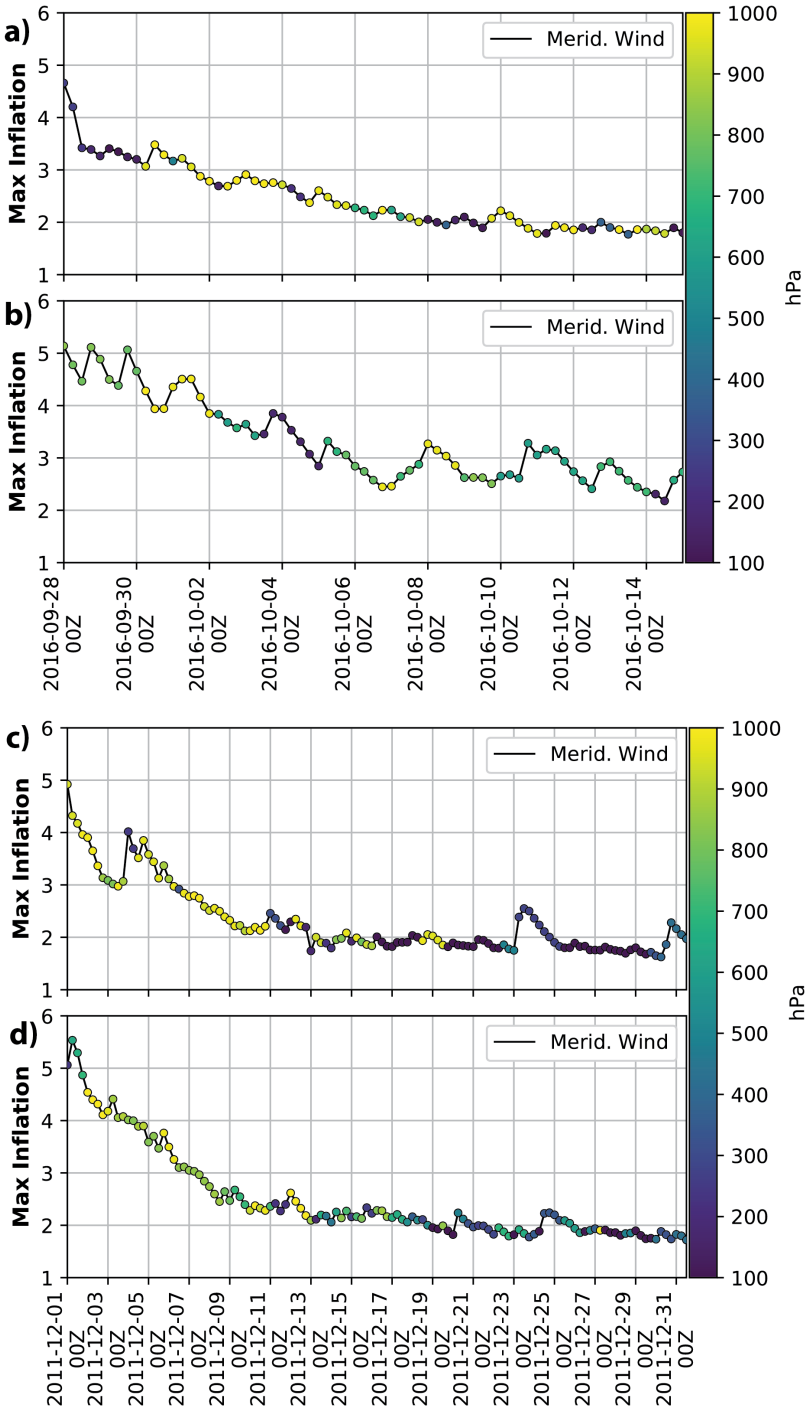

Figure 3.7: Time series showing max inflation associated with the meridional wind over the Arctic (a,c) and over the mid-latitudes (b,d) for experiment 1 (a,b) and experiment 2 (c,d). Dot colors represent the pressure level the max inflation value is at.

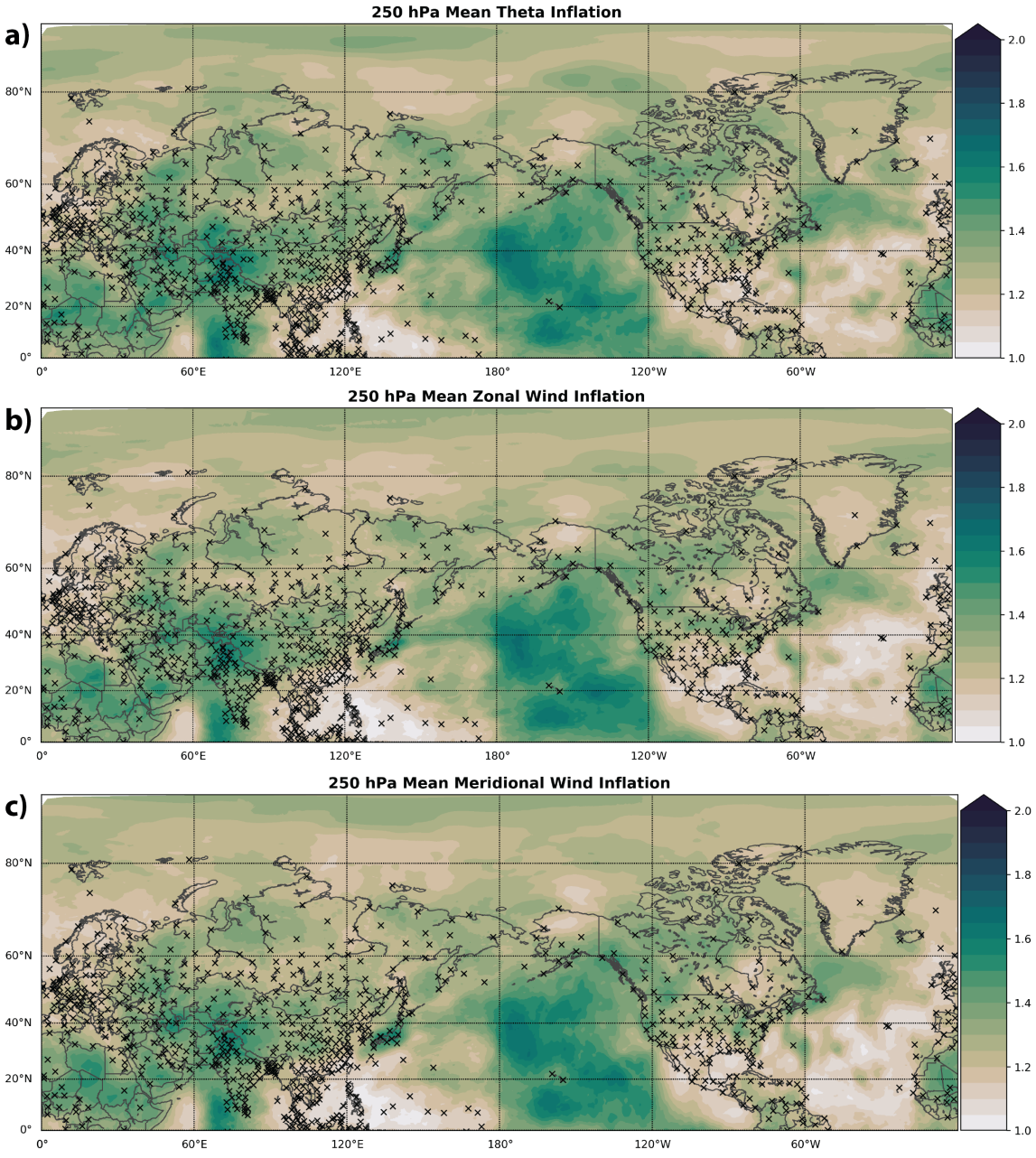

Figure 3.8: Mean (a) potential temperature, (b) zonal- and (c) meridional-wind inflation calculated over experiment 2 cycling period at 250 hPa. Crosses mark locations of radiosonde launch sites.

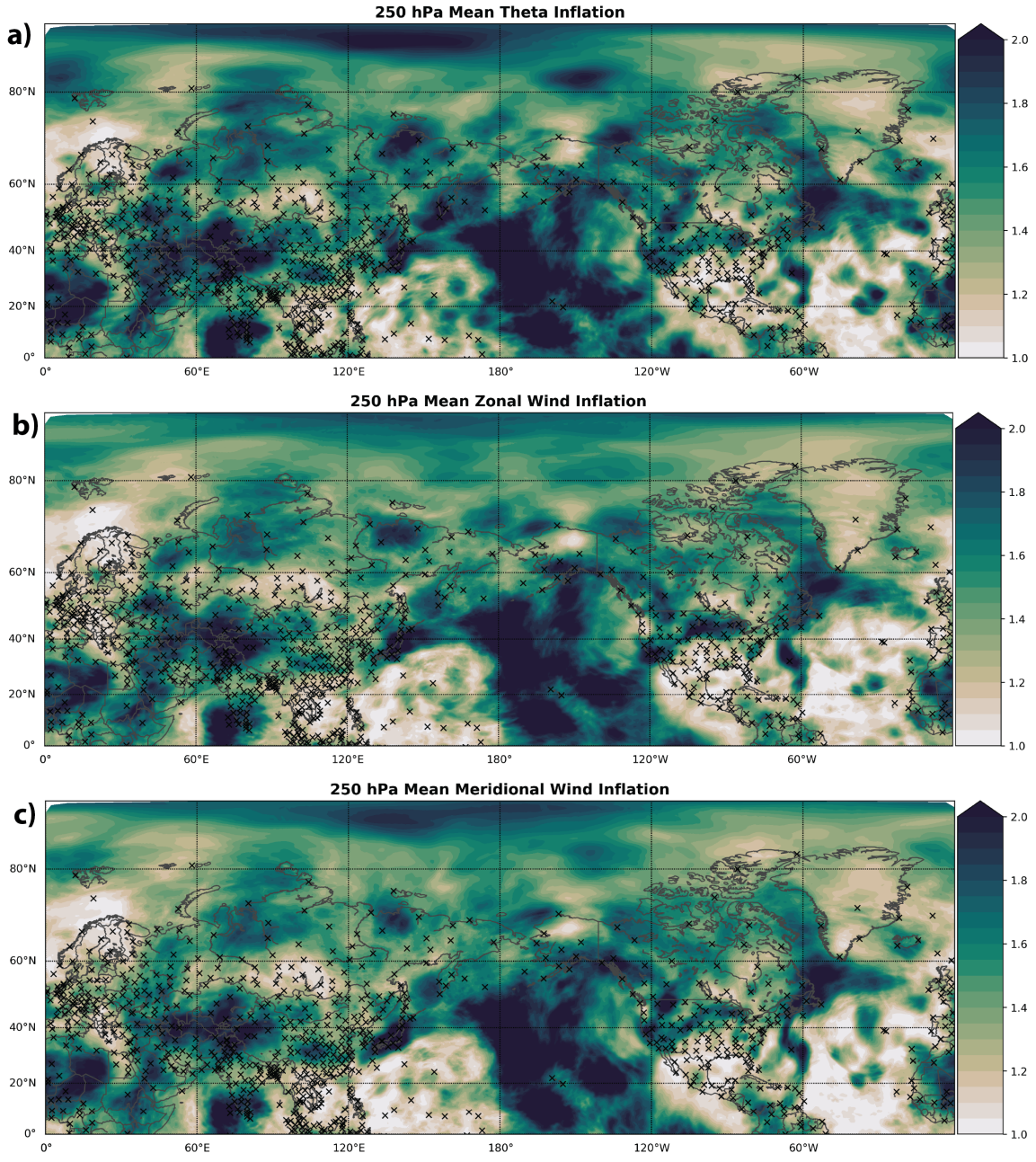

Figure 3.9: Mean (a) potential temperature, (b) zonal- and (c) meridional-wind calculated over the increased inflation period centered on 5 December 2011 in experiment 2 at 250 hPa. Inflation values were averaged over a 2 day window with the center being on 5 December 2011. Crosses mark locations of radiosonde launch sites.

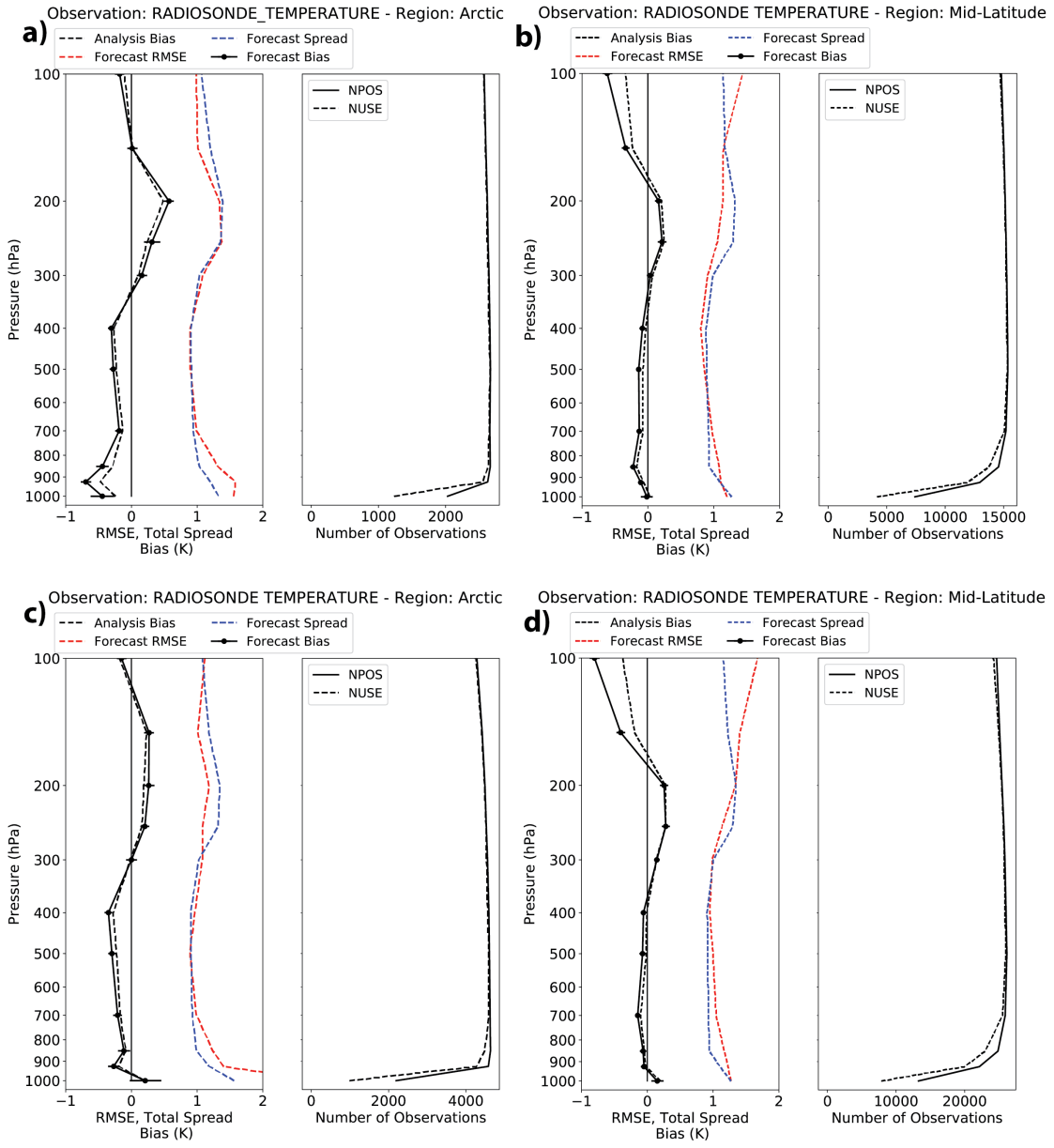

Figure 3.10: Cycling period averaged vertical profiles of analysis bias (dashed black), 6-hour model forecast bias (black), RMSE (dashed red), and ensemble total spread (dashed blue) when compared to radiosonde temperature observations. Profiles are averaged over the Arctic (a,c) and the mid-latitudes (b,d) for both experiment 1 (a,b) and experiment 2 (c,d). Within all panels, the left profile shows cycling period mean values while the right profile shows total observation counts over the cycling period. Error bars represent the 95% confidence interval from bootstrap resampling.

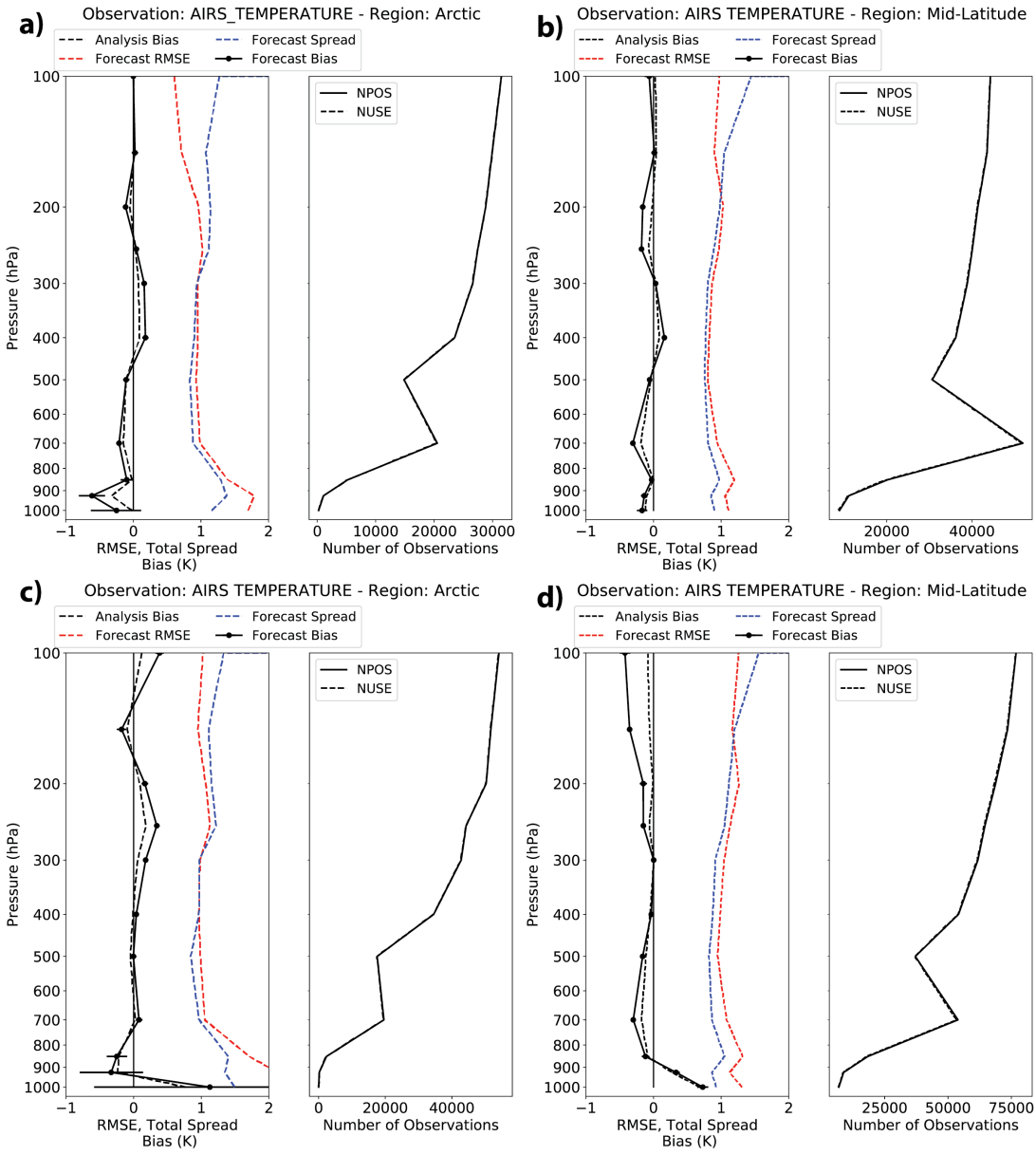

Figure 3.11: Cycling period averaged vertical profiles of analysis bias (dashed black), 6-hour model forecast bias (black), RMSE (dashed red), and ensemble total spread (dashed blue) when compared to AIRS temperature observations. Profiles are averaged over the Arctic (a,c) and the mid-latitudes (b,d) for both experiment 1 (a,b) and experiment 2 (c,d). Within all panels, the left profile shows cycling period mean values while the right profile shows total observation counts over the cycling period. Error bars represent the 95% confidence interval from bootstrap resampling.

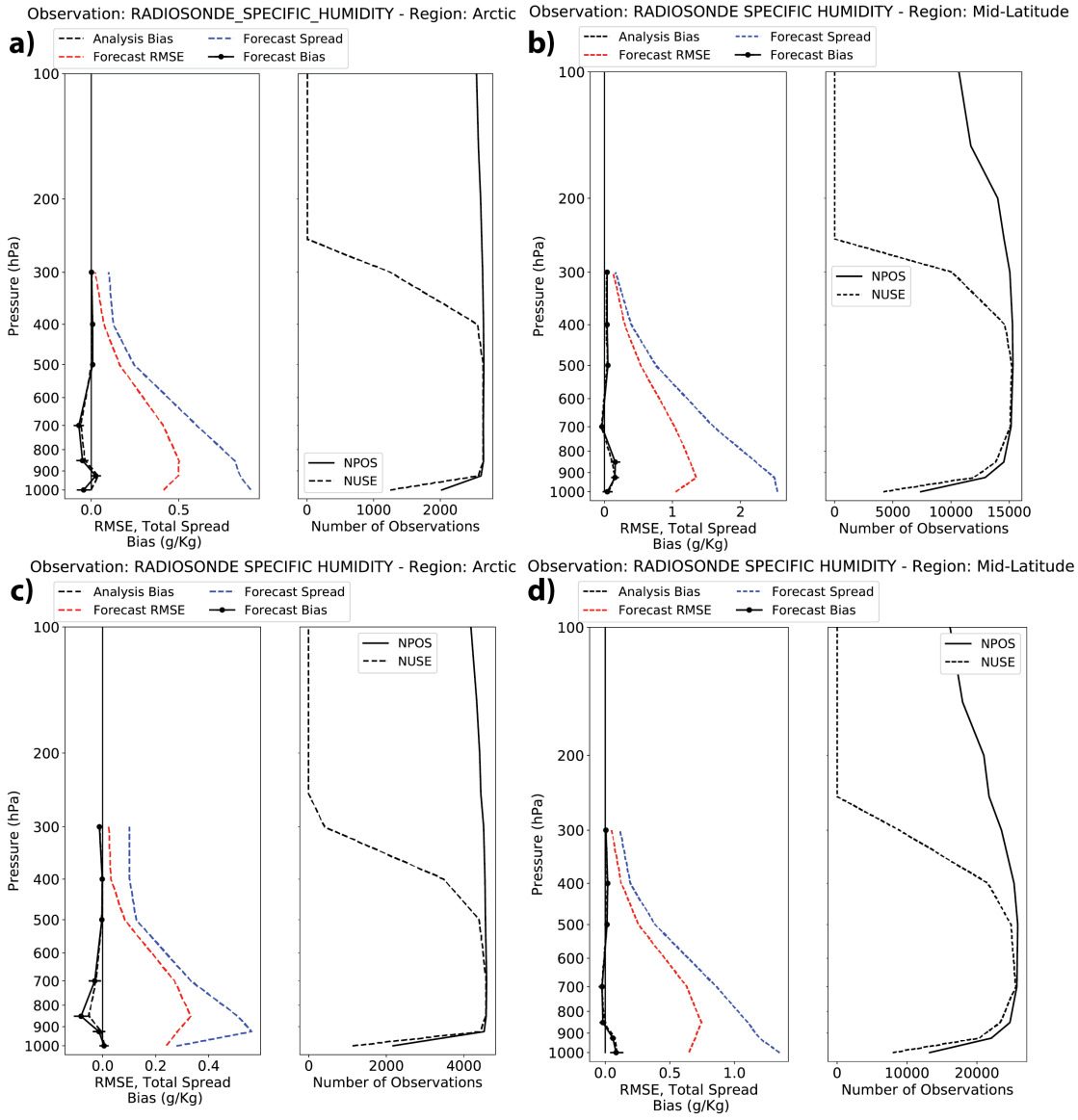

Figure 3.12: Cycling period averaged vertical profiles of analysis bias (dashed black), 6-hour model forecast bias (black), RMSE (dashed red), and ensemble total spread (dashed blue) when compared to radiosonde specific humidity observations. Profiles are averaged over the Arctic (a,c) and the mid-latitudes (b,d) for both experiment 1 (a,b) and experiment 2 (c,d). Within all panels, the left profile shows cycling period mean values while the right profile shows total observation counts over the cycling period. Error bars represent the 95% confidence interval from bootstrap resampling.

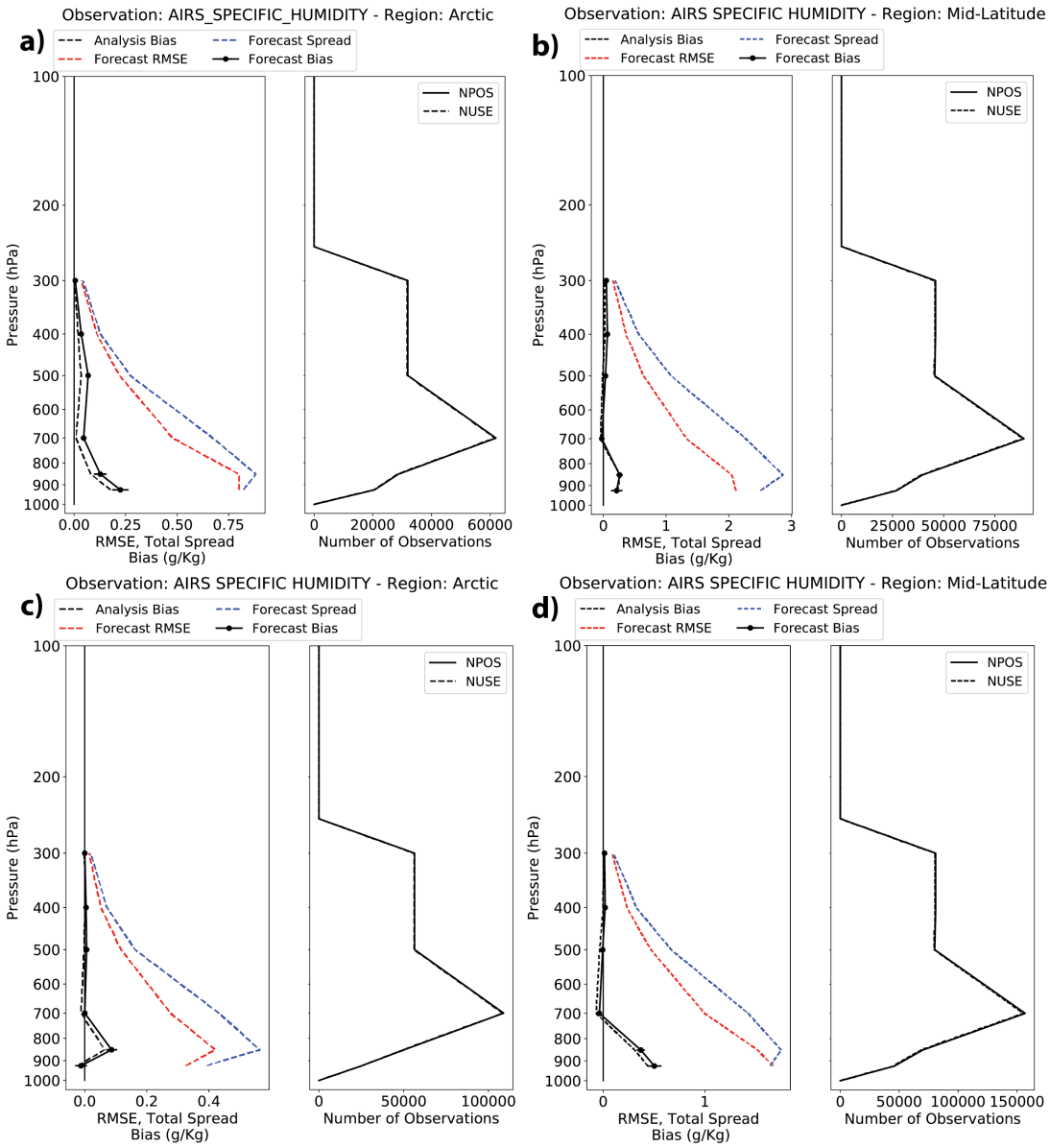

Figure 3.13: Cycling period averaged vertical profiles of analysis bias (dashed black), 6-hour model forecast bias (black), RMSE (dashed red), and ensemble total spread (dashed blue) when compared to AIRS specific humidity observations. Profiles are averaged over the Arctic (a,c) and the mid-latitudes (b,d) for both experiment 1 (a,b) and experiment 2 (c,d). Within all panels, the left profile shows cycling period mean values while the right profile shows total observation counts over the cycling period. Error bars represent the 95% confidence interval from bootstrap resampling.

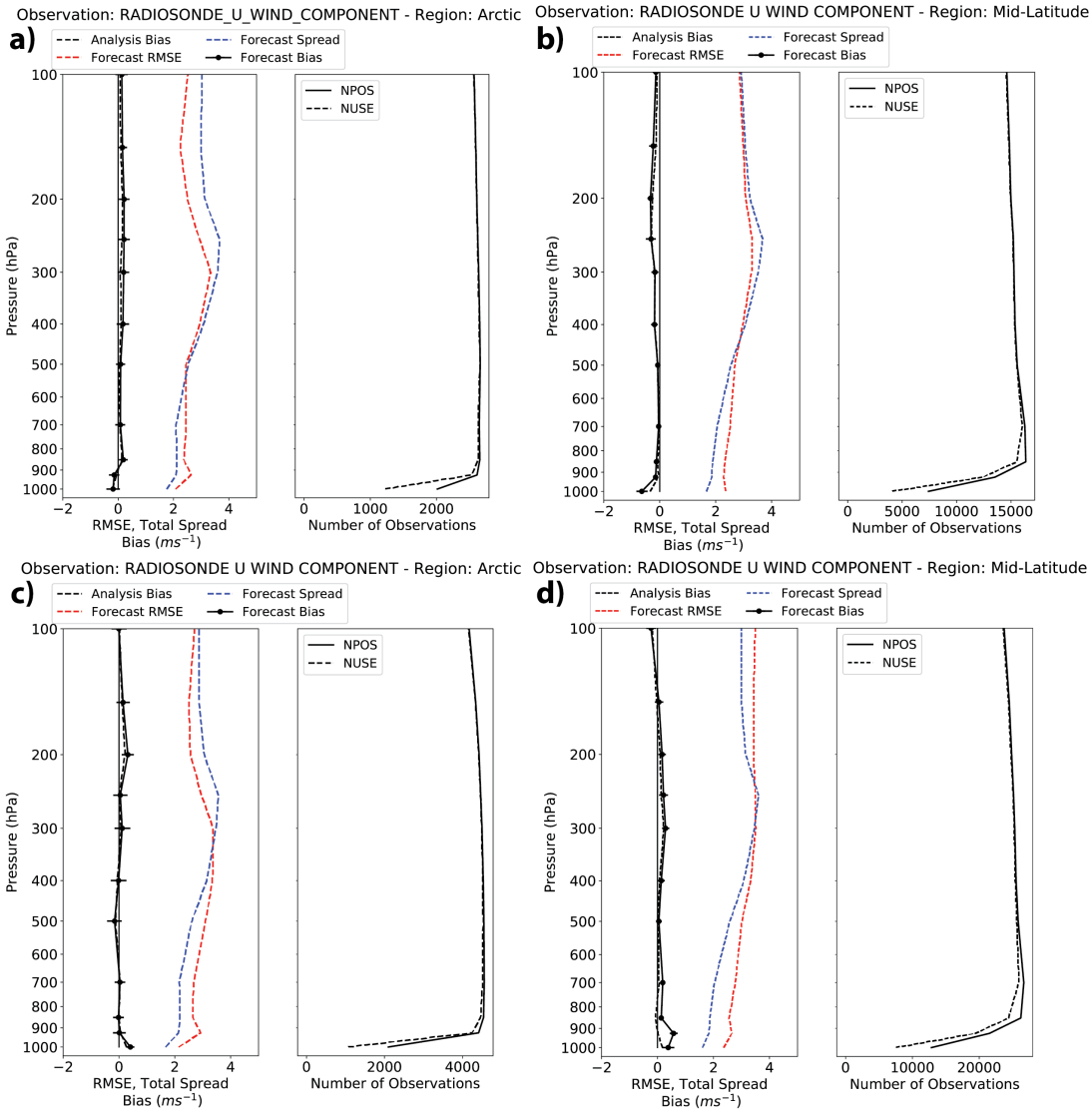

Figure 3.14: Cycling period averaged vertical profiles of analysis bias (dashed black), 6-hour model forecast bias (black), RMSE (dashed red), and ensemble total spread (dashed blue) when compared to radiosonde zonal-wind observations. Profiles are averaged over the Arctic (a,c) and the mid-latitudes (b,d) for both experiment 1 (a,b) and experiment 2 (c,d). Within all panels, the left profile shows cycling period mean values while the right profile shows total observation counts over the cycling period. Error bars represent the 95% confidence interval from bootstrap resampling.

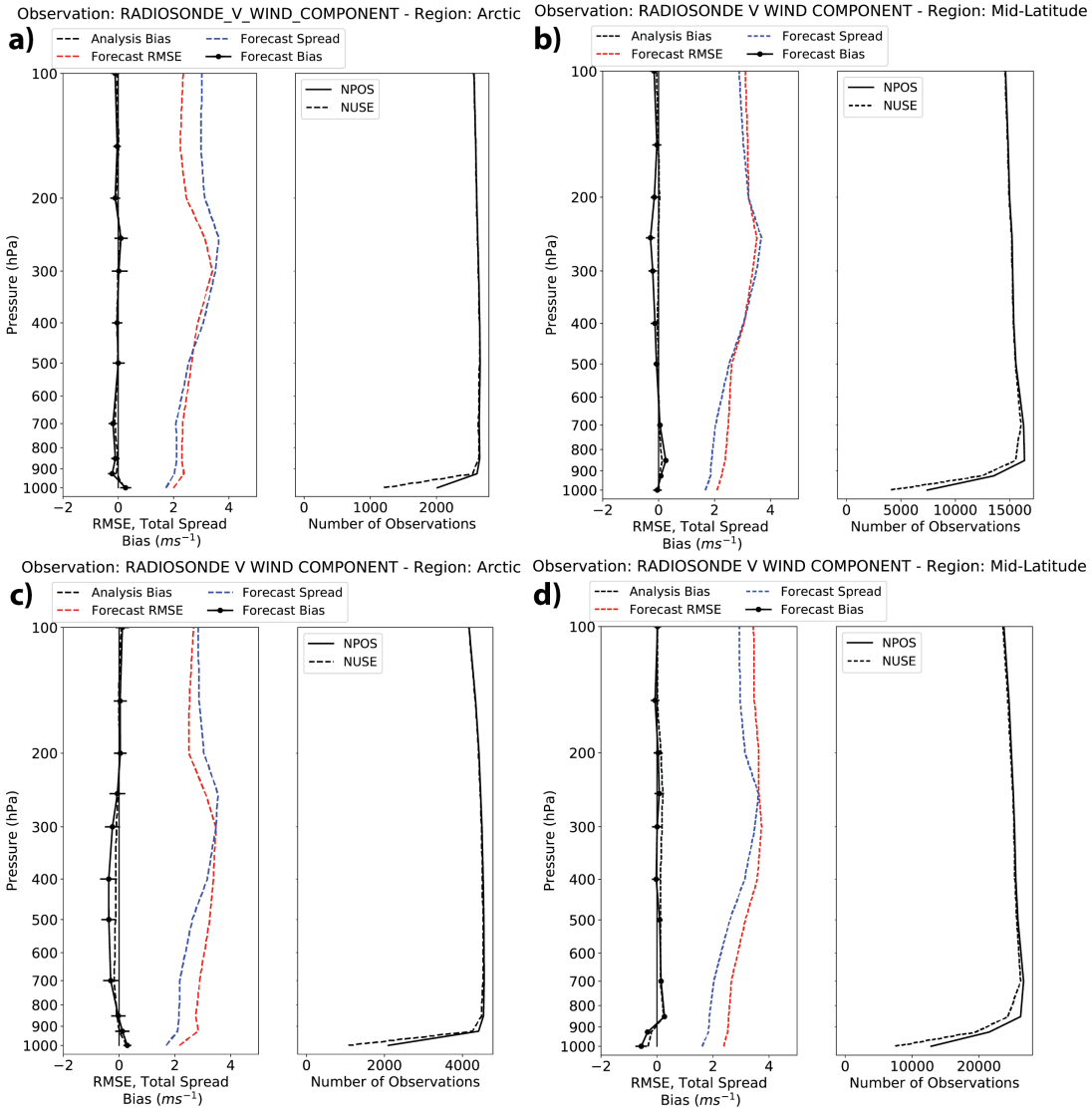

Figure 3.15: Cycling period averaged vertical profiles of analysis bias (dashed black), 6-hour model forecast bias (black), RMSE (dashed red), and ensemble total spread (dashed blue) when compared to radiosonde meridional-wind observations. Profiles are averaged over the Arctic (a,c) and the mid-latitudes (b,d) for both experiment 1 (a,b) and experiment 2 (c,d). Within all panels, the left profile shows cycling period mean values while the right profile shows total observation counts over the cycling period. Error bars represent the 95% confidence interval from bootstrap resampling.

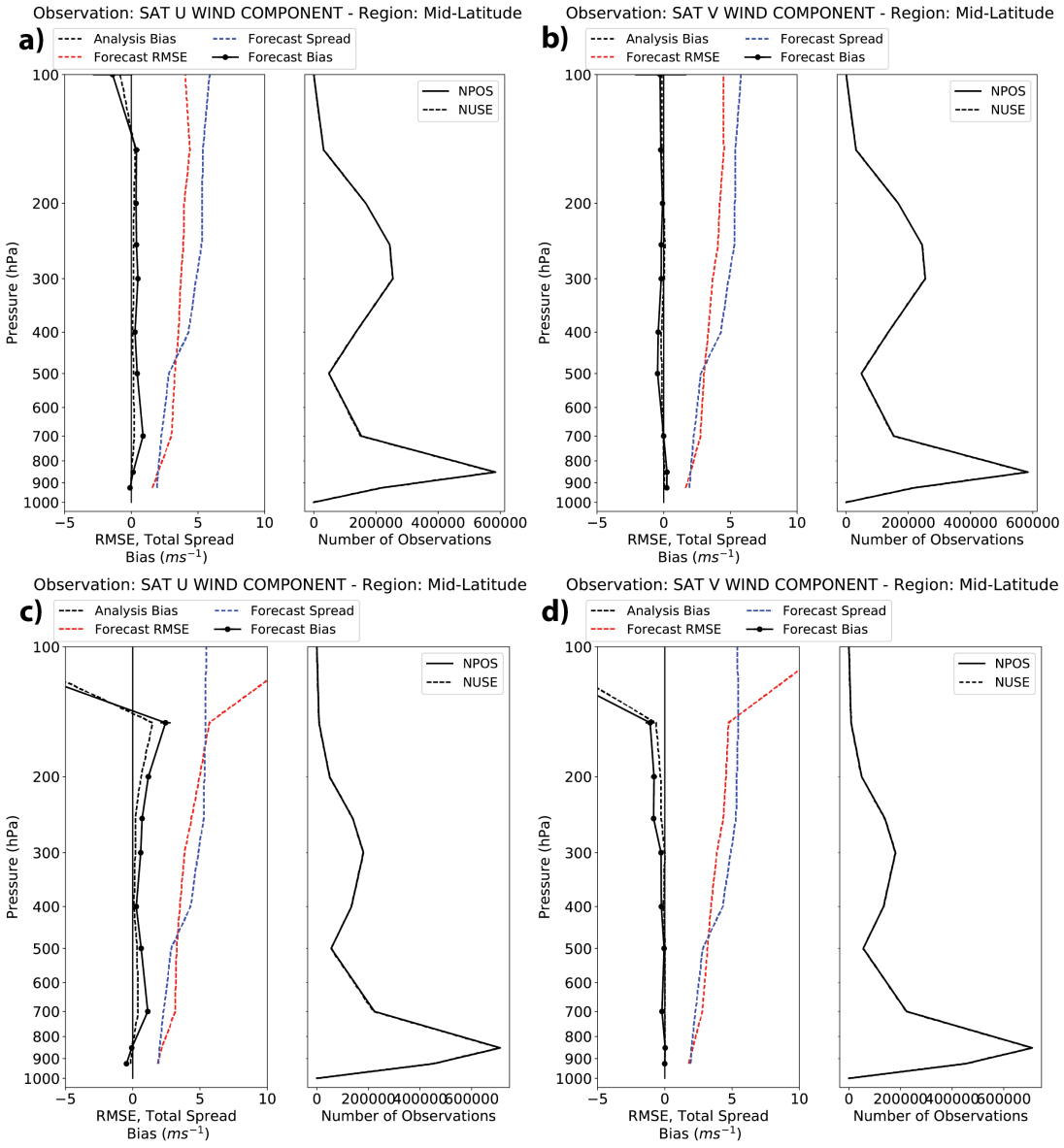

Figure 3.16: Cycling period averaged vertical profiles of analysis bias (dashed black), 6-hour model forecast bias (black), RMSE (dashed red), and ensemble total spread (dashed blue) when compared to geostationary satellite wind observations. Profiles are averaged over the Arctic (a,c) and the mid-latitudes (b,d) for both experiment 1 (a,b) and experiment 2 (c,d). Within all panels, the left profile shows cycling period mean values while the right profile shows total observation counts over the cycling period. Error bars represent the 95% confidence interval from bootstrap resampling.

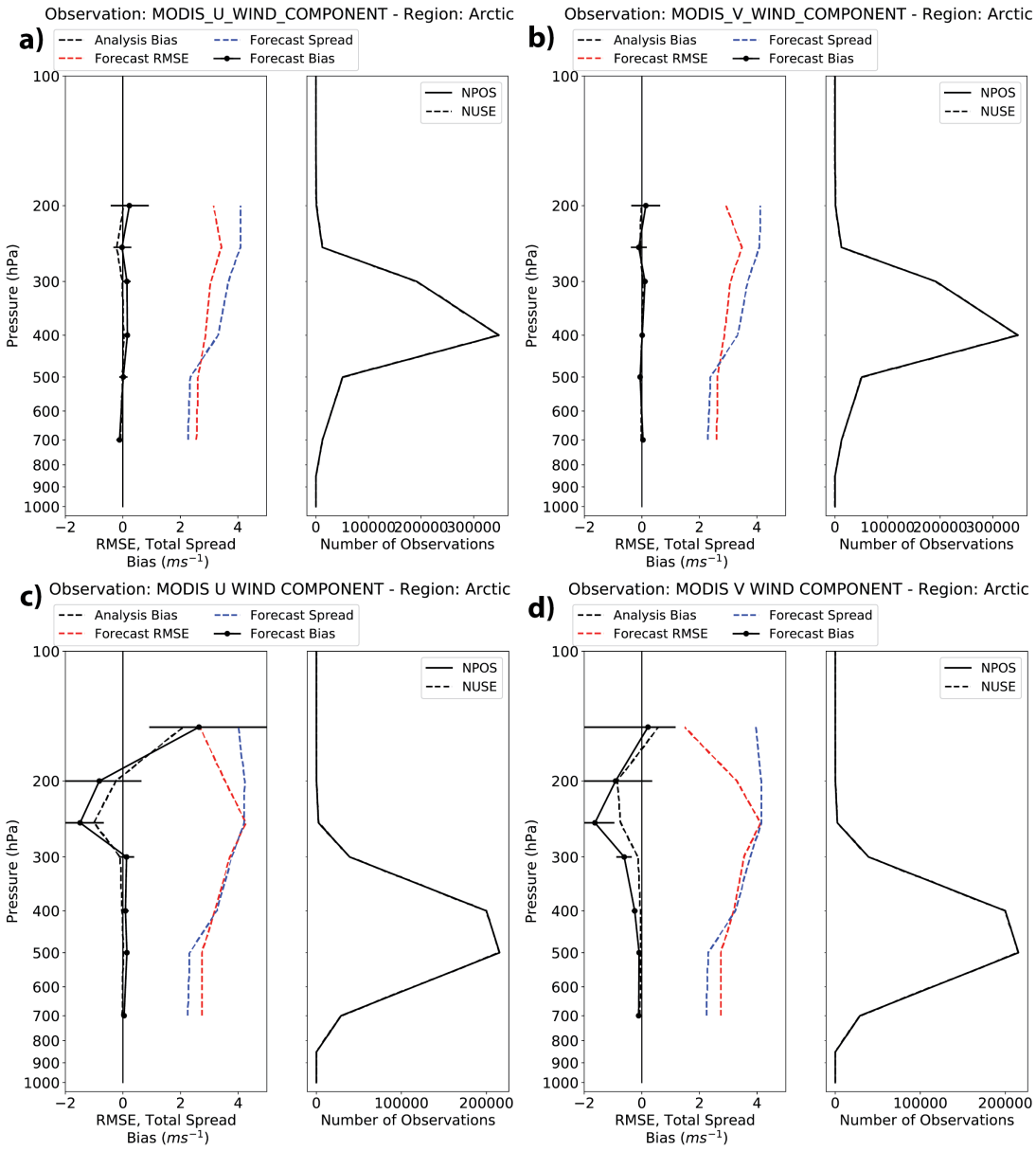

Figure 3.17: Cycling period averaged vertical profiles of analysis bias (dashed black), 6-hour model forecast bias (black), RMSE (dashed red), and ensemble total spread (dashed blue) when compared to modis satellite wind observations. Profiles are averaged over the Arctic (a,c) and the mid-latitudes (b,d) for both experiment 1 (a,b) and experiment 2 (c,d). Within all panels, the left profile shows cycling period mean values while the right profile shows total observation counts over the cycling period. Error bars represent the 95% confidence interval from bootstrap resampling.

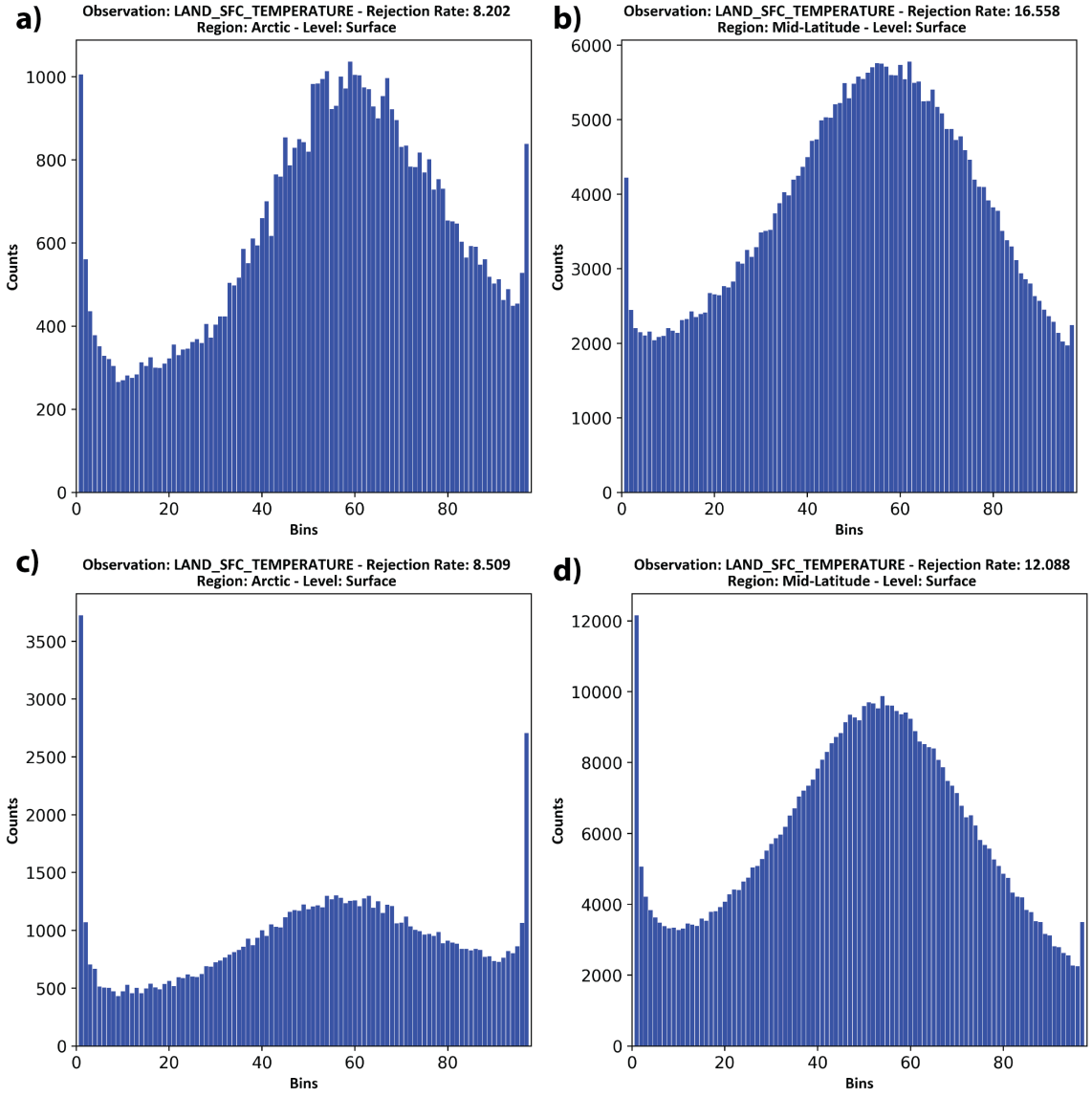

Figure 3.18: Rank Histograms of Automatic Weather Stations (AWS) temperature observations. Rank histograms were computed over the Arctic (a,c) and the mid-latitudes (b,d) for both experiment 1 (a,b) and experiment 2 (c,d). Rejection rate is the percent (%) of the observations that were rejected.

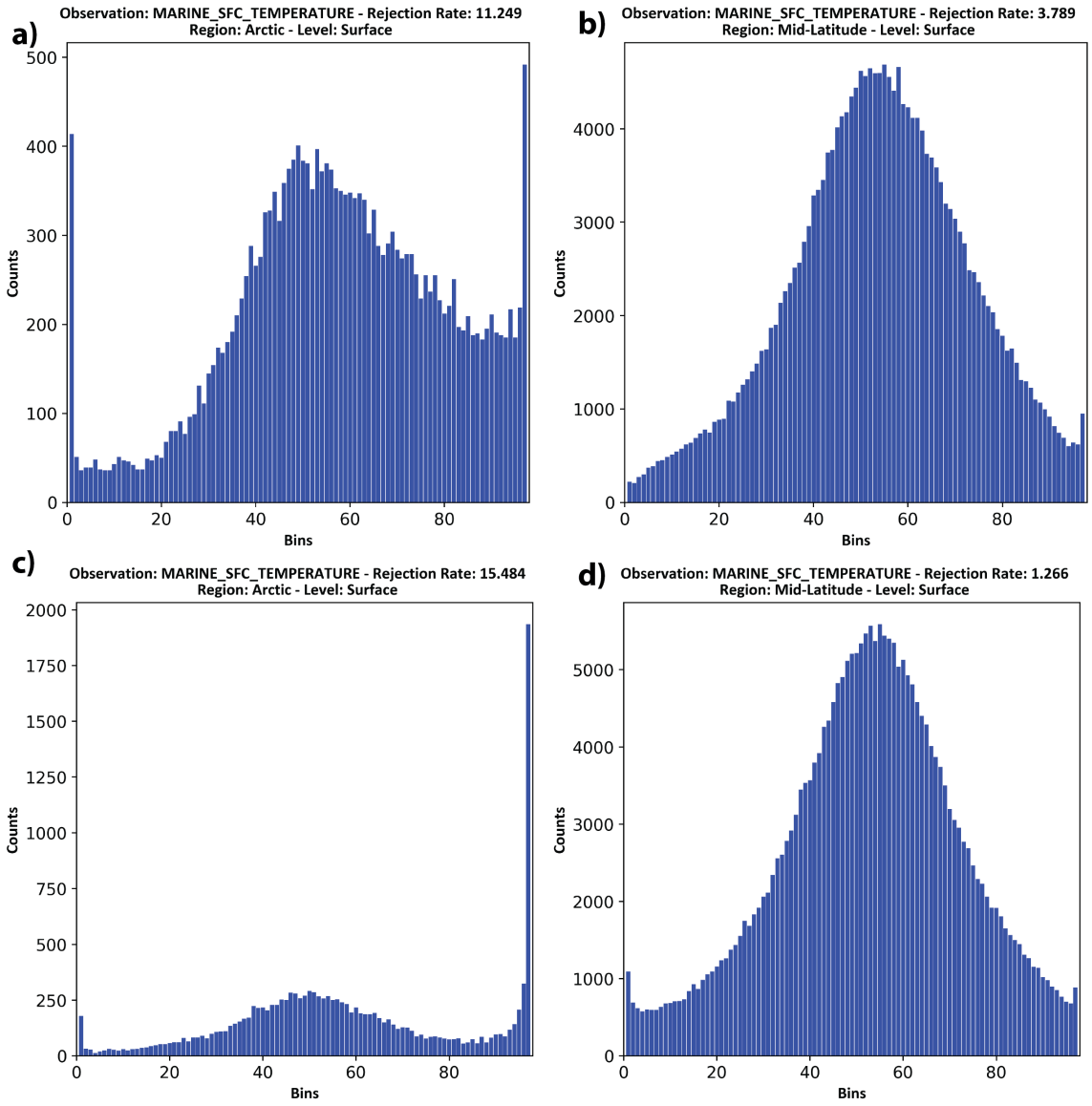

Figure 3.19: Rank histograms of marine buoy temperature observations. Rank histograms are computed over the Arctic (a,c) and the mid-latitudes (b,d) for both experiment 1 (a,b) and experiment 2 (c,d). Rejection rate is the percent (%) of the observations that are rejected.

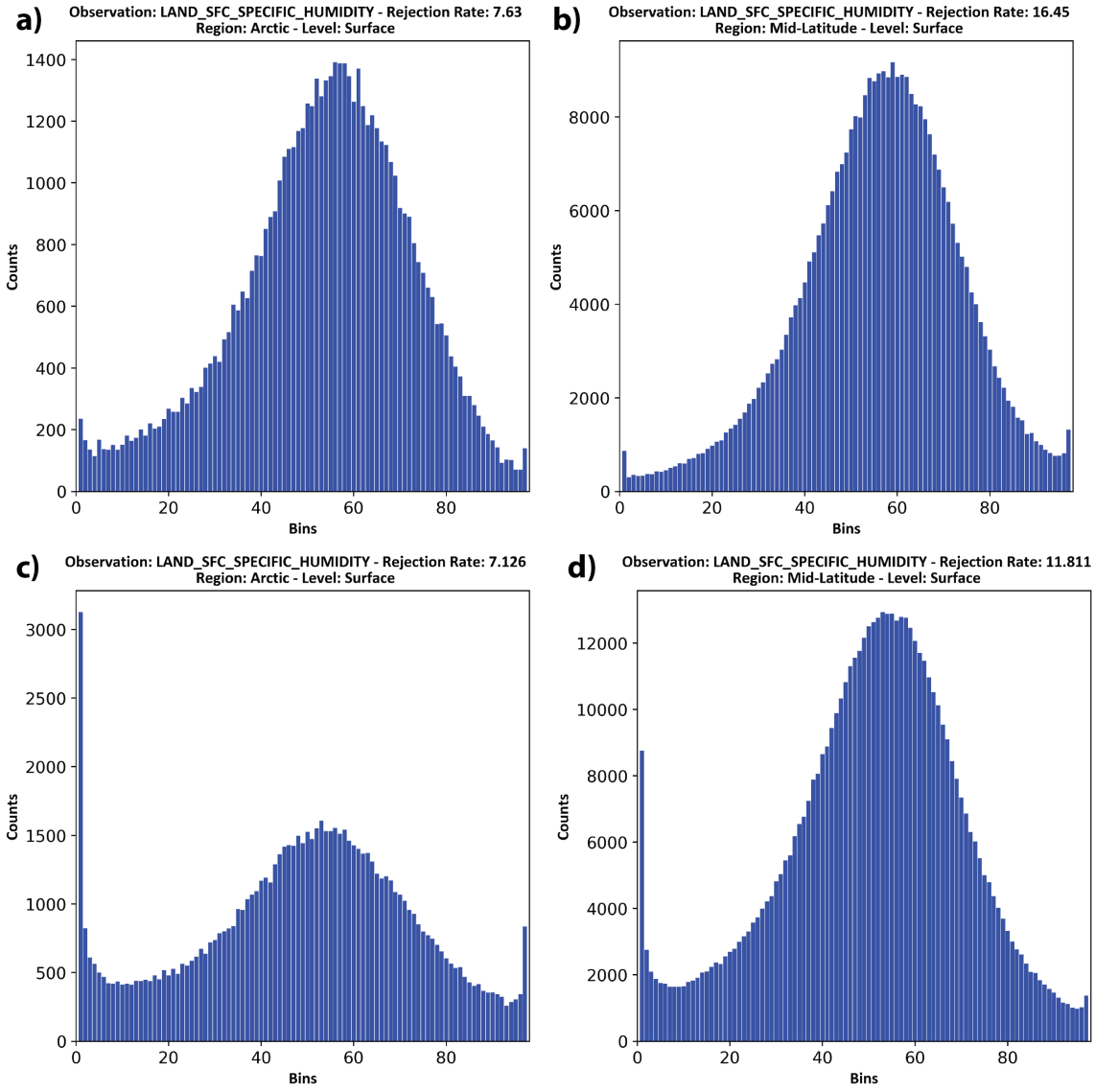

Figure 3.20: Rank histograms of Automatic Weather Stations (AWS) specific humidity observations. Rank histograms are computed over the Arctic (a,c) and the mid-latitudes (b,d) for both experiment 1 (a,b) and experiment 2 (c,d). Rejection rate is the percent (%) of the observations that are rejected.

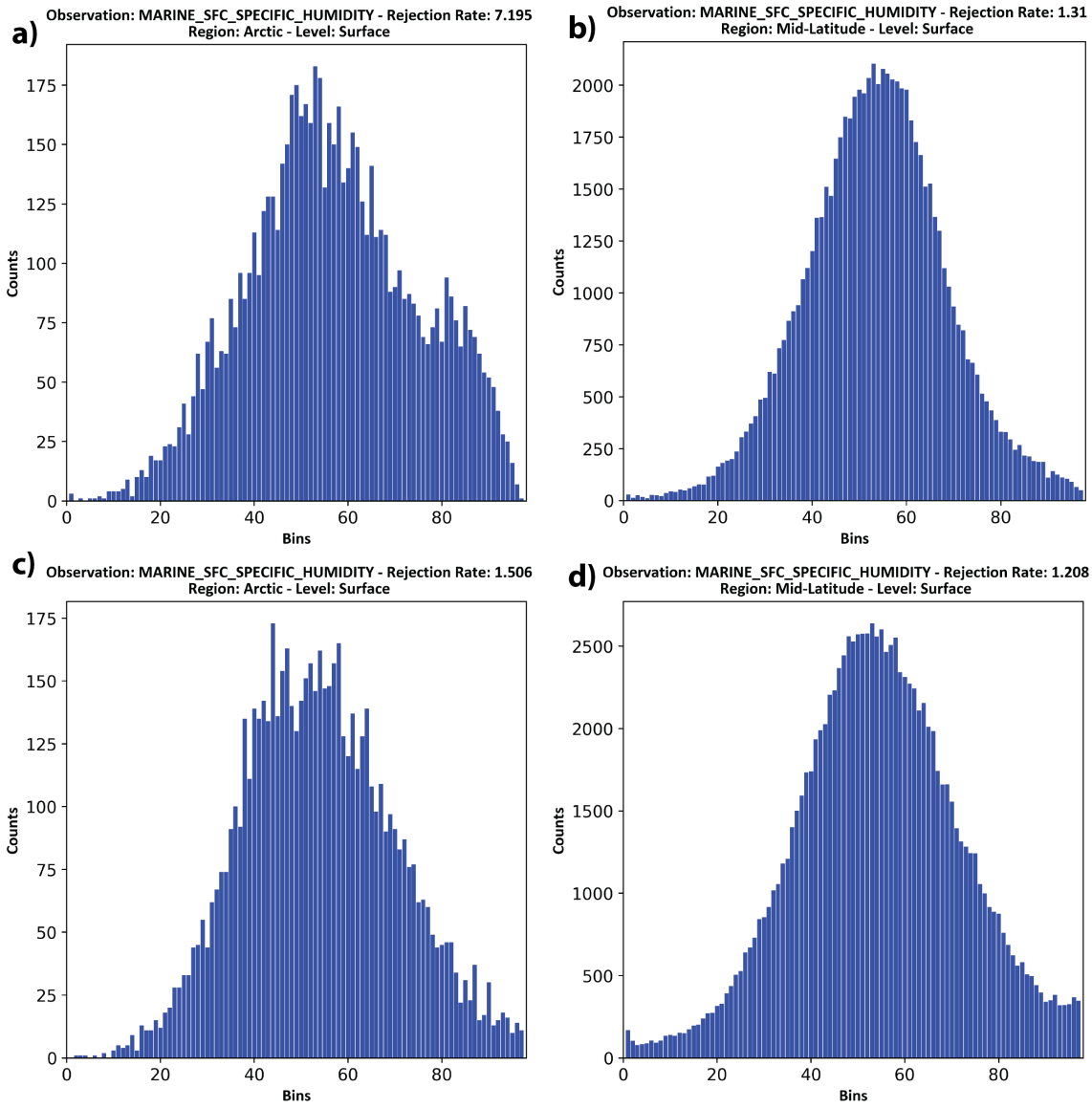

Figure 3.21: Rank histograms of marine buoy specific humidity observations. Rank histograms are computed over the Arctic (a,c) and the mid-latitudes (b,d) for both experiment 1 (a,b) and experiment 2 (c,d). Rejection rate is the percent (%) of the observations that are rejected.

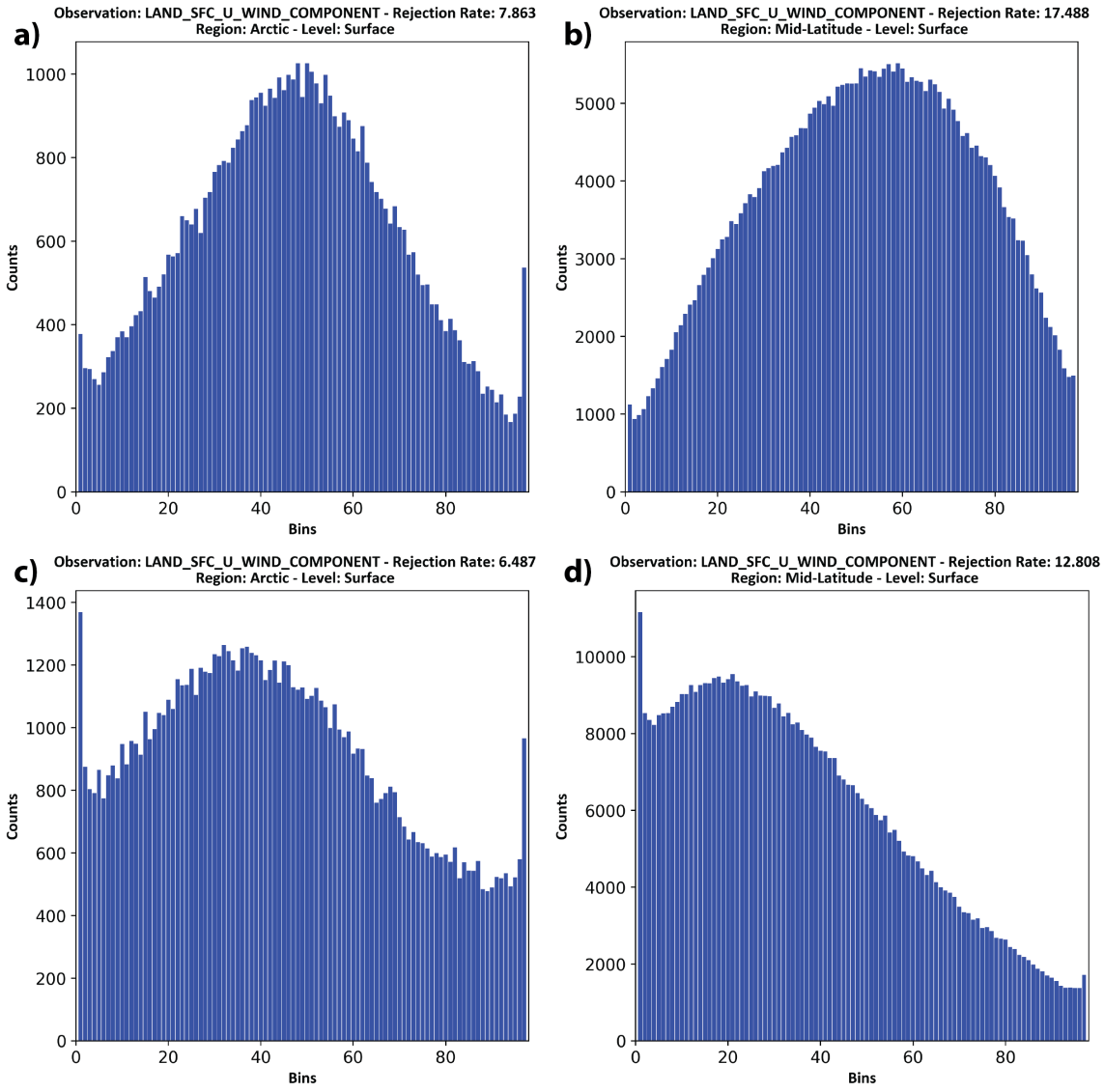

Figure 3.22: Rank histograms of Automatic Weather Stations (AWS) zonal-wind observations. Rank histograms are computed over the Arctic (a,c) and the mid-latitudes (b,d) for both experiment 1 (a,b) and experiment 2 (c,d). Rejection rate is the percent (%) of the observations that are rejected.

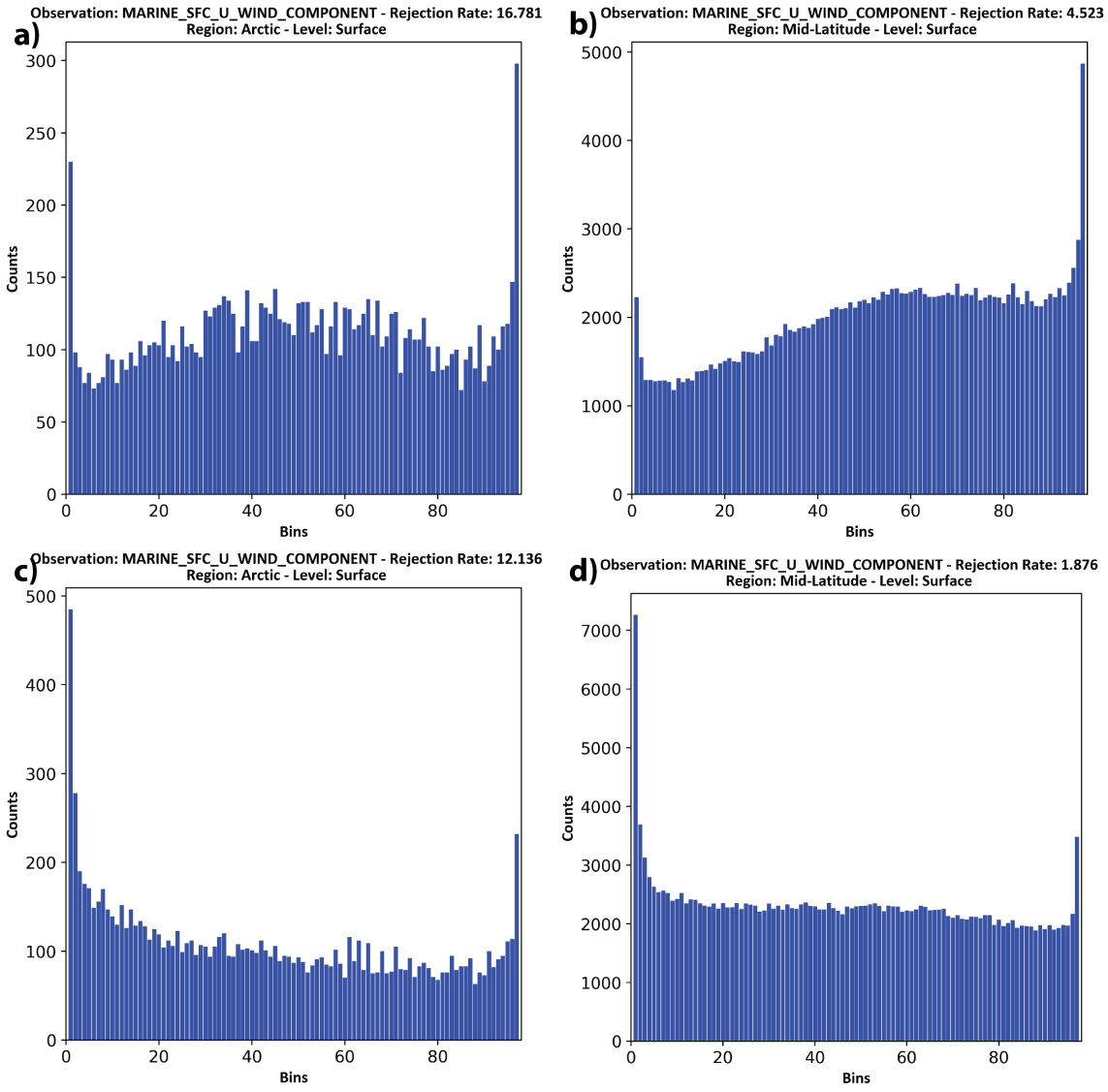

Figure 3.23: Rank histograms of marine buoy zonal wind observations. Rank histograms are computed over the Arctic (a,c) and the mid-latitudes (b,d) for both experiment 1 (a,b) and experiment 2 (c,d). Rejection rate is the percent (%) of the observations that are rejected.

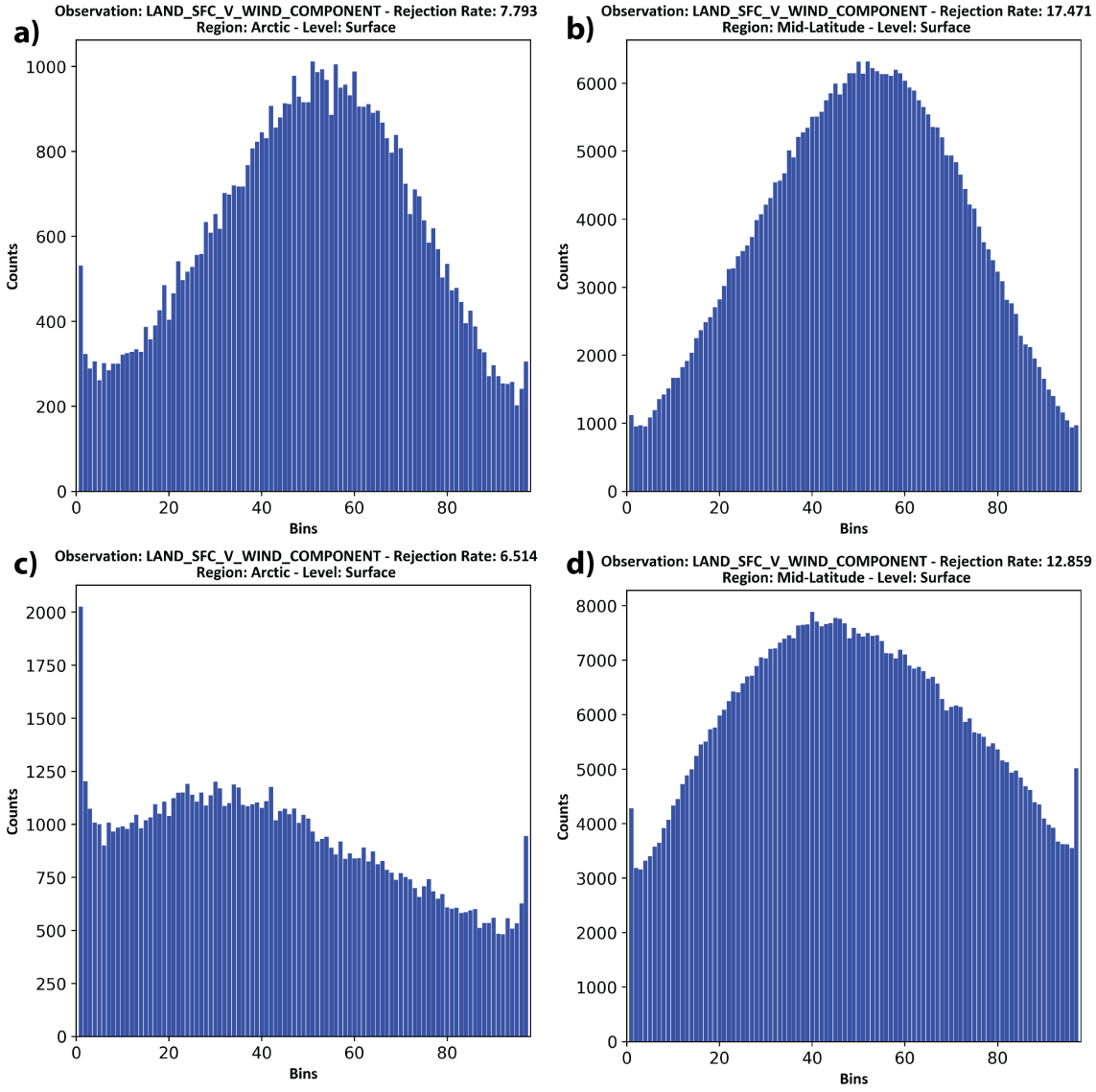

Figure 3.24: Rank histograms of Automatic Weather Stations (AWS) meridional-wind observations. Rank histograms are computed over the Arctic (a,c) and the mid-latitudes (b,d) for both experiment 1 (a,b) and experiment 2 (c,d). Rejection rate is the percent (%) of the observations that are rejected.

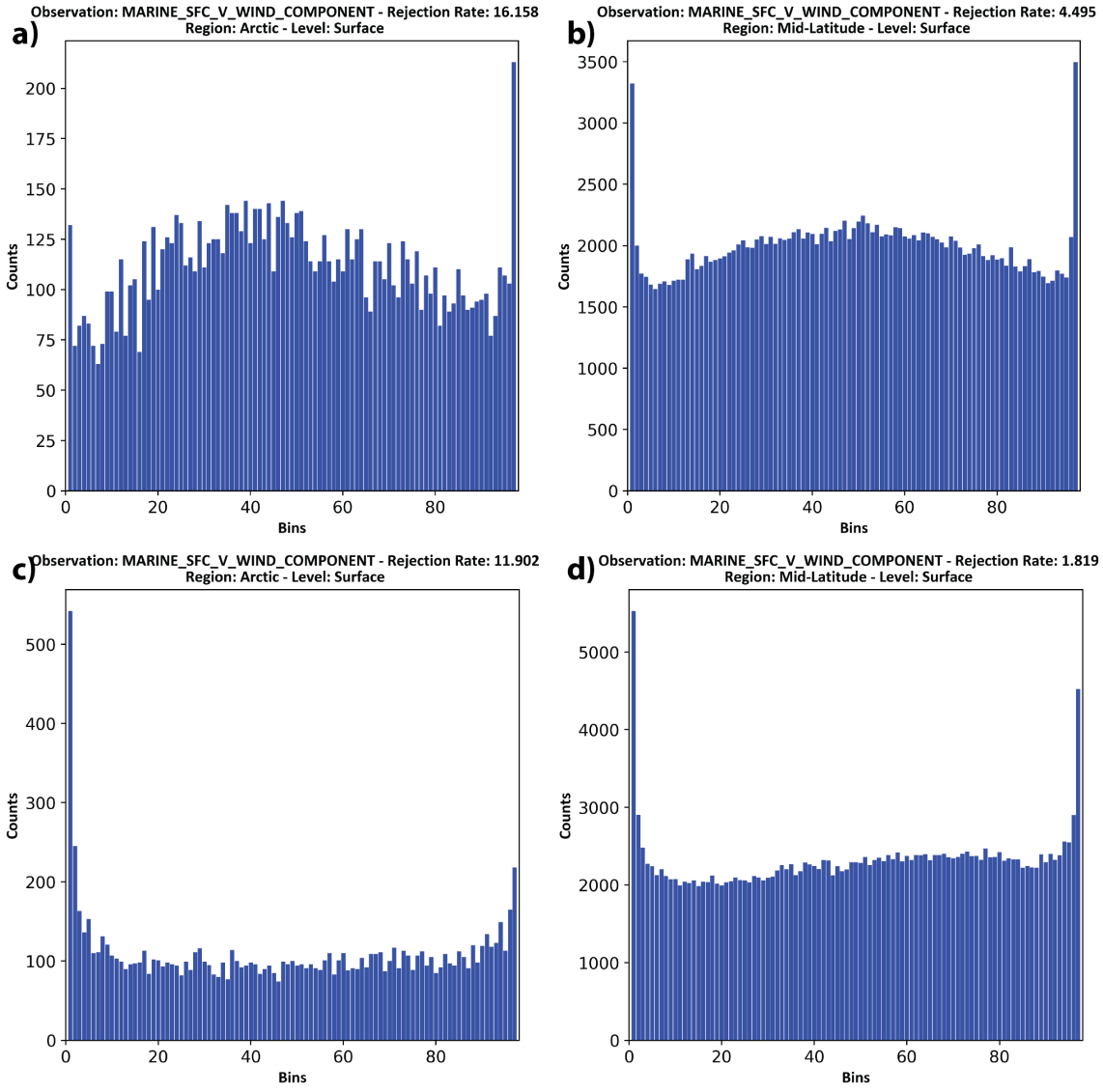

Figure 3.25: Rank histograms of marine buoy meridional wind observations. Rank histograms are computed over the Arctic (a,c) and the mid-latitudes (b,d) for both experiment 1 (a,b) and experiment 2 (c,d). Rejection rate is the percent (%) of the observations that are rejected.

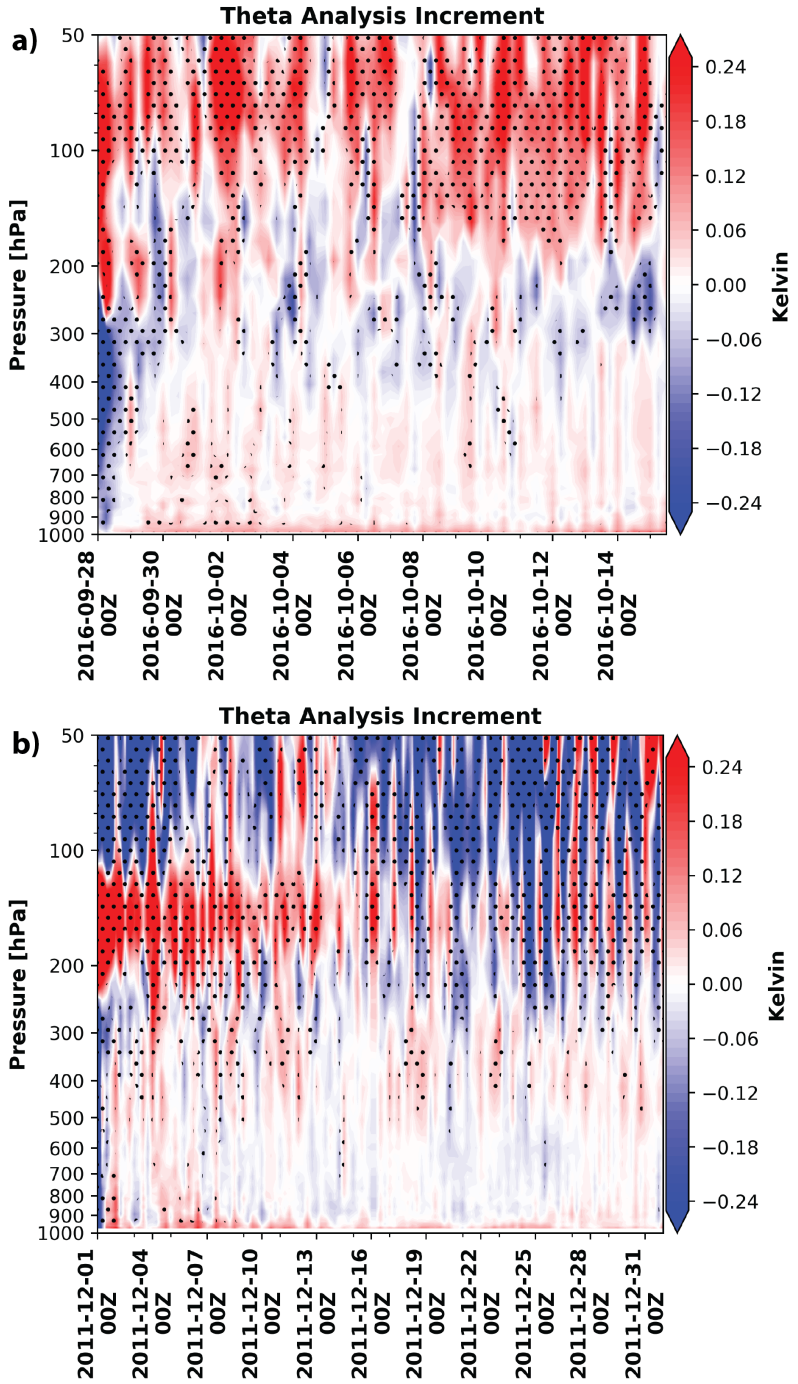

Figure 3.26: MPAS-DART spacially averaged (poleward of 60°N) potential temperature analysis increments time-height-sections for (a) experiment one and (b) experiment two. Stippling shows statistical significance at the 95% confidence interval using a student's t-test.

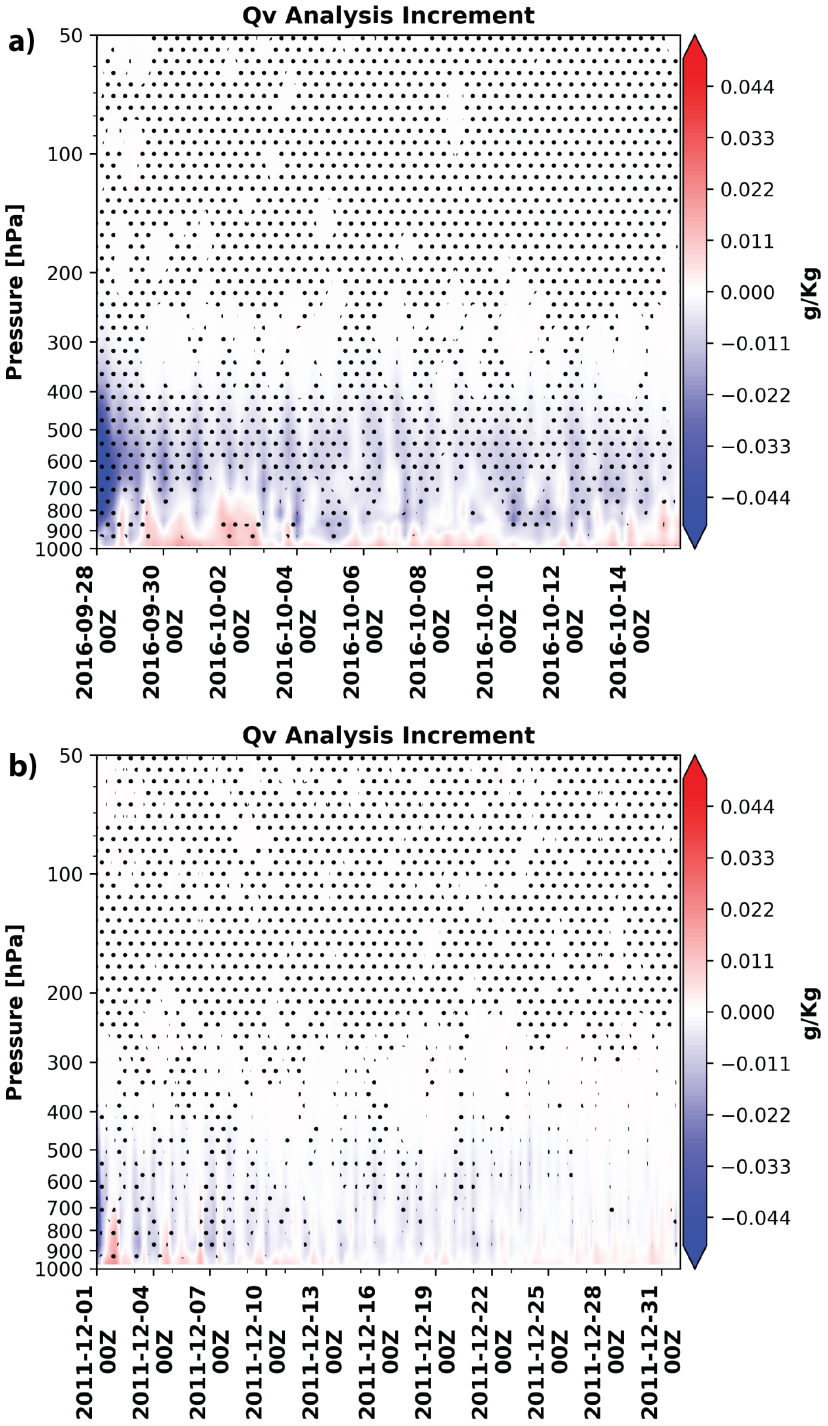

Figure 3.27: MPAS-DART spacially averaged (poleward of 60°N) water vapor analysis increments time-height-sections for (a) experiment one and (b) experiment two. Stippling shows statistical significance at the 95% confidence interval using a student's t-test.

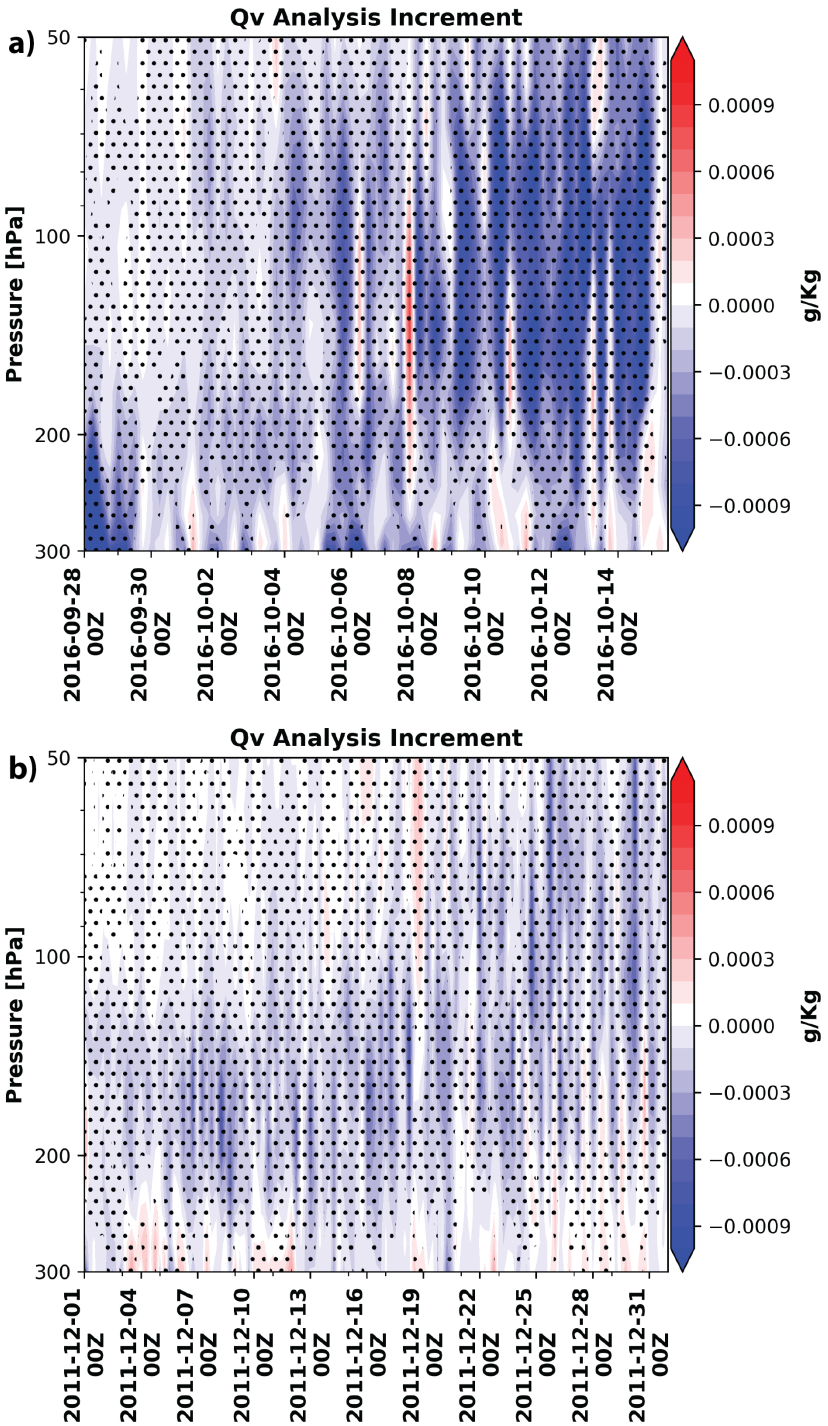

Figure 3.28: The same as Fig. 3.27 but zoomed into the levels spanning 300 to 50 hPa.

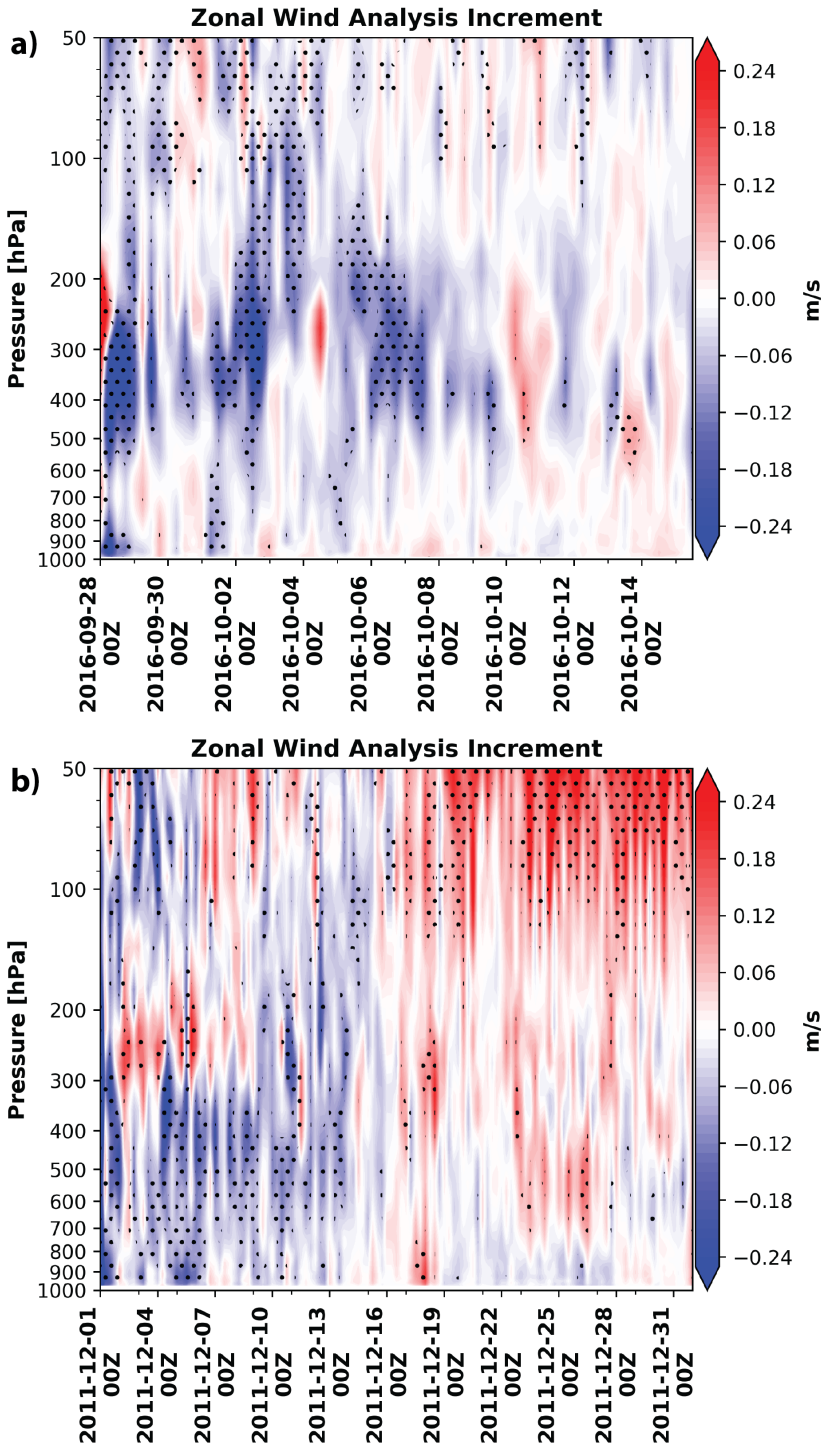

Figure 3.29: MPAS-DART spacially averaged (poleward of 60°N) zonal wind analysis increments time-height-sections for (a) experiment one and (b) experiment two. Stippling shows statistical significance at the 95% confidence interval using a student's t-test.

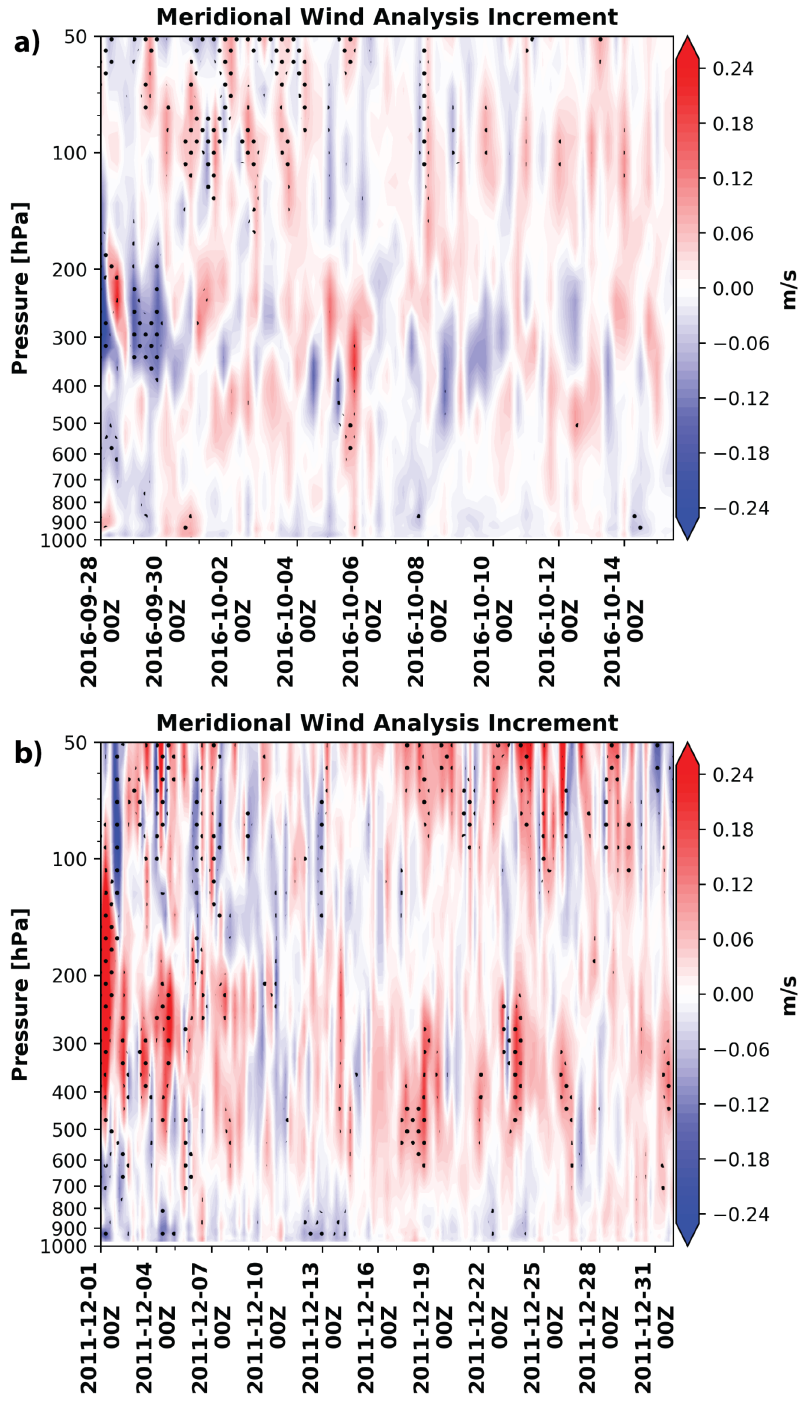

Figure 3.30: MPAS-DART spacially averaged (poleward of 60°N) meridional wind analysis increments time-height-sections for (a) experiment one and (b) experiment two. Stippling shows statistical significance at the 95% confidence interval using a student's t-test.

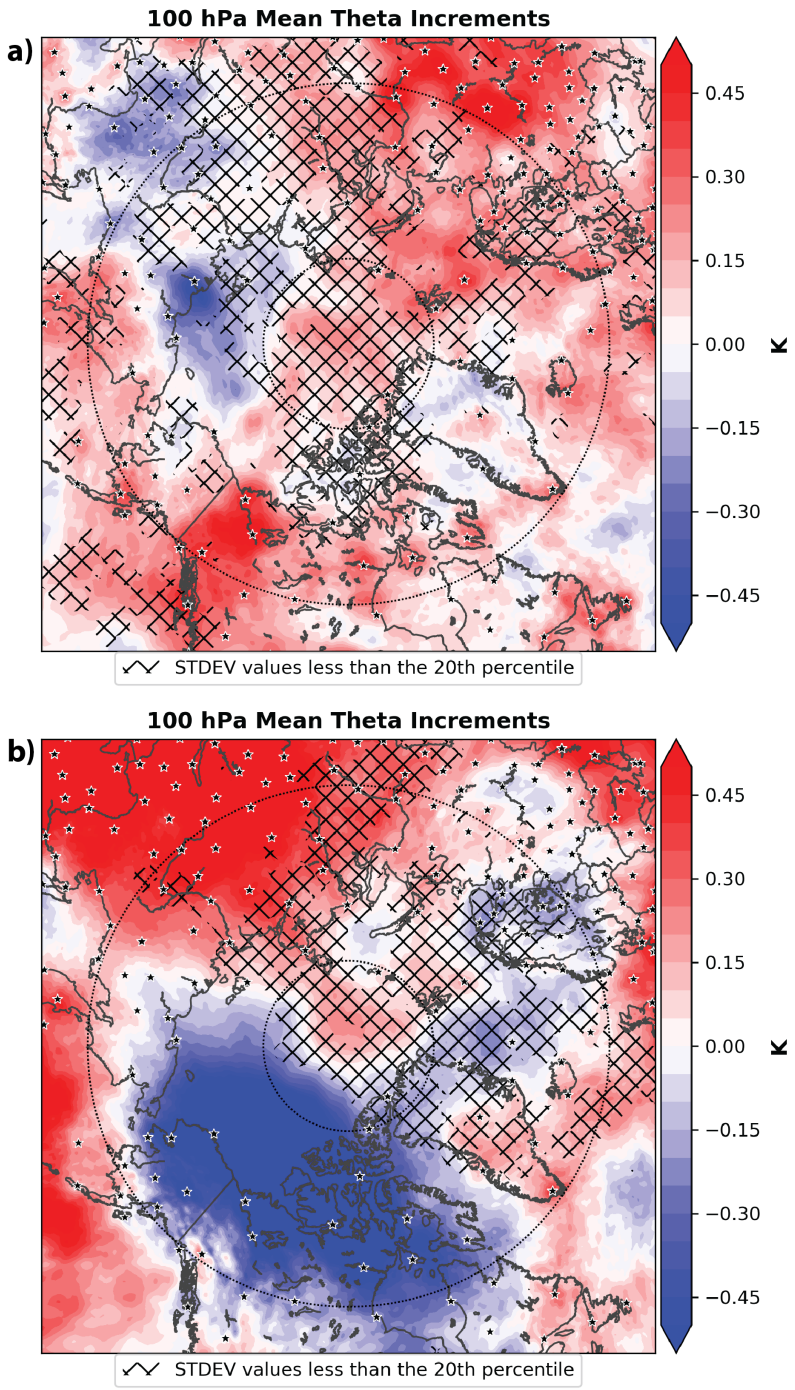

Figure 3.31: Cycling period averaged potential temperature analysis increment at 100 hPa for both (a) experiment one and (b) experiment two. Areas that are below the 20th percentile value of a distribution of the standard deviation values are hatched. Black dashed line represents 60°N latitude. Stars are locations of radiosonde launch sites.

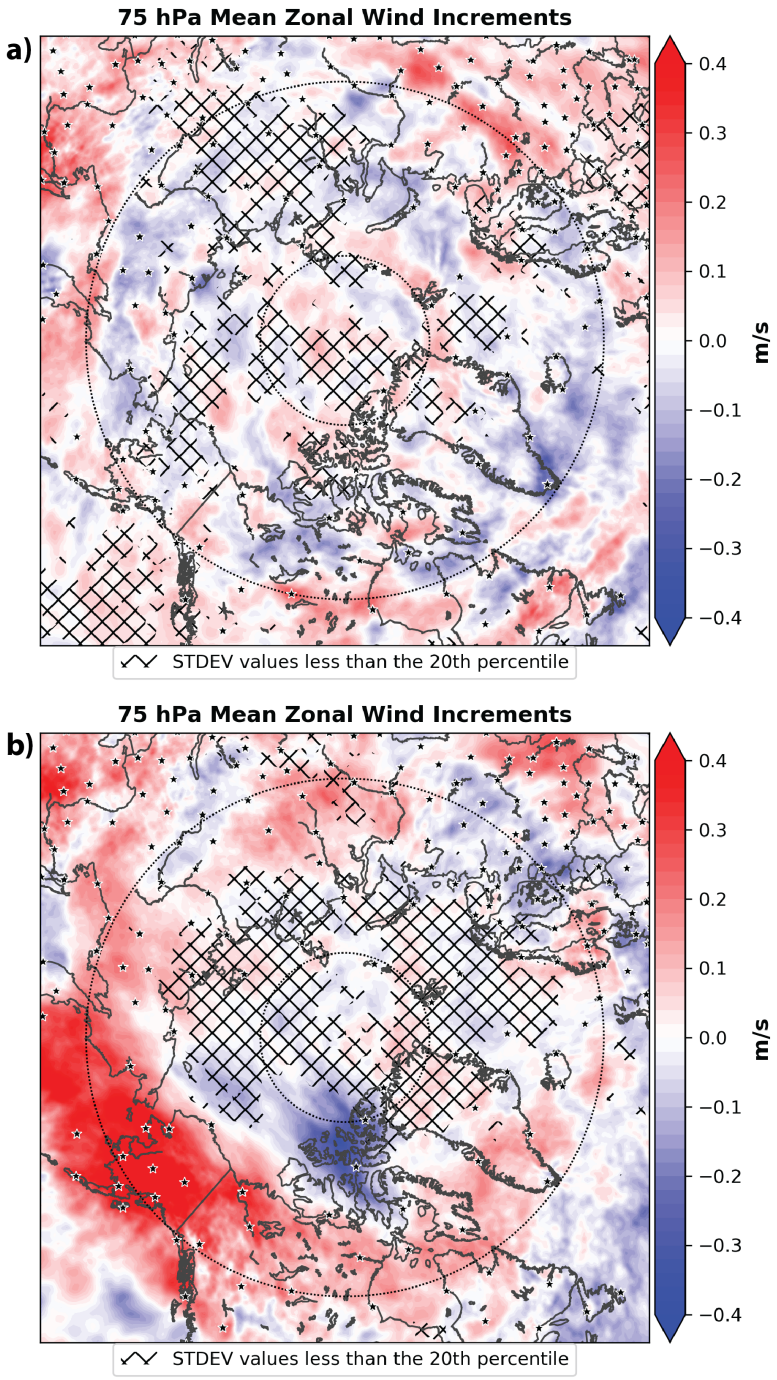

Figure 3.32: Cycling period averaged zonal analysis increment at 75 hPa for both (a) experiment one and (b) experiment two. Areas that are below the 20th percentile value of a distribution of the standard deviation values are hatched. Black dashed line represents 60°N latitude. Stars are locations of radiosonde launch sites.

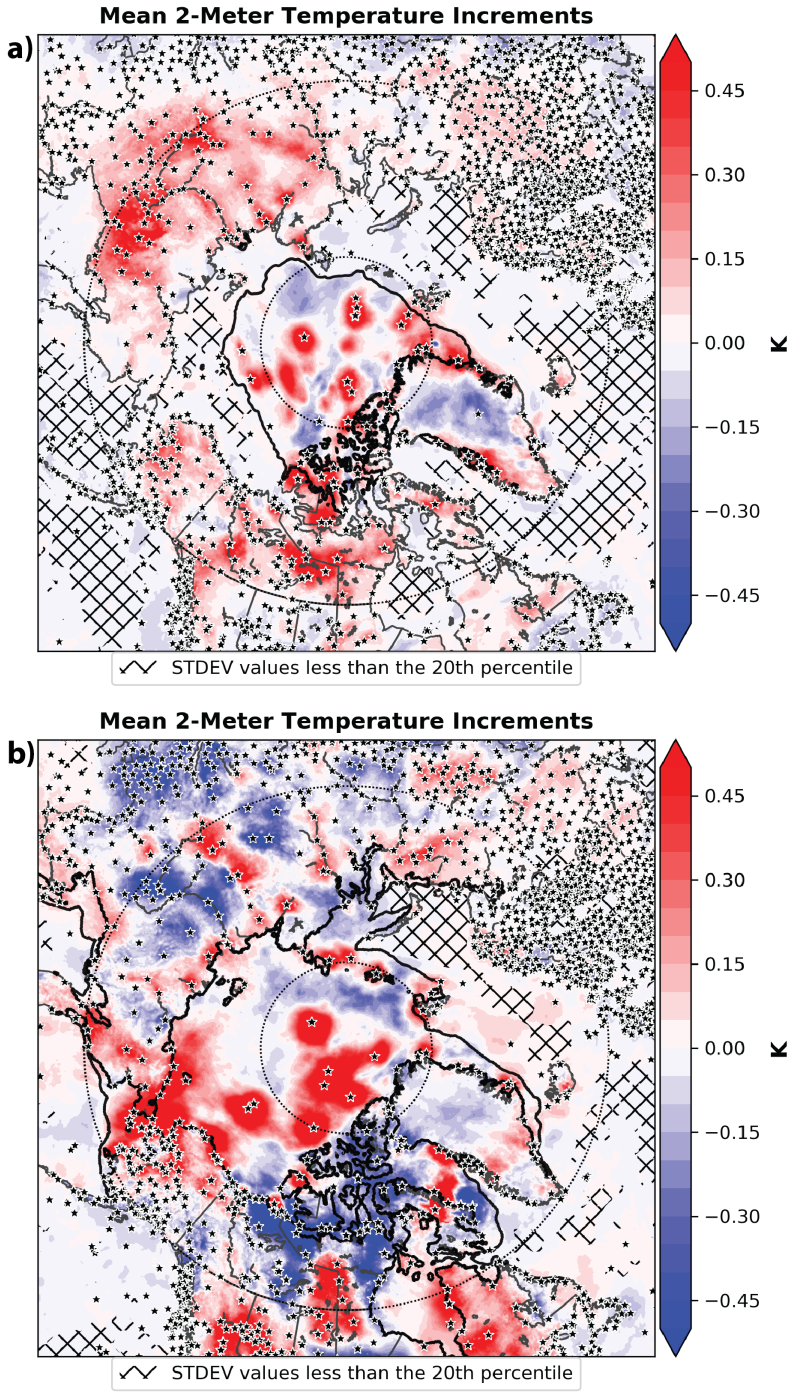

Figure 3.33: Cycling period averaged two-meter temperature analysis increment for both (a) experiment one and (b) experiment two. Areas that are below the 20th percentile value of a distribution of the standard deviation values are hatched. Black dashed line represents 60°N latitude. Stars are locations of land observation sites.

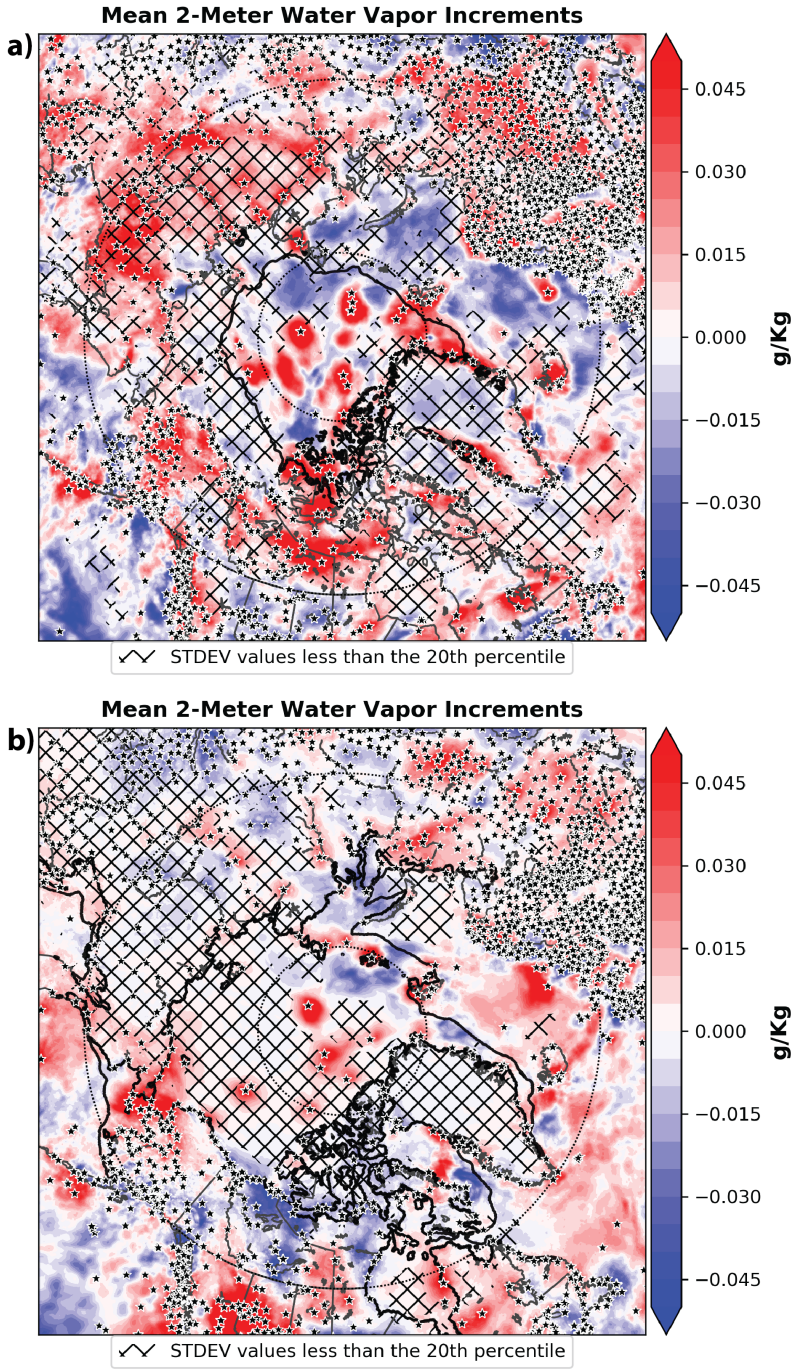

Figure 3.34: Cycling period averaged two-meter water vapor analysis increment for both (a) experiment one and (b) experiment two. Areas that are below the 20th percentile value of a distribution of the standard deviation values are hatched. Black dashed line represents 60°N latitude. Stars are locations of land observation site.

Chapter 4

Investigation of Systematic Errors

In Chapter 3, comparing MPAS-DART to observations along with evaluation of AIs revealed several potential systematic biases in the modeling system. AIs have previously been used to help identify biases in cycling systems (Dee 2005). While AIs can provide helpful indications of areas where background forecast fields do not align with observations, the physical processes connected with the biases still needs to be parsed out. The literature suggests two methods to correct a systematic model bias once identified: off-line (post-processing) or on-line (bias-aware data assimilation). One common off-line approach to remove systematic model biases at observation sites uses model output statistics (MOS) to correct the forecast in a post-processing fashion (Glahn and Lowry 1972). MOS requires a long development period during which the model of interest needs to remain stable with limited changes (Mass et al. 2008). On-line (bias-aware data assimilation) approaches are designed to correct these biases through estimation of parameters that represent them. To estimate the parameters, model for the bias must be formulated along with reference data to estimate the parameters of the bias model (Dee 2005). A third approach is to use analysis increments to help correct systematic biases. Danforth et al. (2007) calculated model bias by computing the difference between 6-hour forecast fields and their corresponding analyses, which are then averaged over many forecasts. The bias was then corrected within the forecast system by adding on a average bias tendency (average model bias divided by 6-hours) to each of the model variables. Each of the above approaches only evaluate and correct the systematic model bias itself instead of improving the representation of physical processes within the model leading to the bias. This study employs a relatively new technique that allows the user to investigate systematic errors indicated by AIs, by evaluating the physical representation of the atmosphere from decomposed model tendencies.

4.1 Mean Initial Tendency and Analysis Increment Method

Few studies on forecast verification have considered model tendencies when diagnosing the physical processes associated with biases. Exceptions to this include work applying the initial tendency method, which was pioneered by Klinker and Sardeshmukh (1992), to different research problems in different modeling setups (Rodwell and Palmer 2007b; Williams and Brooks 2008; Cavallo et al. 2016; Wong et al. 2020). The initial tendency method uses a series of short-term forecasts and analyses produced by a cycling data assimilation system. The model tendencies associated with each physical process are accumulated in the forecast model and averaged over the cycling period, which will allow the user to decompose across the different model processes. Doing so will help the user identify the physical processes that might be driving the systematic errors found in the AIs.

Studies employing the initial tendency method have tracked time-averaged model tendencies over 6-hour model integrations to diagnose systematic errors in their cycling systems (Rodwell and Palmer 2007b; Rodwell and Jung 2008; Cavallo et al. 2016). One important component of the initial tendency method is the use of native analyses (i.e. those generated by the same model as the forecast system) to initialize your forecasts. Non-native analyses can introduce external biases within your cycling system which could have large impacts on your short-term forecasts (Klocke and Rodwell 2014). Cavallo et al. (2016) highlighted the impacts initializing forecasts with non-native analyses and using different physics schemes with the same model. They showed that the tendencies from early forecasts hours were very sensitive to both non-native analyses and the use of different physics schemes. For this study, I will follow closely the procedures laid out in Cavallo et al. (2016). Previous studies showed that systematic model errors can be established using only the mean of the initial forecast tendencies (Klinker and Sardeshmukh 1992; Rodwell and Palmer 2007b); this adaption of the initial tendency method is called the mean initial tendency and analysis (MITA) increment method (Cavallo et al. 2016). The equation for

applying the MITA increment method to potential temperature is described in three different components:

$$\begin{aligned}\underbrace{\sum_{i=1}^{m} INC_i}_{(1)} &= -\Delta t_{da} \sum_{i=0}^{m-1} \overline{\dot{\theta}_i^b} + \theta_{m,0}^a - \theta_{0,0}^a \\ &= \underbrace{-\Delta t_{da} \sum_{i=0}^{m-1} \overline{\dot{\theta}_i^b}}_{(2)} + \underbrace{\text{analysis drift}}_{(3)}.\end{aligned} \tag{4.1}$$

Term one is the summed potential temperature AIs over m data assimilation cycles. Term two is the sum of the average total model forecast tendency over m data assimilation cycles. Since term two contains the total model forecast tendencies, these can be broken down into their individual components:

$$\overline{\dot{\theta}_i^b} = \frac{1}{n} \sum_{j=0}^{n} (\overline{\dot{\theta}}_{\text{dynamics,j}} + \overline{\dot{\theta}}_{\text{radiation,j}} + \overline{\dot{\theta}}_{\text{latent heating,j}} + \overline{\dot{\theta}}_{\text{cumulus,j}} + \overline{\dot{\theta}}_{\text{pbl,j}}) \tag{4.2}$$

where $\dot{\theta}_{\text{dynamics,j}}$, $\dot{\theta}_{\text{radiation,j}}$, $\dot{\theta}_{\text{latent heating,j}}$, $\dot{\theta}_{\text{cumulus,j}}$, $\dot{\theta}_{\text{pbl,j}}$ represent the different model tendencies for potential temperature at forecast step j from the model's physical parameterizations. Lastly, term 3 from equation 4.1 represents the natural evolution in potential temperature that occurs over the duration of the cycling period. If the analysis drift and the accumulated averaged total model tendencies equal, then the AIs should be close to zero since the model is representing the natural evolution of the atmosphere. While the example above is applied to potential temperature, the MITA increment method can be applied to any prognostic variable in the chosen numerical weather model. Since AIs and accumulated model tendencies are required for the entire cycling duration, problems may arise storing the potentially large amount of data, especially possible for a global model system that has 96 members. However, if the cycling system is well-calibrated, and is a non-mixed physics ensemble system, each member is equally likely to correctly represent the atmosphere (Leith 1974). Based on this notion, I randomly choose one member to save accumulated model tendencies and analysis increments for the cycling period. However, choosing one member randomly could include results unique to that member, which needs

to be consider during evaluation. The MITA increment method is applied to MPAS-DART for both cycling experiments described in section 2.4. Combining the information provided by the AIs and the outputted accumulated model tendencies allows this study to trace systematic errors back to representation of physical processes of the atmosphere.

4.1.1 Experiment One

The MITA increment method is applied to all the prognostic variables within MPAS-DART, which are potential temperature, water vapor, zonal- and meridional-wind components for experiment 1 (Table 2.2; Fig. 4.1). For all four variables, the residual line is approximately zero which means the budget (LHS of equation 4.1 minus RHS of equation 4.1) for the MITA increment method equation has been closed (Fig. 4.1).

Starting with potential temperature, total accumulated averaged model tendency shows too much cooling compared to the analysis drift near the surface, leading to warming from observations (Fig. 4.1a). Potential temperature in the middle-troposphere is represented relatively well, which results in small AIs. Further aloft, disagreement between observations and the model is evident just above 200 hPa (Fig. 4.1). There is a disagreement between the observations and model since the AIs and the total accumulated averaged model tendency in this layer are of opposite sign. The layer above 200 hPa containing increased AIs in potential temperature is co-located with the area of significant Arctic averaged AIs (compare Fig. 4.1 to Fig. 3.26a). For water vapor, the model shows too much moisture reduction near the surface compared to the analysis drift, which leads to observations increasing moisture (Fig. 4.1b). Furthermore in the middle troposphere, the total accumulated averaged model tendency is the opposite sign compared to the analysis drift, meaning observations are consistently showing lower amounts of moisture than the model predicts (Fig. 4.1b). Lastly, there is agreement between analysis drift and total accumulated averaged model tendency for the wind components (Fig. 4.1c,d). AIs are relatively small along

with no layers of large separation between total accumulated averaged model tendency and the observations.

This evaluation will focus on the regions where large biases were identified: 1) too much cooling between 200 hPa and 50 hPa, 2) too much cooling near the surface, and 3) too much water vapor reduction near the surface. While my initial investigation also identified disagreement between the model and observations near the model top, MPAS has been shown to have issues in representing stratospheric inertia-gravity waves with coarse vertical resolutions (Skamarock et al. 2019). Thus, errors near the model top are not considered in the present study. The Arctic near-surface region is complex due to the different surface types that are present. As such, the MITA increment method is applied over land, ocean and sea ice separately to compare back to calculations including the entire Arctic domain (Fig. 4.2). The evaluation of different surface types allows for the investigation of whether the increased cooling from the model above 200 hPa has regional characteristics while also investigating the cause of cooling near the surface.

Regardless of surface type, significant increase in cooling from the model is apparent above 200 hPa, which is leading to warming from observations (Fig. 4.2). The cooling from the model over all surface type implies that the previously shown disagreement between the model and observations is not due to regional bias. At the surface, there is too much cooling from the model over land and seaice, but not over the ocean (compare Fig. 4.2b,d to Fig. 4.2c). The total accumulated averaged model tendency matches the analysis drift, which means the model is cooling at the appropriate rate and AIs values are near zero (Fig. 4.2c). To get better insight about which physical processes may be associated with these biases, the total accumulated average model tendency is now decomposed into the separate physics scheme contributions (Fig. 4.3). There are three model-process tendencies above 200 hPa: longwave radiation, shortwave radiation, and dynamics. The only model-process tendency that is directly cooling in the layer from 200 hPa to 50 hPa is the longwave radiation scheme (Fig. 4.3). The largest magnitude in cooling from the longwave radiation

scheme is occurring around 100 hPa, which coincides with the largest magnitude of cooling in the total accumulated average model tendency (compare 4.3 to Fig. 4.2). Near the surface over land and seaice, the dominant model-process tendency scheme directly acting to cool is the longwave radiation scheme (Fig. 4.3b,d). The near surface longwave cooling may be connected back to the increase in near surface water vapor. Note that over sea ice, dynamics also contributes to cooling.

Since moisture can impact longwave cooling, further investigation into positive water vapor AIs near the surface is warranted (Fig. 3.27). The MITA increment method is applied to the different surfaces over the Arctic (Fig. 4.4). The model is reducing the moisture at the surface at a faster rate than what the analysis drift shows over all surfaces except over the ocean (compare Fig. 4.4a,c,d to Fig. 4.4c). To further investigate the strong reduction in water vapor near the surface, total accumulated averaged model tendency is again decomposed into the individual model-process tendencies (Fig. 4.5). Over land and sea ice, the dominant parameterization scheme reducing water vapor near the surface is the convection parameterization scheme, which is responsible for representing sub-grid scale cloud processes (Fig. 4.5b,d). The convection and the microphyics schemes are responsible for the formation and representation of clouds. Over land, the convection and microphyics schemes contrast with each other on cloud formation near the surface. The convection scheme is using water vapor to make clouds where microphysics scheme is evaporating clouds back to water vapor (Fig. 4.5b). The water vapor disagreement between physics schemes could be a result of the order MPAS is computing the individual model physic tendencies (Donahue and Caldwell 2018). Over sea ice, the microphysics scheme is comparatively small to the convection scheme (Fig. 4.5d). In general, the microphyics scheme is reducing water vapor just above the surface over both land and sea ice but increasing water vapor at the surface over land (Fig. 4.5). There may also be a disagreement on the positioning of clouds with the convection scheme producing clouds near the surface while the microphysics scheme is producing clouds aloft.

Since both the microphysics and convective scheme are non-active above 200 hPa, the dominant feature that can absorb and reemit longwave radiation is water vapor. Arctic averaged profiles of cycling period averaged analysis water vapor are computed from the MPAS-DART ensemble average, MPAS-DART member 70 (the member used for the MITA increment method), GEFS, and ERA5 (Fig. 4.6a,b). Near the surface, there is increased moisture in MPAS-DART compared to other analyses produced by global models, but the profiles became similar higher up in the atmosphere (Fig. 4.6a). Focusing on the region above 200 hPa, a bias in moisture is evident, where MPAS-DART has a positive water vapor bias with respect to GEFS and ERA5 analysis (Fig. 4.6b). The region of increased water vapor in MPAS-DART member 70 is co-located with the region of enhanced longwave cooling (compare Fig. 4.6b to Fig. 4.2).

To further investigate increased water vapor within MPAS-DART, Arctic averaged profiles of analysis water vapor at initialization time are computed (Fig. 4.6c,d). For MPAS-DART, these profiles are the MPAS initialization files produced from the GEFS lagged forecasts that were provided to the MPAS source code. From the surface to the middle troposphere, there is more water vapor within MPAS-DART compared to GEFS and ERA5 (Fig. 4.6c). This may explain the discrepancies in total accumulated average model tendency and analysis drift found for water vapor near the surface. The increased water vapor within MPAS-DART could drive the convection scheme to erroneously produce clouds near the surface. Erroneous cloud presence would than lead to erroneous longwave radiative tendencies due to the associated cloud-radiative feedbacks. Focusing on levels above 200 hPa, there is overall too much water vapor within MPAS-DART compared to GEFS and ERA5 analysis (Fig. 4.6d). It is apparent that MPAS-DART is initialized with too much water vapor at the start of the cycling period. Thus, I hypothesize that the water vapor bias was introduced into MPAS-DART from a subroutine within the WPS software.

For NCEP products, the relative humidity values are initially with respect to both liquid and ice. In order to get correct specific humidity values in MPAS initial conditions, the

GEFS relative humidity values need to be adjusted so that they represent relative humidity with respect to liquid only, not both liquid and ice. To obtain the modified relative humidity values from GEFS, the data must be passed through a WRF WPS subroutine, which will modify the values before MPAS source code computes specific humidity values for initial conditions (Bolton 1980; Murphy and Koop 2005). When the relative humidity fix is applied, the calculated specific humidity from relative humidity has a better match to the specific humidity within the GEFS data (Fig. 4.7).

Looking at averaged longwave radiation model tendency profile, there is increased cooling at the top of the increased moisture layer and a reduction in cooling at the bottom of the layer (Fig. 4.8). The enhanced cooling at the top is a result of longwave radiation being lost to space with little above this layer to absorb longwave radiation. In contrast to the layers where water vapor decreases with height, the bottom of the layer is absorbing more from the layers below, reducing the amount of longwave cooling that would otherwise occur from radiative processes.

Recall from the MITA increment method enhanced cooling was found from the longwave radiation scheme in the layers spanning 200 hPa up to 50 hPa. Furthermore, there is increased cooling near the surface also associated with to the longwave radiation scheme, which is the dominant parameterization scheme providing the cooling in the model. Regarding water vapor near the surface, there is an increase in the reduction of water vapor within the model which is associated with the convective scheme dominating the tendency budget. Furthermore, there are challenges representing atmospheric evolution over sea ice with static characteristics (sea ice thickness, sea ice albedo, etc) and uncertainties in sea ice data (Figs. 4.9 and 4.10). In experiment 1, sea ice concentration was set to GFS analysis values which may not be representative of the observed sea ice concentration. There is overall too much moisture initialized into MPAS-DART evident in the comparisons with GEFS and ERA5. The moisture bias found between 200 hPa and 100 hPa is co-located

with enhance cooling from the longwave radiation scheme. I hypothesize that the enhanced cooling above this layer is a result of the moisture bias, which will be tested later.

4.1.2 Experiment Two

Based on the results above, changes were implemented to MPAS-DART for experiment 2: 1) initializing moisture using the relative humidity fix and 2) observed sea ice data used for the sea ice concentration instead of GFS sea ice concentration data. A quick comparison between experiment 1 and 2 can still provide information about the sensitivity of previously identified issues to the changes implemented in the modeling system. Briefly, the similarities and differences between the MITA increment method profiles from experiments 1 and 2 are introduced here (compare Fig. 4.1 to Fig. 4.11). Experiment 2 indicates there is a reduction in the moisture bias which was previously identified between 200 hPa and 100 hPa in experiment one (compare Fig. 4.12 to Fig. 4.6). For potential temperature, the cooling associated with the total accumulated averaged model tendency in the layers from 200 hPa to 50 hPa is reduced compared to experiment 1 (Fig. 4.11a to Fig. 4.1a). However, warming in the total accumulated averaged model tendency increases starting just above 100 hPa, which is of similar sign as the analysis drift. The reduction in water vapor associated with the total accumulated averaged model tendency is similar to experiment one, but of reduced magnitude (compare Fig. 4.1b to Fig. 4.11b). There is a decrease in zonal wind speed from the model starting at 100 hPa and above (Fig. 4.11c). This decrease in zonal windspeed was not found in experiment 1. The collocation of increased warming and decreased zonal winds suggests a possible connection. Further discussion of the comparisons between experiments will provided later in this section.

Potential temperature total accumulated averaged model tendency calculations over land are different than the calculations over the entire Arctic, over sea ice and over ocean (Fig. 4.13). The increase in warming aloft from the model is strongest over sea ice (Fig. 4.13d). Over ocean, there is warming, but it does occur aloft close to the damping layer

(Fig. 4.13c). Enhanced cooling aloft from the model found in experiment 1 over all surface types is not present in experiment 2 regardless of surface type (compare Fig. 4.2 to Fig. 4.13). However, it is apparent that the increased warming from the model is regionally localized over the top of the pole in the Arctic. To investigate the increased warming over sea ice, the total accumulated average model tendency is decomposed into individual model-process tendencies (Fig. 4.14). The dominant model-process tendencies over sea ice active above 100 hPa are dynamics and longwave radiation (Fig. 4.14d). Dynamical processes are acting to warm the layers above 100 hPa, which is consistent with tendencies that would be associated with temperature advection. The cooling associated with the longwave radiation scheme is similar over land and over sea ice, lending evidence that the net tendencies over sea ice are related to the dynamics (compare Fig. 4.14b to Fig. 4.14d). Near the surface, enhanced cooling from the model is only noted over sea ice in experiment 2 instead of over land and ocean as in experient 1 (compare Fig. 4.13 to Fig. 4.2). This cooling is dominated by longwave radiation and dynamics over sea ice (Fig. 4.14d). The model cooling could be a result of the longwave radiation scheme cooling temperatures over sea ice and advection of the resulting cooler air by the model dynamics. Applying the relative humidity fix to initialize with corrected water vapor values could be leading to a better representation of clouds near the surface over land (compare Fig. 4.2b to Fig. 4.13b). Separating experiment 2 MITA increment method profiles over the different surface types reveal similar profiles as those found in experiment one (Fig. 4.15 to Fig. 4.4). However, there is a reduction in the overall rates of water vapor reduction in experiment 2 compared to experiment 1 (compare (Fig. 4.15) to (Fig. 4.4)). Reduction in water vapor rates could be associated with the different water vapor initialization process for experiment 2, but there also is generally less moisture in experiment 2 which would reduce the rate of water vapor change. Also similar to experiment 1, the convective parameterization scheme is the most active scheme reducing moisture near the surface (Fig. 4.16). Despite the new moisture initialization process

for experiment two, the model is reducing moisture too quickly near the the surface and this loss dervies from the convective scheme.

There were significant positive AIs for zonal wind above 100 hPa in experiment two which were not found in experiment one (Fig. 3.29). The gravity wave absorbing layer applied in model starts at 22 km ($\sim$ 40 hPa), which means evaluation can only be done up to this level. The MITA increment method profiles also shows a model-induced reduction in the zonal wind in experiment 2, which is not found in experiment one (compare Fig. 4.17c to Fig. 4.17c). Furthermore, the region above 100 hPa that is characterized by stronger reductions in zonal wind by the model is co-located with increased warming from the model, especially over the pole (compare Fig. 4.17c to Fig. 4.14). The decomposition of the model-process tendencies show both dynamics and gravity wave drag by orography (GWDO) are working to reduce the zonal wind above 100 hPa, which is not present in experiment 1 (compare Fig. 4.17d to 4.17b).

4.1.3 Summary

The MITA increment method enabled further investigation into previously identified systematic errors in MPAS-DART. The significant positive potential temperature AIs above 200 hPa found in experiment one was associated with enhanced cooling from the longwave radiation scheme. Additionally, the enhanced cooling from longwave radiation scheme was connected back to a moisture bias present at the same level. Longwave radiation profiles between experiments shows a reduction in the magnitude of cooling in experiment 2, which used different moisture initialization. Since experiment 2 was ran during a different time period, further evaluation is needed to clarify if enhanced cooling is related to the moisture bias or just related to seasonal differences in model cooling leading to sensitivities. Future work would include re-running experiment 1 with the modified moisture profiles to confirm results found in experiment 2.

Near surface AIs showed warming and moistening from observations, implying there was too much cooling and drying from the model. Experiment one showed too much cooling for all surfaces expect over ocean, while experiment two only showed too much cooling over seaice. Regardless of experiment and surface type, the convection scheme was the dominant process reducing water vapor near the surface. Wong et al. (2020) discussed biases within the boundary layer that developed when switching to the "new" Tiedtke convection parameterization scheme. Further investigation is needed to determine if the "new" Tiedtke convection scheme chosen within MPAS-DART is appropriate for high latitude weather. Temperature improvements over land in experiment 2 may be linked back to the different moisture initialization process, but more investigation is needed to be certain.

Lastly over the pole, a reduction in zonal wind from the model tendencies above 100 hPa was identified, and was co-located with warming in potential temperature from the model. Since wave breaking frequency over the North Pacific during the winter time is very common (Martius and Rivière 2016), the interaction of tropospheric Rossby waves propagating into the stratosphere might not be captured correctly in MPAS-DART (Holton et al. 1995; Domeisen et al. 2018). Furthermore, poor representation of stratospheric inertia-gravity waves due to coarse vertical resolution above the tropopause may result in noise and spurious structures (Skamarock et al. 2019). It is possible that model top is too low, which hinders the ability to represent the lower portion of the stratosphere.

The MITA increment method was used to evaluate a significant negative zonal wind bias found in the lower-stratosphere in experiment 1, negative potential temperature and water vapor bias near the surface, and significant potential temperature bias in the upper-troposphere lower-stratosphere region in experiment 1. Due to TPVs residing in the upper-levels of the atmosphere, and that studies have shown moisture can impact TPV evolution, the focus of this of the remainder chapter will be on understanding the moisture bias impacts found in experiment one.

4.2 WRF Single Column Sensitivity Simulations

To test the hypothesis that the enhanced cooling above 200 hPa is driven by the moisture bias would require MPAS-DART being re-cycled over the experiment 1 time period. The computational expense of re-cycling MPAS-DART is not feasible. One research tool that is not computationally expensive to run is the WRF single column model (SCM), provided with the standard WRF code. A SCM is a one-dimensional (in the vertical) computational model that represents a specific column of the atmosphere only through the specified parameterization schemes (Zhang et al. 2016). WRF-SCM does not include the changes within the column from the 3D dynamical core, instead provides a method to isolate the effects of the different parameterization schemes and processes in the column. In the simplest setting, a SCM calculates the time evolution of the vertical distribution of temperature, wind, and moisture without direct representation horizontal and vertical advective tendencies (Zhang et al. 2016). However, these advective tendencies can be represented by applying a 2D or 3D specified large-scale forcing which can help represent a full 3D computational model (Randall and Cripe 1999; Xie et al. 2003, 2006; Kennedy et al. 2011). This simplifies interpretation of impacts model-process tendencies by removing feedbacks from the dynamical core. Different studies have used the WRF-SCM to investigate various atmospheric processes (Hacker and Angevine 2013; Huang et al. 2013; Pithan et al. 2016; Lee et al. 2017).

To test the effects of the moisture bias, 24 6-hour WRF-SCM simulations were ran over 105 sea ice grid points during the experiment one cycling period. The same physics packages that were used in MPAS-DART cycling are used in the WRF-SCM. Analyses from MPAS-DART member 70 were used to obtain the 105 sea ice grid profiles to initialize the WRF-SCM simulations. Two sets of simulations were ran: one with increased moisture at the same level as the previously identified moisture bias and one with decreased moisture at that same level. The adjustment of water vapor in the analysis profiles was achieved by calculating the moisture bias over the 105 sea ice grid points over the entire cycling period

(24 times) of experiment 1. This produced distributions of water vapor bias profiles at each of the 105 sea ice grid points. The 5th and 95th percentile values from the water vapor bias profile distributions were used to adjust the water vapor values in the analyses for the 105 sea ice grid points over the entire cycling period of experiment one.

$$\mathrm{Qv}_{\mathrm{Adjusted}} = \mathrm{Qv}_{\mathrm{Orginal}} - \mathrm{Qv}_{\mathrm{Calculated\ Bias}} \tag{4.3}$$

In equation 4.3, $\mathrm{Qv}_{\mathrm{Orginal}}$ is the original MPAS-DART water vapor, $\mathrm{Qv}_{\mathrm{Calculated\ Bias}}$ is the calculated 5th or 95th percentile water vapor bias, and $\mathrm{Qv}_{\mathrm{Adjusted}}$ is the adjusted water vapor value used in WRF-SCM simulations. For most cases, the 5th percentile water vapor bias value is negative, from equation 4.3 this means the 5th percentile adjusted water vapor profiles will have more water vapor. When water profiles were adjusted, if values exceeded saturation, or 100% relative humidity, they were then adjusted to be just below saturation (or 99% relative humidity). Likewise, 95th percentile water vapor bias value is usually positive, which means the 95th adjusted water vapor profiles will have less water vapor. The water vapor adjustments are shown plotting the distributions of water vapor profiles when adjusted by the 5th and 95th percentile bias values (Fig. 4.18). In the layer spanning from 200 to 50 hPa, which is the region of the water vapor bias within MPAS-DART, there is an increase in the distribution of water vapor when adjusted by the 5th percentile water vapor bias value. Conversely, there is a decrease in the distribution of water vapor when adjusted by the 95th percentile water vapor bias value. While there are larger differences in the distribution of water vapor near the surface, the focus of the simulation will be in the layer that contained the moisture bias within MPAS-DART. Lastly, only water vapor was adjusted in the profiles used to initialize the WRF-SCM simulations.

Since WRF-SCM is both computationally inexpensive and the file size is small, potential temperature model tendency profiles are output every time step for each of model-process tendencies. Outputting every time step allows for model tendencies to be accumulated and averaged in a similar manner as in the MITA increment method. However since this is a single column model, there is no accumulated average dynamics tendency unless

it is specified through boundary conditions forcing the single column. Focusing on the region between 200 and 50 hPa, there is a reduction in the magnitude of cooling from the total accumulated average model tendency with water vapor profiles that have less water vapor (95th percentile simulations; Fig. 4.19a). There is a reduction in cooling on the order of $\sim$0.5 K day^{-1} when less water vapor is present in the analysis profiles versus when more water vapor is present in analysis profiles. The only model-process tendency that is active in the layers between 200 and 50 hPa is the longwave radiation scheme since there is no dynamic model tendency in WRF-SCM. There is a reduction in the magnitude of the longwave cooling in the simulations with less water vapor (Fig. 4.19b). The shape of the longwave cooling profile in the layer of interest matches perfectly with the total accumulated averaged model tendency (compare Fig. 4.19b to Fig. 4.19a). So the $\sim$0.5 K day^{-1} reduction in cooling seen in the total accumulated average model tendency is coming from the reduction in cooling from the longwave radiation scheme. The reduction in model cooling supports the hypothesis that the moisture bias was driving the enhanced cooling from the longwave radiation that was found using the MITA increment method.

4.3 NAWDEX Observations

Up to this point, the moisture bias found above 200 hPa in experiment one has only been investigated from a model tendency perspective. Approaching the issue from a model tendency perspective is mainly due to the lack of high quality, consistently available conventional observations over the Arctic. However, this study aims to understand the potential impacts of the moisture bias on TPV evolution during forecast integration. A field campaign occurred during the same time as the cycling period for experiment one called the **N**orth **A**tlantic **W**aveguide and **D**ownstream Impact **E**xperiment (NAWDEX). The NAWDEX field campaign explored the impacts of diabatic effects on the jet stream and those impacts on downstream high impact weather through the use of aircrafts (Schäfler et al. 2018). A flight mission during the NAWDEX field campaign was one of the first

known targeted observation flight through a TPV on 6 October 2016. This TPV is referred to as the NAWDEX TPV for this study. During the flight through the NAWDEX TPV, the aircraft released 20 dropsondes spanning 9:17 UTC to 11:55 UTC (Fig. 4.20a). These dropsondes were released around and through the center of the NAWDEX TPV at a level near 350 hPa (Fig. 4.20b). The dropsondes were able to resolve the associated jet streak maximum situated just above the tropopause fold as well as the enhanced moisture gradient right below the tropopause (Fig. 4.20b). The NAWDEX TPV dropsondes offer a novel observational view of the vertical moisture distribution previously only depicted in numerical models.

Before the dropsondes could be assimilated within the MPAS-DART system, some modifications needed to be made. The NAWDEX dropsonde profiles had vertical sampling rate of about once every 1 hPa, which is different than conventional radiosonde data on mandatory and significant levels (NCEP 2020). To stay consistent with conventional radiosondes but not degrade the information content from the dropsondes, each profile was interpolated to levels with 50 hPa spacing. Furthermore, the dropsonde data did not come with observation errors, so DART-provided observation errors for dropsonde temperature, wind components, and water vapor were applied to stay consisted with specification of other observation errors within MPAS-DART. The provided DART dropsonde observation errors are similar to the observation errors applied to radiosonde observations. These observation errors are similar to what other studies shown concerning radiosonde and dropsondes (Wang et al. 2013a; Dirksen et al. 2014). Since the dropsonde observations coverage spans times from 9 UTC to 12 UTC, modifications had to be made to stay consisted with the 3-hour observation window set within MPAS-DART. Typically, cycling for MPAS-DART involves 6-hourly cycling with data assimilation steps occurring at 00,06,12,18 UTC with a observation window of 3 hours (Fig. 4.21a). When assimilating the NAWDEX dropsondes, this includes a special assimilation step at 09 UTC that will contain all dropsonde observations that fall in that 3-hour window. Then a 3-hour forecast is ran to 12 UTC were the

rest of the dropsondes along with all observations that are included in normal cycling will be assimilated (Fig. 4.21b). The adapted cycling method will ensure that the observation window is consistent across experiments. The dropsondes recorded several observation types, but only temperature, wind components and water vapor were assimilated within the MPAS-DART system. This portion of the study will evaluate the impacts of the well-positioned observations of the NAWDEX TPV, specifically related to the moisture bias. There are two different experiments presented here, forecasts with NAWDEX observations assimilated and forecasts without NAWDEX observations assimilated.

The net impact of dropsonde observations in MPAS-DART analyses is first evaluated. AIs associated only with the dropsonde observations (not mean AIs across all observations) are used to determine the magnitude of the impacts to MPAS-DART analyses (Fig. 4.22). Overall, dropsonde observations are having some impact on the analyses, with varying degrees of magnitude. For dropsonde temperatures, the AI increases temperature most dominantly in the middle-troposphere, which implies the temperature observations are attempting to correct the cold bias previously identified in MPAS-DART (Fig. 4.22a, Figs. 3.10 and 3.11). The dropsonde water vapor observations are primarily decreasing moisture in the lower portion of the middle-troposphere, in agreement with the water vapor AIs averaged over the Arctic (Fig. 4.22c, Fig. 3.27). Additionally, the spike in water vapor AI at 600 hPa results from a large difference between one dropsonde observation and MPAS-DART. Lastly, dropsondes are acting to increase wind speeds, on average, for both wind components except for v-wind above 500 hPa (Fig. 4.22d).

To further evaluate the impacts the dropsondes are having on the NAWDEX TPV, cross-section analysis composite differences were calculated for the 96 different realizations of the NAWDEX TPV from each experiment (Fig. 4.23). Statistical significance is identified in the differences between the two experiments by applying a student t-test. Potential temperature comparisons show significant differences identified in the tropopause fold region (Fig. 4.23a). There is a large, positive difference in potential temperature with a narrow

area of negative differences just below where potential temperature values are smaller when NAWDEX dropsondes are assimilated. There are significant decreases in EPV within the tropopause fold region when NAWDEX dropsonde are assimilated, which means the fold is enhanced (Fig. 4.23b). For water vapor, there is a significant reduction in water vapor just below the tropopause in the core of the TPV extending towards the surface, which increases the gradient of moisture across the tropopause (Fig. 4.23c). Lastly, there is a significant increase in the normal wind component when NAWDEX observations are assimilated (Fig. 4.23d). The increase in the normal wind component could be related to the tropopause fold being pulled back towards the center of the NAWDEX TPV, which is highlighted by the differences in EPV, or the increase in the gradient of potential temperature. Overall, the dropsonde observations are having significant impacts on the MPAS-DART analyses.

Mean analysis differences between the 96 NAWDEX TPV realizations for two experiments shows areas of large significant differences. However since this is a relatively large dataset, it is useful to analyze the variability within the model analyses of the two experiments. The spatial representation of a TPV can be explored though analysis of a single variable, potential temperature, on the 2 PVU surface. To do so, empirical orthogonal function (EOF) analysis is applied determine the leading modes of variability of the 2 PVU potential temperature field within the two different experiments (Wilks 2011). Vertical TPV structure manifests across several variables. As such, multivariate EOF analysis is applied to NAWDEX TPV cross-sections for potential temperature, water vapor, and the normal wind component to determine the leading modes of co-variability among those different field variables. To compute the EOFs, the data from both experiments were combined to compute an ensemble mean which was then used to compute anomalies for the fields of interest. To compute the EOFs, singular value decomposition (SVD) is applied to the calculated anomalies. The standardized principal components (PCs) series is computed, which allows this study to determine which members from the two experiments match the leading mode of variability. The significance of each EOF in the analysis is determined by

applying the equations from North et al. (1982), and calculating the standard error for the eigenvalues. This technique provides a method to determine which EOFs are significantly separated from each other. For this study, the 95% confidence interval is used to determine which EOF modes are significantly separated, and thus which modes to further investigate. Eigenvalue significance is calculated for both the spatially computed EOFs and the TPV cross-section multivariate EOFs (Fig. 4.24). For the spatial eigenvalues, the two leading modes, EOFs 1,2, and 3 are distinguishable from each other with 95% confidence (Fig. 4.24a). For this study, EOFs 1 and 2 will be the focus for investigating the variability in the 2 PVU potential temperature field since these modes will explain the highest percentage of the variability within the data. There is significant separation between eigenvalue 1 and 2 for the multivariate EOFs, but this is not the case for eigenvalues 2 and 3 (Fig. 4.24b). Furthermore, EOFs 4 and 5 are statistically distinguishable, however, the amount of explained variance will be lower compared to EOF 1. From this evaluation, only multivariate EOF 1 will be used to investigate TPV cross-sections.

Examining first the spatial variability associated with the NAWDEX TPV, a dipole pattern indicates the TPV position is the leading mode of variability with the explained variance at 24.6% (Fig. 4.25a). The PCs describe how each of the ensemble member represents the corresponding EOF pattern. Large positive PCs correspond strongly to the EOF pattern, large negative PCs correspond strongly to the opposite of the EOF pattern, and PCs that are close to zero have no resemblance to the EOF pattern. The separated PCs for the experiment with NAWDEX observations assimilated shows most members match the EOF 1 pattern with little spread in the PC values (Fig. 4.25a). For the experiment without NAWDEX observations assimilated, the PCs show that most members have the opposite pattern than EOF 1 and there is a larger spread in the PCs (Fig. 4.25a). This implies that when NAWDEX observations are assimilated there is a shift in the NAWDEX TPV position in almost all of the ensemble members. EOF 2 potentially reflects variability of the NAWDEX TPV intensity, where positive PCs represent a more intense TPV and negative

PCs represents a less intense TPV (Fig. 4.25b). The explained variance is lower at 8.7%, which is further reasoning for not investigating past EOF 2. For both experiments, the center of the highest proability of PCs is centered at zero, but there is smaller spread in the PCs for the experiment with NAWDEX observations assimilated (Fig. 4.25b). This implies that with the assimilation of the NAWDEX observations, there is less spread in the strength of the TPV.

The multivariate EOF (MV-EOF) analysis is used to investigate the leading modes of variability for the structure of the TPV. MV-EOF 1 highlights an increase in the separation of the potential temperature contours, an increase in the normal component of the wind speed inside the TPV center, and a decrease in water vapor just below the tropopause (Fig. 4.26a). Once again, there is smaller spread in the PCs when NAWDEX observations are assimilated and larger spread in PCs when NAWDEX observations are not assimilated (Fig. 4.26a). Furthermore, the NAWDEX observations shift the PCs towards zero, which means the ensemble is better capturing both sides of the leading mode.

Overall, the EOF analysis helped display the variability within MPAS-DART analyses when assimilating NAWDEX dropsonde versus when NAWDEX dropsondes are not assimilated. Spatially, there are impacts on TPV position and on the spread of the TPV intensity when NAWDEX observations are assimilated. Furthermore, there are impacts on the TPV structure and variability when assimilating NAWDEX dropsondes.

Since there were large impacts on the analyses when NAWDEX observations were assimilated, investigation of sensitivities of forecasts to dropsonde observations are further evaluated. Five-day forecast were performed for both NAWDEX simulations (with and without assimilating the NAWDEX observations). First focusing on spatial differences, there are statistically significant differences at the analysis time, consistent with the spatial EOF-1 pattern discussed above (Fig. 4.27a and Fig. 4.25a). The data assimilation impacts of the dropsonde observations extend out from the TPV of interest (Fig. 4.27a), which means the representation of other atmospheric features could be positively impacted as

well. As forecasts progress, there are statistically significant differences along the gradient in potential temperature and near the center of the TPV (Fig. 4.27b-f). While there are areas of statistically significant differences out to forecast hour 60, the magnitudes of the differences are relatively small. Lastly, there is a region of EPV that that cuts off and splits form the main TPV at forecast hour 24 when NAWDEX observations are assimilated (Fig. 4.27c). Future work should include further investigation into why the cutoff EPV formed only when assimilating NAWDEX observations.

Comparison of the NAWDEX TPV for the two experiments is completed by tracking the feature of interest throughout the forecast period. A previously developed and tested watershed TPV tracker was used in this study (Szapiro and Cavallo 2018). NAWDEX TPV object counts and median forecast track positions for both experiments show that the TPV of interest evolved along similar paths in both experiments (compare Figs. 4.28 and 4.28). Lastly, the median forecasted minimum potential temperature associated with the NAWDEX TPV is also very similar (Fig. 4.28). The similarities in TPV minimum potential temperature is in agreement with the spatially computed differences in the 2 PVU potential temperature field discussed above. The spread in potential temperature associated with the NAWDEX TPV for both experiments is computed to compare differences in intensity (Fig. 4.29). At analysis time, the spread in NAWDEX TPV potential temperatures is smaller and shifted towards lower values for the with NAWDEX observations assimilated versus without NAWDEX observations assimilated (compare Fig. 4.29b to Fig. 4.29a). As forecast hour increases, the NAWDEX TPV potential temperatures for each experiment drift closer together, and by forecast day-1 the values are very similar (compare Fig. 4.29b to Fig. 4.29a). This suggests that there are differences between experiments at analysis time but as forecast time increases, the differences get washed out and the forecasts become quite similar.

Ling et al. (2014) found similar analysis and forecast results when investigating the impacts of including special radiosonde profiles from a field campaign evaluating the Madden–Julian oscillation. For the NAWDEX TPV case, the small differences in forecasts are related back to the localized nature of the perturbations induced by the NAWDEX dropsondes. Since the perturbations are very localized, the regions surrounding the NAWDEX TPV start to dominate the evolution of forecasted fields, which starts to overpower any impacts of the NAWDEX perturbations.

While there was a moisture reduction below the tropopause when NAWDEX observations were assimilated, the differences in the forecast were quite small. Furthermore, focusing only on the NAWDEX TPV provides only one case while there are many TPVs present through the cycling period. Since ERA5 was shown to have a lower moisture values in the region where MPAS-DART was shown to have a bias, comparisons to ERA5 allows for broader evaluation of the impact of moisture on TPV evolution. This study tracked all 6-hour forecasted TPVs within MPAS-DART member 70 and all analysis TPVs in ERA5. Furthermore, TPVs were tracked in both MPAS-DART experiment 1 and 2 to test the effects of the different water vapor initialization process. The tracking period for the TPVs was the length of the cycling period for the MPAS-DART experiments. For experiment 1, the median potential temperature for the TPVs in their early lifetimes was similar between MPAS-DART and ERA5 (Fig. 4.30a). As TPV lifetime increases, ERA5 has lower potential temperature values compared to MPAS-DART (Fig. 4.30a). The process rates associated with the longwave radiation cooling for the moisture bias could take longer than a few days. While there is a multitude of possible reasons for this, one reason could be the reduction moisture which was found in ERA5 compared to MPAS-DART member 70. However, in MPAS-DART experiment 2 there are similar median TPV potential temperature values not only in the early lifetimes but also in the later lifetimes (Fig. 4.30b). The similarities in later lifetime median TPV potential temperatures could be highlighting the impacts the reduction in moisture has on forecasted TPV intensity within MPAS-DART. Lastly, there

is better agreement with ERA5 in the distribution of the lifetime minimum TPV potential temperatures for MPAS-DART experiment 2 compared to experiment 1 (Fig. 4.31). For experiment one, there were larger TPV lifetime potential temperature minimums compared to ERA5. Once again, this could be highlighting the moisture bias impacts on TPV evolution for the different moisture initialization process. Future work should include re-running experiment 1 with the improved moisture initialization process to fully understand moisture impacts on TPVs.

Overall, the NAWDEX dropsonde observations impart significant impacts in both the analyses and forecasts. The magnitude of those impacts seemed larger in the analyses produced in the data assimilation cycle compared to the forecasts produced by the model. There was a shift in the TPV position and reduction in magnitude when NAWDEX dropsonde observations were assimilated. Also, there were impacts on the TPV structure in the analysis, which included a reduction in water vapor along the tropopause. The forecast differences for the NAWDEX TPV were small and quite localized, when comparing experiments with and without NAWDEX observations assimilated. However, differences were found when tracking TPVs in MPAS-DART member 70 for the two MPAS-DART experiments and comparing to ERA5. There was better agreement at later lifetimes in the median TPV potential temperatures between ERA5 and MPAS-DART experiment 2 versus experiment 1. These results suggest the improved moisture profiles in experiment 2 improved TPV evolution. However, to fully quantify the differences between experiments would require re-running experiment 1 to fully evaluate the impact of the moisture initialization technique.

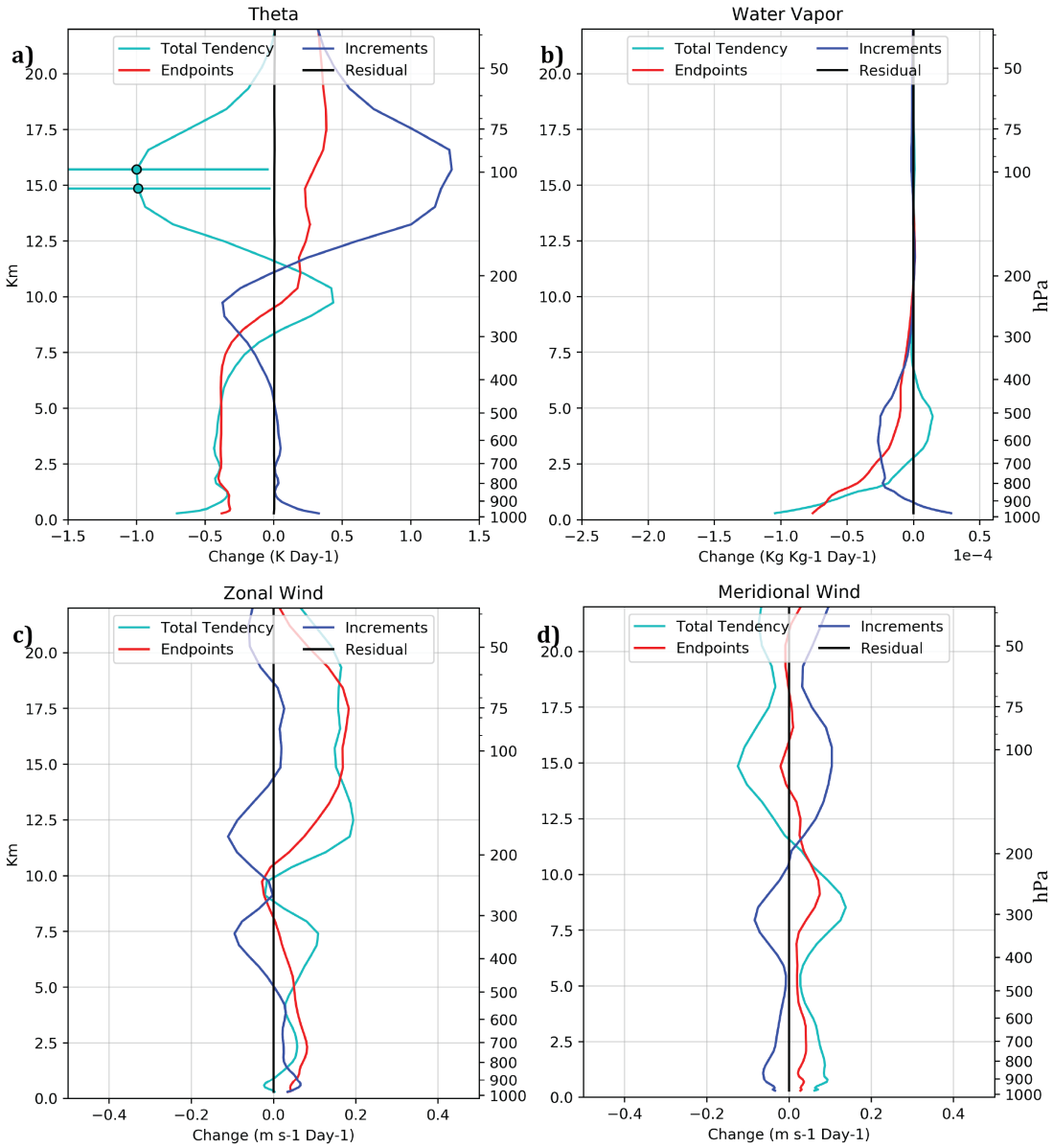

Figure 4.1: Experiment one spatially averaged profiles of MITA increment method for (a) potential temperature, (b) water vapor, (c) zonal wind, and (d) meridional wind over the Arctic. Each colored line represents a different term in equation 4.1. The black line is the residual which is the difference between the RHS and LHS in equation 4.1. Error bars are included on the total accumulated average model tendency profiles only at points where the 70% confidence intervals (Cavallo et al. 2016) do not cross zero, indicating the profile values are statistically different from zero.

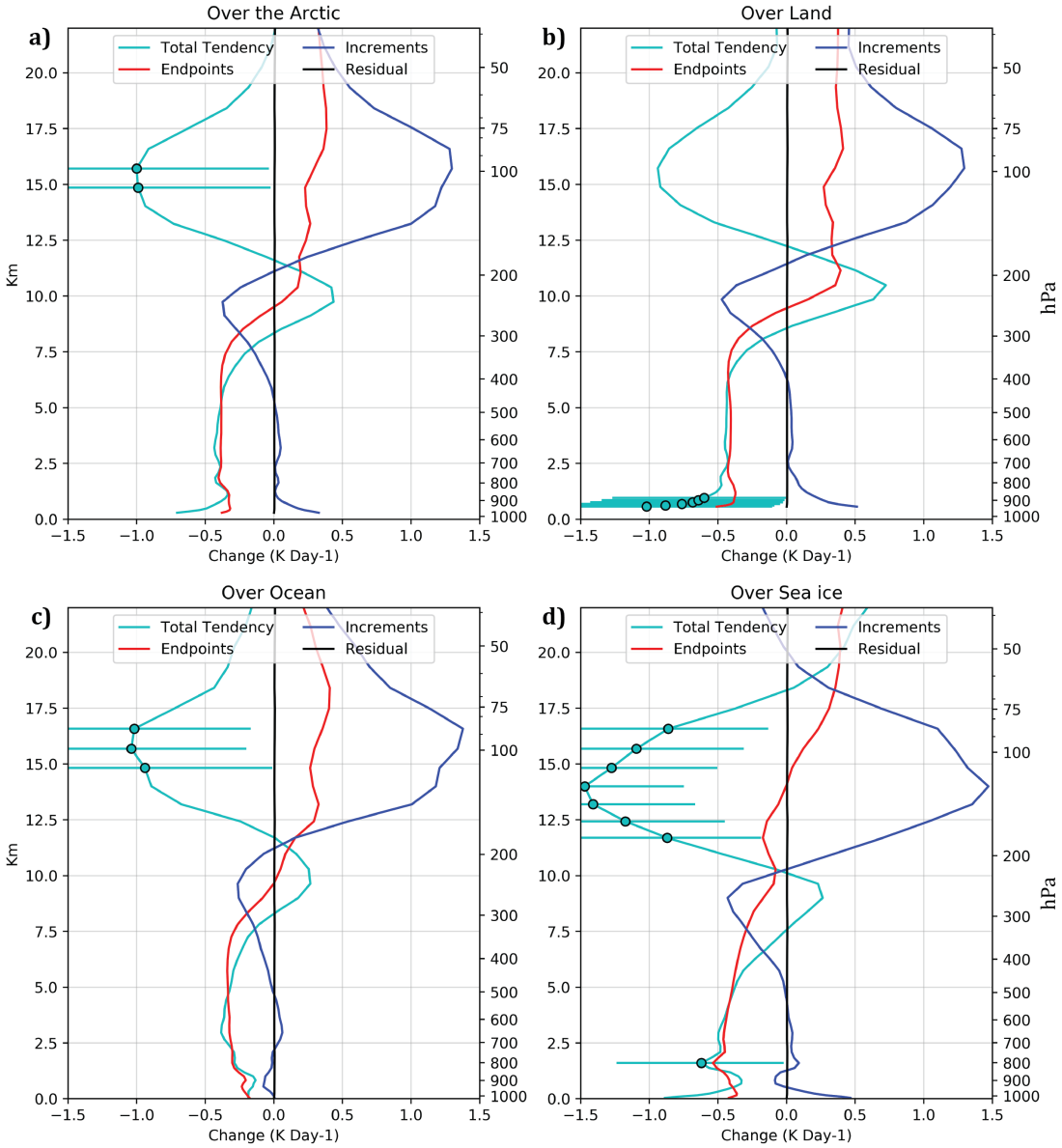

Figure 4.2: Experiment one spatially averaged profiles of MITA increment method for potential temperature (a) over the Arctic, (b) over land in the Arctic, (c) over ocean in the Arctic, and (d) over seaice in the Arctic. Each colored line represents a different term in equation 4.1. The black line is the residual which is the difference between the RHS and LHS in equation 4.1. Error bars are included on the total accumulated average model tendency profiles only at points where the 70% confidence intervals (Cavallo et al. 2016) do not cross zero, indicating the profile values are statistically different from zero.

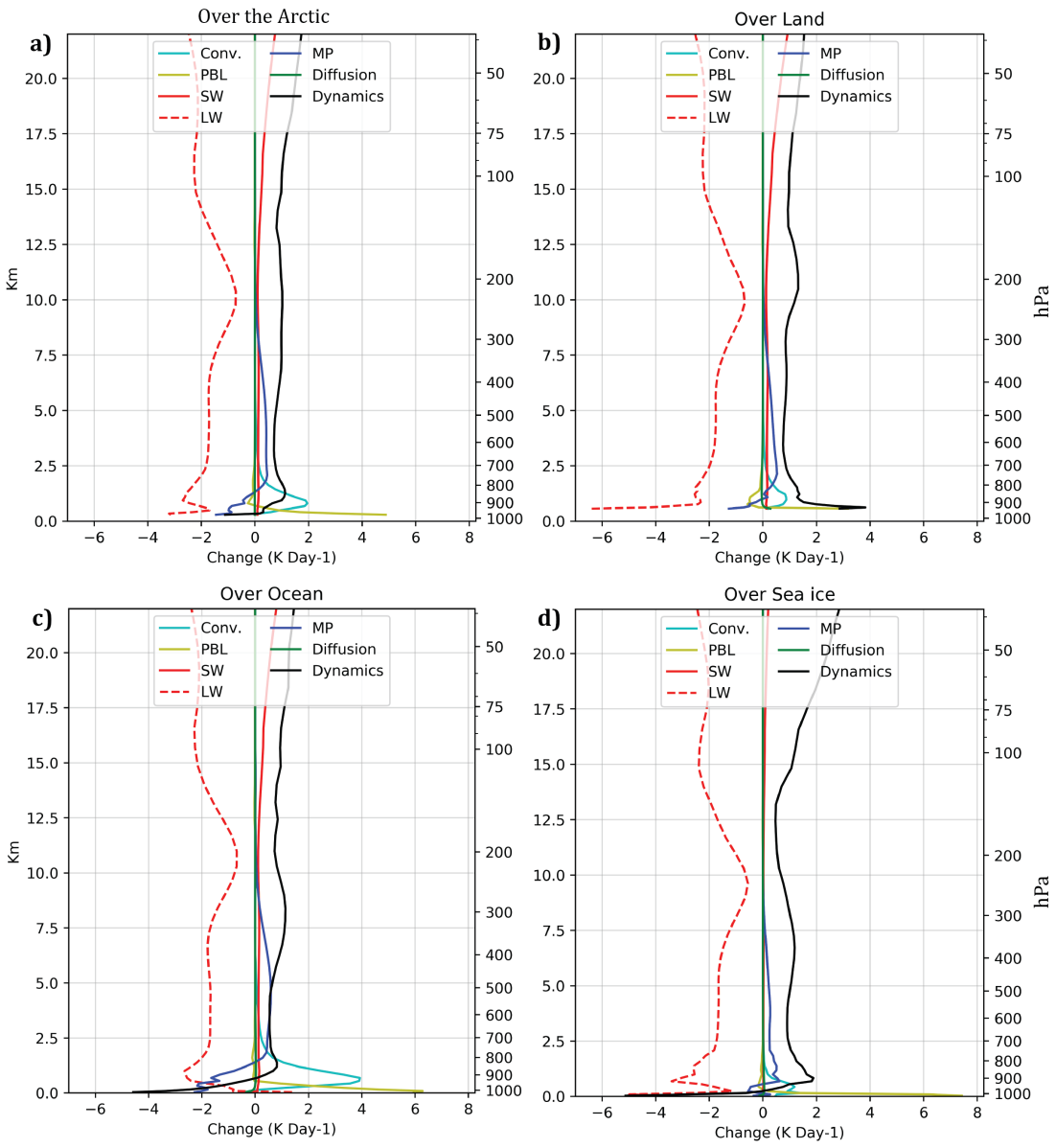

Figure 4.3: Experiment one spatially averaged accumulated model tendencies for potential temperature (a) over the Arctic, (b) over land in the Arctic, (c) over ocean in the Arctic, and (d) over seaice in the Arctic. Each colored line represents a different physics tendency representing potential temperature.

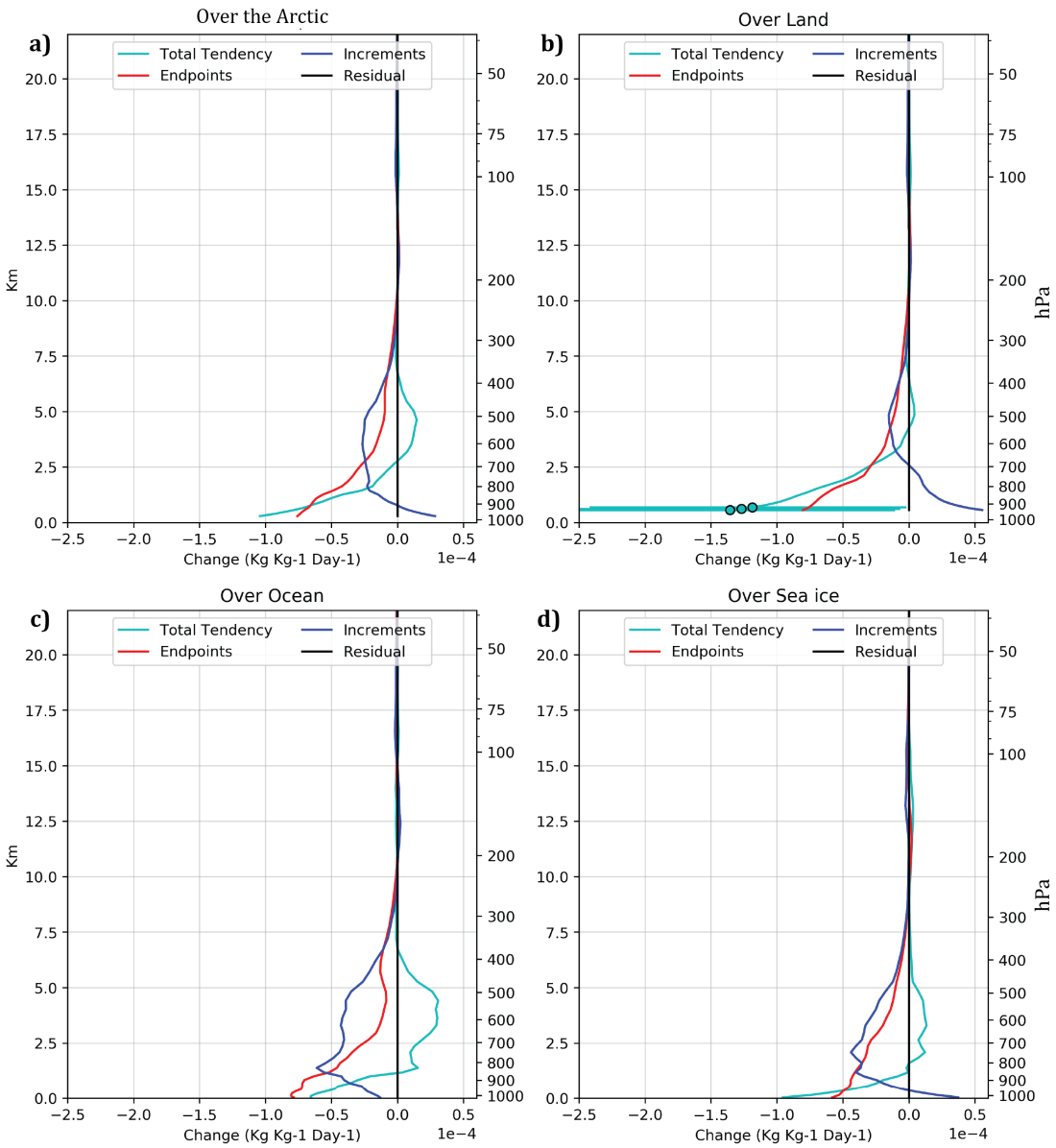

Figure 4.4: Experiment one spatially averaged profiles of MITA increment method for water vapor (a) over the Arctic, (b) over land in the Arctic, (c) over ocean in the Arctic, and (d) over seaice in the Arctic. Each colored line represents a different term in equation 4.1. The black line is the residual which is the difference between the RHS and LHS in equation 4.1. Error bars are included on the total accumulated average model tendency profiles only at points where the 70% confidence intervals (Cavallo et al. 2016) do not cross zero, indicating the profile values are statistically different from zero.

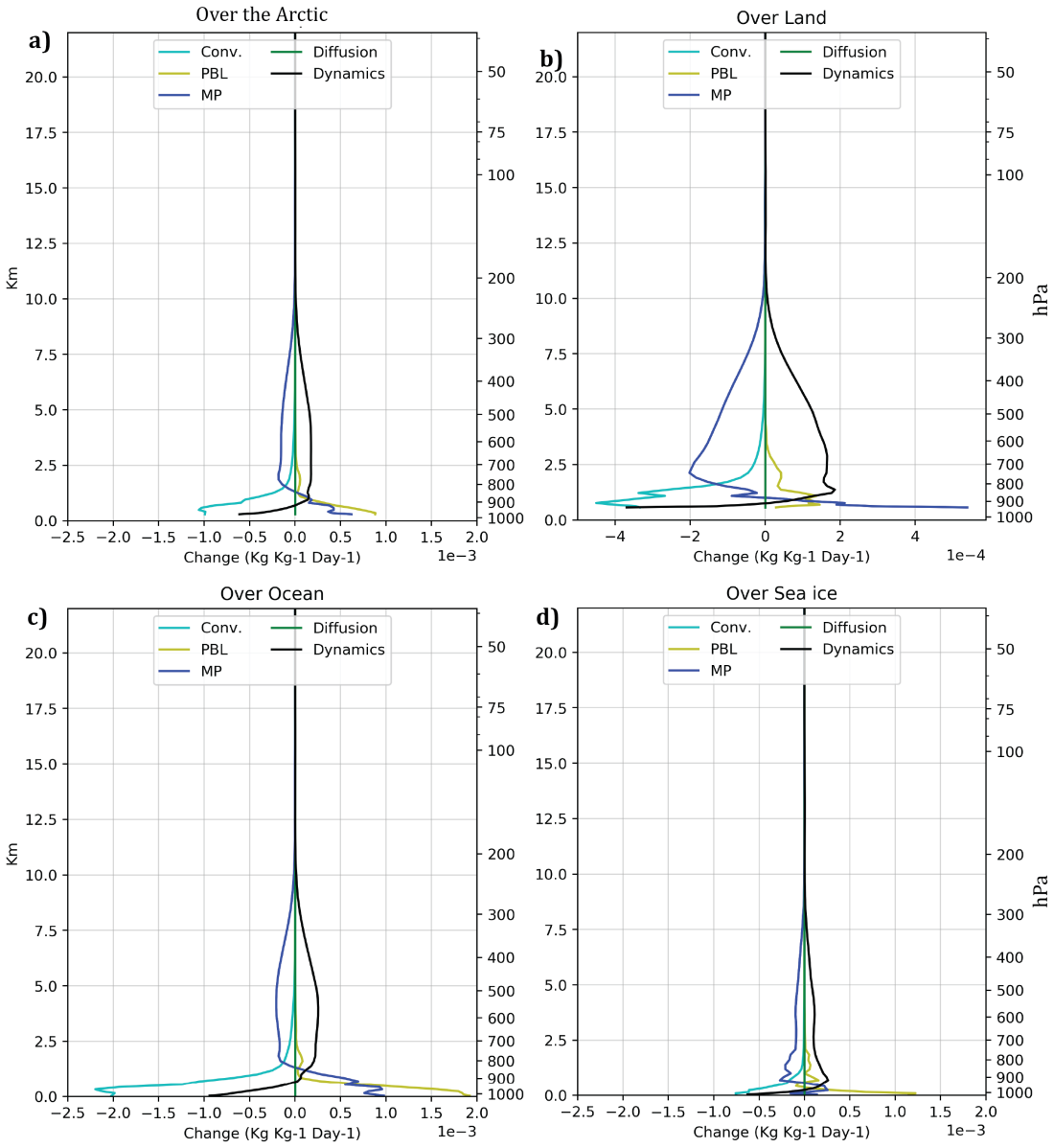

Figure 4.5: Experiment one spatially averaged accumulated model tendencies for water vapor (a) over the Arctic, (b) over land in the Arctic, (c) over ocean in the Arctic, and (d) over seaice in the Arctic. Each colored line represents a different physics tendency representing qv.

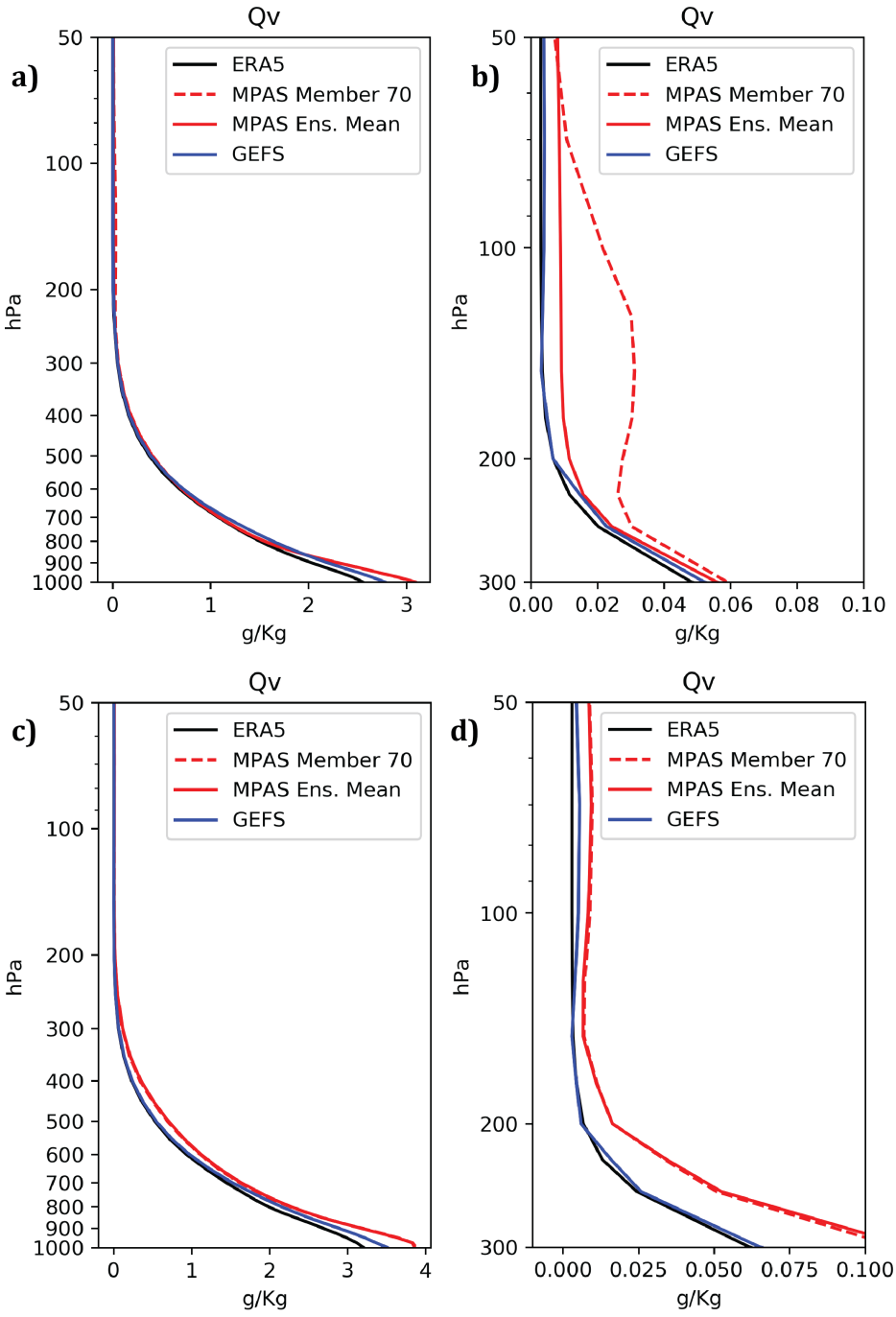

Figure 4.6: Arctic averaged water vapor profiles (a,b) averaged over the cycling period and (c,d) at initialization time for experiment one. MPAS ensemble average (solid red line), MPAS member 70 (dashed red line), and control member GEFS (solid blue line) are compared to ERA5 (solid black line).

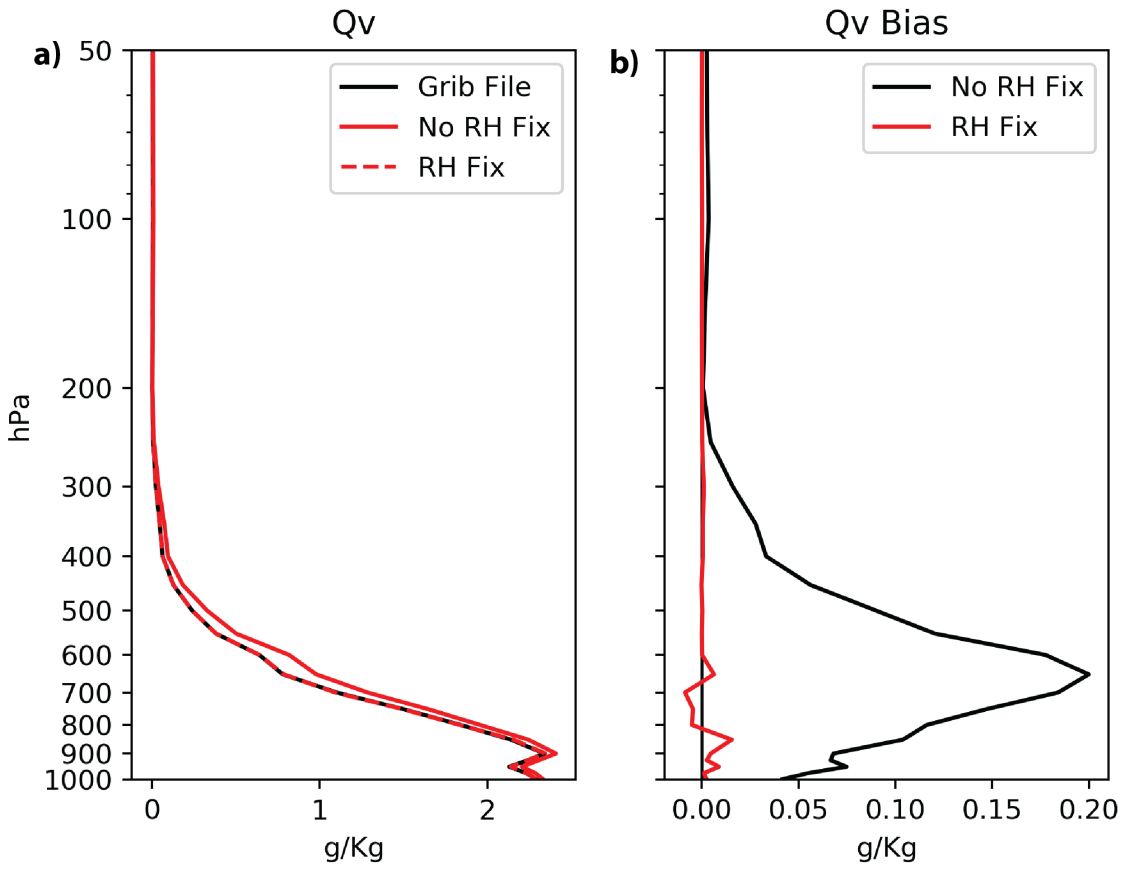

Figure 4.7: (a) GEFS Water vapor profiles comparing computed water vapor from relative humidity when the WPS subroutine fix is applied (dashed red line) versus when the relative humidity fix is not applied (solid red line). The solid black is the water vapor profile provided from the GEFS data. (b) Water vapor bias profiles comparing when the relative humidity fix is applied versus when the fix is not applied.

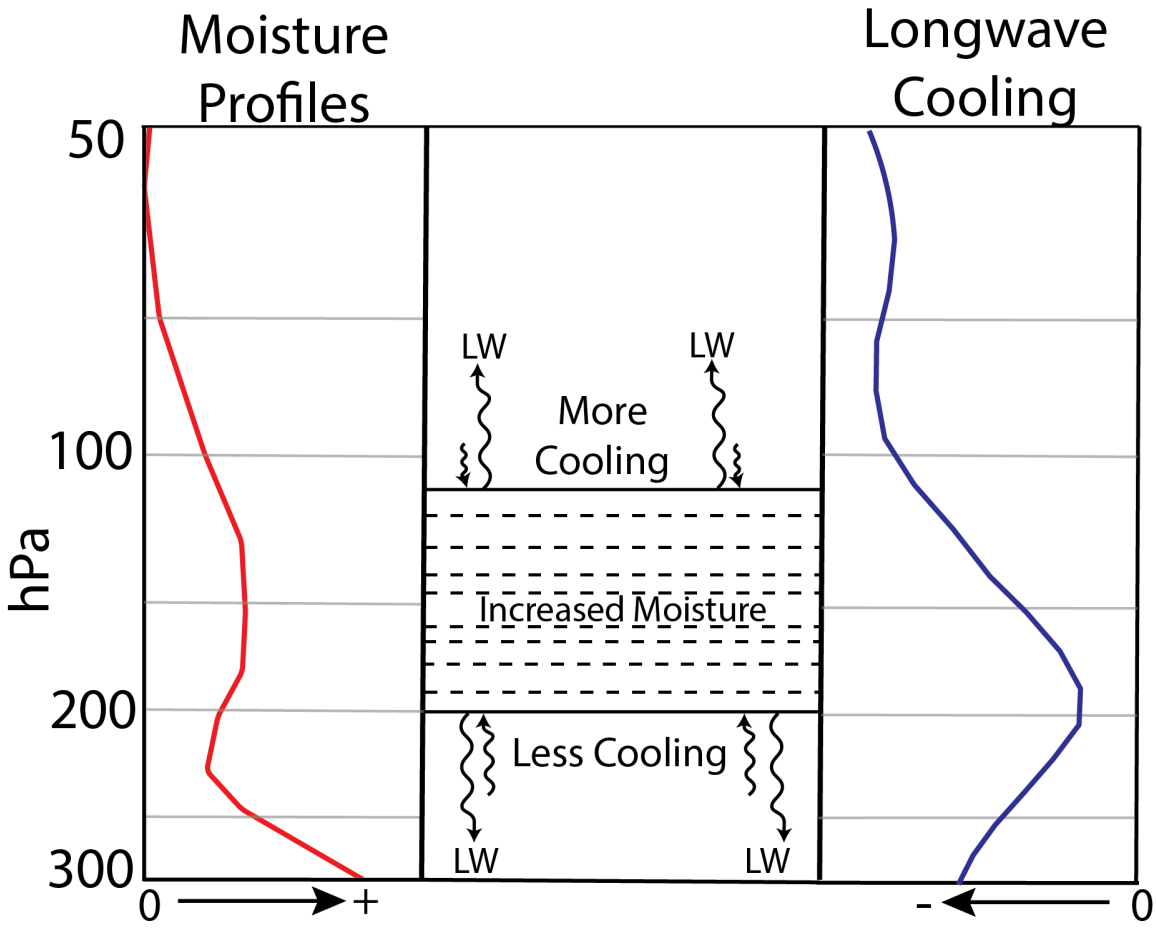

Figure 4.8: Schematic illustrating the radiative cooling linked back to the increase in moisture. The red line represents the moisture profile found in MPAS-DART member 70. The black wiggly lines represent longwave (LW) radiation being absorbed and reemitted from the layer with increased moisture. The moisture gradient in shown by the black dashed lines. The longwave wave cooling profile from MPAS-DART member 70 is shown with by the blue line.

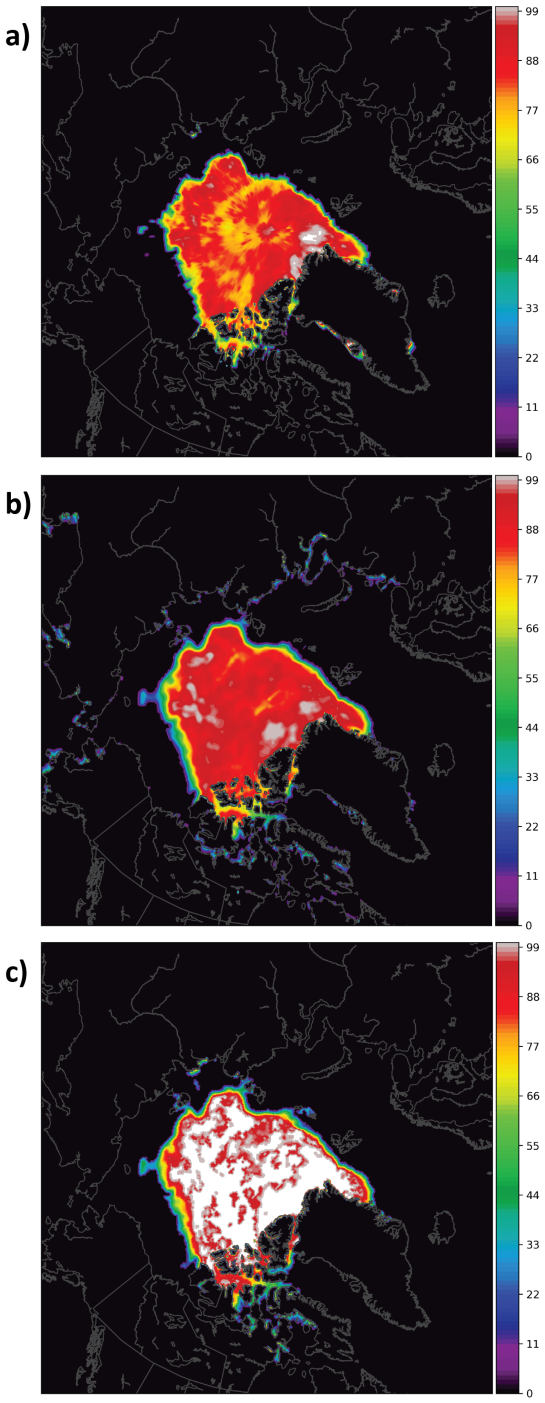

Figure 4.9: Sea ice concentration provided from (a) NCEP GFS, (b) ERA5, and (c) passive microwave satellite from National Snow and Ice Data Center (NSIDC) that are valid on 8 October 2016 at 00 UTC.

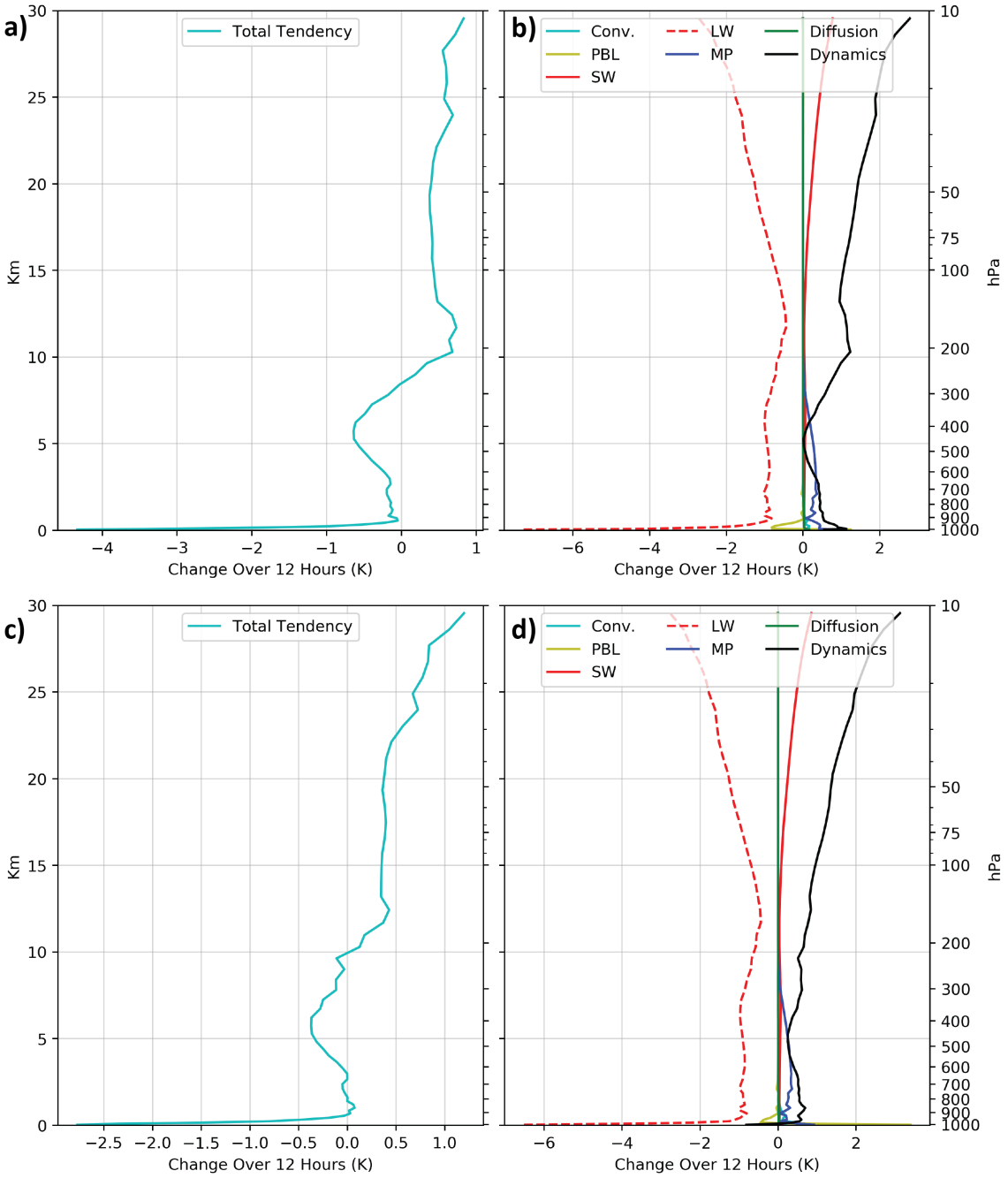

Figure 4.10: Accumulated model tendency profiles for simulations initialized using sea ice concentration data from (a,b) GEFS and (c,d) ERA5. Figures (a,c) represent total accumulated averaged model tendency while figures (b,d) are the decomposed model tendencies.

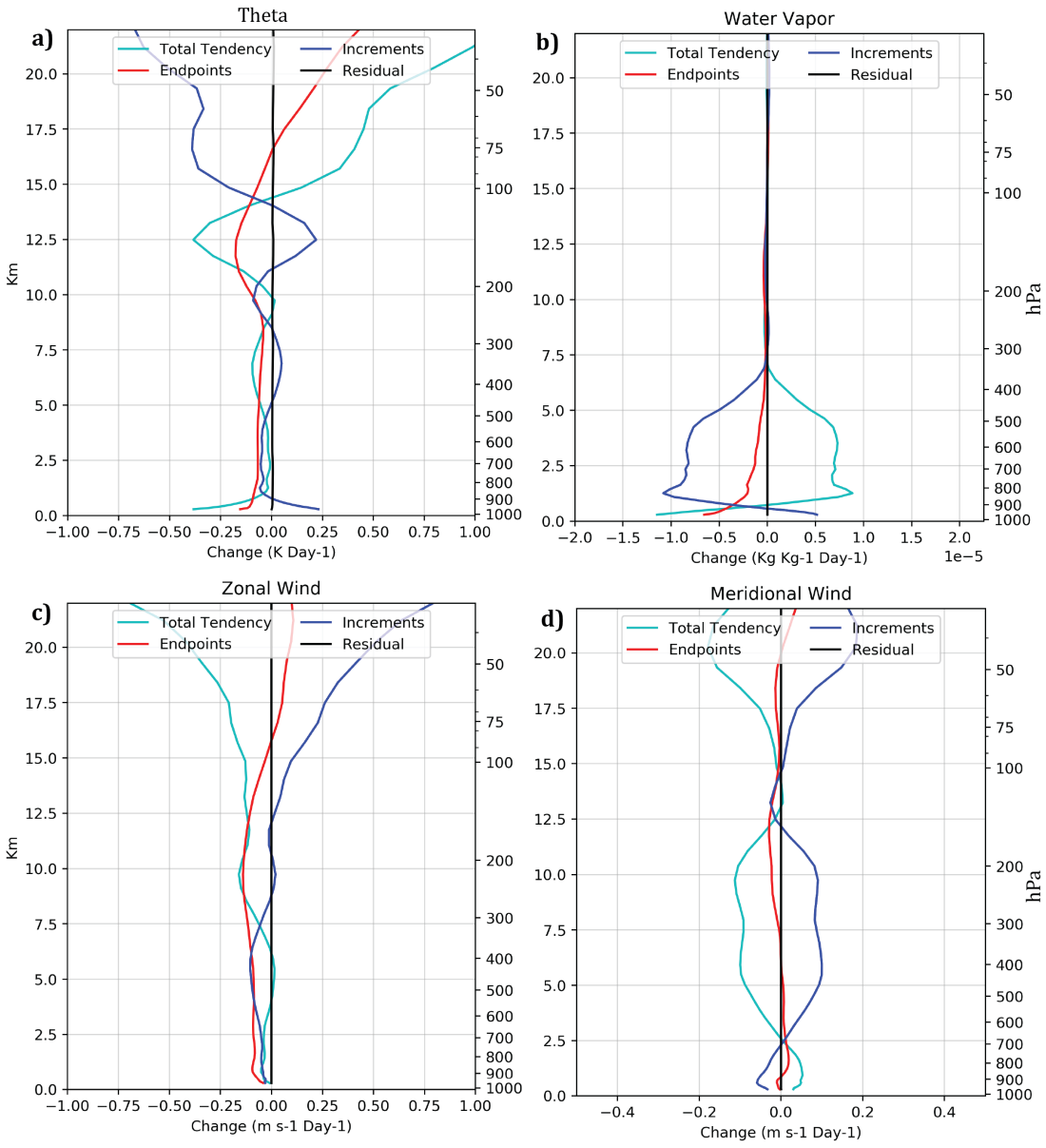

Figure 4.11: Experiment two spatially averaged profiles of MITA increment method for (a) potential temperature, (b) water vapor, (c) zonal wind, and (d) meridional wind over the Arctic. Each colored line represents a different term in equation 4.1. The black line is the residual which is the difference between the RHS and LHS in equation 4.1. Error bars are included on the total accumulated average model tendency profiles only at points where the 70% confidence intervals (Cavallo et al. 2016) do not cross zero, indicating the profile values are statistically different from zero.

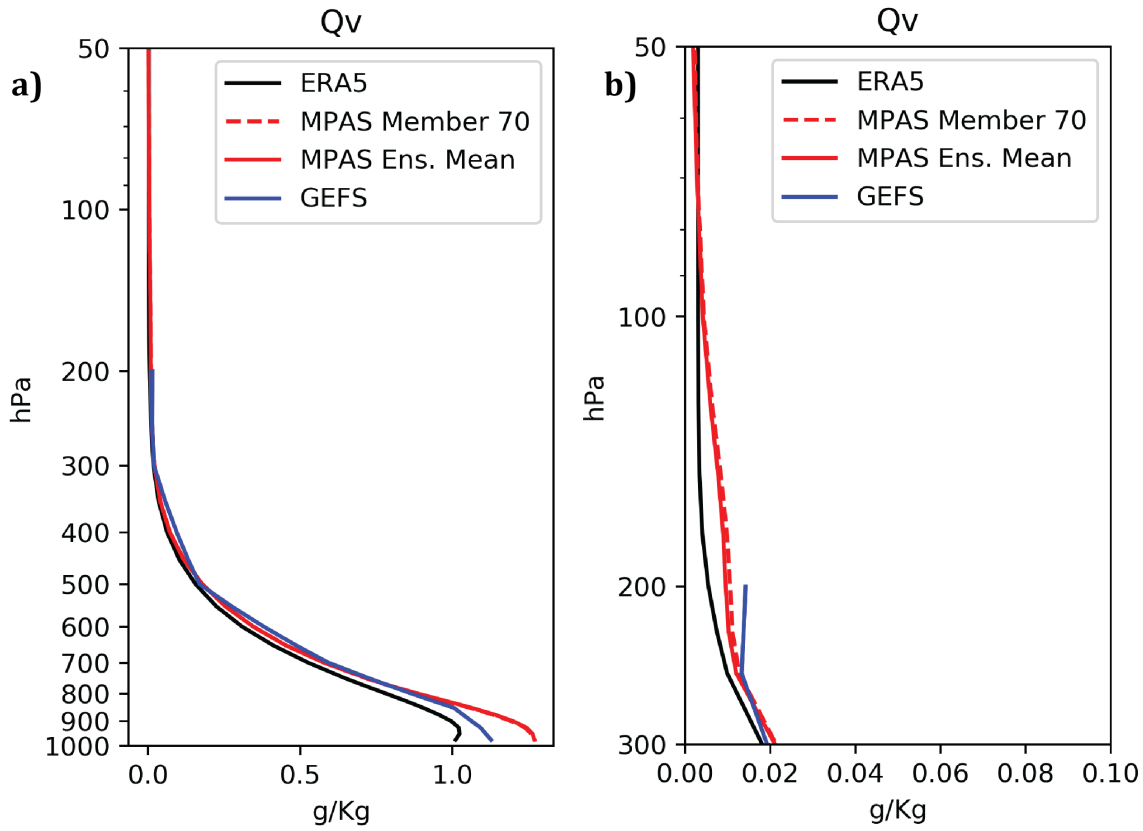

Figure 4.12: Arctic averaged water vapor profiles (a,b) averaged over the cycling period for experiment two. MPAS ensemble average (solid red line), MPAS member 70 (dashed red line), and control member GEFS (solid blue line) are compared to ERA5 (solid black line).

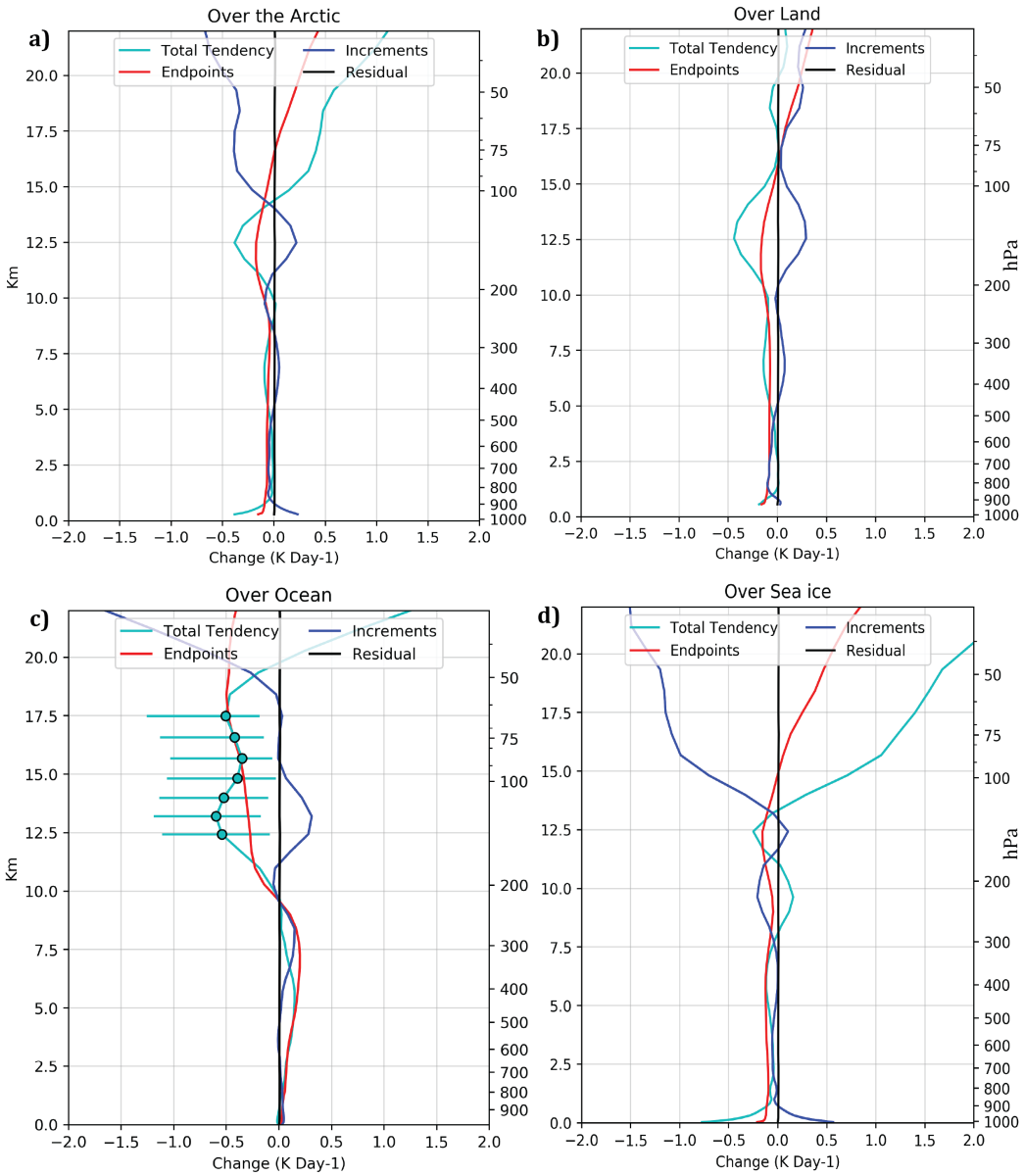

Figure 4.13: Experiment two spatially averaged profiles of MITA increment method for potential temperature (a) over the Arctic, (b) over land in the Arctic, (c) over ocean in the Arctic, and (d) over seaice in the Arctic. Each colored line represents a different term in equation 4.1. The black line is the residual which is the difference between the RHS and LHS in equation 4.1. Error bars are included on the total accumulated average model tendency profiles only at points where the 70% confidence intervals (Cavallo et al. 2016) do not cross zero, indicating the profile values are statistically different from zero.

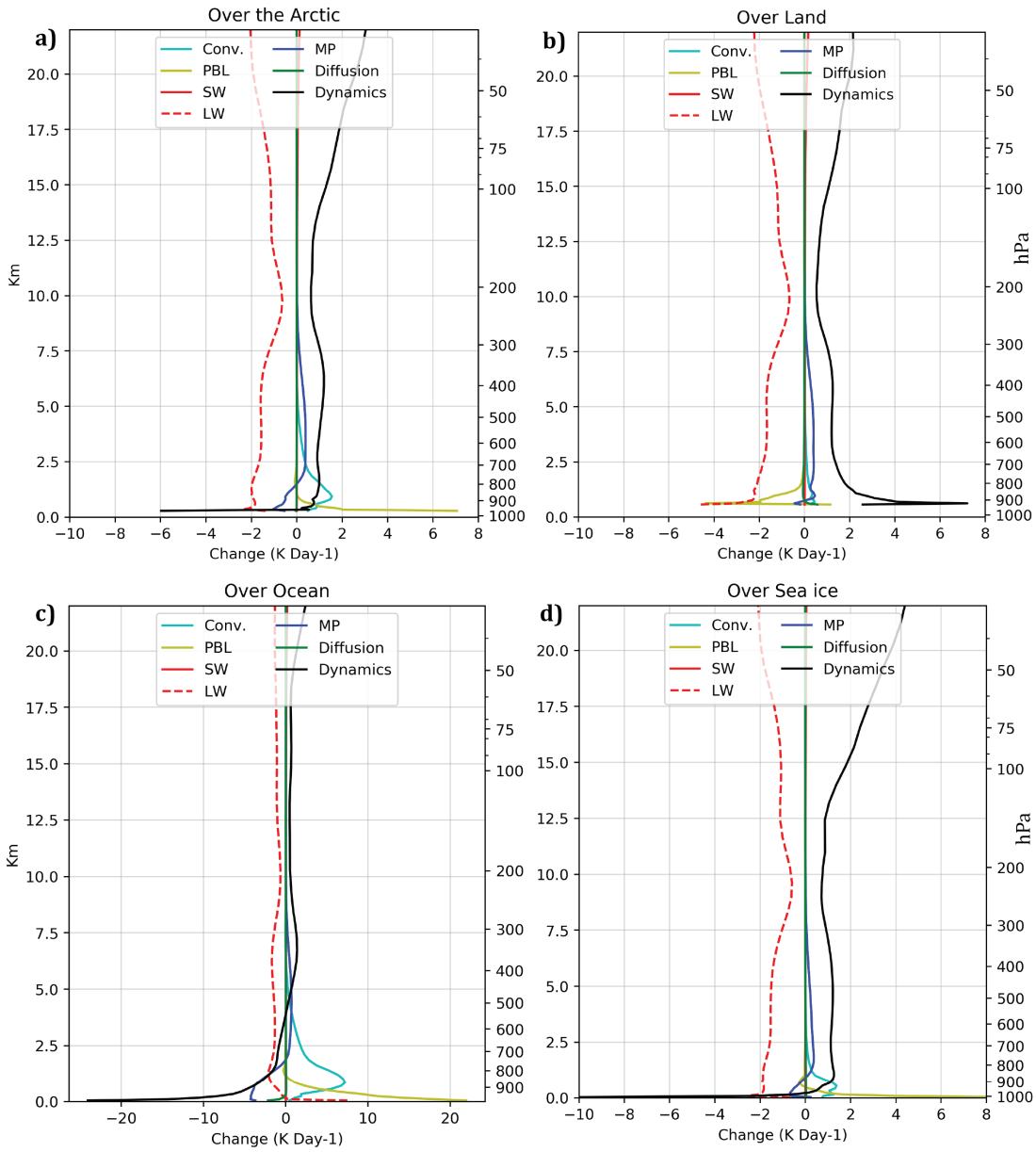

Figure 4.14: Experiment two spatially averaged accumulated model tendencies for potential temperature (a) over the Arctic, (b) over land in the Arctic, (c) over ocean in the Arctic, and (d) over seaice in the Arctic. Each colored line represents a different physics tendency representing potential temperature.

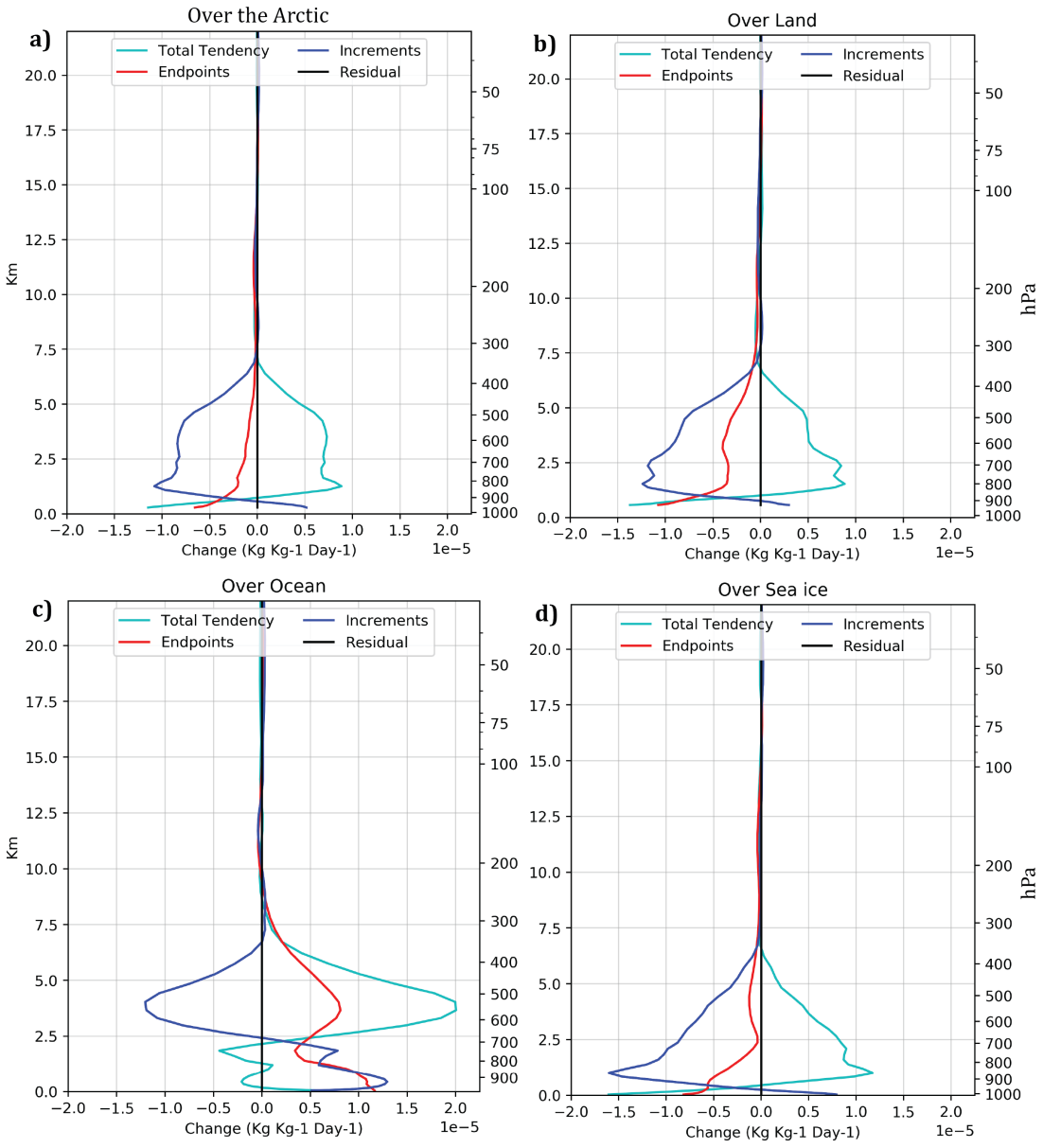

Figure 4.15: Experiment two spatially averaged profiles of MITA increment method for water vapor (a) over the Arctic, (b) over land in the Arctic, (c) over ocean in the Arctic, and (d) over seaice in the Arctic. Each colored line represents a different term in equation 4.1. The black line is the residual which is the difference between the RHS and LHS in equation 4.1. Error bars are included on the total accumulated average model tendency profiles only at points where the 70% confidence intervals (Cavallo et al. 2016) do not cross zero, indicating the profile values are statistically different from zero.

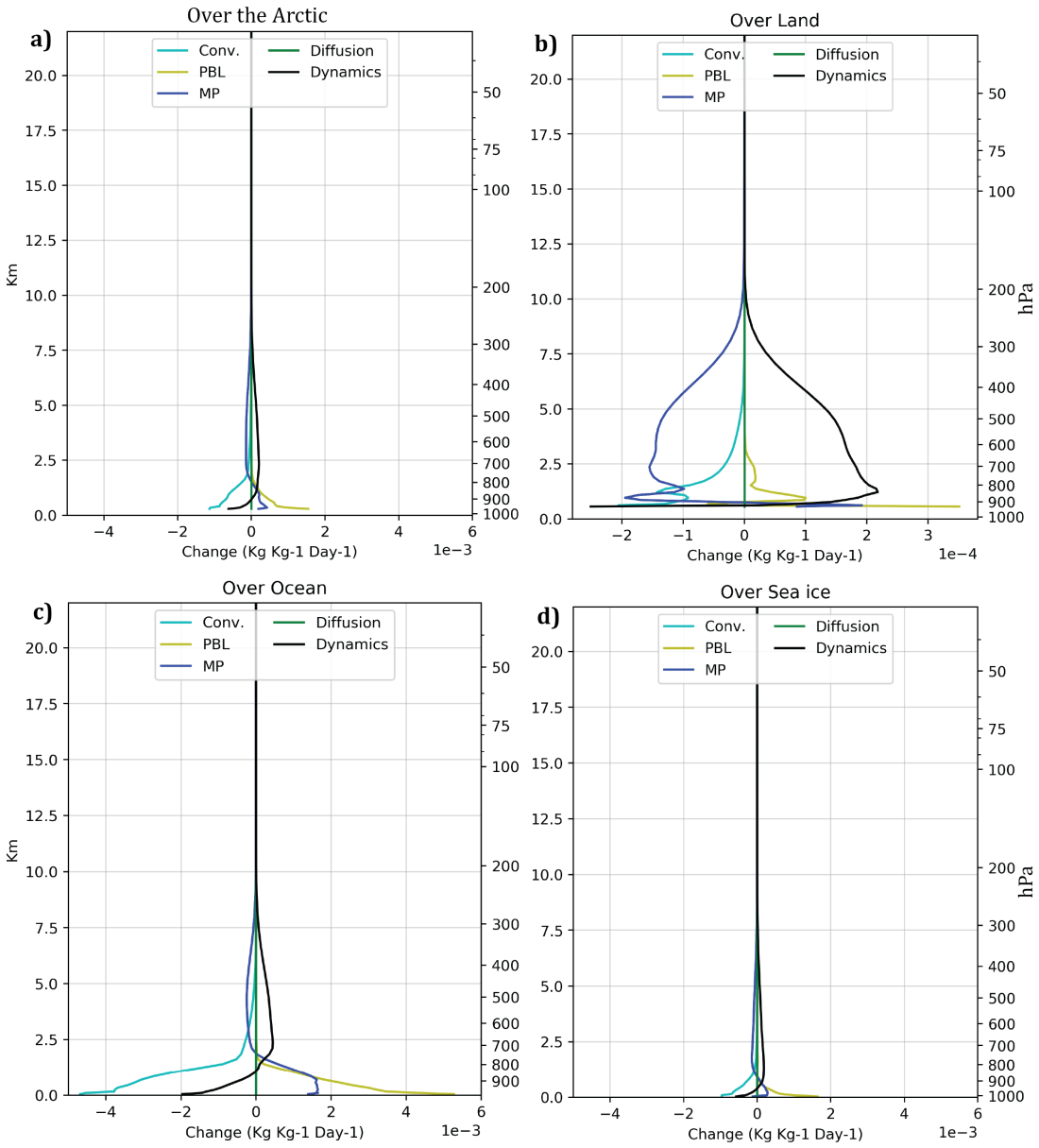

Figure 4.16: Experiment two spatially averaged accumulated model tendencies for water vapor (a) over the Arctic, (b) over land in the Arctic, (c) over ocean in the Arctic, and (d) over seaice in the Arctic. Each colored line represents a different physics tendency representing qv.

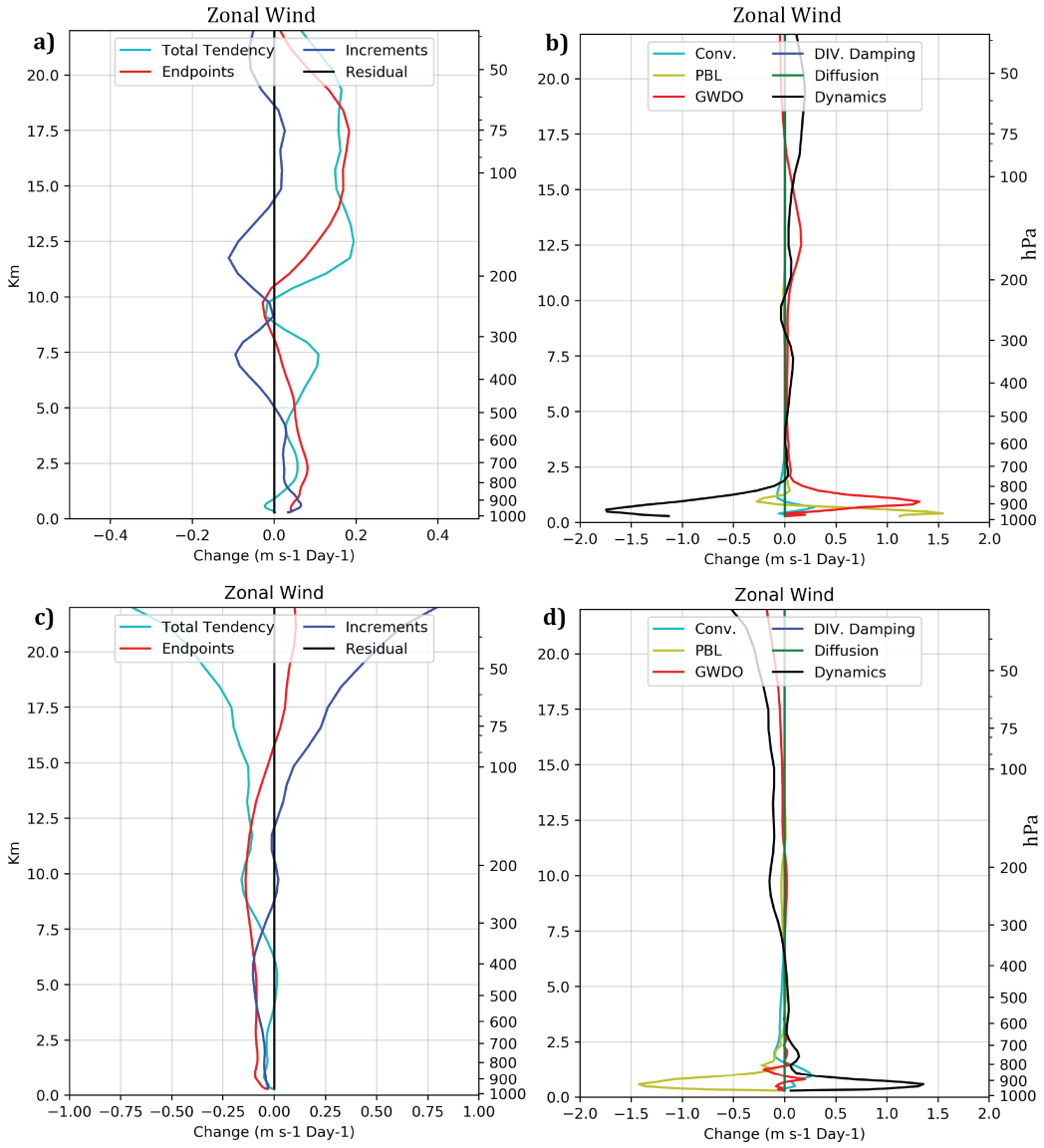

Figure 4.17: Arctic spatially averaged (a,c) MITA increment method and (b,d) accumulated model tendencies for zonal wind for (a,b) experiment one and (c,d) experiment two. (a,c) Each colored line represents a different term in equation 4.1. The black line is the residual which is the difference between the RHS and LHS in equation 4.1. Error bars are included on the total accumulated average model tendency profiles only at points where the 70% confidence intervals (Cavallo et al. 2016) do not cross zero, indicating the profile values are statistically different from zero. (b,d) Each colored line represents a different physics tendency representing the zonal wind.

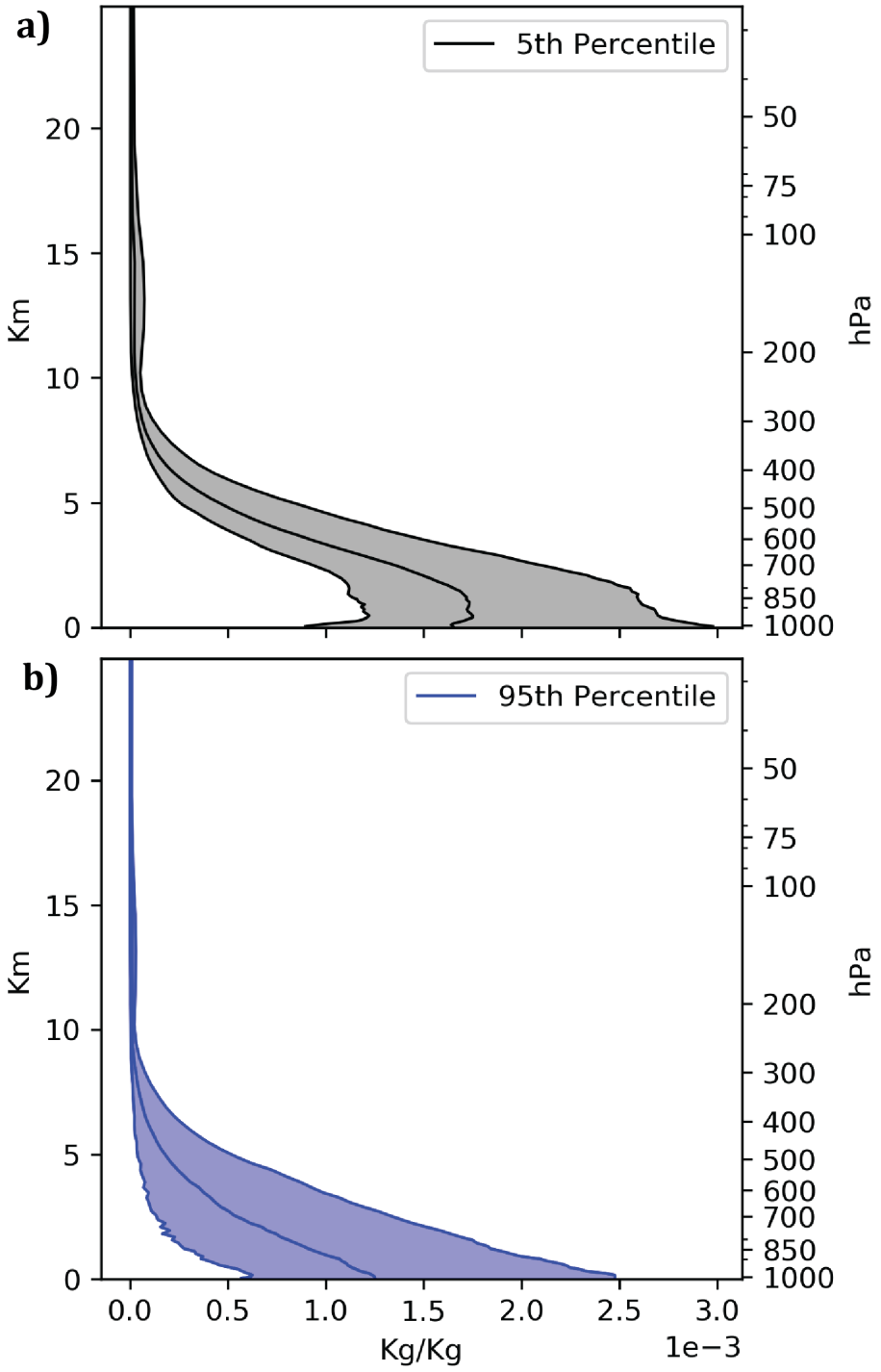

Figure 4.18: Water vapor profiles used to initialize WRF single column simulations. (a) Represents an increase in water vapor while (b) represents a decrease in water vapor. Shading represents distribution of water vapor within the profiles.

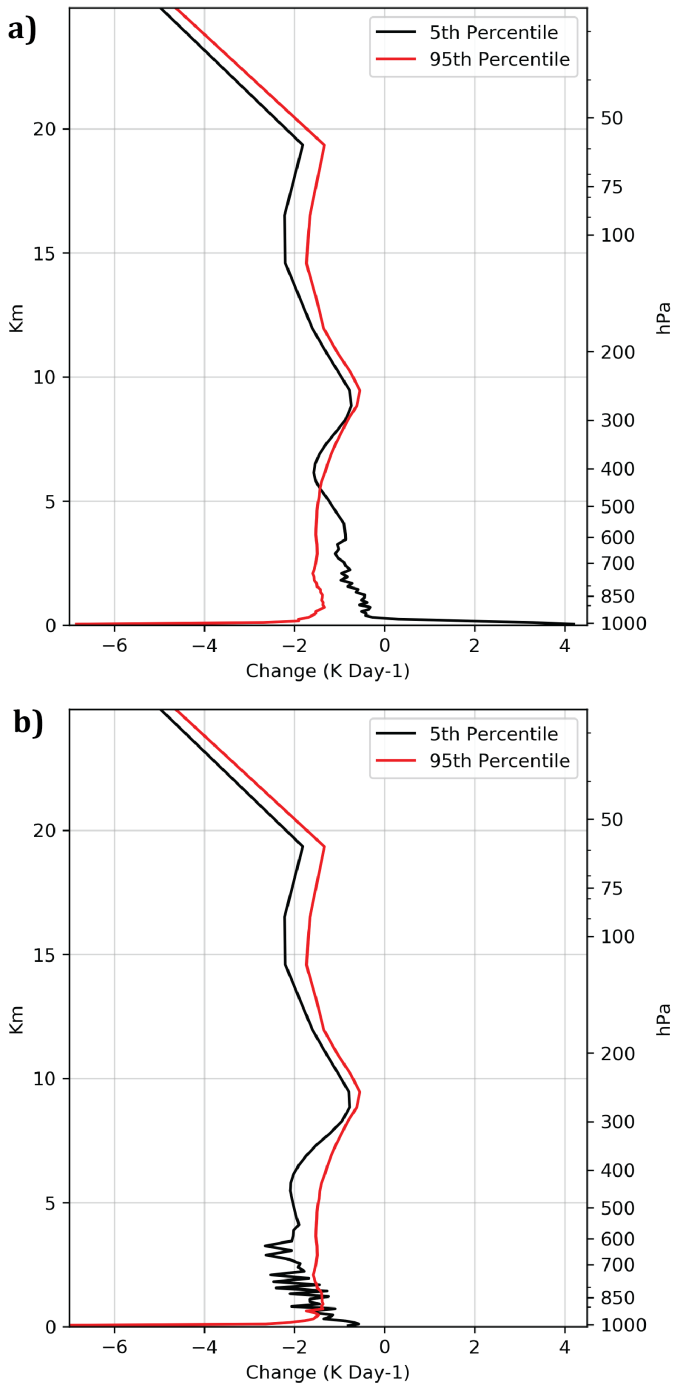

Figure 4.19: WRF single column model (a) accumulated total tendencies and (b) accumulated longwave radiation tendency averaged over 105 sea ice grid points spanning experiment one cycling period. Shading represents 95% of the adjusted water vapor distribution. The solid lines represent the mean of the adjusted water vapor distribution.

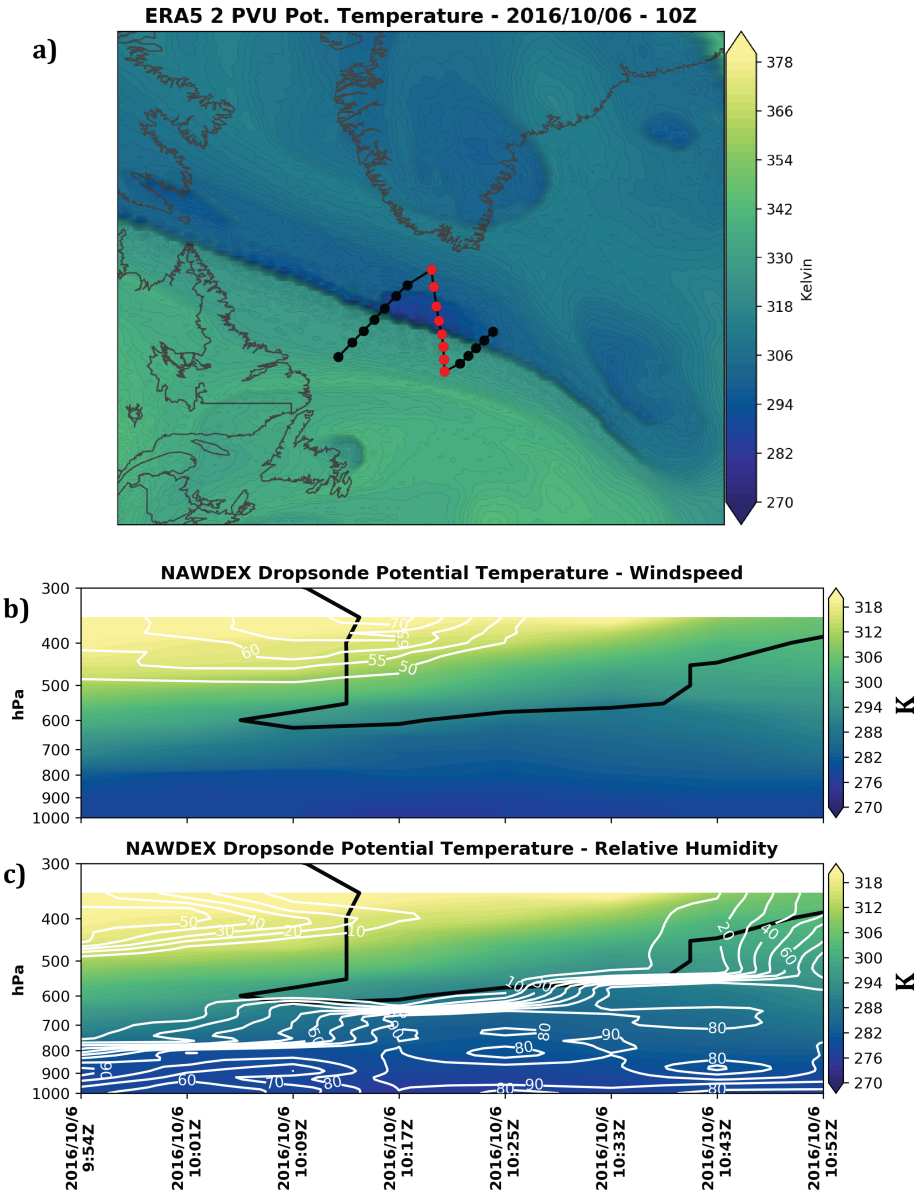

Figure 4.20: (a) Black line with dots represents the flight path through TPV of interest. Red line with dots represents the dropsonde profiles used to time-height cross-sections. (b) Time-height cross-section showing dropsonde potential temperature (colorfill), ERA5 2 PVU surface (thick black line), and dropsonde wind speed (white contours). (c) Time-height cross-section showing dropsonde potential temperature (colorfill), ERA5 2 PVU surface (thick black line), and dropsonde relative humidityy (white contours).

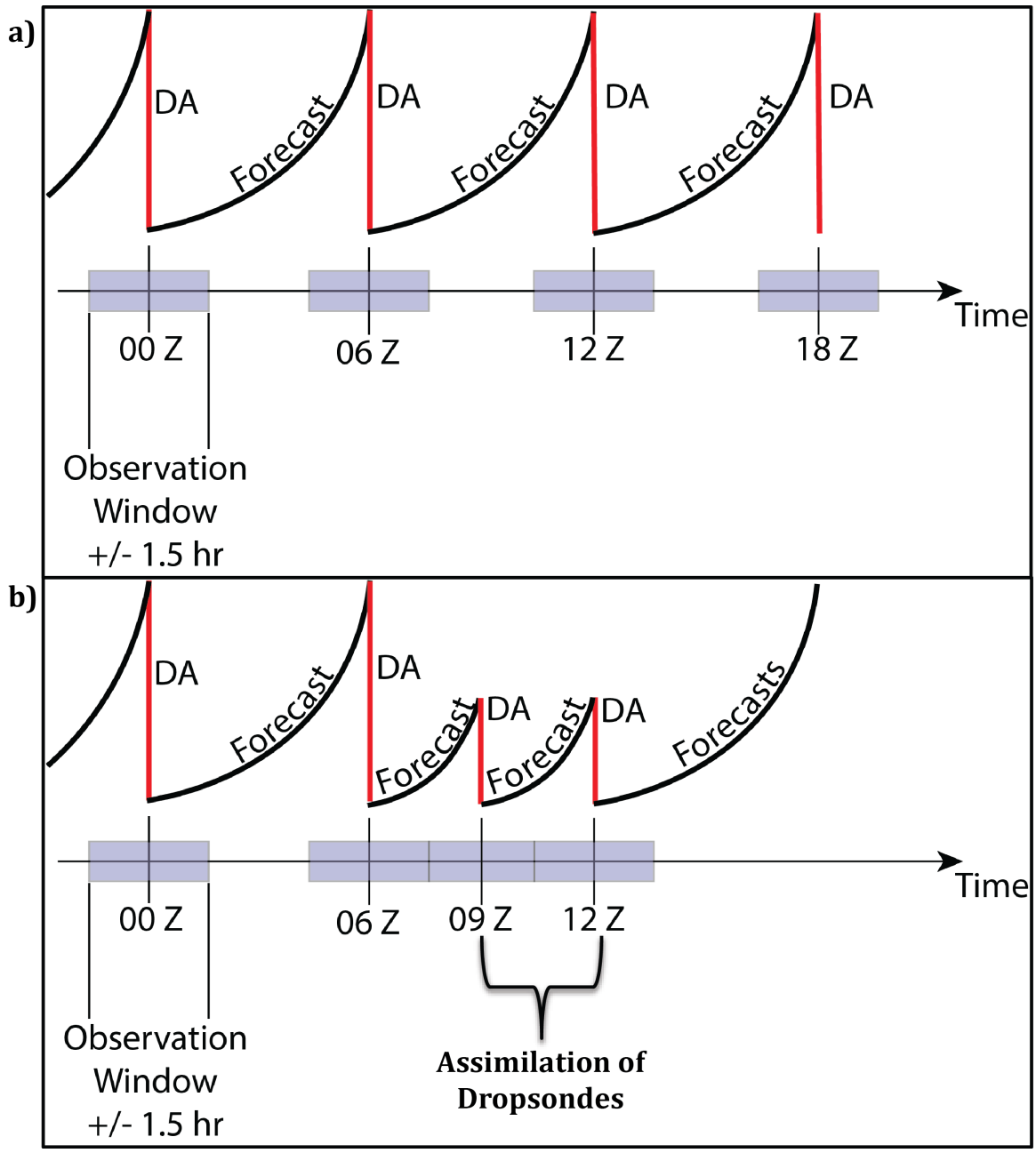

Figure 4.21: Schematics showing MPAS-DART cycling procedures for (a) without NAWDEX observations assimilated and (b) when NAWDEX observations are assimilated. The black lines correspond to MPAS forecasts while the red lines are the data assimilation step. The shaded boxes represent the observation window.

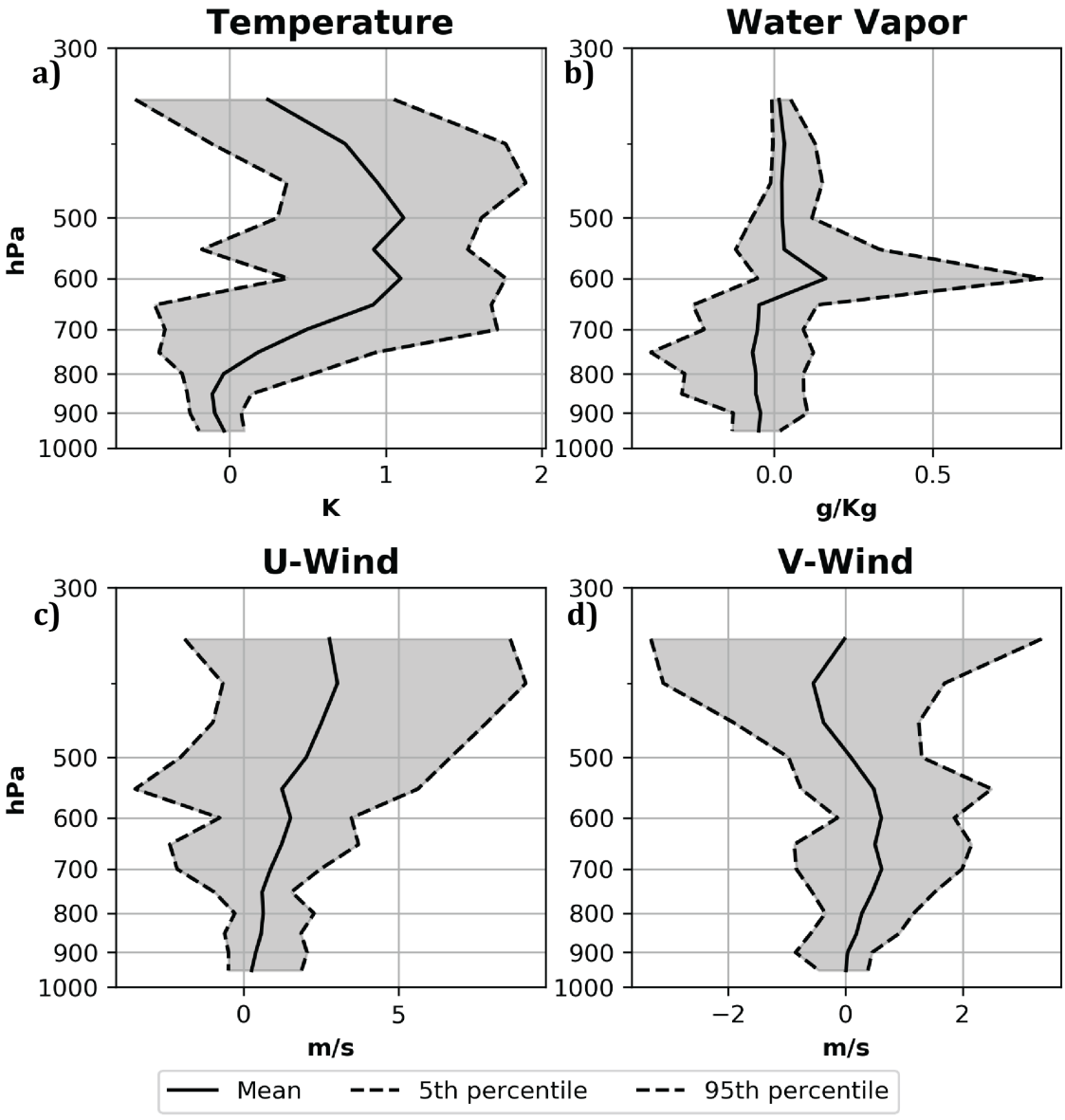

Figure 4.22: Analysis increment associated only from NAWDEX dropsonde (a) temperature, (b) water vapor, (c) zonal-wind, and (d) meridional wind.

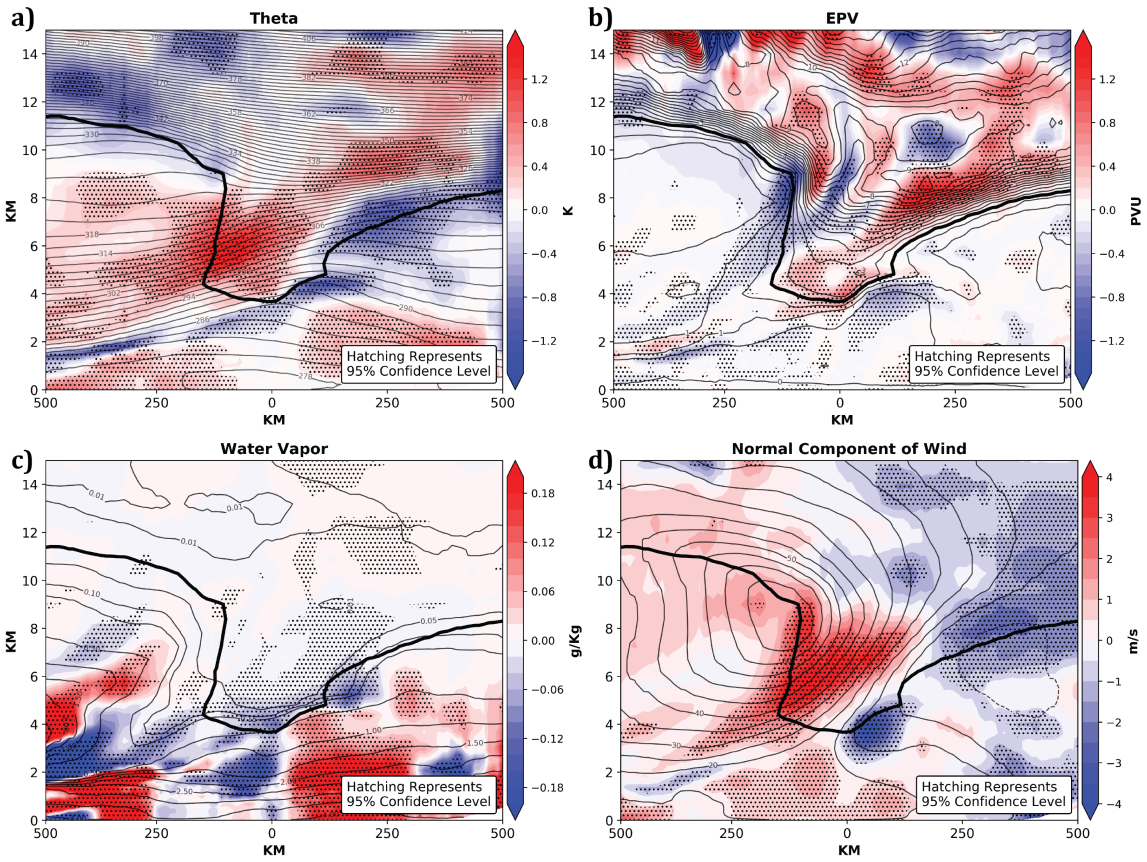

Figure 4.23: TPV composite cross-section differences between experiments with NAWDEX dropsondes versus without NAWDEX dropsonde observations for (a) potential temperature, (b) Ertel's potential vorticity (EPV), (c) water vapor, and (d) normal component of wind (positive values correspond to wind coming out of page).

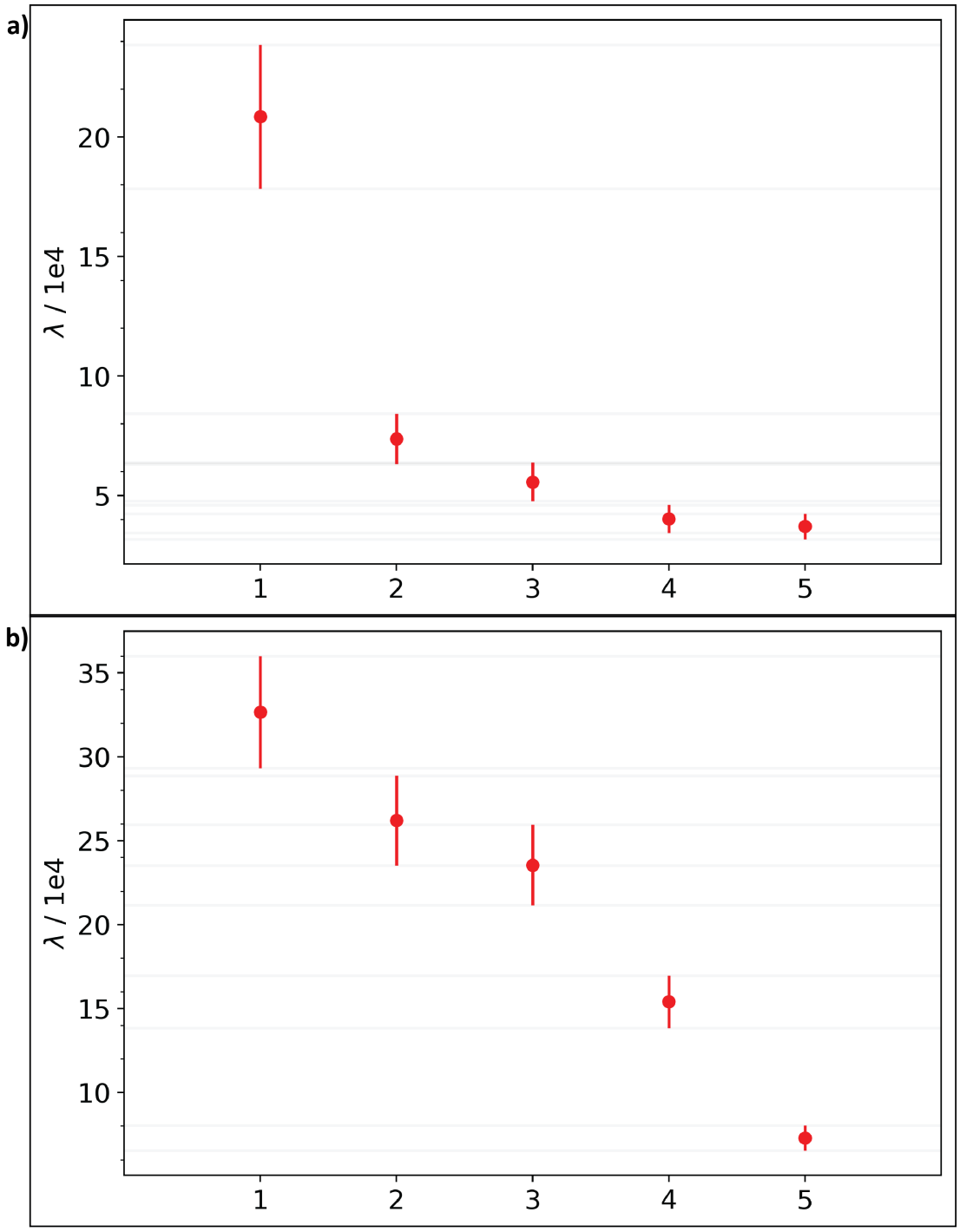

Figure 4.24: Eigenvalue spectrum's for (a) spatial EOF analysis and (b) NAWDEX TPV Multivariate EOF (MVEOF) analysis. The calculation of the eigenvalue spectrum follows the equations in North et al. (1982).

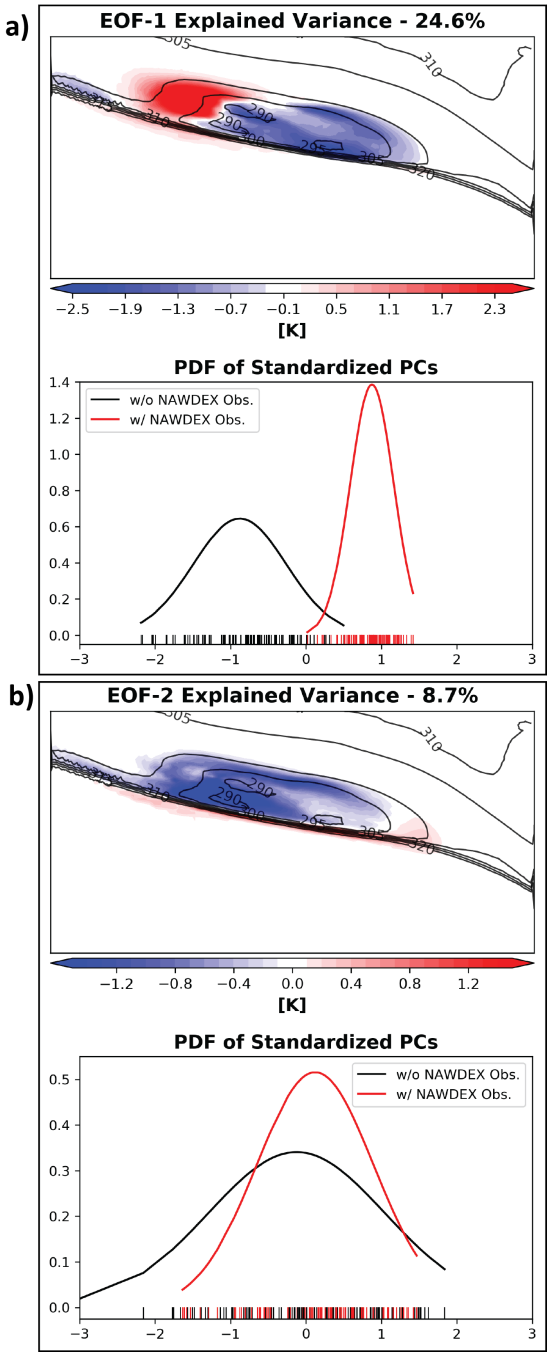

Figure 4.25: EOFs (a) 1 and (b) 2 of the 2 PVU potential temperature analysis field for the NAWDEX TPV for both experiments with NAWDEX dropsondes assimilated and without NAWDEX dropsonde assimilated. Proability density functions (PDF) are computed for each experiments PCs.

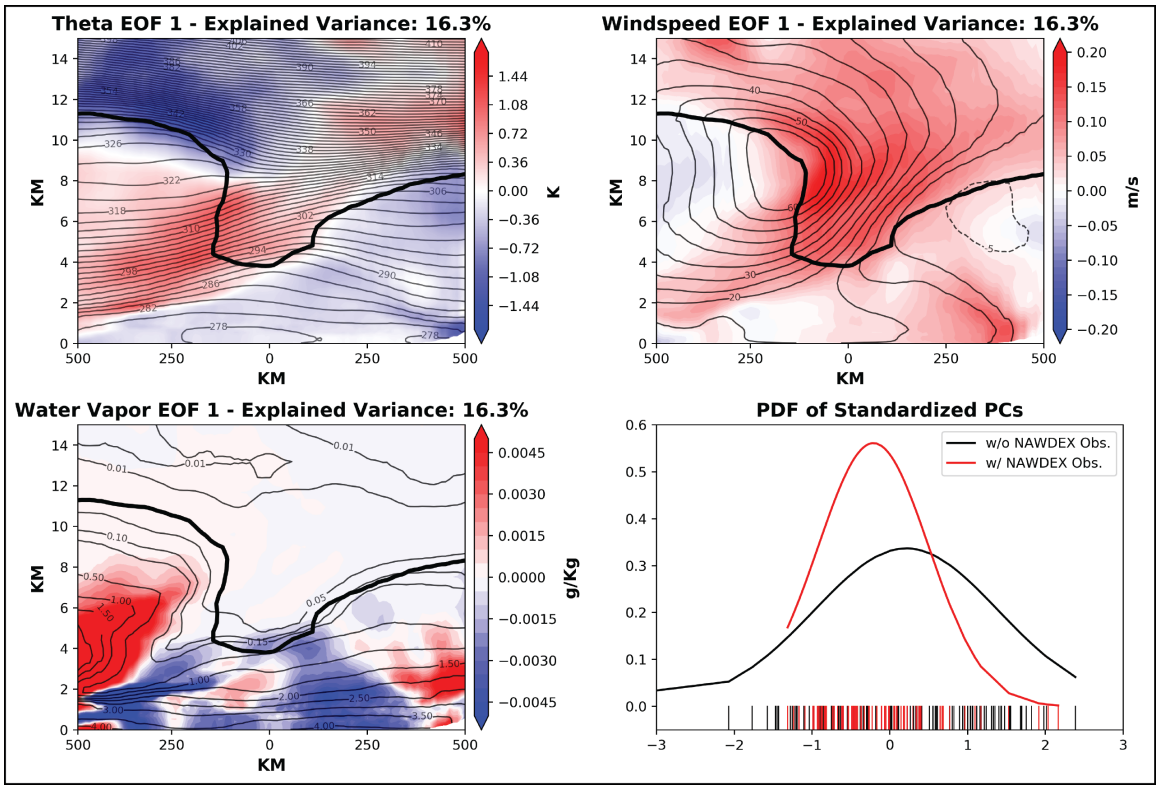

Figure 4.26: Multivariate EOF 1 that contains cross-section analysis potential temperature, normal component wind speed, and water vapor for both experiments with NAWDEX dropsondes assimilated and without NAWDEX dropsonde assimilated.

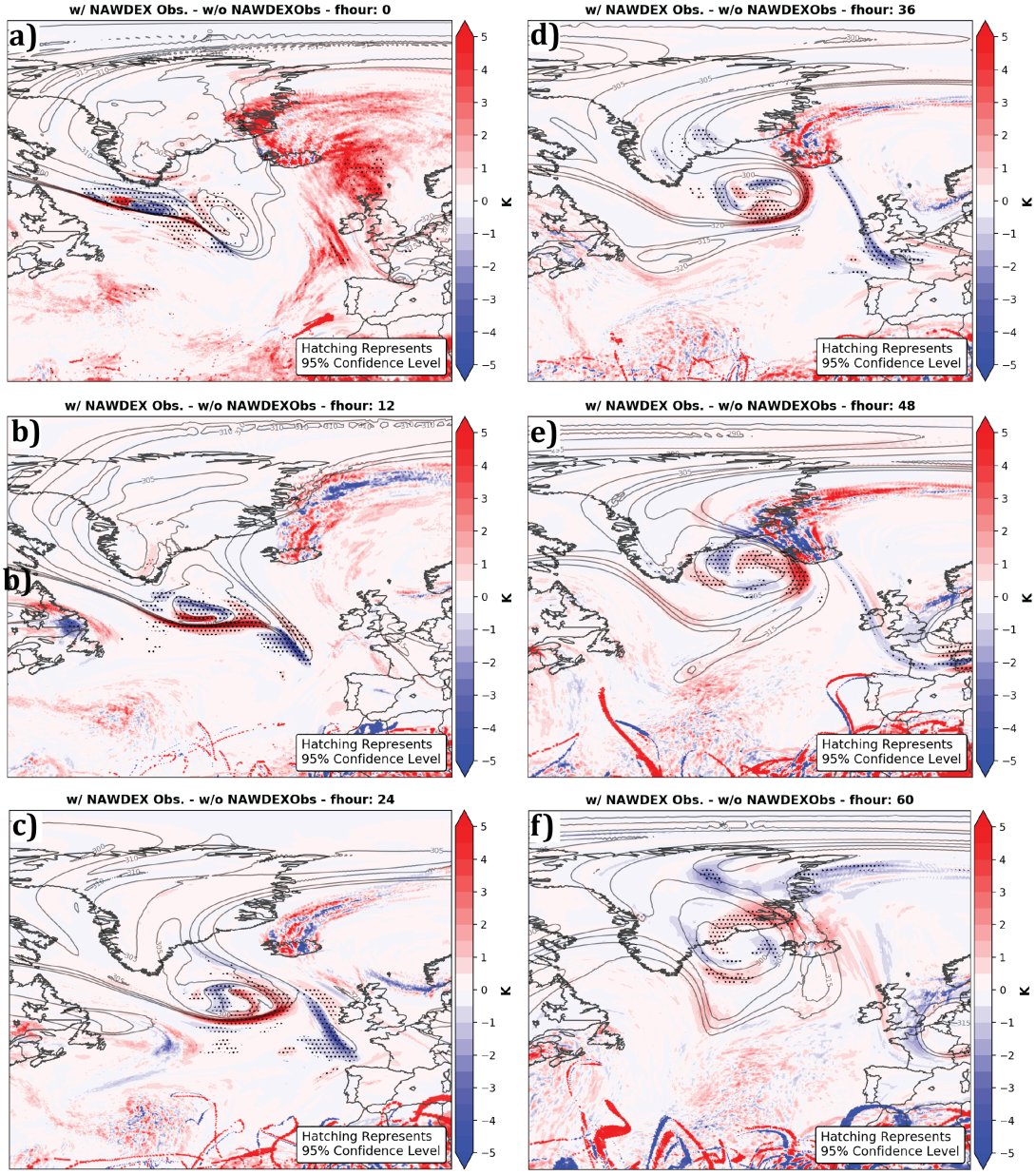

Figure 4.27: 2 PVU potential temperature differences between experiments with NAWDEX observations assimilated vesus without NAWDEX observations assimilated valid at forecast hour (a) 0, (b) 12, (c) 24, (d) 36, (e) 48, and (f) 60. Hatching represents significant differences at the 95% confidence level. Significance testing was calculated using a student t-test. The grey contours are ensemble mean 2 PVU potential temperature from the experiment where NAWDEX observations were assimilated.

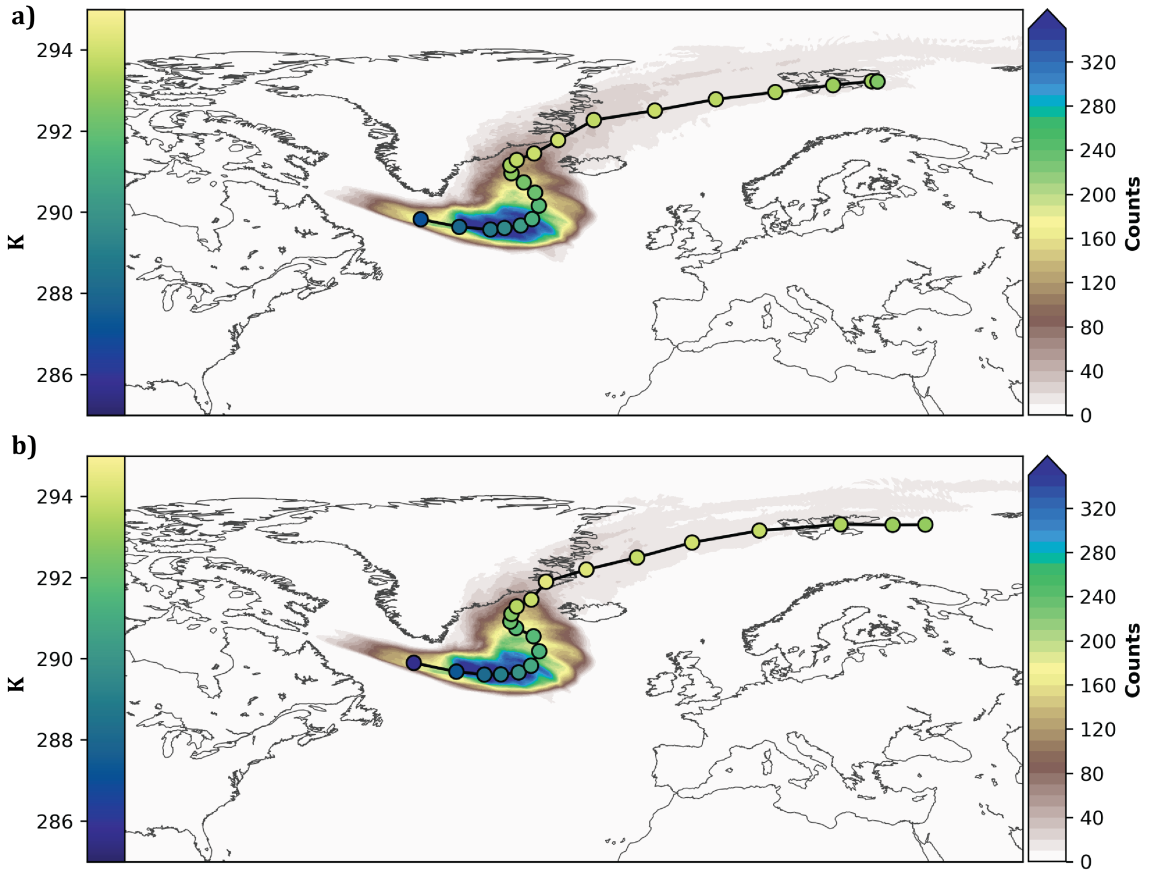

Figure 4.28: TPV counts (colorfill), median track position (black line), and median minimum potential temperature associated with tpv (colored dots) for the 96 realization of the NAWDEX TPV for experiments (a) with NAWDEX dropsondes assimilated and (b) without NAWDEX dropsondes assimilated.

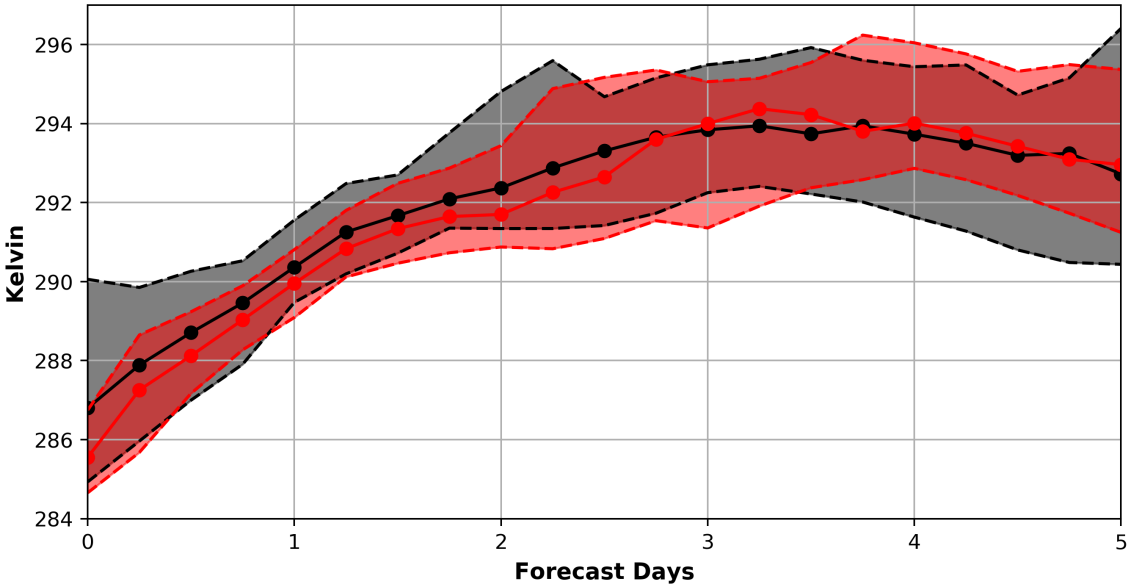

Figure 4.29: Potential temperature distribution throughtout the forecast for the NAWDEX TPV for experiments with NAWDEX dropsondes assimilated (red) and without NAWDEX dropsondes assimilated (black). The shading shows the range of 95% of the potential temperature distribution and the dotted line is the median of the potential temperature distribution.

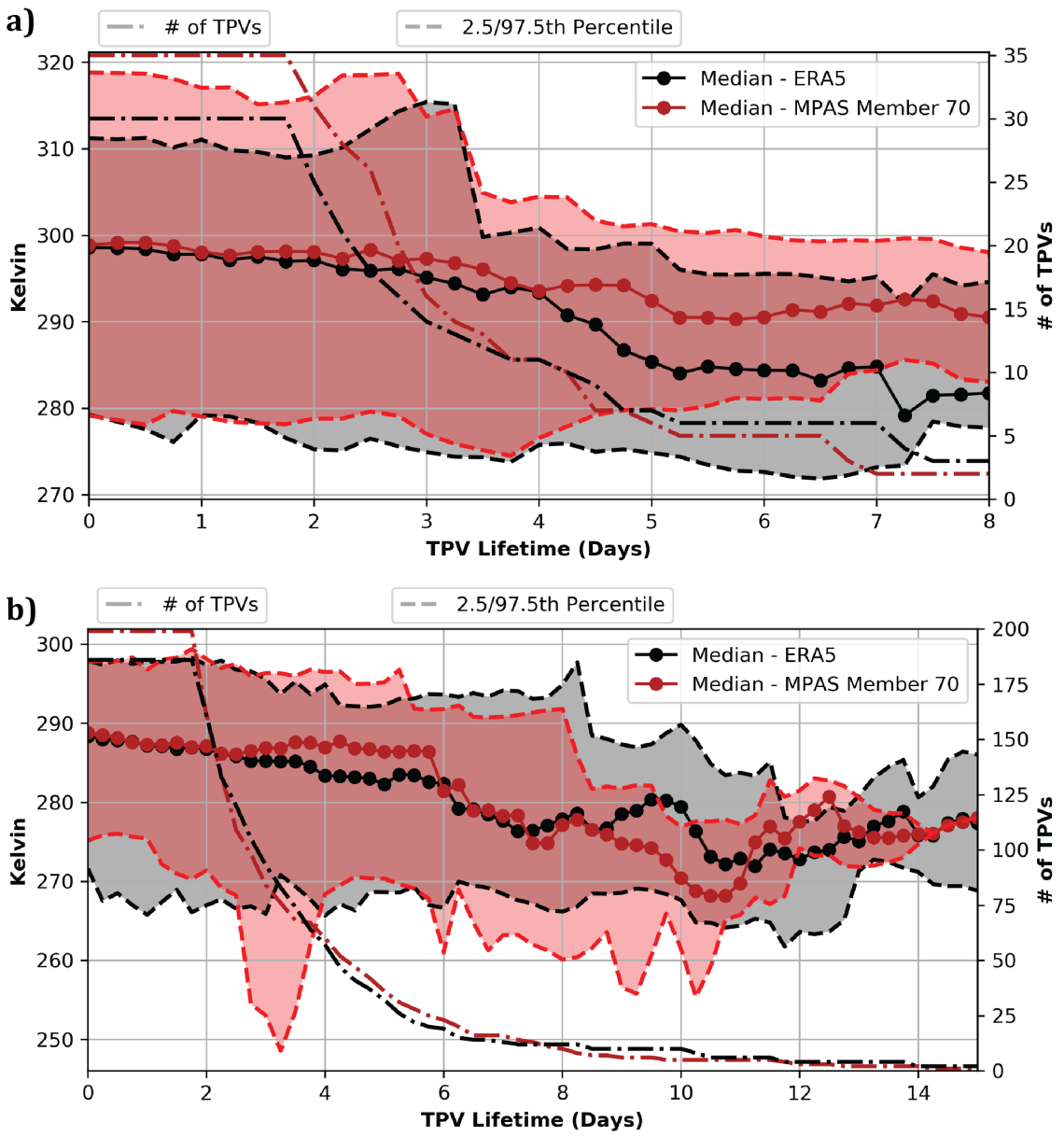

Figure 4.30: MPAS-DART member 70 and ERA5 TPV characteristics for TPV tracks spanning the entire cycling period for (a) experiment one and (b) experiment two. Time series shows median TPV potential temperature (lines with dots), spread in the potential temperature associated with TPVs (shading), and number of TPVs that last some lifetime (dot-dashed line, values on the y-axis). MPAS-DART member 70 TPV tracks were computed using 6-hour forecasts while ERA5 TPV tracks were computed using analyses.

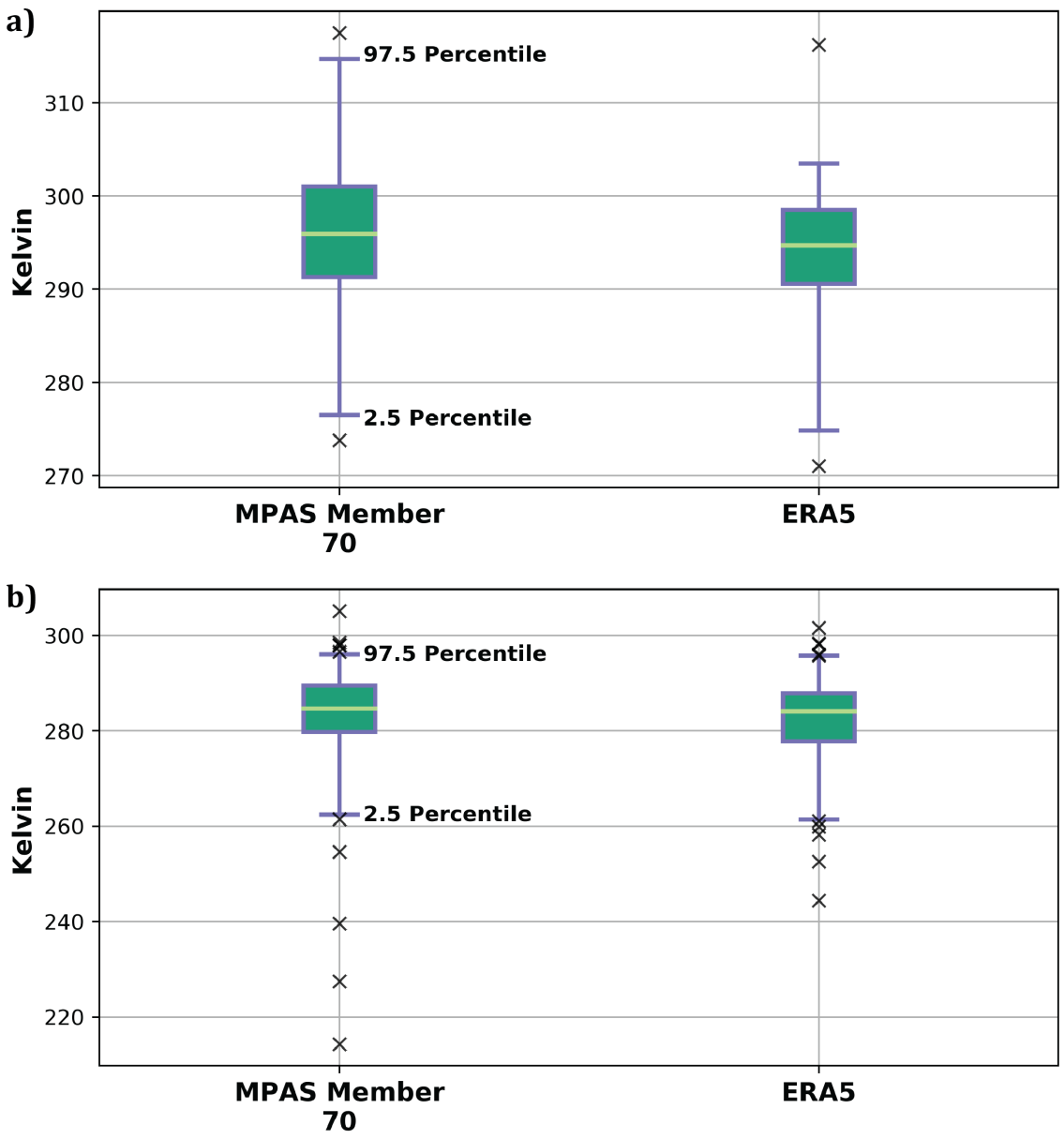

Figure 4.31: MPAS-DART member 70 and ERA5 TPV characteristics for TPV tracks spanning the entire cycling period for (a) experiment one and (b) experiment two. Box and whisker plot shows minimum potential temperature for each TPV that last longer that two days. MPAS-DART member 70 TPV tracks were computed using 6-hour forecasts while ERA5 TPV tracks were computed using analyses.

Chapter 5

TPV and Rossby Wave Initiation Case Study

5.1 Introduction

The forecast skill of global models has increased over the mid-latitudes in recent decades (Yang 2017). However, few studies have focused on the ability of global models to predict the Arctic region. Those studies have focused on the seasonal averaged forecast skill in the Arctic and initially found low scores compared to the mid-latitudes, but in recent years, Arctic skill scores have gradually increased to those found in the mid-latitudes (Jung and Matsueda 2016). However, daily anomaly correlation coefficient (ACC) scores remain more variable in the Arctic compared to the mid-latitudes with more ACC scores dropping to below 0.6 (Fig. 1.3). Understanding impacts of Arctic predictability on mid-latitude on mid-latitude forecast skill could improve lead-times of skill over the mid-latitudes (Francis and Vavrus 2012; Jung et al. 2014; Francis and Vavrus 2015; Semmler et al. 2016). Jung et al. (2014) found that nudging the Arctic region towards reanalysis during forecast integration reduces forecast errors over the mid-latitudes at later forecast lead times. More recent work expanding on Jung et al. (2014) found the largest reduction in forecast error in the mid-latitudes occurs over Northern Asia (Semmler et al. 2018). The reduction in RMSE could imply that a dominant pathway exists for features to leave the Arctic and impact mid-latitude weather. While there are different processes, both Arctic and non-Arctic related, that could be impacting the forecast skill in this region, one common Arctic feature that can migrate into the mid-latitudes and interact with weather systems is the TPV (Fig. 5.1). Previous chapters evaluate the ability of the NWP model within the cycling system to represent TPVs in both analysis and forecasts (t-5 to t=0 in Fig. 5.1). This chapter will investigate the impacts TPVs can have on the generation of Rossby waves (t=0 and beyond in Fig. 5.1).

Rossby wave initiation and propagation has been studied extensively throughout the literature. Chapter 1 provides a more in depth look at some of those studies. Most studies focus on the equatorward side of the jet stream, where upper-tropospheric negative PV anomalies primarily form as a result of diabatic processes associated with large convective systems (Rodwell et al. 2013), warm conveyor belts of extra-tropical cyclones (Madonna et al. 2014; Martínez-Alvarado et al. 2016), or recurving tropical cyclones (Archambault et al. 2013; Grams and Archambault 2016). Fewer studies focus on the poleward side of the jet where PV anomalies are located (Kew et al. 2010; Davies and Didone 2013; Röthlisberger et al. 2018). An isolated positive PV anomaly located near the jet stream could act to perturb the jet stream and initiate a Rossby wave on the nearby enhanced PV gradient (Davies and Didone 2013). The strength of the Rossby wave response would depend on strength and scale of the PV anomaly along with the location relative to the jet (Schwierz et al. 2004b). Poleward PV anomalies, the focus of this study, can result from wave breaking (Martius et al. 2010) or from TPV generation processes. Perturbations to the jet stream associated with a poleward PV anomaly can lead to surface cyclogenesis (Kew et al. 2010). Röthlisberger et al. (2018) describes four important ingredients for a wintertime rossby wave initiation (RWI): 1) PV anomaly approaching the jet on the poleward side around time of RWI, (2) moisture transport leading to latent heat release which creates a negative PV anomaly on southern side of the jet, (3) baroclinic structure with a surface low forming downstream of a PV anomaly, and (4) an amplified downstream ridge with enhanced deformation once RWI has started. However, the study does not conclude which of the four ingredients is dynamically dominant in the RWI events, leading to the conclusion that some combination of the ingredients must be important. The present study will investigate the impacts of different TPV characteristics on RWI and the sensitivities of the downstream forecasts.

5.2 Methods

Rossby wave packet identification datasets have been produced using different feature-based techniques which would include RWI events (Glatt and Wirth 2014; Souders et al. 2014; Grazzini and Vitart 2015). This study will use the RWI dataset produced by Röthlisberger et al. (2016). RWIs were identified by geometric changes in the 2 PVU surface contour on different isentropic levels (Röthlisberger et al. 2016). The highest frequency of RWIs is over the North Pacific during the wintertime (Fig. 5.2). There is also RWI frequency over the North Atlantic in most seasons (Fig. 5.2).

Starting from the RWI dataset, TPVs are identified which were located near the RWI events in order to identify our case study. Forecast sensitivities associated with TPVs and other large-scale characteristics are investigated through the use of ensemble sensitivity analysis (ESA; Hakim and Torn 2008). The formulation of ESA uses linear relations and gaussian statistics (Hakim and Torn 2008). For a given ensemble size M, the original expression for ESA is a linear regression of M sized forecast metrics to M sized state variables, where the forecast metric is the dependent variable and the state variable is the independent variable (Torn and Hakim 2008),

$$\frac{\partial J}{\partial x} = \frac{cov(\mathbf{J},\mathbf{x})}{var(\mathbf{x})}. \tag{5.1}$$

From equation 5.1, $\mathbf{J}$ is the forecast metric and $\mathbf{x}$ is the state variable for $1 \times M$ ensemble estimates. Furthermore, *cov* denotes the covariance of $\mathbf{J}$ and $\mathbf{x}$ while *var* represents the variance of $1 \times M$ state variables. Using this formulation, the linear regression describes how the forecast metric (dependent variable) is changing as the state variable (independent variable) is changing and carries the units of the forecast metric over the state variable. In more recent studies, the ESA formula is modified to divide by both the standard deviation of the forecast metric and state variable (Chang et al. 2013; Zheng et al. 2013), to provide the following equation for the sensitivity,

$$\text{“sensitivity”} = \frac{cov(\mathbf{J},\mathbf{x})}{\sqrt{var(\mathbf{J})}\sqrt{var(\mathbf{x})}}. \tag{5.2}$$

This sensitivity is dimensionless and is equal to the correlation between the forecast metric and the state variable. Another way to interpret equation 5.2 is as sensitivity computed for forecast metrics with the variance normalized (Chang et al. 2013).

This study employs the correlation form of ESA (eq. 5.2), which is defined as "sensitivity" for this rest of this study. ESA has been applied to many different research problems which includes sensitivities to initial conditions (Torn and Hakim 2009), extra-tropical cyclones (Torn and Hakim 2009; Chang et al. 2013; Zheng et al. 2013), precipitation forecasts (Torn and Hakim 2008), African easterly waves (Torn 2010), and mesoscale convection forecasts (Bednarczyk and Ancell 2015; Hill et al. 2016). Statistical significance of the calculated sensitivity is computed using a t-test with the null hypothesis that there is no linear relationship between the forecast metric and the state variable (correlation is zero). This study computed sensitivity values over the entire domain, but will highlight regions where statistical significance is achieved at the 95% confidence interval. In this study, the multiple instances of ESA are used with varying forecast metric (**J**)–state variable (**x**) pairs: analysis TPV intensity–250 hPa windspeed; analysis TPV position–250 hPa windspeed; TPV intensity–250 hPa height; analysis TPV position–250 hPa height; analysis TPV position–precipitable water; analysis TPV position–poleward moisture flux; minimum sea level pressure–320 K PV; minimum sea level pressure–320 K windspeed; minimum sea level pressure–preicipitable water; minimum sea level pressure–poleward moisture flux.

When using ESA, a forecast metric must be chosen. Various forecast metrics are employed in previous studies, but all usually include taking a statistical measure (e.g. average, max, min, etc) over a defined area in the region of interest (Torn and Hakim 2008; Chang et al. 2013). A recent approach combines ESA with EOF analysis to investigate the forecasts sensitivities associated with the dominant modes of variability (Zheng et al. 2013). For this study, forecast sensitivities associated with different TPV characteristics are evaluated. Using a watershed TPV tracker (Szapiro and Cavallo 2018), two metrics are computed to test their sensitivities in forecasts: TPV intensity and position. TPV intensity

is defined as the minimum potential temperature associated with the TPV of interest, while the position of the TPV is computed as distance from TPV center to the jet stream. These metrics provide a method to test the impacts of both TPV position and intensity on downstream development of RWI. Furthermore, investigation of sensitivities of forecast surface low pressure development to upstream PV features is considered for two different time periods. Minimum forecast surface low pressures are calculated for the different ensemble members over a specified region, described below.

To select an individual RWI event for this case study, only wintertime North Pacific events are considered. This ensured the maximum number of events to be considered since the North Pacific had the most RWI events (Fig. 1.4). Combining the RWI dataset with TPV tracks, the distance between RWI events and the closest TPV is calculated. To be considered, TPV genesis had to start north of 65°N latitude. Composites centered on RWI events show both a more enhanced negative anomaly in 2 PVU potential temperature and larger increase in windspeed when TPVs are close (within less than 1000 km) versus when they far (more than 2500 km) away (Fig. 5.3). When TPV are far away the pattern in potential temperature anomalies and the shift in windspeed max resembles a wave breaking pattern which may be the reason the RWI was identified. Furthermore, the probability of a TPV associated with a RWI event is higher in the wintertime over the North Pacific as compared to summer (Fig. 1.4). Lastly, RWI events identified before 2008 could not considered for this case study since GEFS forecasts used for ensemble initialization are not available. Applying a 1000 km threshold for distance between RWIs and TPVs (e.g., considering only "close" cases) leaves 97 cases for consideration. Periods when no surface cyclone is present and periods where forecast skill remained high are not considered. Out of the remaining dates, the RWI event chosen for this study occurred on 31 December 2011 at 00z. MPAS-DART forecasts are produced starting 12 hours prior to the identified RWI (i.e., 31 December 2011 at 12z), which allows MPAS-DART to model the evolution of the RWI-TPV interaction. Five-day forecasts are produced for all 96 ensemble members.

5.3 RWI Case Study Description

The evolution of the RWI event chosen for this case study is investigated with ERA5 analyses (Fig. 5.4). Twelve hours prior to the RWI event, a TPV was situated just to the northeast of Japan, and the zonal jet appears relatively undisturbed (Fig. 5.4 a). At the time of the RWI event, small undulations in the 2 PVU potential temperature surface formed along with a more northerly component to the wind in the location of the RWI (Fig. 5.4 b). The undulations in the 2 PVU potential temperature surface started to intensify while a surface low pressure system began to develop 24 hours after RWI occurred (Fig. 5.4 b-d). The surface low pressure system associated with the RWI continued to deepen until it reached a minimum pressure of around 970 hPa at 72 hours after the RWI (Fig. 5.4 e-h). Furthermore, a second TPV formed over Siberia and slowly progressed towards the jet stream, which led to the formation of a second surface pressure system apparent on 3 January 2012 at 00z (Fig. 5.4). The interaction of the Siberia TPV and jet stream produced a RWI event, which is captured with the RWI dataset.

In order to evaluate whether MPAS-DART forecasts produce a reasonable evolution of this event, the following diagnostics are chosen: 2 PVU potential temperature and wind, and mean sea level pressure. Evaluations are performed with respect to ERA5. Three MPAS-DART ensemble members are excluded due to these members not identifying the 2 PVU surface but identifies spurious features in MPAS potential vorticity near the model top being instead.

At analysis time, the ensemble mean position and strength of the TPV of interest in MPAS-DART is very similar to that found in ERA5 (compare Fig. 5.5 a to Fig. 5.4 a). Furthermore, the position and shape of the zonal jet is similar between ERA5 and MPAS-DART analyses. However, differences in analyses become apparent near the US continent. The ERA5 2 PVU potential temperature analysis shows a trough just off the California coast which does not appear in MPAS-DART ensemble mean (compare Fig. 5.5 a to Fig. 5.4 a). The misrepresentation of the trough in the MPAS-DART analyses could be related to

the mesh transition zone of coarser resolution located in that region (Fig. 2.7). Regardless, the MPAS-DART representation of the TPV of interest matches the ERA5 analysis reasonably well in the higher resolution mesh region near the time of the RWI event (compare Fig. 5.5 b to Fig. 5.4 b).

At the time of the RWI, forecast differences in the mean sea level pressure field become apparent downstream of the RWI, where ERA5 shows lower surface low pressures than MPAS-DART (compare Fig. 5.5 b to Fig. 5.4 b). Differences in sea level pressure is likely related to the same misrepresentation of the trough just west of California discussed above. The MPAS-DART evolution of the RWI is captured relatively well by MPAS-DART but timing of the surface low pressure development associated with the RWI differs slightly with ERA5 (compare Fig. 5.5 c-e to Fig. 5.4 c-e). Furthermore, the continued deepening of the surface low pressure in MPAS-DART is not as intense as what is shown in the ERA5 analyses (compare Fig. 5.5 f-h to Fig. 5.4 f-h). While some differences exist between MPAS-DART and ERA5, overall the MPAS-DART forecasts simulate the evolution of the fields reasonably. Lastly, evaluation of the ensemble's spread-skill relationship is completed to determine the spread is capturing enough uncertainty. Profiles of the spread-skill relationship was evaluate against observations back in Chapter 3 where there was good agreement between RMSE and total spread within MPAS-DART 6-hour forecasts throughtout the cycling. For these particular forecasts, the spread-skill relationship is in agreement for the early forecast times but the agreement disappears as forecast time increase to around 1.5 days (Not Shown). The RMSE within the forecasts grow quicker than the ensemble, meaning our ensemble becomes under-dispersive as forecast hours grow. Even so, the quality of the ensemble remains good up to 2 days which is the maximum length of a forecast used for ESA calculations.

Next, a comparison of the structures associated with the TPV of interest are evaluated for both MPAS-DART and ERA5. Cross-sections are computed through the middle of the TPV from ERA5 and MPAS-DART ensemble mean analysis fields (Fig. 5.6). In ERA5,

the TPV extends down to around 700 hPa and the circulation associated with the TPV is captured relatively well (Fig. 5.6 a). In MPAS-DART, the TPV also extends down to around 700 hPa but the circulation associated with the TPV is less well represented (Fig. 5.6 b). The distance of the TPV to the jet stream, situated around 200 hPa, is similar between MPAS-DART and ERA5 (compared Fig 5.6 b to Fig 5.6 a). Furthermore, there is evidence of a jet superposition present in both MPAS-DART and ERA5, which is the vertical stacking of the subtropical and polar jet stream (Defant and Taba 1957; Winters and Martin 2014). The chosen case of interest is located in a region with high jet superposition event frequency (Christenson et al. 2017). Jet superposition is also apparent on the 2 PVU potential temperature surface, which is highlighted by the enhanced potential gradient located equatorward of the TPV of interest in both MPAS-DART and ERA5 (Figs. 5.5 and 5.4). The enhanced 2 PVU potential temperature gradient near the TPV of interest could result in a nearly vertical tropopause structure extending from the polar to the subtropical tropopause (Winters and Martin 2014). Overall, the vertical structure is in good agreement between the two modeling systems.

Evaluation of the RWI event indicates two areas well-suited for investigation of forecast sensitivities using ESA. The first evaluation period focuses on TPV characteristics, including intensity and position relative to the jet stream, and their impacts on the development of the RWI (Fig. 5.7 a). This evaluation period spans 30 December 2011 at 12z to 31 December 2011 at 6z which captures TPV evolution leading up to the RWI. The second evaluation period focuses on the formation of the surface low pressure that develops downstream of the RWI. This evaluation period spans 31 December 2011 at 00z (time of RWI) to 1 January 2012 at 12z. ESA is performed on all above-listed pairs which use minimum sea level pressure as the forecast metric ($\mathbf{J}$) within a box around the region where the surface low develops (Fig. 5.7 b). The 2 PVU potential temperature surface is noisy due to interpolation issues, thus PV on the 320 K potential temperature surface (this level is coincident with the identified RWI) is used since it can act as a proxy for the location

of the TPV of interest. Connections between the development of the surface low pressure system and upstream characteristics of the PV and windspeed surface are investigated.

5.4 Results from Case Studies

Previous literature proposes that PV anomalies on the poleward side of the jet could induce a Rossby wave (Davies and Didone 2013). While some studies imply that TPVs could act to induce Rossby waves (Röthlisberger et al. 2016, 2018), no studies to-date have evaluated it from the TPV framework (2 PVU potential temperature). The first evaluation period focuses on TPV characteristics in the MPAS-DART analyses and their impacts on Rossby wave development downstream (Fig. 5.5 a). TPV minimum potential temperature and distance between the TPV and jet stream are evaluated (Fig. 5.8). These TPV characteristics are computed for each analysis ensemble member, excluding the 3 aforementioned members. The average TPV minimum potential temperature across ensemble members is $\sim$275 K with individual member values from 273 to 279 K (Fig. 5.8 a). The average TPV-jet stream distance is $\sim$1000 km and ranges from 500 km to 1200 km (Fig. 5.8 b).

Sensitivities of wind speed and height forecasts at 250 hPa are now investigated, since the maximum in the jet stream is situated at this level (Fig. 5.6 b). At analysis time near the TPV, there is a small region of significant negative correlation, which means lower TPV mimimum potential temperatures were associated with stronger 250 hPa wind speeds (Fig. 5.9 a). Lower TPV potential temperatures imply an enhanced the potential temperature gradient, and, in turn, increased wind speeds. Closer to the RWI event, the patterns of correlation became less organized and less significant suggesting there is not a linear relationship between TPV mimimum potential temperature and 250 hpa wind speed (Fig. 5.9 b-d).

For TPV-jet stream distance, there are significant negative correlations in the region around the TPV, meaning lower distances are associated with stronger 250 hPa wind speeds (Fig. 5.10 a). TPVs that are closer to the jet stream enhance the potential temperature

gradient, which, in turn, leads to stronger wind speeds. As time progresses towards the RWI event, the regions of significant negative correlation propagate downstream and are present up to the time of the RWI event (Fig. 5.10 b-d). In general, sensitivities of 250 hPa wind speeds forecasts to the TPV-jet stream distance are larger and have a longer-lasting impact than the sensitivities associated with TPV minimum potential temperature.

In the region of the RWI, greater 250 hPa heights are expected as the Rossby wave starts to grow. There are no significant correlations through the early forecast period when evaluating the sensitivity of the 250 hPa heights to TPV minimum potential temperature (Fig. 5.11 a-d). There is not a linear relationship between TPV minimum potential temperature and 250 hPa heights. In the evaluation of sensitivities associated with TPV-jet stream distance, there are small areas of significant correlations in the analysis time (Fig. 5.12 a). However, as forecast time increases there are growing significant negative correlations in the region downstream of the TPV and near the RWI event (Fig. 5.12 b-d). This implies that smaller TPV-jet stream distance in the analysis are connected to increased 250 heights downstream. The 250 hPa heights and wind speeds have similar forecast sensitivity to TPV-jet stream distances. Also, there is stronger association between the RWI event and TPV-jet stream distance than the RWI event and TPV minimum potential temperature. This suggests that the relative position of the TPV to the jet stream is more impactful on Rossby wave development, consistent with previous studies on PV anomalies (Schwierz et al. 2004a; Davies and Didone 2013). Lastly, TPVs that are close to the jet stream help enhance 2 PVU potential temperature gradient (and thus the vertical structure of PV), which is associated with an increase in wind speeds in a superimposed jet stream (Winters and Martin 2014). A stronger jet stream may intensify the horizontal and vertical motion associated with the ageostrophic circulation (Handlos and Martin 2016), leading to an enhancement of downstream high-impact weather (Defant 1959; Hoskins and Berrisford 1988; Winters and Martin 2014, 2016).

In the development of a RWI, moisture transport leading to latent release is one of the four critical ingredients (Röthlisberger et al. 2018). Moisture and poleward moisture flux sensitivities are investigated in relation to the TPV-jet stream distances, since that is where the largest significant sensitivities are found in 250 hPa heights and windspeed. Precipitable water is used to quantify the change in total column water vapor associated with distances between the TPV and the jet stream. Poleward moisture flux is computed as a product between 925 hPa meridional wind component v (cm s^{-1}) and the 925 hPa mixing ratio (kg kg^{-1}), which follows the method of Winters and Martin (2014). Precipitable water is not provided in the MPAS-DART analysis, so computed sensitivities start at forecast hour six. At forecast hour six, there is a small area of significant positive correlation just south of Japan and an area of significant negative correlation just east downstream of Japan (Fig. 5.13 a). As forecast hour evolves, the region of significant negative correlation persists while the region of significant positive correlation declines (Fig. 5.13 b-d). The significant negative correlation means shorter TPV-jet stream distances may result in an increase in precipitable water downstream. To investigate the connection between moisture transport and RWIs, poleward moisture flux sensitivity to TPV-jet stream distances are computed. In the early forecast periods, there are no large areas of significant correlations in the region of increased poleward moisture flux (Fig. 5.14 a,b). However, there is a small area of significant negative correlations co-located in the region of increased poleward moisture flux at forecast hour 12 (Fig. 5.14 c). The significant negative correlation suggests an increase in poleward moisture flux with shorter TPV-jet stream distances. Winters and Martin (2014) finds increased poleward moisture flux associated with jet superposition event in response to the superposed jet's ageostrophic circulation. TPVs that are closer to the jet stream could further enhance the jet streak, which could aid in stronger ageostrophic circulations increasing moisture in the vicinity. Lastly, larger regions of significant correlations for precipitable water are found compared to the poleward moisture flux, but this could be a result of moisture flux being computed on the 925 hPa surface. Since precipitable water is

total column integrated value, the increase in moisture might be occurring at levels above 925 hPa. While areas of significant correlations are relatively small, the impacts of moisture transport might be more associated with a surface cyclone that develops once there is enough dynamically driven rising motion.

The surface low pressure as a result of the RWI is not as well represented in the ensemble mean when compared to ERA5 (compared Fig. 5.5e to Fig. 5.4e). To investigate sensitivities associated with the development of the surface low pressure, minimum sea level pressures were identified in the development region of the surface low (Fig. 5.7 a). The average minimum sea level pressure for the surface cyclone of interest is $\sim$978 hPa while ranging from 969 hPa to 986 hPa (Fig. 5.15 a). While the sea level pressure ensemble mean for the surface low pressure is around 988 hPa, there are some ensemble members where a strong surface cyclone develops. At the time and location of the RWI, there is a small area of significant positive correlation, suggesting lower values of potential vorticity would later result in lower pressures (Fig. 5.16 a). The above sensitivity highlights a potential vorticity gradient sensitivity where a shift in the gradient can have impacts downstream. Since this is occurring around the location of the RWI event, this could imply that the forecast sensitivity is related to the development of the RWI. As forecast lead times increased, the significant positive correlation evolves downstream into the development area of the surface low pressure (marked by the box in Fig. 5.16 b-d). Twelve hours prior to the peak strength of the surface low pressure, there is a large area of significant positive correlation within the surface low development region and an area of significant negative correlations just downstream of it (Fig. 5.16 d). Significant positive correlations mean lower surface pressures are associated with lower values of PV at the time of peak surface cyclone intensity. The lower values of PV may be related to the amplified ridge that is in place within the area where the surface low pressure develops and intensifies. Furthermore, the significant negative correlations found just downstream of the development of the surface low pressure

could be representing the trough position and its effect on the development of the surface cyclone.

Forecast sensitivities of 250 hPa wind speed to TPV-jet stream distances are found in the area of the RWI, which motivates investigation of the sensitivity of surface low pressure development to the wind speed on the 320 K potential temperature surface (Fig. 5.17). At the time of the RWI, there is a dipole pattern in sensitivities near the RWI location where there are significant positive and negative correlations (Fig. 5.17 a). The significant positive correlations mean a decrease in wind speed is associated with lower surface pressures, and the significant negative correlations mean a increase in wind speed is associated with lower surface pressure. The dipole pattern of correlations suggests stronger wind speeds are shifted upstream in instances with lower surface pressures. As forecast lead times increase, the dipole pattern in sensitivities appears downstream in the region of surface low pressure development (Fig. 5.17 b-d). Twelve hours prior to the peak strength of the surface low pressure, there are significant negative correlations within the region of the surface low pressure development extending downstream around the trough (Fig. 5.17 d). Furthermore, there is a dipole pattern with both significant negative and positive correlations around the trough (Fig. 5.17 d). Within the surface low pressure development region, significant negative correlations show that an increase in the wind speeds is connected to lower surface pressures. This may be highlighting the importance of the upper-level large-scale deformation thought to be connected to RWIs (Röthlisberger et al. 2018). Furthermore, this may be representing divergence aloft, which would further aid in the development of the surface low pressure.

Since diabatic processes and moisture transport are linked to deepening extratropical cyclones (Knippertz and Wernli 2010; Liberato et al. 2011; Fink et al. 2012), which motivates investigation of the roles moisture and moisture transport play in the development of the surface low pressure. At the time of the RWI, there is a small area of significant negative correlation in the region of the identified RWI (Fig. 5.18 a). The area of significant

negative correlation is largest in magnitude in the area of the surface cyclone peak intensity (Fig. 5.18 b-d). The significant negative correlations suggest a deeper surface pressure cyclone forms if there are large values of precipitable water. At early forecast times near the RWI, larger values of precipitable water result in a strong surface low pressure, indicated by the negative correlations. In terms of poleward moisture flux, there are small scattered areas of significant positive and negative correlations at the time of the RWI (Fig. 5.19 a). As forecast hours progress, there is a dominant area of significant negative correlation in the region where the poleward moisture flux is enhanced (Fig. 5.19 a-d). Twelve hours prior to the surface low's maximum intensity, there is a tri-pole (positive-negative-positive) pattern in significant correlations associated with the poleward moisture flux (Fig. 5.19 d). The forecast surface low pressure sensitivities associated with both precipitable water and poleward moisture flux begin upstream around the RWI event and then appear downstream in the location of the cyclone development. The increase in moisture in and around the surface cyclone development region aid in development of the Rossby wave through diabatic effects (Rodwell et al. 2013; Stensrud 2013). Since moisture sensitivities are relatively small for analysis TPV-jet stream distances (Figs. 5.13 and 5.14), the development of the surface cyclone has the largest impact on the moisture transport, which likely plays a role in the RWI.

Overall, the sensitivities are largest for TPV-jet stream distances compared to TPV intensity for the development of the RWI event. If a TPV is closer to the jet stream, potential temperature gradients on the tropopause – and hence the corresponding wind speeds – may be greater. Also, TPVs closer to the jet stream allow the induced flow around the PV anomaly to modify the flow, which would have a larger impact on perturbing the jet stream. In superpostion jet cases, closer TPVs steepen the potential vorticity wall and increase horizontal gradients in potential temperature. Since jet superposition events are linked to high-impact weather (Bosart et al. 1996b; Christenson 2013), better understanding of their roles on the development of RWI events could help increase predictability.

Moisture transport sensitivities are small for both considered TPV characteristics, but there is a small connection implying TPVs that are in relatively close proximity to the jet stream result in increased moisture near the time of the RWI. It is still unclear if this response is related to the jet superposition ageostrophic circulation (Winters and Martin 2014) or if closer TPVs simply lead to quicker development of a surface low pressure, which drives the moisture transport. The sensitivities associated with the development of the surface cyclone start near the RWI location and are large for both the potential vorticity and the windspeed on the 320 K potential temperature surface. The large magnitudes of the significant negative correlations found for the sensitivities to the windspeeds could be indicative of the importance of divergence associated with downstream ridging (Röthlisberger et al. 2018). Lastly, the moisture sensitivities for the surface cyclone development are present near the RWI and downstream. Strong surface low pressure is linked to either an increase in precipitable water or increased poleward moisture flux. Further investigation is needed to determine if the increase in moisture is a result of a stronger cyclone advecting the moisture poleward or if the stronger low pressure is a result of the moisture increase.

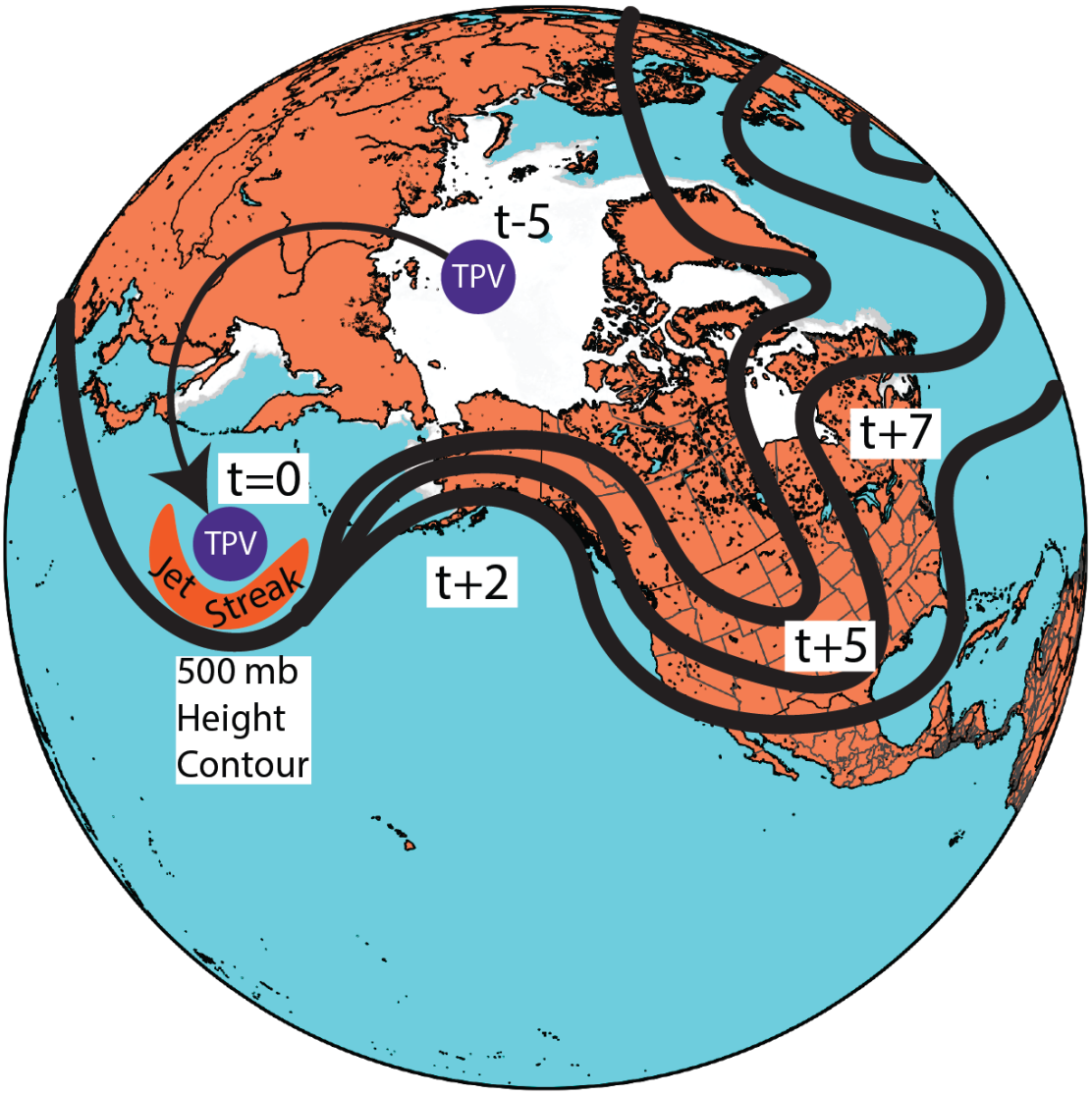

Figure 5.1: Diagram showing a TPV (blue circle) and mid-latitude interaction. Times -5 to 0 are analysis representative of a TPV moving out of the Arctic and interacting with a jet streak (red). Times 0 to +7 are forecast representative of the height field (black contours) propagating downstream. The different black contours represent the uncertainty associated with the forecast height field.

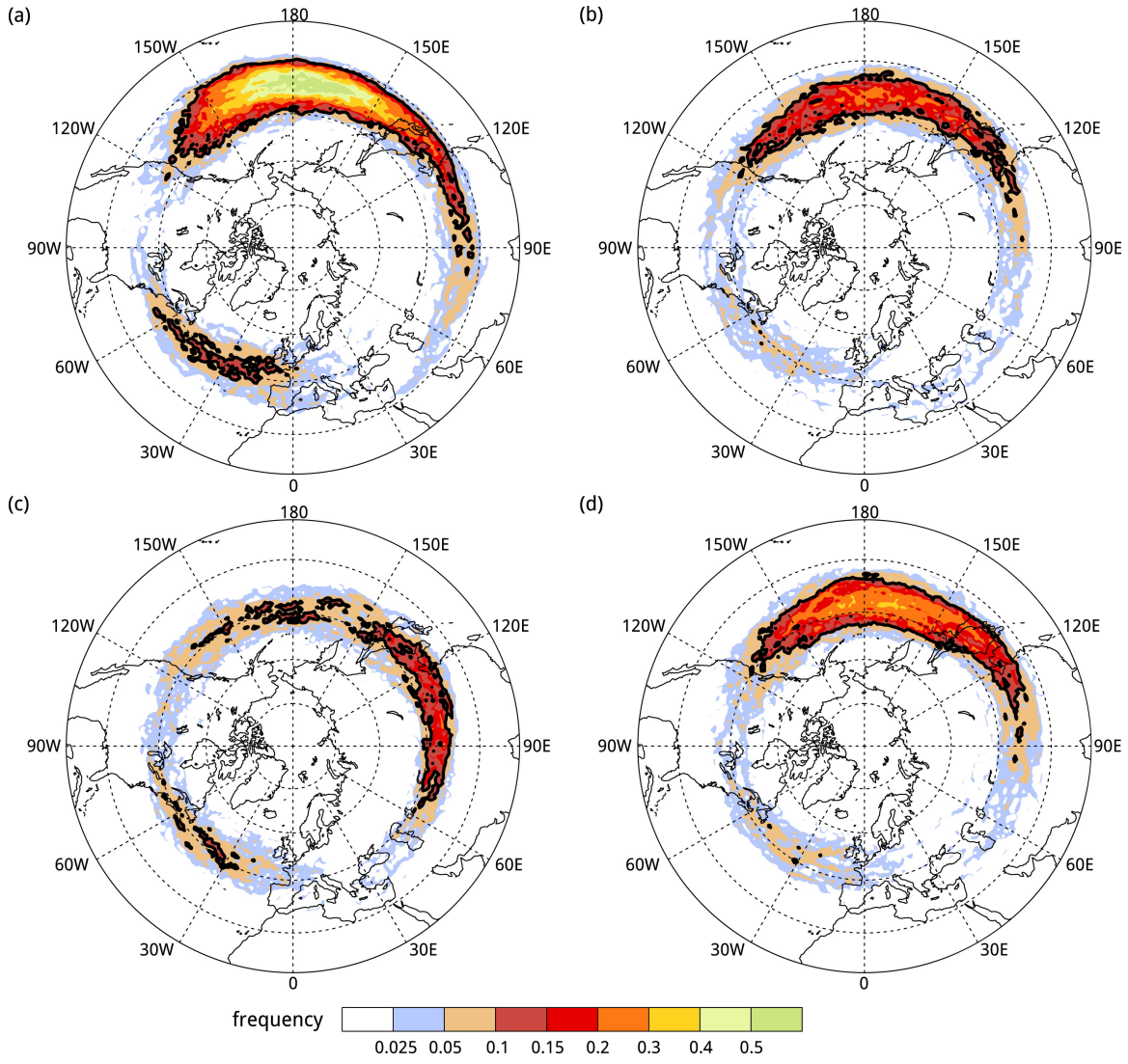

Figure 5.2: Seasonal climatology of gridded RWI segments (frequency is per month and per 1° by 1° grid box) for (a) DJF, (b) MAM, (c) JJA, and (d) SON. The value of 0.1 is highlighted by the black contour. Figure is from from Röthlisberger et al. (2016)

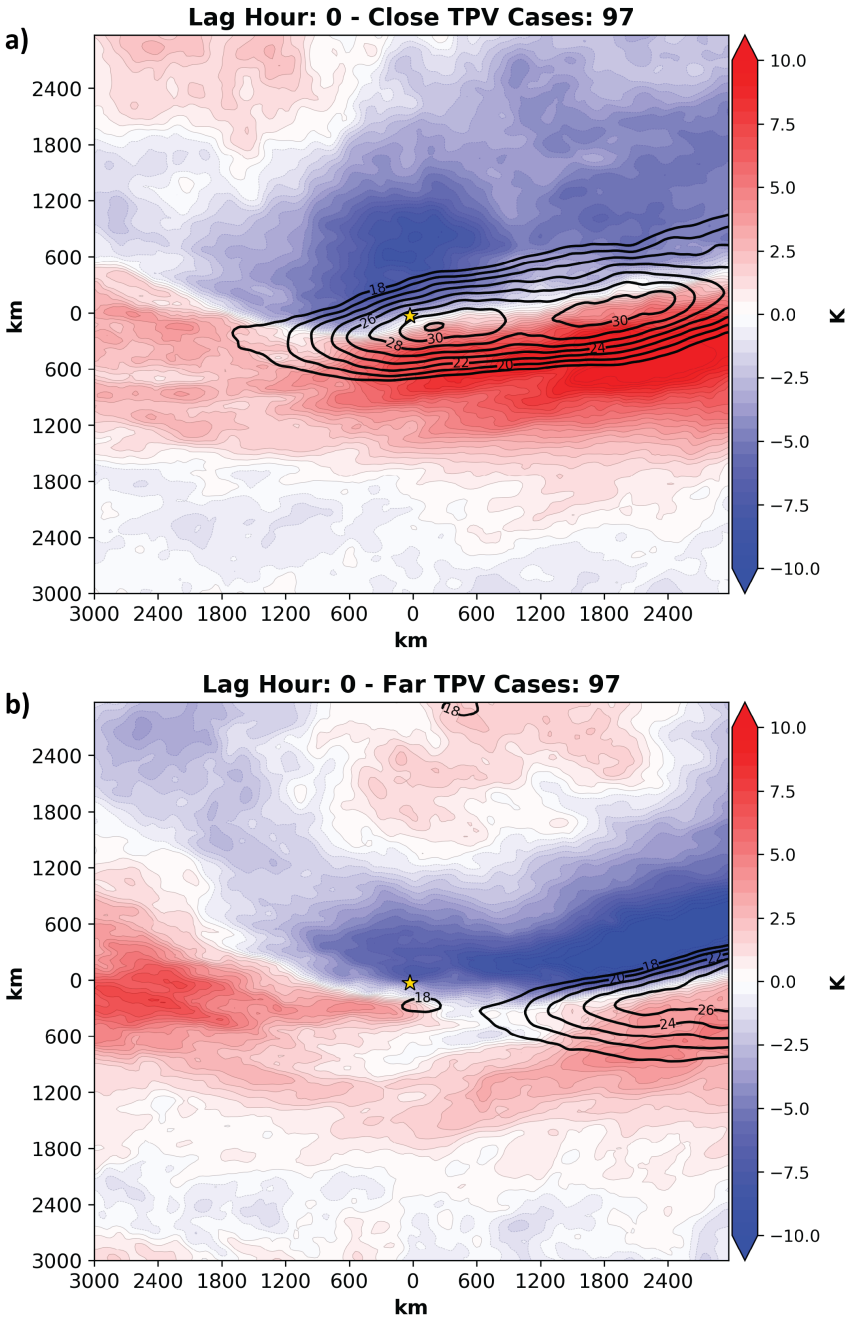

Figure 5.3: RWI event centered composites of 2 PVU potential temperature anomalies (colorfill, K) and windspeed anomalies (contours, knots) for (a) 15th percentile ((within less than 1000 km) and (b) 85th percentile (more than 2500 km) concerning TPV RWI distance. Anomalies were calculated from a ERA5 climatology spanning 1980 to 2010.

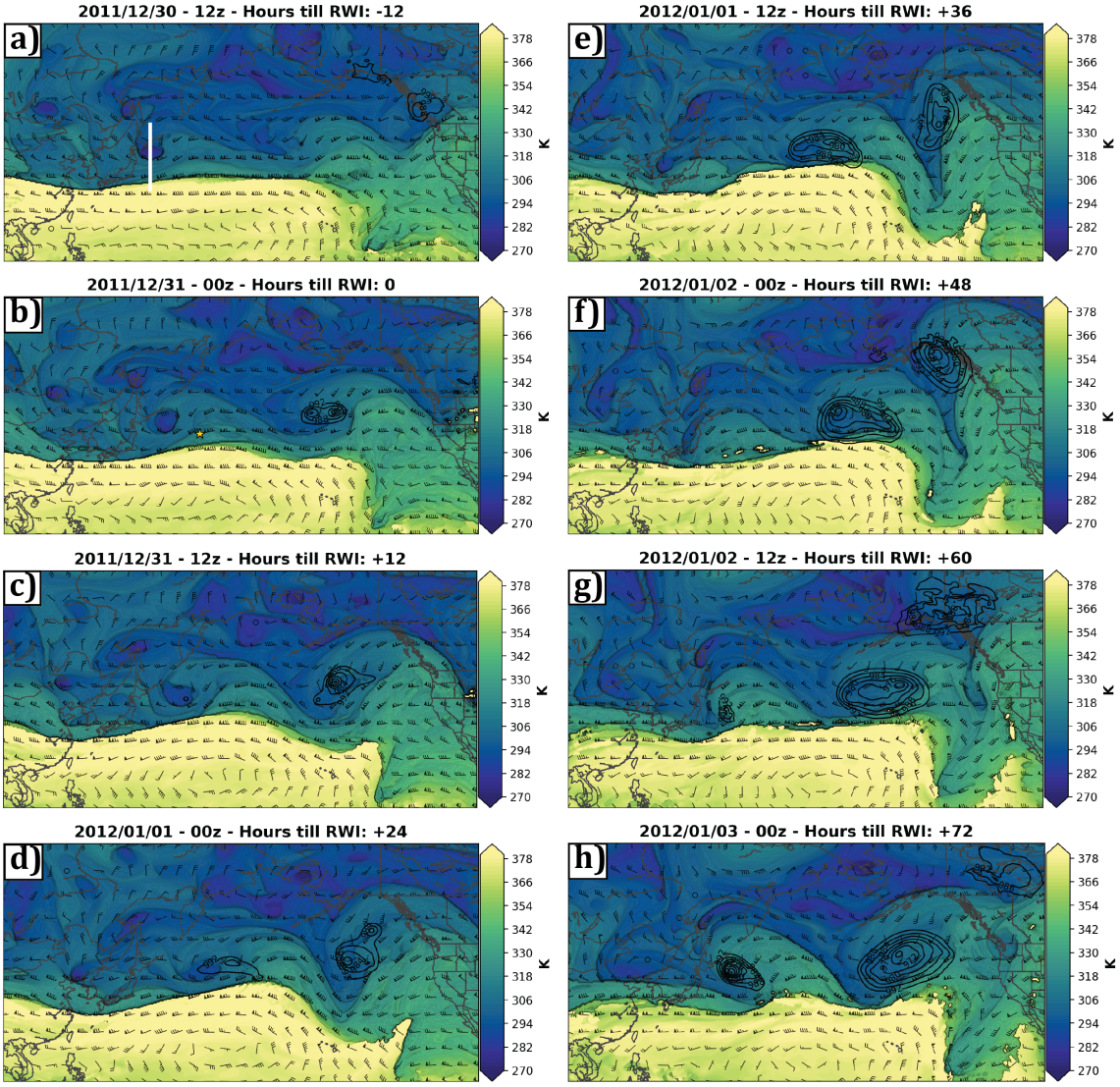

Figure 5.4: ERA5 analysis of 2 PVU potential temperature (colorfill, K), 2 PVU wind (barbs, knots), and mean sea level pressure (black contours, hPa) for (a) 12 hours prior to RWI, (b) time of RWI, (c) 12 hours after, (d) 24 hours after, (e) 36 hours after, (f) 48 hours after, (g) 60 hours after and (h) 72 hours after the RWI event occurred. The gold star represents the location of the identified RWI event. Analysis cross-section through TPV of interest is denoted by the white line.

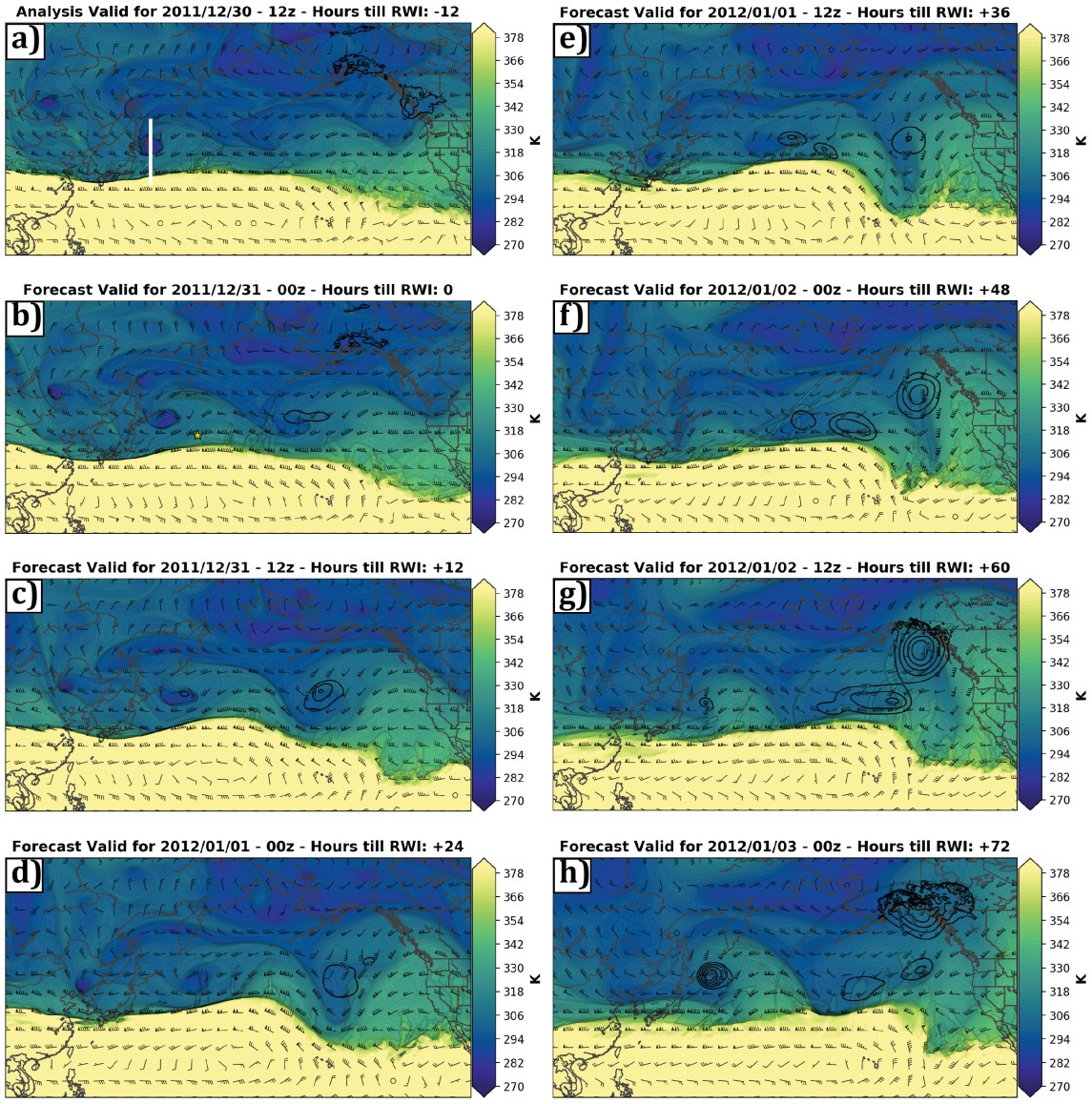

Figure 5.5: MPAS-DART analysis and forecasts ensemble mean of 2 PVU potential temperature (colorfill, K), 2 PVU wind (barbs, knots), and mean sea level pressure (black contours, hPa) for (a) 12 hours prior to RWI, (b) time of RWI, (c) 12 hours after, (d) 24 hours after, (e) 36 hours after, (f) 48 hours after, (g) 60 hours after and (h) 72 hours after the RWI event occurred. The gold star represents the location of the identified RWI event. Analysis cross-section through TPV of interest is denoted by the white line.

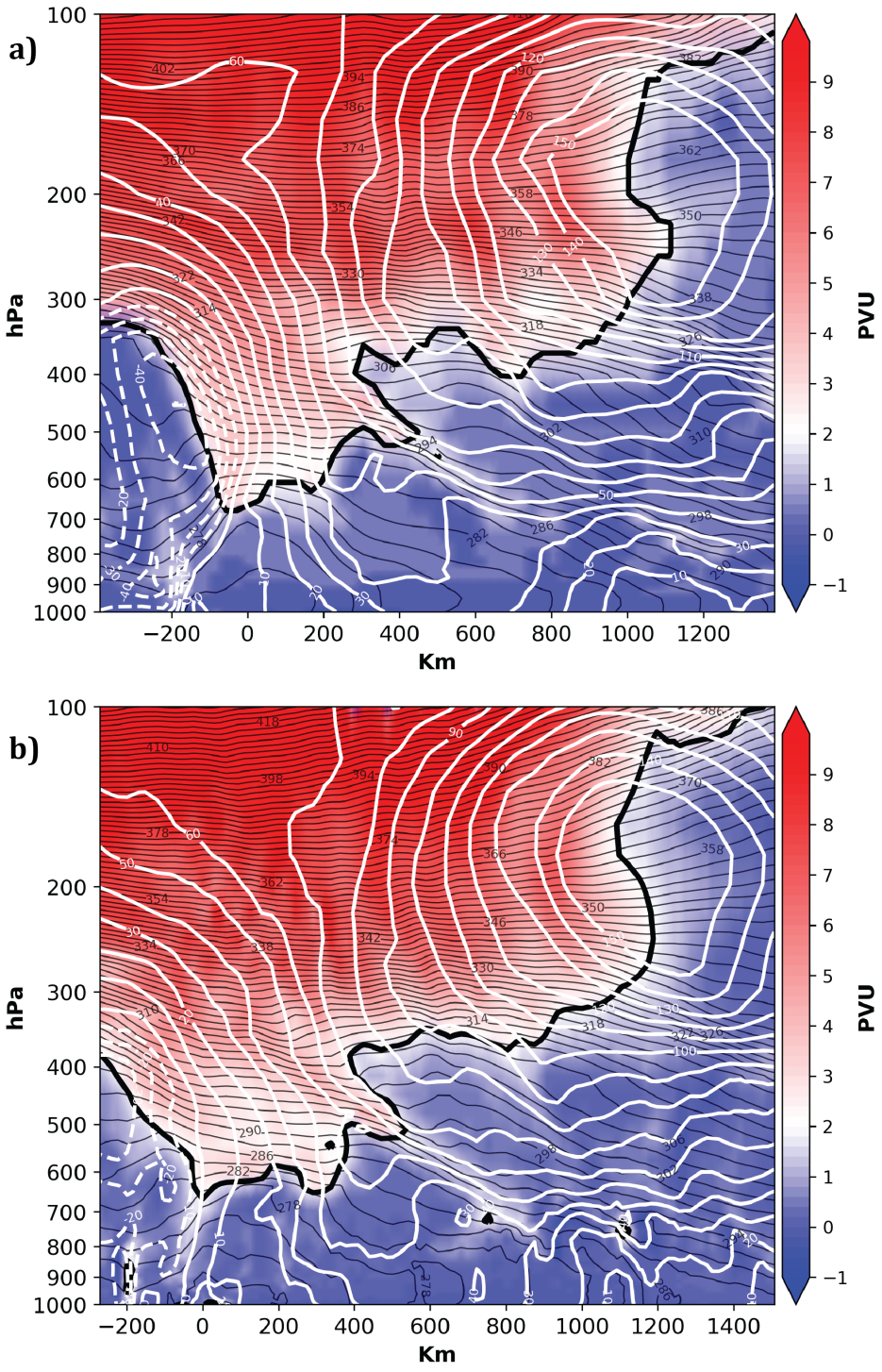

Figure 5.6: North-south cross-section through TPV of interest showing potential vorticity (colorfill, PVU), potential temperature (black contours, K) and zonal windspeed (white contours, knots) for (a) ERA5 and (b) MPAS-DART ensemble mean analysis.

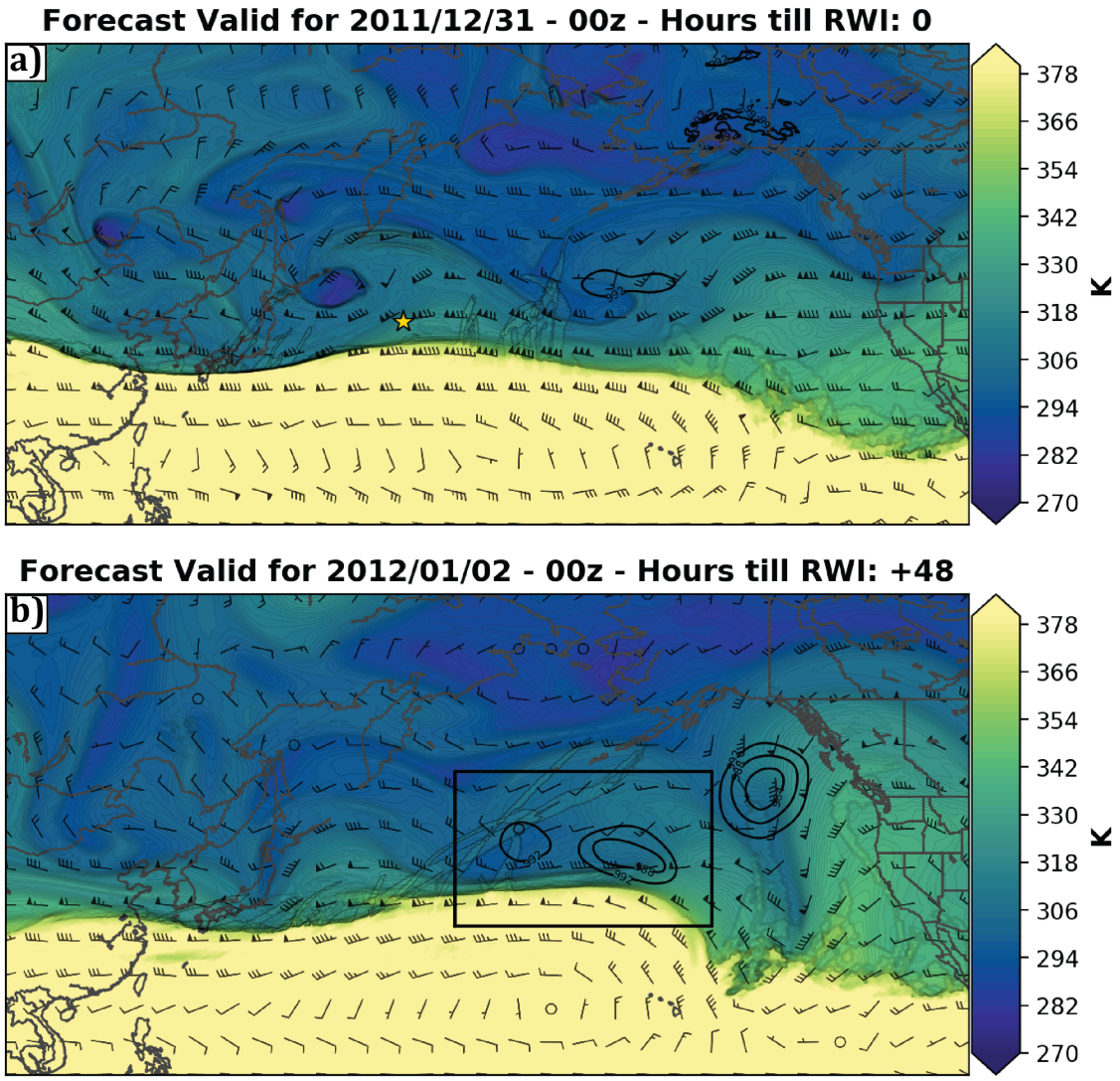

Figure 5.7: MPAS-DART ensemble average 2 PVU potential temperature (colorfill, K), 2 PVU wind (barbs, knots), and mean sea level pressure (black contours, hPa) for (a) at the time of the RWI event and (b) 72 hours after initial RWI event. Black boxes denote the area that minimum sea level pressures were computed for each ensemble member.

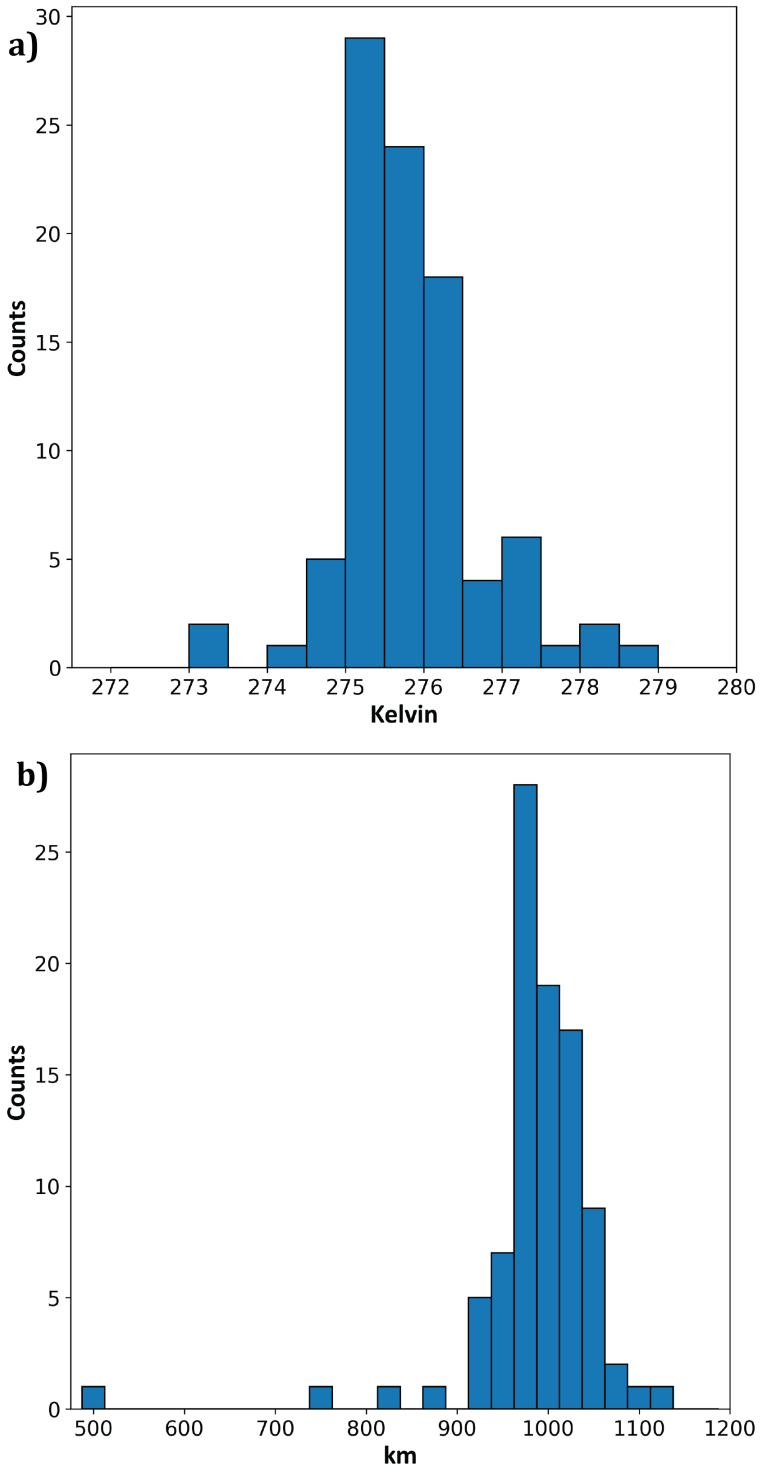

Figure 5.8: Histograms showing analysis (a) minimum potential temperature and (b) distance to the jet stream for the TPV.

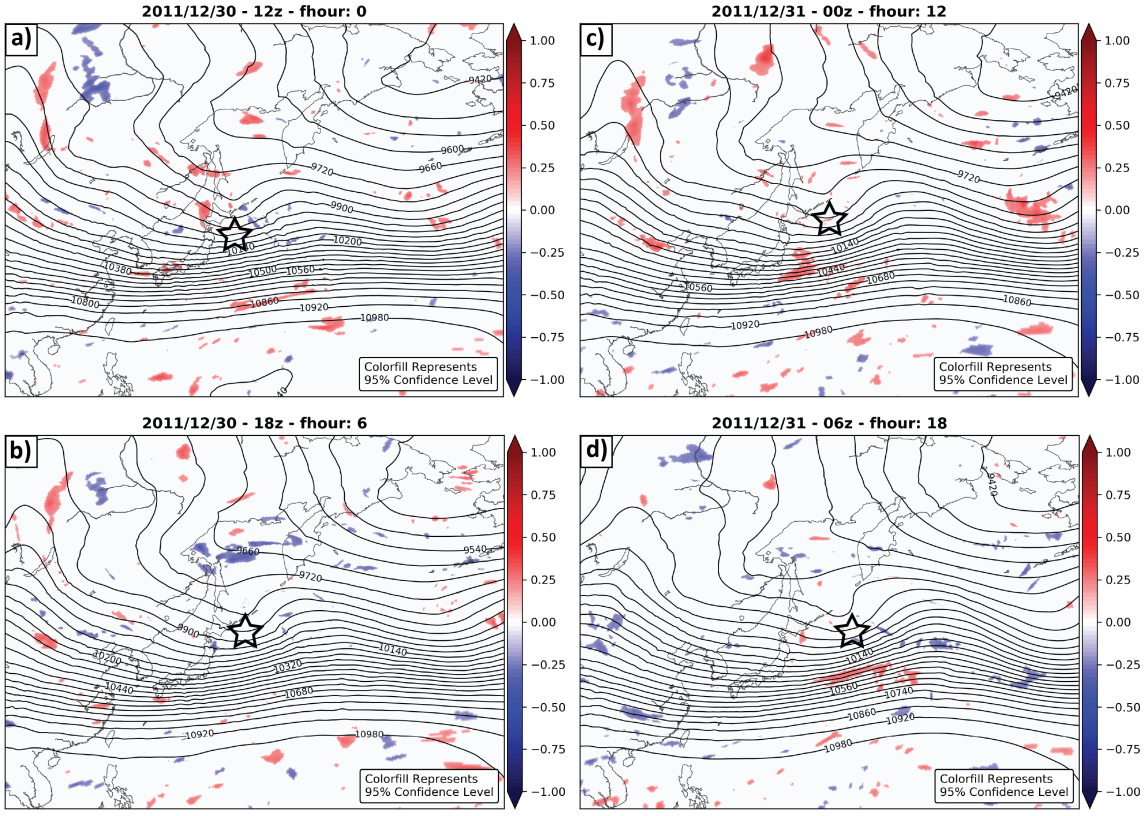

Figure 5.9: Sensitivity (Eq. 5.2) of 250 hPa windspeed to analysis minimum potential temperature associated with TPV of interest for forecast hours (a) 0, (b) 6, (c) 12, and (d) 18. Black contours are the ensemble mean 250 hPa geopotential heights (m) surface. Black stars indicate relative position of TPV of interest. RWI occurred on 31 December 2011 at 00z.

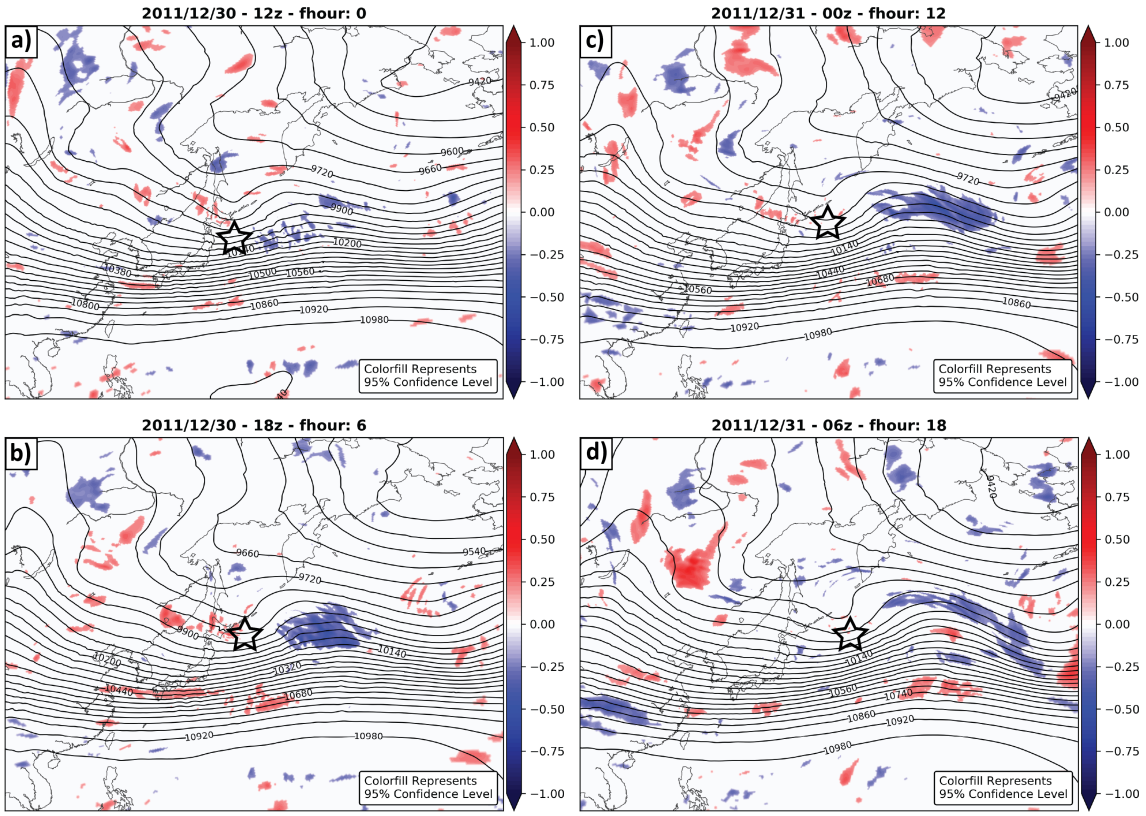

Figure 5.10: Sensitivity (Eq. 5.2) of 250 hPa windspeed to the distance from the jet stream to TPV in the analysis for forecast hours (a) 0, (b) 6, (c) 12, and (d) 18. Black contours are the ensemble mean 250 hPa geopotential heights (m) surface. Black stars indicate relative position of TPV of interest. RWI occurred on 31 December 2011 at 00z.

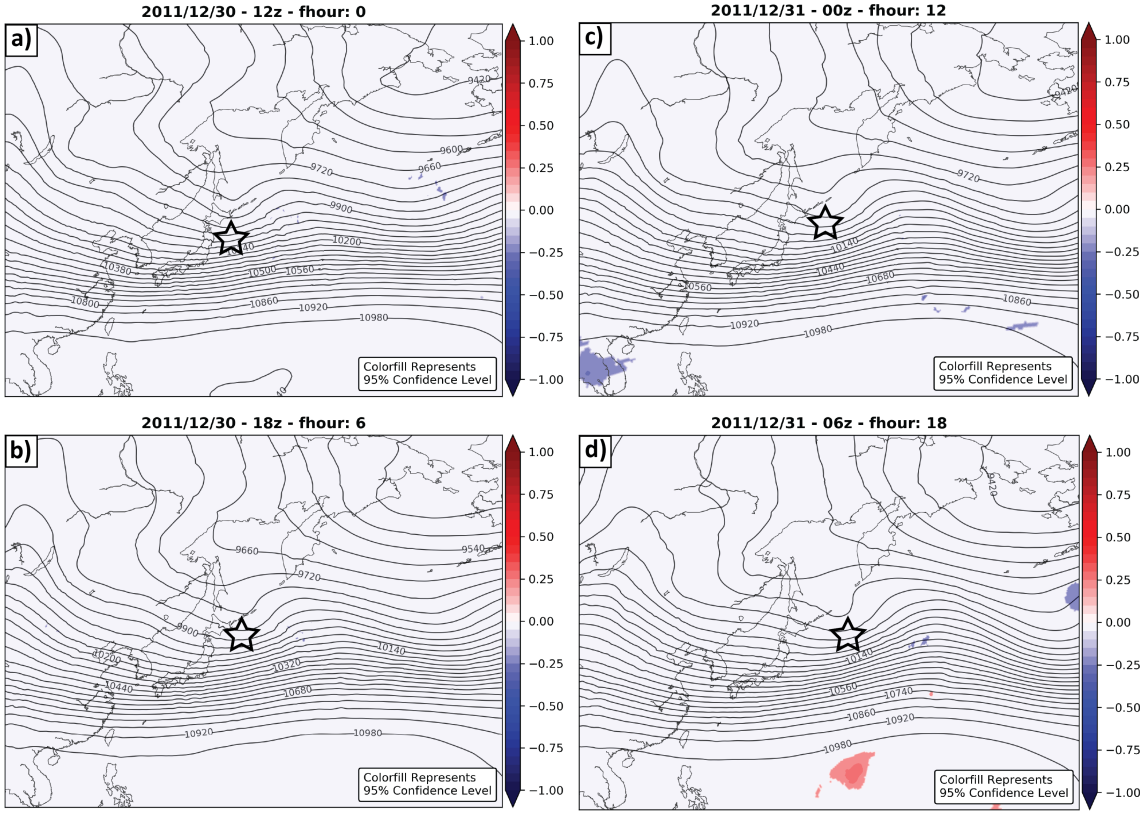

Figure 5.11: Sensitivity (Eq. 5.2) of 250 hPa windspeed to analysis minimum potential temperature associated with TPV of interest for forecast hours (a) 0, (b) 6, (c) 12, and (d) 18. Black contours are the ensemble mean 250 hPa geopotential heights (m) surface. Black stars indicate relative position of TPV of interest. RWI occurred on 31 December 2011 at 00z.

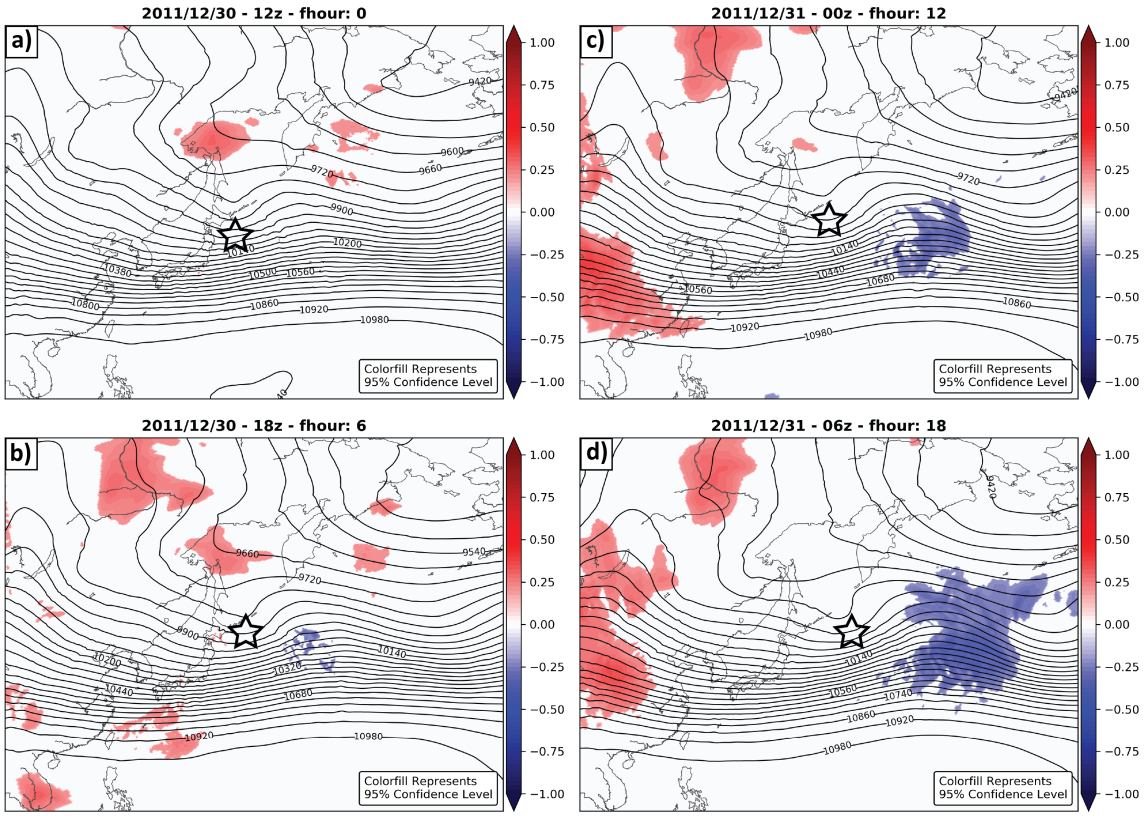

Figure 5.12: Sensitivity (Eq. 5.2) of 250 hPa windspeed to the distance from the jet stream to TPV in the analysis for forecast hours (a) 0, (b) 6, (c) 12, and (d) 18. Black contours are the ensemble mean 250 hPa geopotential heights (m) surface. Black stars indicate relative position of TPV of interest. RWI occurred on 31 December 2011 at 00z.

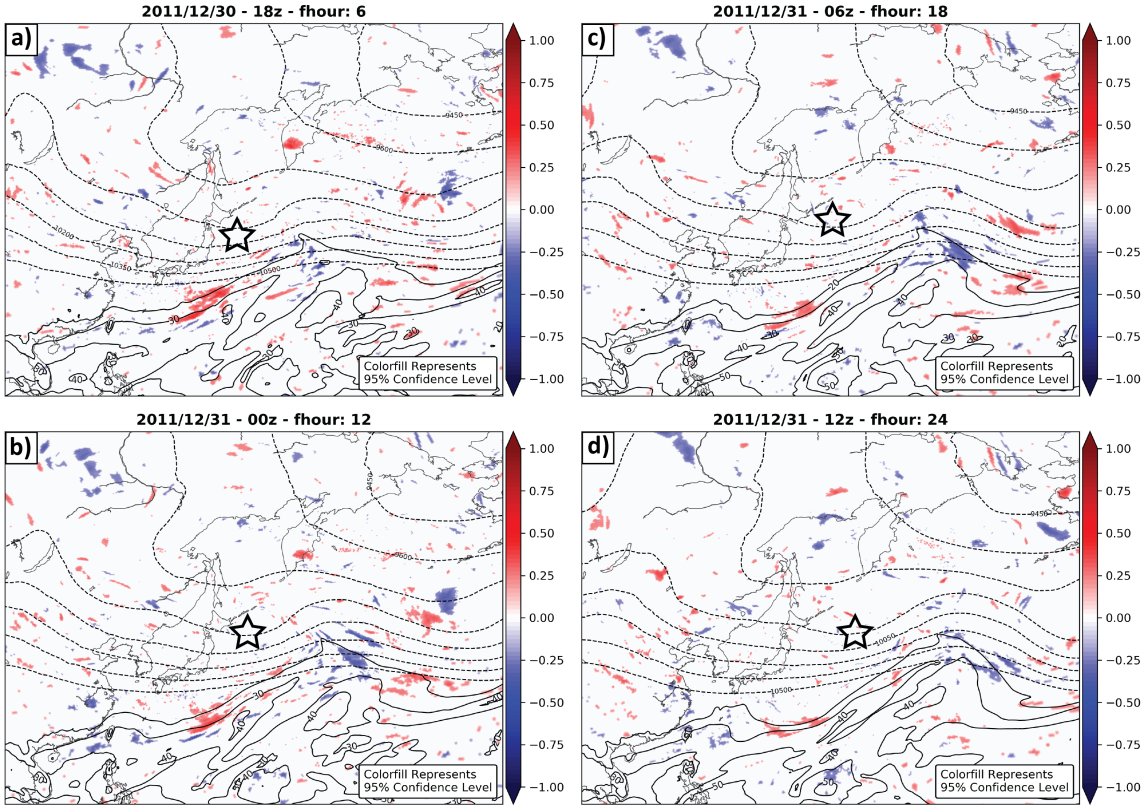

Figure 5.13: Sensitivity (Eq. 5.2) of precipitable water (Kg m^{-2}) to the distance from the jet stream to TPV in the analysis for forecast hours (a) 6, (b) 12, (c) 18, and (d) 24. Black contours are the ensemble mean precipitable water. Black dashed contours are the ensemble mean 250 hPa geopotential heights (m) surface. Black stars indicate relative position of TPV of interest. RWI occurred on 31 December 2011 at 00z.

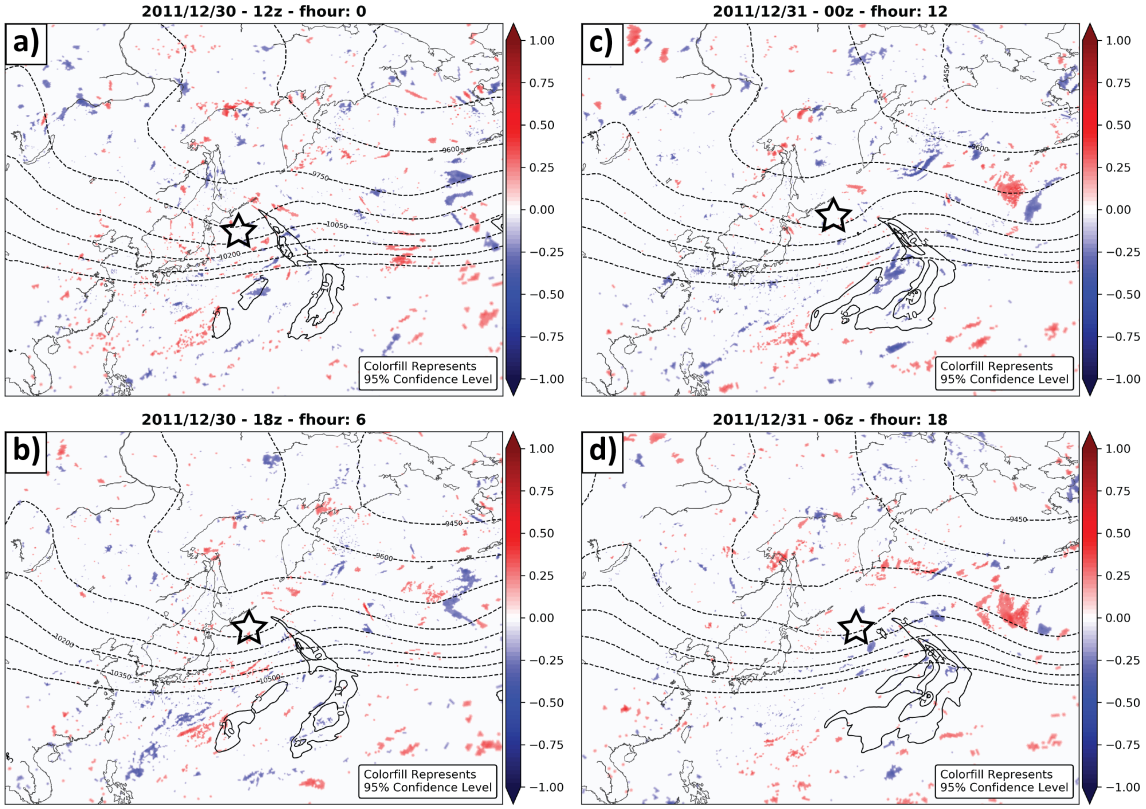

Figure 5.14: Sensitivity (Eq. 5.2) of poleward moisture flux (cm s^{-1}) to the distance from the jet stream to TPV in the analysis for forecast hours (a) 6, (b) 12, (c) 18, and (d) 24. Black contours are the ensemble mean poleward moisture flux. Black dashed contours are the ensemble mean 250 hPa geopotential heights (m) surface. Black stars indicate relative position of TPV of interest. RWI occurred on 31 December 2011 at 00z.

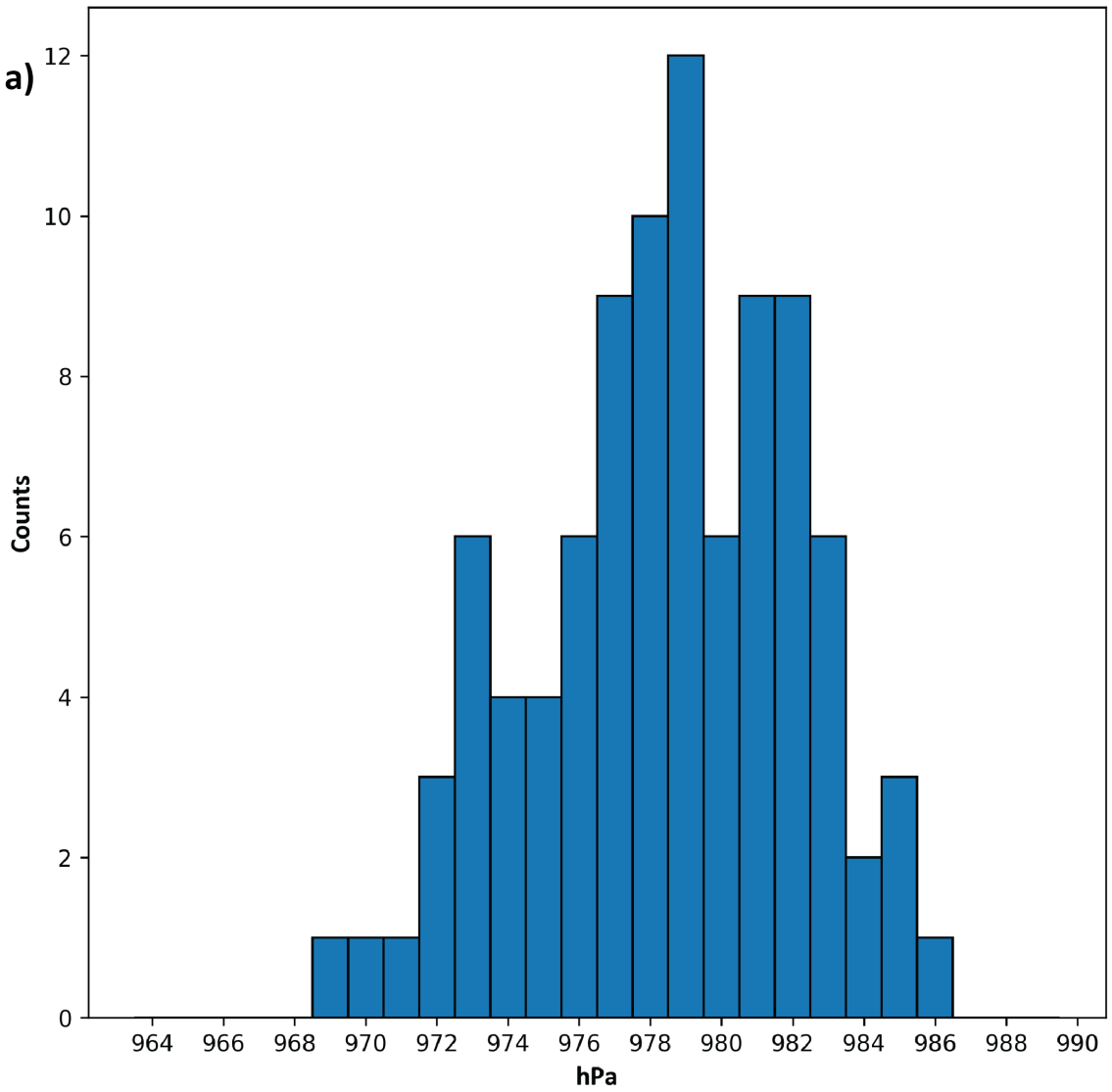

Figure 5.15: Histogram of minimum sea level pressures from each ensemble member within the sensitivity box.

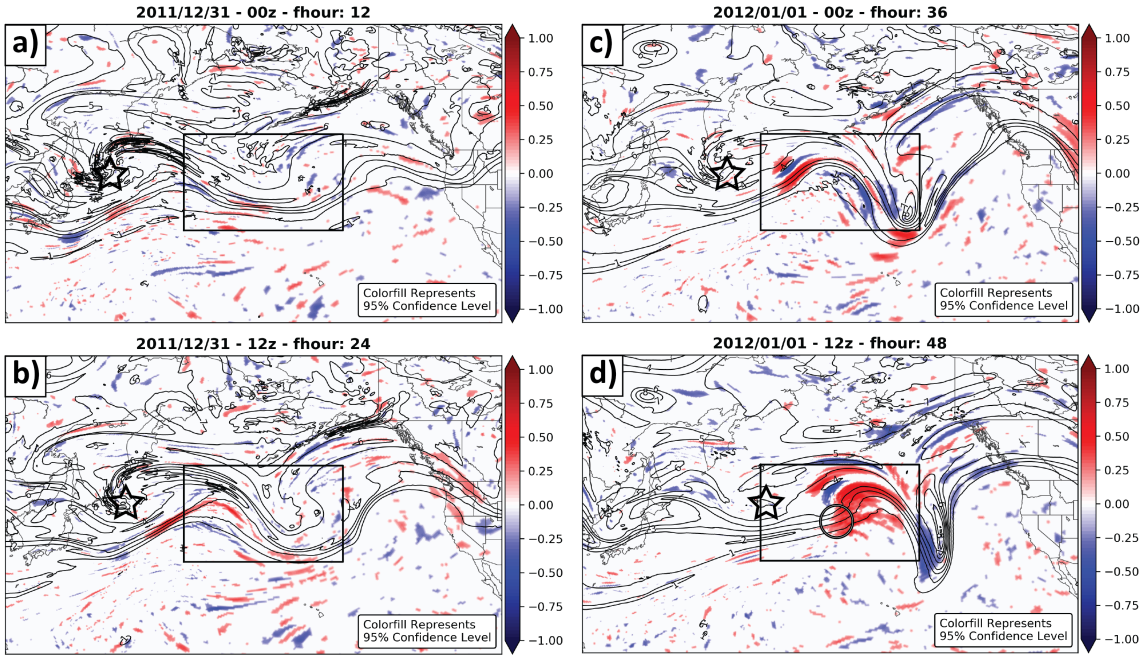

Figure 5.16: Sensitivity (Eq. 5.2) of mean sea level pressure to potential vorticity on 320 Kelvin surface for forecast hours (a) 12, (b) 24, (c) 36, and (d) 48. Black contours are the ensemble mean potential vorticity (PVU) on the 320 Kelvin potential temperature surface. The black box represents the sensitivity box where minimum surface pressures where computed for each ensemble member. Black stars indicate relative position of TPV of interest. Black circle is relative position of surface cyclone. RWI occurred on 31 December 2011 at 00z.

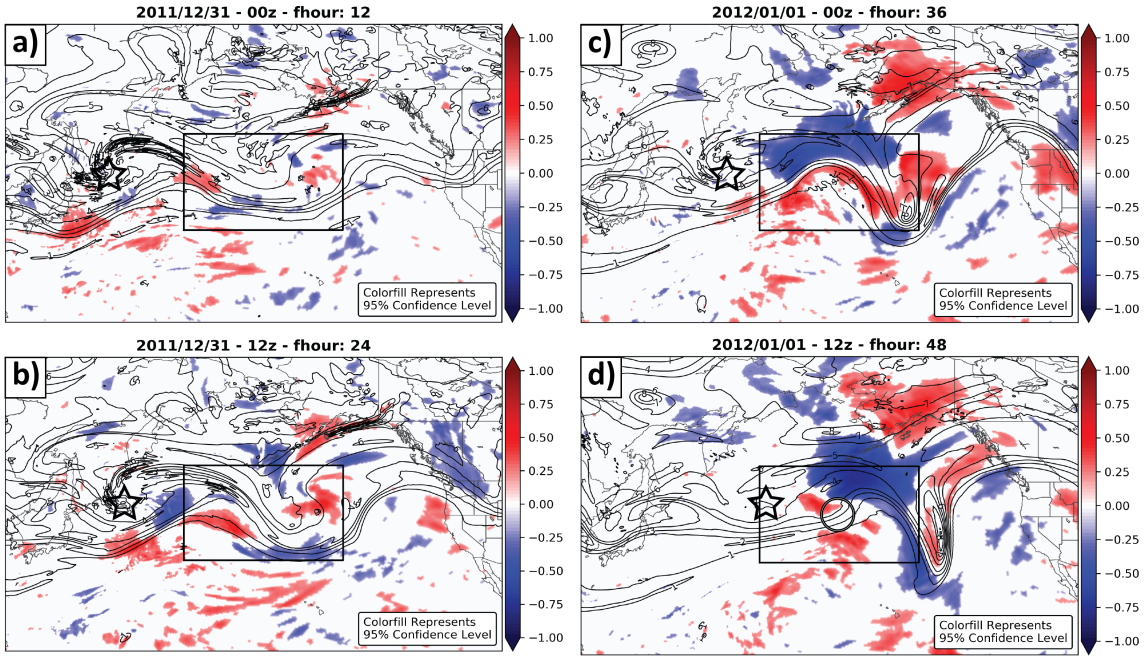

Figure 5.17: Sensitivity (Eq. 5.2) of mean sea level pressure to wind speeds on the 320 Kelvin surface for forecast hours (a) 12, (b) 24, (c) 36, and (d) 48. Black contours are the ensemble mean potential vorticity (PVU) on the 320 Kelvin potential temperature surface. The black box represents the sensitivity box where minimum surface pressures where computed for each ensemble member. Black stars indicate relative position of TPV of interest. Black circle is relative position of surface cyclone. RWI occurred on 31 December 2011 at 00z.

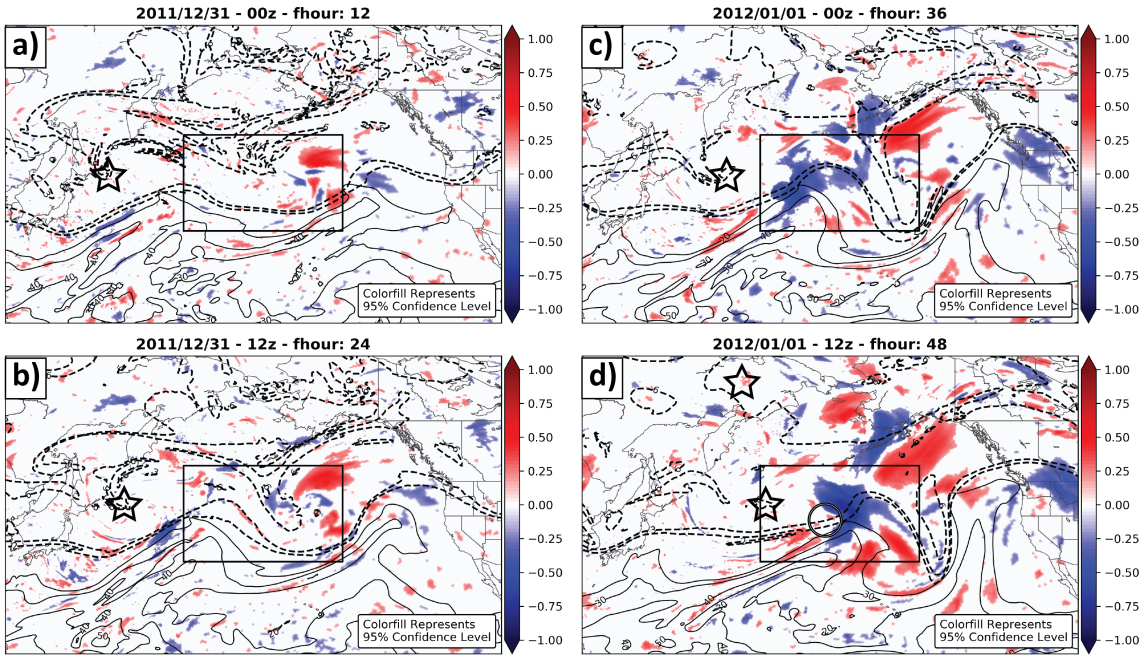

Figure 5.18: Sensitivity (Eq. 5.2) of mean sea level pressure to precipitable water (Kg m^{-2}) for forecast hours (a) 12, (b) 24, (c) 36, and (d) 48. Black contours are the ensemble mean precipitable water. Black dashed contours show the ensemble mean 2, 3, and 6 potential vorticity (PVU) contours on 320 Kelvin potential temperature surface. The black box represents the sensitivity box where minimum surface pressures where computed for each ensemble member. Black stars indicate relative position of TPV of interest. Black circle is relative position of surface cyclone. RWI occurred on 31 December 2011 at 00z.

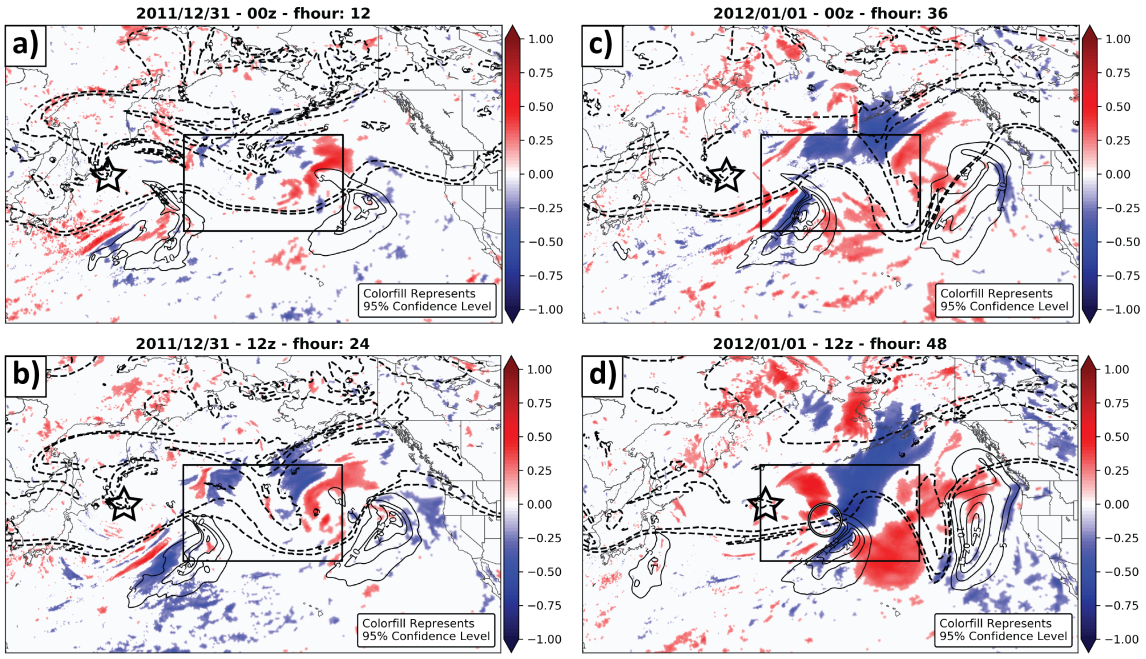

Figure 5.19: Sensitivity (Eq. 5.2) of mean sea level pressure to poleward moisture flux (cm s^{-1}) for forecast hours (a) 12, (b) 24, (c) 36, and (d) 48. Black contours are the ensemble mean poleward moisture flux. Black dashed contours show the ensemble mean 2, 3, and 6 potential vorticity (PVU) contours on 320 Kelvin potential temperature surface. The black box represents the sensitivity box where minimum surface pressures where computed for each ensemble member. Black stars indicate relative position of TPV of interest. Black circle is relative position of surface cyclone. RWI occurred on 31 December 2011 at 00z.

Chapter 6

Conclusions

The Arctic has been changing over recent decades. Temperatures are rising more rapidly than elsewhere via Arctic amplification (Serreze and Francis 2006; Blunden and Arndt 2013) and sea ice is rapidly declining (Screen and Simmonds 2010a). It is important to quantify how these observed rapid changes in the Arctic may impact mid-latitude weather that effects large portions of the general population. Studies have begun to explore the impacts changes observed in Arctic have on mid-latitude weather (Min et al. 2011; Coumou and Rahmstorf 2012; Westra et al. 2013). Cohen et al. (2014b) proposes three dynamical pathways through which the observed rapid changes over the Arctic can effect the mid-latitudes, but there are still large uncertainties surrounding such pathways (Barnes 2013). An improved physical understanding of the processes through which energy can be transferred from the Arctic to the mid-latitudes is critical in order to understand what their implications may be.

Tropopause polar vortices (or TPVs) are features frequently observed in the Artic that can migrate into the mid-latitudes. These long-lived, coherent vortices are defined by closed potential temperature contours on the 2 PVU potential vorticity surface. Due to the fact that TPVs reside in the upper-troposphere lower-stratosphere of the Arctic away from the jet stream, their maintenance and intensification are primarily to diabatic effects (Cavallo and Hakim 2010). Climatological data show a preferred pathway through which TPVs move from the Arctic to the mid-latitudes over the North Pacific/Northern Asia in the wintertime (Fig. 1.4), in agreement with Semmler et al. (2018), suggesting this is a pathway for information from the Arctic to enter the mid-latitudes.

TPVs can interact with the jet stream in the mid-latitudes, leading to perturbations which can lead to Rossby wave initiation (RWI) (Kew et al. 2010; Davies and Didone

2013). Most RWI studies focus on upper-tropospheric negative PV anomalies related to diabatic effects (Rodwell et al. 2013; Madonna et al. 2014; Grams and Archambault 2016), while fewer studies focus on PV anomalies on the poleward side of the jet stream (Röthlisberger et al. 2018). Further understanding of the processes related to TPVs interacting with the jet stream may increase predictability of RWI events and lead to improvements in downstream forecasts.

In order to model TPV evolution correctly and any associated impacts in mid-latitudes such as RWI events, numerical weather prediction (NWP) models must be able to represent important TPV-related process accurately, such as latent heating, radiation, and moisture. In this study, the development and application of a new research tool, MPAS-DART, to study TPVs and their impacts on atmospheric flow is implemented and evaluated. This study is one of the first to explore the application of MPAS-DART in the Arctic. The tool is evaluated against observations to identify any potential limitations, particularly those which could potentially impact the representation of TPVs. A newly developed process-based method is used to identify and investigate potential biases. Next, some of the first ever in-situ observations of a TPV are assimilated to quantify observation impacts on TPV representation in a case study. Lastly, sensitivities related to TPV characteristics and the development of an RWI event are evaluated.

The modeling system used for this study, MPAS-DART, is an ensemble Kalman filter (EnKF) data assimilation system coupled with the Model for Prediction Across Scale (MPAS) global model. The use of a global model provides a method to capture the evolution of the atmosphere in both the Arctic and the mid-latitudes. MPAS is a non-hydrostatic global model that allows smooth transitions from coarse resolutions to finer resolutions. This feature allows for mesoscale mesh resolutions over the Arctic, fine enough to resolve TPVs, while reducing computational expense by applying coarse resolution elsewhere. The background error covariances in MPAS-DART are flow-dependent, allowing information

to spread to appropriate locations across the domain based on the physical state of the atmosphere for a given time, such as along fronts and across synoptic scale cyclones. Since the Arctic is a data sparse region, the use of a flow-dependent background error covariance is especially important (Whitaker et al. 2004; Jung and Leutbecher 2007; Whitaker et al. 2009). Furthermore, deficiencies in the model physics parameterization schemes can be isolated in a cycling EnKF system, allowing for process-based corrections. The non-hydrostatic core within MPAS allows for better representation of mesoscale processes that might not be well-captured in global models with hydrostatic cores, such as tropical cyclones, squall lines, and TPVs.

The number of observations over the Arctic is relatively limited in comparison to the dense conventional observation coverage over the mid-latitudes (Fig. 2.1 a). Over the Arctic, there is a gap in conventional observation coverage, which puts more weight on polar orbiting satellite observations (Fig. 2.1 b). Data assimilation over the Arctic relies heavily on polar orbiting satellite observations, as these account for the highest percentage of observations assimilated over the region (Fig. 2.3 a). Including these polar orbiting satellite observations increases the assimilated observation count in MPAS-DART by $\sim$25,000 (in addition to available conventional observations), which can improve analyses. The combination of EnKF and MPAS in MPAS-DART provides accurate analyses for this study. To explore a variety of research questions throughout this work, two different MPAS-DART cycling experiments are ran for fall 2016 and winter 2011 (experiment 1 and 2, respectively; see Table 2.2).

Ensemble inflation can provide a good estimate of similarity between the model and observation, where reduced inflation values imply better agreement. Evaluation of maximum ensemble inflation shows an overall decrease with time for both experiments. For early cycling times in experiment 2, there is a slight increase in the maximum ensemble inflation that may be a result of model stability issues, which reducing the model time step resolves. Both experiments exhibit biases of similar magnitude and sign with respect to

radiosonde temperatures, windspeeds, and specific humidity over different regions on the globe. However, biases are inconsistent between observation types over the Arctic. At the surface, both spread and bias issues are present within MPAS-DART. Analysis increment is used to see how the observations are affecting the background forecasts. This allows evaluation of these biases, which reveals three main areas this study focuses on for further investigation:

1. In experiment 1, potential temperature shows a significant negative bias above 200 hPa when averaged over the Arctic through the cycling period. No preferred regional biases are found.

2. In experiment 2, zonal wind shows a significant negative bias above 100 when averaged over the Arctic through the cycling period. Regionally, there is a positive bias over the North Pacific Ocean extending to Alaska at 75 hPa. Co-located with this pattern at 100 hPa, a dipole pattern in potential temperature biases suggests a connection between the zonal wind and temperature gradient.

3. In both experiments, potential temperature and water vapor biases near the surface are positive through the cycling periods. Over sea ice, potential temperature and water vapor biases are positive near observation locations.

The biases highlighted above are the main focus for investigation. While other biases may be present, the above are highlighted because two reside in the upper-troposphere lower-stratosphere (UTLS) where TPVs are located, and the other is near the surface, where complex surface types over the Arctic may play an important role.

To further investigate these three biases, a relatively new technique, the mean initial tendency and analysis (MITA) increment method, is applied to MPAS-DART. The MITA increment method combines model physics and dynamics tendencies with analysis increments to (1) provide information about bias patterns on a grid beyond the points where

observations are available for comparison, and (2) decompose the biased model into contributions from individual component tendencies to identify the physical mechanisms responsible for the bias. Application of the MITA increment method for the three biases show the following results:

1. The model is consistently cooling temperatures in the 50-200 hPa layer where observations are consistently warming temperatures, implying there is a cold model bias in this layer. This cooling is present over all Arctic surface types with varying magnitude. The only contributor to the cooling in this layer is the longwave radiation scheme.

2. A moisture bias is located in the same region as the enhanced cooling and is found to be related to the method by which moisture is initialized in MPAS-DART. WRF-SCM experiments are performed to further evaluate this moisture bias in isolation from the full model physics and dynamical processes in the full MPAS-DART. These experiments show that less moisture in that layer leads to reduced longwave cooling associated with radiative processes in a moist layer (see Fig. 4.8). When relative humidity is computed with respect to water only during the moisture initialization process, which is the case in experiment 2, longwave cooling reduces in this layer.

3. Too much cooling is identified near the surface over all surface types expect for over ocean. Cooling near the surface is dominated by longwave radiation scheme contributions. Further, water vapor reduction is large near the surface over both land and sea ice, mainly driven by the convection parameterization scheme. This bias still occurs in experiment 2 with a different moisture initialization process mentioned above.

4. In experiment 2, the model consistently decreases zonal winds speed above 100 hPa where observations are consistently increasing wind speed. The model dynamics and the gravity wave drag parameterization are the only two model tendencies that

are actively decelerating the wind. Furthermore, the model dynamics tendency is acting to increase temperatures above 100 hPa, especially over sea ice. The warming and under-representation of zonal wind above 100 hPa are likely connected, and may suggest poor representation of UTLS interactions. This may be related to vertical grid spacing in the upper levels (Skamarock et al. 2019).

Special dropsonde observations collected during the NAWDEX field campaign are assimilated within the MPAS-DART system to investigate their impacts on mitigating the moisture bias on the representation of the TPV in both analyses and forecasts. The observations have positive impacts on TPV position and intensity and improved representation TPV vertical structure. An EOF approach reveals that assimilation of dropsonde observations reduces the spread in the variability of TPV position and intensity. The dominant pattern of TPV vertical structure variance is associated with position of the upper-level front, the jet streak position, and the magnitude of moisture near the tropopause. There are differences in the forecast position and intensity of the TPV in the early forecast times between experiments. However, those differences become relatively small at later forecast lead times. At these later times, TPV potential temperature and position are similar between the experiments. It is hypothesized that the relatively small perturbations induced by these observations influence only a small area, and are subsequently overwhelmed by the physical processes associated with the MPAS-DART moisture bias over time. To quantify the impacts of the moisture bias on more than just one TPV, tracks are computed for both MPAS-DART member 70 6-hour forecast TPVs and ERA5 analysis TPVs. In MPAS-DART experiment 1, the median TPV potential temperature in early lifetimes are similar to ERA5 TPVs, but later in their lifetimes, ERA5 TPVs have lower potential temperatures. In MPAS-DART experiment 2, there is better agreement between MPAS-DART and ERA5 TPV potential temperatures throughout TPV lifetime. It is hypothesized that this is due to the different initialization process for this experiment. The longwave radiation process rates associated with the moisture bias may be longer than several days. While normal

longwave cooling is around $\sim$2 K Day^{-1} throughout troposphere during the fall/winter times (Turner et al. 2018), MPAS-DART has a slight decrease than an increase in longwave cooling in the UTLS region where the moisture bias is located. While work still needs to be done to determine how sensitive TPV evolution is varying moisture profiles, studies have shown the importance moisture has on growing TPV intensity (Cavallo and Hakim 2012, 2013). So, longer-lived TPVs have a longer duration of time for which they intensify via the erroneous longwave cooling rates that result from the moisture bias in experiment 1.

Few studies investigate the impacts that TPVs have on RWIs. This study evaluates the relationship between analysis TPV characteristics and the development of a specific RWI event. The RWI event chosen has a superposition structure in the analysis of the jet stream, with the polar and subtropical jets vertically stacked in the atmosphere. While this study will just evaluate one TPV-RWI event, this will provide a basis for future work in this area. An ensemble sensitivity analysis is employed, where a correlation approach is used to determine the sensitivities. The RWI forecast sensitivities are stronger for analysis TPV-jet stream distances than analysis TPV intensity. There are stronger windspeeds and greater heights at 250 hPa for shorter TPV-jet stream distances at the time of the RWI. There are small areas of precipitable water and poleward moisture flux sensitivities associated with TPV-jet stream distances. Forecast sensitivities are also computed for the downstream development of a surface cyclone associated with RWI event. There are small areas of significant sensitivity at the time of the RWI for both potential vorticity and windspeed near the increased PV gradient, which is the position of the jet stream. These small sensitivities grow downstream and are largest within the region of the most intense period for the surface cyclone's life cycle. Small changes upstream in the position of the PV gradient or jet stream can have large impacts on the development of the surface cyclone. An increase in the poleward moisture flux at the time of the RWI is associated with a deeper surface cyclone. In this particular case, small sensitivities occurring upstream can impact the surface cyclone in the the downstream forecasts. Further investigation is needed to determine

the impacts the developing surface low pressure has on the poleward moisture flux or if the TPV position relative to the jet stream could play an important role on the moisture flux.

This study is one of the first to explore the application of MPAS-DART in the Arctic. Systematic biases in the MPAS-DART modeling system are identified, and linked to the representation of particular physical processes. However, the modelling system framework could be further improved. More WRF-SCM and MPAS simulations are needed to further test whether the convection scheme chosen for MPAS-DART is appropriate for Arctic studies. Raising the model top to include more of the stratosphere could allow for better representation of upper-troposphere lower-stratosphere processes and the stratospheric polar vortex. Additionally, increasing the number of vertical levels could offer better representation of atmospheric features in the lower stratosphere. It was clear that model representation of near surface variables is greatly influenced by the model surface type (e.g., sea ice, land, ocean, etc.). Improved understanding of coupled processes would be important for representation of Arctic land-atmosphere feedback. In the evaluation of TPV-RWI interactions, this study only considers a single RWI case. Further evaluation of more RWI cases could help quantify the impacts TPV characteristics may have on RWI development and determine the importance of jet superposition in RWI-TPV interactions.

Even with increasing average forecast skill, Arctic daily forecast skill scores still remain variable (Jung and Matsueda 2016). Several factors contribute to poor forecast skill, including lack of conventional observations, model resolution, well suited parameterization options, and the relative scarcity of global model evaluation efforts focused on this region. Since the majority of Arctic observations are satellite derived products, large uncertainties may be carried into model (Zhu et al. 2014). This study assimilates special NAWDEX dropsondes and finds significant improvements in representation of TPV characteristics in the analysis, but those improvements do not carry into the forecast, where impacts are nearly negligible after one day. Similar results are found in an assimilation study focused

on the Madden-Julian Oscillation (DYNAMO; Ling et al. 2014). The Arctic poses additional challenges for NWP, since the Rossby radius of deformation is small, resulting in smaller features that must be well resolved for accurate analyses and prediction (Bromwich et al. 2018; Zhang et al. 2019). In this work, that challenge is overcome through the use of a global model on a non-uniform mesh. This enables the required mesh resolution to represent important Arctic features, like TPV, well while also including mid-latitudes through the use of a global domain.

Most parameterization schemes available in today's numerical models were not developed for application in the Arctic (Sotiropoulou et al. 2016; Hines and Bromwich 2017). Results from this study suggest that the convection scheme may be overactive in moisture modification near the surface. Global models like the one used here have largely not been evaluated in the Arctic (Jung and Leutbecher 2007; Judt 2020). Evaluation is challenging in this region given the general lack of in-situ observational coverage. Here, that challenge is addressed by applying the MITA increment method (Cavallo et al. 2016), which can provide information about biases beyond points where observations are available. Additionally, the MITA method enables the decomposition of biases into individual physical contributions. This study is able to connect identified biases to physical processes that may be driving them.

Although this study makes progress in the development and evaluation of a global model in this region, challenges remain. Like studies before it (Bauer et al. 2016; Jung and Matsueda 2016; Lawrence et al. 2019), this study shows that the complex Arctic surface remains difficult to represent. Further development of coupled modeling would aid in both in better representation of evolving surface types and the complex coupled interactions occurring over the surface. Better understanding how Arctic processes are treated within model parameterization is still needed. The convection parameterizaton scheme is identified as potentially erroneous in this study, raising questions about the applicability of this scheme in the Arctic and the need for a convection scheme at all. In boarder terms,

this work determines there is still a need for a baseline of TPV forecast skill within global models to understand for which TPV processes and under which conditions forecast skill deteriorates.

Previous studies provide the initial evaluation of TPV characteristics and evolution mechanisms for intensification and maintenance (Cavallo and Hakim 2010, 2013). The present study expands on the mechanisms important to TPV evolution by exploring the impacts of moisture in the UTLS region and connections to diabatic processes that effect TPVs. Furthermore, this study shows that a misrepresentation of moisture in the UTLS region can lead to under-intensification of forecast TPV. Since TPV are sub-synoptic scale vortices (Hakim and Canavan 2005b), their evolution is sensitive to the representation of mesoscale processes in NWP models. However, most global NWP models use a hydrostatic core, which can make representation of mesoscale processes more difficult (Kato 1997; Wedi and Malardel 2010). This study uses a non-hydrostatic global model with mesoscale resolution over the Arctic to represent TPVs. Furthermore, most studies of TPVs rely on numerical depiction of the feature, which could include inherent model biases (Køltzow et al. 2019). Here, special dropsondes from a field campaign provide an observational depiction of spatial TPV characteristics and specify vertical moisture distribution. The observations confirm the vertical moisture gradient situated just below the tropopause shown in modeling studies (Cavallo and Hakim 2013). Earlier work describes the ways TPVs move around and potentially beyond the Arctic (Cavallo and Hakim 2010) and the role PV anomalies can play in mid-latitude development of Rossby waves (Röthlisberger et al. 2018) and downstream cyclogenesis (Kleinschmidt 1950). This study connects these ideas and investigates relationships between TPVs and Rossby wave initiations, showing that Rossby wave initiation is more sensitive to TPV position than TPV intensity. Additionally, the relationship between TPVs and moisture transport near the Rossby wave initiation, which previous studies have identified as an important ingredient (Röthlisberger et al. 2018), is weaker than expected. Lastly, the development of a RWI does not guarantee

cyclogenesis, however, sea level pressure (e.g., the development of a surface cyclone) is shown to be sensitive to the position of the TPV-enhanced PV gradient at the time of the RWI, which suggests TPV characteristics may still be important early in the cyclogenesis process.

While this study contributes to the understanding of TPV characteristics and the role these features can play in mid-latitude weather, there are still open questions. More high-quality, in-situ observations are needed over the Arctic to gain a better temporal and spatial understanding of TPV evolution and maintenance mechanisms. Moisture is sparse in the Arctic but plays important roles in Arctic processes like TPVs (Cavallo and Hakim 2013). Moisture is difficult to observe, and in the Arctic, most observations are remotely retrieved and carry sometimes large uncertainty (Lawrence et al. 2019). As such, special in-situ observations, particularly of moisture, in the Arctic can be powerful. Further understanding of physical mechanisms associated with TPV-Rossby-wave interactions is still needed. Toward this end, field campaigns and numerical simulation studies would be useful. Field campaigns could provide much-needed observational data for the investigation of TPV-Rossby-wave interactions and the important physical mechanisms therein. Idealized simulations could further determine and quantify the sensitivities of Rossby wave initiation to TPV characteristics in both dry and moist atmospheres. Finally, more real-data based case studies using an ensemble framework could extend our understanding of sensitivities associated with TPV-Rossby wave interactions and downstream development of surface cyclones.

Bibliography

Ahmadi-Givi, F., G. Graig, and R. Plant, 2004: The dynamics of a midlatitude cyclone with very strong latent-heat release. *Quarterly Journal of the Royal Meteorological Society*, **130 (596)**, 295–323.

Allen, R. J., and S. C. Sherwood, 2008: Warming maximum in the tropical upper troposphere deduced from thermal winds. *Nature Geoscience*, **1 (6)**, 399–403.

Allen, R. J., and C. S. Zender, 2011: Forcing of the Arctic Oscillation by Eurasian snow cover. *Journal of Climate*, **24 (24)**, 6528–6539.

Anderson, J., T. Hoar, K. Raeder, H. Liu, N. Collins, R. Torn, and A. Avellano, 2009: The data assimilation research testbed: A community facility. *Bulletin of the American Meteorological Society*, **90 (9)**, 1283–1296.

Anderson, J. L., 1996: A method for producing and evaluating probabilistic forecasts from ensemble model integrations. *Journal of Climate*, **9 (7)**, 1518–1530.

Anderson, J. L., 2001: An ensemble adjustment Kalman filter for data assimilation. *Monthly Weather Review*, **129 (12)**, 2884–2903.

Anderson, J. L., 2007: An adaptive covariance inflation error correction algorithm for ensemble filters. *Tellus A*, **59 (2)**, 210–224.

Anderson, J. L., 2009: Spatially and temporally varying adaptive covariance inflation for ensemble filters. *Tellus A: Dynamic Meteorology and Oceanography*, **61 (1)**, 72–83.

Anwender, D., P. A. Harr, and S. C. Jones, 2008: Predictability associated with the downstream impacts of the extratropical transition of tropical cyclones: Case studies. *Monthly Weather Review*, **136 (9)**, 3226–3247.

Archambault, H. M., L. F. Bosart, D. Keyser, and J. M. Cordeira, 2013: A climatological analysis of the extratropical flow response to recurving western North Pacific tropical cyclones. *Monthly Weather Review*, **141 (7)**, 2325–2346.

Armstrong, T. E., G. W. Rogers, and G. Rowley, 1978: *The circumpolar north: a political and economic geography of the Arctic and Sub-Arctic*, Vol. 639. Taylor & Francis.

Bader, J., M. D. Mesquita, K. I. Hodges, N. Keenlyside, S. Østerhus, and M. Miles, 2011: A review on Northern Hemisphere sea-ice, storminess and the North Atlantic Oscillation: Observations and projected changes. *Atmospheric Research*, **101 (4)**, 809–834.

Bannister, R., 2017: A review of operational methods of variational and ensemble-variational data assimilation. *Quarterly Journal of the Royal Meteorological Society*, **143 (703)**, 607–633.

Barnes, E. A., 2013: Revisiting the evidence linking Arctic amplification to extreme weather in midlatitudes. *Geophysical research letters*, **40 (17)**, 4734–4739.

Barwell, B., and A. Lorenc, 1985: A study of the impact of aircraft wind observations on a large-scale analysis and numerical weather prediction system. *Quarterly Journal of the Royal Meteorological Society*, **111 (467)**, 103–129.

Bauer, P., L. Magnusson, J.-N. Thépaut, and T. M. Hamill, 2016: Aspects of ECMWF model performance in polar areas. *Quarterly Journal of the Royal Meteorological Society*, **142 (695)**, 583–596.

Baumgart, M., M. Riemer, V. Wirth, F. Teubler, and S. T. Lang, 2018: Potential vorticity dynamics of forecast errors: A quantitative case study. *Monthly Weather Review*, **146 (5)**, 1405–1425.

Bednarczyk, C. N., and B. C. Ancell, 2015: Ensemble sensitivity analysis applied to a southern plains convective event. *Monthly Weather Review*, **143 (1)**, 230–249.

Benjamin, S. G., B. E. Schwartz, and R. E. Cole, 1999: Accuracy of ACARS wind and temperature observations determined by collocation. *Weather and Forecasting*, **14 (6)**, 1032–1038.

Bergeron, T., 1935: On the physics of clouds and precipitation. *Proc. 5th Assembly UGGI, Lisbon, Portugal, 1935*, 156–180.

Bierdel, L., T. Selz, and G. Craig, 2018: Theoretical aspects of upscale error growth on the mesoscales: Idealized numerical simulations. *Quarterly Journal of the Royal Meteorological Society*, **144 (712)**, 682–694.

Bishop, C. H., B. J. Etherton, and S. J. Majumdar, 2001: Adaptive sampling with the ensemble transform Kalman filter. Part I: Theoretical aspects. *Monthly weather review*, **129 (3)**, 420–436.

Blunden, J., and D. S. Arndt, 2013: State of the climate in 2012. *Bull. Amer. Meteor. Soc.*, **94 (8)**, S1–S238.

Bolton, D., 1980: The computation of equivalent potential temperature. *Monthly weather review*, **108 (7)**, 1046–1053.

Bonavita, M., E. Hólm, L. Isaksen, and M. Fisher, 2016: The evolution of the ECMWF hybrid data assimilation system. *Quarterly Journal of the Royal Meteorological Society*, **142 (694)**, 287–303.

Bormann, N., and J.-N. Thépaut, 2004: Impact of MODIS polar winds in ECMWF's 4DVAR data assimilation system. *Monthly weather review*, **132 (4)**, 929–940.

Bosart, L. F., 1981: The Presidents' Day snowstorm of 18–19 February 1979: A subsynoptic-scale event. *Monthly Weather Review*, **109 (7)**, 1542–1566.

Bosart, L. F., 1999: Observed cyclone life cycles. *The Life Cycles of Extratropical Cyclones*, Springer, 187–213.

Bosart, L. F., G. J. Hakim, K. R. Tyle, M. A. Bedrick, W. E. Bracken, J. J. Dickinson, and D. M. Schultz, 1996a: Large-scale antecedent conditions associated with the 12-14 March 1993 cyclone ("Superstorm '93") over eastern North America. *Monthly Weather Review*, **124**, 1865–1891.

Bosart, L. F., G. J. Hakim, K. R. Tyle, M. A. Bedrick, W. E. Bracken, M. J. Dickinson, and D. M. Schultz, 1996b: Large-scale antecedent conditions associated with the 12–14 March 1993 cyclone ("Superstorm'93") over eastern North America. *Monthly weather review*, **124 (9)**, 1865–1891.

Branstator, G., 2002: Circumglobal teleconnections, the jet stream waveguide, and the North Atlantic Oscillation. *Journal of Climate*, **15 (14)**, 1893–1910.

Bromwich, D., and Coauthors, 2018: The Arctic system reanalysis, version 2. *Bulletin of the American Meteorological Society*, **99 (4)**, 805–828.

Carrassi, A., M. Bocquet, L. Bertino, and G. Evensen, 2018: Data assimilation in the geosciences: An overview of methods, issues, and perspectives. *Wiley Interdisciplinary Reviews: Climate Change*, **9 (5)**, e535.

Cavallo, S. M., J. Berner, and C. Snyder, 2016: Diagnosing model errors from time-averaged tendencies in the weather research and forecasting (WRF) model. *Monthly Weather Review*, **144 (2)**, 759–779.

Cavallo, S. M., and G. J. Hakim, 2009: Potential vorticity diagnosis of a tropopause polar cyclone. *Monthly Weather Review*, **137 (4)**, 1358–1371.

Cavallo, S. M., and G. J. Hakim, 2010: The composite structure of tropopause polar cyclones from a mesoscale model. *Monthly Weather Review*, **138 (10)**, 3840–3857, doi: 10.1175/2010MWR3371.1.

Cavallo, S. M., and G. J. Hakim, 2012: Radiative impact on tropopause polar vortices over the arctic. *Monthly Weather Review*, **140 (5)**, 1683–1702.

Cavallo, S. M., and G. J. Hakim, 2013: The physical mechanisms of tropopause polar cyclone intensity change. *J. Atmos. Sci.*, **70**, 3359–3373.

Cavallo, S. M., R. T. Torn, C. Snyder, C. Davis, W. Wang, and J. Done, 2013: Evaluation of the Advanced Hurricane WRF data assimilation system for the 2009 Atlantic hurricane season. *Monthly Weather Review*, **141 (2)**, 523–541.

Chagnon, J. M., and S. L. Gray, 2015: A diabatically generated potential vorticity structure near the extratropical tropopause in three simulated extratropical cyclones. *Monthly Weather Review*, **143 (6)**, 2337–2347.

Chagnon, J. M., S. L. Gray, and J. Methven, 2013: Diabatic processes modifying potential vorticity in a North Atlantic cyclone. *Quart. J. Roy. Meteor. Soc.*, **139 (674)**, 1270–1282.

Chang, E. K., 2000: Wave packets and life cycles of troughs in the upper troposphere: Examples from the Southern Hemisphere summer season of 1984/85. *Monthly Weather Review*, **128 (1)**, 25–50.

Chang, E. K., M. Zheng, and K. Raeder, 2013: Medium-range ensemble sensitivity analysis of two extreme Pacific extratropical cyclones. *Monthly Weather Review*, **141 (1)**, 211–231.

Chen, F., and J. Dudhia, 2001: Coupling an advanced land surface-hydrology model with the Penn State-NCAR MM5 modeling system. Part I: Model implementation and sensitivity. *Monthly Weather Review*, **129 (4)**, 569–585.

Chou, S.-H., B. Zavodsky, G. Jedlovec, and W. Lapenta, 2009: Data assimilation and regional forecasts using Atmospheric InfraRed Sounder (AIRS) profiles. *Preprints, 16 th Conf. on Satellite Meteorology & Oceanography Conference, Phoenix, Arizona, Amer. Meteor. Soc., P*, Vol. 6.

Christenson, C., 2013: A synoptic-climatology of Northern Hemisphere polar and subtropical jet superposition events. Ph.D. thesis, MS thesis, Dept. of Atmospheric and Oceanic Sciences, University of Wisconsin-Madison.

Christenson, C. E., J. E. Martin, and Z. J. Handlos, 2017: A synoptic climatology of Northern Hemisphere, cold season polar and subtropical jet superposition events. *Journal of Climate*, **30 (18)**, 7231–7246.

Clayton, A. M., A. C. Lorenc, and D. M. Barker, 2013: Operational implementation of a hybrid ensemble/4D-Var global data assimilation system at the Met Office. *Quarterly Journal of the Royal Meteorological Society*, **139 (675)**, 1445–1461.

Cohen, J., J. C. Furtado, J. Jones, M. Barlow, D. Whittleston, and D. Entekhabi, 2014a: Linking Siberian snow cover to precursors of stratospheric variability. *Journal of Climate*, **27 (14)**, 5422–5432.

Cohen, J., J. Jones, J. C. Furtado, and E. Tziperman, 2013: Warm Arctic, cold continents: a common pattern related to Arctic sea ice melt, snow advance, and extreme winter weather. *Oceanography*, **26 (4)**, 150–160.

Cohen, J., and Coauthors, 2014b: Recent Arctic amplification and extreme mid-latitude weather. *Nature Geoscience*, **7 (9)**, 627.

Cohen, J. L., J. C. Furtado, M. A. Barlow, V. A. Alexeev, and J. E. Cherry, 2012: Arctic warming, increasing snow cover and widespread boreal winter cooling. *Environmental Research Letters*, **7 (1)**, 014 007.

Coumou, D., and S. Rahmstorf, 2012: A decade of weather extremes. *Nature Climate Change*, **2 (7)**, 491–496.

Cucurull, L., J. Derber, R. Treadon, and R. Purser, 2007: Assimilation of global positioning system radio occultation observations into NCEP's global data assimilation system. *Monthly Weather Review*, **135 (9)**, 3174–3193.

Curry, J., 1983: On the formation of continental polar air. *Journal of the Atmospheric Sciences*, **40 (9)**, 2278–2292.

Curry, J., and Coauthors, 2000: FIRE Arctic clouds experiment. *Bulletin of the American Meteorological Society*, **81 (1)**, 5–29.

Curry, J. A., J. L. Schramm, W. B. Rossow, and D. Randall, 1996: Overview of Arctic cloud and radiation characteristics. *Journal of Climate*, **9 (8)**, 1731–1764.

Danard, M. B., 1964: On the influence of released latent heat on cyclone development. *Journal of Applied Meteorology*, **3 (1)**, 27–37.

Danforth, C. M., E. Kalnay, and T. Miyoshi, 2007: Estimating and correcting global weather model error. *Monthly Weather Review*, **135 (2)**, 281–299.

Davies, H. C., and M. Didone, 2013: Diagnosis and dynamics of forecast error growth. *Monthly Weather Review*, **141 (7)**, 2483–2501.

Davis, C. A., D. A. Ahijevych, W. Wang, and W. C. Skamarock, 2016: Evaluating medium-range tropical cyclone forecasts in uniform-and variable-resolution global models. *Monthly Weather Review*, **144 (11)**, 4141–4160.

Davis, C. A., and K. A. Emanuel, 1991: Potential vorticity diagnostics of cyclogenesis. *Monthly Weather Review*, **119 (8)**, 1929–1953.

Davis, C. A., E. D. Grell, and M. Shapiro, 1996: The balanced dynamical nature of a rapidly intensifying oceanic cyclone. *Monthly Weather Review*, **124 (1)**, 3–26.

Davis, C. A., M. T. Stoelinga, and Y.-H. Kuo, 1993: The integrated effect of condensation in numerical simulations of extratropical cyclogenesis. *Monthly Weather Review*, **121 (8)**, 2309–2330.

Day, J. J., and K. I. Hodges, 2018: Growing land-sea temperature contrast and the intensification of Arctic cyclones. *Geophys. Res. Lett.*, **45 (8)**, 3673–3681.

Dee, D. P., 2005: Bias and data assimilation. *Quarterly Journal of the Royal Meteorological Society*, **131 (613)**, 3323–3343.

Defant, F., 1959: On the hydrodynamic instability caused by approach of subtropical and polar front jet stream in northern latitudes before the onset of strong cyclogenesis. *Rossby Memorial Volume: The atmosphere and sea in motion*, 305–325.

Defant, F., and H. Taba, 1957: The threefold structure of the atmosphere and the characteristics of the tropopause. *Tellus*, **9 (3)**, 259–274.

Derksen, C., and R. Brown, 2012: Spring snow cover extent reductions in the 2008–2012 period exceeding climate model projections. *Geophysical Research Letters*, **39 (19)**.

Devasthale, A., J. Sedlar, M. Tjernström, and A. Kokhanovsky, 2020: A climatological overview of arctic clouds. *Physics and Chemistry of the Arctic Atmosphere*, Springer, 331–360.

Dirksen, R., M. Sommer, F. Immler, D. Hurst, R. Kivi, and H. Vömel, 2014: Reference quality upper-air measurements: Gruan data processing for the vaisala rs92 radiosonde. *Atmospheric Measurement Techniques*, **7 (12)**.

Domeisen, D. I., O. Martius, and B. Jiménez-Esteve, 2018: Rossby wave propagation into the Northern Hemisphere stratosphere: The role of zonal phase speed. *Geophysical Research Letters*, **45 (4)**, 2064–2071.

Donahue, A. S., and P. M. Caldwell, 2018: Impact of physics parameterization ordering in a global atmosphere model. *Journal of Advances in Modeling Earth Systems*, **10 (2)**, 481–499.

Du, Q., V. Faber, and M. Gunzburger, 1999: Centroidal voronoi tessellations: Applications and algorithms. *SIAM review*, **41 (4)**, 637–676.

Emanuel, K. A., M. Fantini, and A. J. Thorpe, 1987: Baroclinic instability in an environment of small stability to slantwise moist convection. part i: Two-dimensional models. *Journal of the Atmospheric Sciences*, **44 (12)**, 1559–1573.

Findeisen, W., 1938: Kolloid-meteorologische vorgänge bei neiderschlags-bildung. *Meteor. Z*, **55**, 121–133.

Fink, A. H., S. Pohle, J. G. Pinto, and P. Knippertz, 2012: Diagnosing the influence of diabatic processes on the explosive deepening of extratropical cyclones. *Geophysical Research Letters*, **39 (7)**.

Fletcher, C. G., S. C. Hardiman, P. J. Kushner, and J. Cohen, 2009: The dynamical response to snow cover perturbations in a large ensemble of atmospheric gcm integrations. *Journal of Climate*, **22 (5)**, 1208–1222.

Fortin, V., M. Abaza, F. Anctil, and R. Turcotte, 2014: Why should ensemble spread match the rmse of the ensemble mean? *Journal of Hydrometeorology*, **15 (4)**, 1708–1713.

Francis, J. A., and E. Hunter, 2006: New insight into the disappearing arctic sea ice. *Eos, Transactions American Geophysical Union*, **87 (46)**, 509–511.

Francis, J. A., and S. J. Vavrus, 2012: Evidence linking Arctic amplification to extreme weather in mid-latitudes. *Geophys. Res. Lett.*, **39 (L06801)**, doi:10.1029/2012GL051000.

Francis, J. A., and S. J. Vavrus, 2015: Evidence for a wavier jet stream in response to rapid arctic warming. *Environmental Research Letters*, **10 (1)**, 014 005.

Gaspari, G., and S. E. Cohn, 1999: Construction of correlation functions in two and three dimensions. *Quarterly Journal of the Royal Meteorological Society*, **125 (554)**, 723–757.

Gemmill, W., B. Katz, and X. Li, 2007: Daily real-time global sea surface temperature-high resolution analysis at noaa/ncep. *NCEP Off. Note*, **260**, 39.

Giannakaki, P., and O. Martius, 2016: An object-based forecast verification tool for synoptic-scale rossby waveguides. *Weather and Forecasting*, **31 (3)**, 937–946.

Gillett, N. P., D. A. Stone, P. A. Stott, T. Nozawa, A. Y. Karpechko, G. C. Hegerl, M. F. Wehner, and P. D. Jones, 2008: Attribution of polar warming to human influence. *Nature Geoscience*, **1 (11)**, 750.

Girard, E., and J. A. Curry, 2001: Simulation of Arctic low-level clouds observed during the FIRE Arctic Clouds Experiment using a new bulk microphysics scheme. *Journal of Geophysical Research: Atmospheres*, **106 (D14)**, 15 139–15 154.

Glahn, H. R., and D. A. Lowry, 1972: The use of model output statistics (MOS) in objective weather forecasting. *Journal of Applied Meteorology*, **11 (8)**, 1203–1211.

Glatt, I., and V. Wirth, 2014: Identifying rossby wave trains and quantifying their properties. *Quarterly Journal of the Royal Meteorological Society*, **140 (679)**, 384–396.

Grams, C. M., and H. M. Archambault, 2016: The key role of diabatic outflow in amplifying the midlatitude flow: A representative case study of weather systems surrounding western North Pacific extratropical transition. *Monthly Weather Review*, **144 (10)**, 3847–3869.

Grams, C. M., and Coauthors, 2011: The key role of diabatic processes in modifying the upper-tropospheric wave guide: A North Atlantic case-study. *Quart. J. Roy. Meteor. Soc.*, **137 (661)**, 2174–2193.

Graversen, R. G., T. Mauritsen, M. Tjernström, E. Källén, and G. Svensson, 2008: Vertical structure of recent Arctic warming. *Nature*, **451 (7174)**, 53.

Graversen, R. G., and M. Wang, 2009: Polar amplification in a coupled climate model with locked albedo. *Climate Dynamics*, **33 (5)**, 629–643.

Gray, S. L., C. Dunning, J. Methven, G. Masato, and J. M. Chagnon, 2014: Systematic model forecast error in rossby wave structure. *Geophysical Research Letters*, **41 (8)**, 2979–2987.

Grazzini, F., and F. Vitart, 2015: Atmospheric predictability and rossby wave packets. *Quarterly Journal of the Royal Meteorological Society*, **141 (692)**, 2793–2802.

Gyakum, J. R., 1983: On the evolution of the qe ii storm. ii: Dynamic and thermodynamic structure. *Monthly Weather Review*, **111 (6)**, 1156–1173.

Ha, S., C. Snyder, W. C. Skamarock, J. Anderson, and N. Collins, 2017: Ensemble Kalman filter data assimilation for the Model for Prediction Across Scales (MPAS). *Monthly Weather Review*, **145 (11)**, 4673–4692.

Haarsma, R. J., F. Selten, and G. J. van Oldenborgh, 2013: Anthropogenic changes of the thermal and zonal flow structure over Western Europe and Eastern North Atlantic in CMIP3 and CMIP5 models. *Climate dynamics*, **41 (9-10)**, 2577–2588.

Hacker, J. P., and W. M. Angevine, 2013: Ensemble data assimilation to characterize surface-layer errors in numerical weather prediction models. *Monthly Weather Review*, **141 (6)**, 1804–1821.

Hakim, G. J., 2000: Climatology of coherent structures on the extratropical tropopause. *Monthly Weather Review*, **128**, 385–406.

Hakim, G. J., 2005: Vertical structure of midlatitude analysis and forecast errors. *Monthly Weather Review*, **133 (3)**, 567–578.

Hakim, G. J., and A. K. Canavan, 2005a: Observed cyclone–anticyclone tropopause vortex asymmetries. *Journal of the Atmospheric Sciences*, **62 (1)**, 231–240.

Hakim, G. J., and A. K. Canavan, 2005b: Observed cyclone-anticyclone tropopause asymmetries. *J. Atmos. Sci.*, **62 (1)**, 231–240.

Hakim, G. J., and R. D. Torn, 2008: Ensemble synoptic analysis. *Synoptic—Dynamic Meteorology and Weather Analysis and Forecasting*, Springer, 147–161.

Hamill, T. M., 2001: Interpretation of rank histograms for verifying ensemble forecasts. *Monthly Weather Review*, **129 (3)**, 550–560.

Hamill, T. M., and C. Snyder, 2000: A hybrid ensemble Kalman filter-3D variational analysis scheme. *Monthly Weather Review*, **128 (8)**, 2905–2919.

Handlos, Z. J., and J. E. Martin, 2016: Composite analysis of large-scale environments conducive to western Pacific polar/subtropical jet superposition. *Journal of Climate*, **29 (19)**, 7145–7165.

Hardiman, S. C., P. J. Kushner, and J. Cohen, 2008: Investigating the ability of general circulation models to capture the effects of eurasian snow cover on winter climate. *Journal of Geophysical Research: Atmospheres*, **113 (D21)**.

Hardy, K. R., D. P. Hinson, G. Tyler, and E. Kursinski, 1992: Atmospheric profiles from active space-based radio measurements. *Preprint, Sixth Conf. on Satellite Meteorology and Oceanography*, Atlanta, GA, Amer. Meteor. Soc., 420–423.

Harvey, B. J., J. Methven, and M. H. Ambaum, 2016: Rossby wave propagation on potential vorticity fronts with finite width. *Journal of Fluid Mechanics*, **794**, 775–797.

Healy, S., 2008: Forecast impact experiment with a constellation of GPS radio occultation receivers. *Atmospheric Science Letters*, **9 (3)**, 111–118.

Healy, S., A. Jupp, and C. Marquardt, 2005: Forecast impact experiment with GPS radio occultation measurements. *Geophysical Research Letters*, **32 (3)**.

Hersbach, H., and Coauthors, 2019: Global reanalysis: goodbye ERA-Interim, hello ERA5. *ECMWF Newsl*, **159**, 17–24.

Hill, A. J., C. C. Weiss, and B. C. Ancell, 2016: Ensemble sensitivity analysis for mesoscale forecasts of dryline convection initiation. *Monthly Weather Review*, **144 (11)**, 4161–4182.

Hines, K. M., and D. H. Bromwich, 2017: Simulation of late summer Arctic clouds during ASCOS with Polar WRF. *Monthly Weather Review*, **145 (2)**, 521–541.

Hines, K. M., D. H. Bromwich, L.-S. Bai, M. Barlage, and A. G. Slater, 2011: Development and Testing of Polar WRF. Part III: Arctic Land. *Journal of Climate*, **24 (1)**, 26–48.

Hohenegger, C., and C. Schar, 2007: Atmospheric predictability at synoptic versus cloud-resolving scales. *Bulletin of the American Meteorological Society*, **88 (11)**, 1783–1794.

Holland, M. M., and C. M. Bitz, 2003: Polar amplification of climate change in coupled models. *Climate Dyn.*, **21 (3-4)**, 221–232.

Hollingsworth, B. A., A. Lorenc, M. Tracton, K. Arpe, G. Cats, S. Uppala, and P. Kållberg, 1985: The response of numerical weather prediction systems to FGGE level IIb data. Part I: Analyses. *Quarterly Journal of the Royal Meteorological Society*, **111 (467)**, 1–66.

Holton, J. R., 2004: *An introduction to dynamic meteorology*. 4th ed., Elsevier Academic Press, 535 pp.

Holton, J. R., P. H. H. M. E., McIntyre, A. R. Douglass, R. B. Rood, and L. Pfister, 1995: Stratosphere-troposphere exchange. *Rev. Geophys.*, **33 (4)**, 403–439.

Honda, M., J. Inoue, and S. Yamane, 2009: Influence of low arctic sea-ice minima on anomalously cold eurasian winters. *Geophysical Research Letters*, **36 (8)**.

Hong, S.-Y., and J.-O. J. Lim, 2006: The WRF single-moment 6-class microphysics scheme (WSM6). *J. Korean Meteor. Soc*, **42 (2)**, 129–151.

Hong, S.-Y., Y. Noh, and J. Dudhia, 2006: A new vertical diffusion package with an explicit treatment of entrainment processes. *Monthly Weather Review*, **134 (9)**, 2318–2341.

Hoskins, B., and P. Berrisford, 1988: A potential vorticity perspective of the storm of 15–16 October 1987. *Weather*, **43 (3)**, 122–129.

Hoskins, B. J., M. E. McIntyre, and A. W. Robertson, 1985: On the use and significance of isentropic potential vorticity maps. *Quarterly Journal of the Royal Meteorological Society*, **111 (470)**, 877–946.

Houtekamer, P., and F. Zhang, 2016: Review of the ensemble Kalman filter for atmospheric data assimilation. *Monthly Weather Review*, **144 (12)**, 4489–4532.

Hovmöller, E., 1949: The trough-and-ridge diagram. *Tellus*, **1 (2)**, 62–66.

Huang, C.-Y., Y. Zhang, W. C. Skamarock, and L.-H. Hsu, 2017: Influences of large-scale flow variations on the track evolution of Typhoons Morakot (2009) and Megi (2010): Simulations with a global variable-resolution model. *Monthly Weather Review*, **145 (5)**, 1691–1716.

Huang, H.-Y., A. Hall, and J. Teixeira, 2013: Evaluation of the WRF PBL parameterizations for marine boundary layer clouds: Cumulus and stratocumulus. *Monthly Weather Review*, **141 (7)**, 2265–2271.

Hunt, B. R., E. J. Kostelich, and I. Szunyogh, 2007: Efficient data assimilation for spatiotemporal chaos: A local ensemble transform Kalman filter. *Physica D: Nonlinear Phenomena*, **230 (1)**, 112–126.

Iacono, M. J., J. S. Delamere, E. J. Mlawer, M. W. Shephard, S. A. Clough, and W. D. Collins, 2008: Radiative forcing by long-lived greenhouse gases: Calculations with the AER radiative transfer models. *Journal of Geophysical Research: Atmospheres*, **113 (D13)**.

Inoue, J., and M. E. Hori, 2011: Arctic cyclogenesis at the marginal ice zone: A contributory mechanism for the temperature amplification? *Geophys. Res. Lett.*, **38 (12)**.

Janjić, Z. I., 2002: Nonsingular implementation of the Mellor–Yamada level 2.5 scheme in the NCEP Meso model. *NCEP office note*, **437**, 61.

Jones, G. S., S. F. Tett, and P. A. Stott, 2003: Causes of atmospheric temperature change 1960–2000: A combined attribution analysis. *Geophysical Research Letters*, **30 (5)**.

Jones, T. A., and D. J. Stensrud, 2012: Assimilating AIRS temperature and mixing ratio profiles using an ensemble Kalman filter approach for convective-scale forecasts. *Weather and Forecasting*, **27 (3)**, 541–564.

Judt, F., 2018: Insights into atmospheric predictability through global convection-permitting model simulations. *Journal of the Atmospheric Sciences*, **75 (5)**, 1477–1497.

Judt, F., 2020: Atmospheric Predictability of the Tropics, Middle Latitudes, and Polar Regions Explored through Global Storm-Resolving Simulations. *Journal of the Atmospheric Sciences*, **77 (1)**, 257–276.

Jung, T., 2005: Systematic errors of the atmospheric circulation in the ECMWF forecasting system. *Quarterly Journal of the Royal Meteorological Society*, **131 (607)**, 1045–1073.

Jung, T., M. A. Kasper, T. Semmler, and S. Serrar, 2014: Arctic influence on subseasonal midlatitude prediction. *Geophys. Res. Lett.*, **41**, 3676–3680, doi:10.1002/2014GL059961.

Jung, T., and M. Leutbecher, 2007: Performance of the ECMWF forecasting system in the Arctic during winter. *Quarterly Journal of the Royal Meteorological Society*, **133 (626)**, 1327–1340.

Jung, T., and M. Matsueda, 2016: Verification of global numerical weather forecasting systems in polar regions using TIGGE data. *Quart. J. Roy. Meteor. Soc.*, **142 (695)**, 574–582.

Jung, T., and Coauthors, 2016: Advancing polar prediction capabilities on daily to seasonal time scales. *Bull. Amer. Meteor. Soc.*, doi:10.1175/BAMS-D-14-00246.1.

Kalesse, H., and Coauthors, 2016: Understanding rapid changes in phase partitioning between cloud liquid and ice in stratiform mixed-phase clouds: An Arctic Case Study. *Monthly Weather Review*, **144 (12)**, 4805–4826.

Kalman, R. E., 1960: A new approach to linear filtering and prediction problems. *Journal of Fluids Engineering*, **82 (1)**, 35–45.

Kato, T., 1997: Hydrostatic and non-hydrostatic simulations of moist convection: Review and further study. *Meteorology and Atmospheric Physics*, **63 (1-2)**, 39–51.

Kennedy, A. D., X. Dong, B. Xi, S. Xie, Y. Zhang, and J. Chen, 2011: A comparison of MERRA and NARR reanalyses with the DOE ARM SGP data. *Journal of Climate*, **24 (17)**, 4541–4557.

Kew, S. F., M. Sprenger, and H. C. Davies, 2010: Potential vorticity anomalies of the lowermost stratosphere: A 10-yr winter climatology. *Monthly Weather Review*, **138**, 1234–1249, doi:10.1175/2009MWR3193.1.

Key, J. R., D. Santek, C. S. Velden, N. Bormann, J.-N. Thepaut, L. P. Riishojgaard, Y. Zhu, and W. P. Menzel, 2003: Cloud-drift and water vapor winds in the polar regions from MODISIR. *IEEE Transactions on Geoscience and Remote Sensing*, **41 (2)**, 482–492.

Kleinschmidt, E., 1950: On the structure and origin of cyclones (Part I). *Meteor. Rundsch*, **3**, 1–6.

Klemp, J., J. Dudhia, and A. Hassiotis, 2008: An upper gravity-wave absorbing layer for nwp applications. *Monthly Weather Review*, **136 (10)**, 3987–4004.

Klemp, J. B., 2011: A terrain-following coordinate with smoothed coordinate surfaces. *Monthly Weather Review*, **139 (7)**, 2163–2169.

Klinker, E., and P. D. Sardeshmukh, 1992: The diagnosis of mechanical dissipation in the atmosphere from large-scale balance requirements. *J. Atmos. Sci.*, **49**, 608–627.

Klocke, D., and M. J. Rodwell, 2014: A comparison of two numerical weather prediction methods for diagnosing fast-physics errors in climate models. *Quart. J. Roy. Meteor. Soc.*, **140 (679)**, 517–524.

Knippertz, P., and H. Wernli, 2010: A Lagrangian climatology of tropical moisture exports to the Northern Hemispheric extratropics. *Journal of Climate*, **23 (4)**, 987–1003.

Køltzow, M., B. Casati, E. Bazile, T. Haiden, and T. Valkonen, 2019: An NWP Model Intercomparison of Surface Weather Parameters in the European Arctic during the Year of Polar Prediction Special Observing Period Northern Hemisphere 1. *Weather and Forecasting*, **34 (4)**, 959–983.

Kuhl, D. D., T. E. Rosmond, C. H. Bishop, J. McLay, and N. L. Baker, 2013: Comparison of hybrid ensemble/4DVar and 4DVar within the NAVDAS-AR data assimilation framework. *Monthly Weather Review*, **141 (8)**, 2740–2758.

Kumar, A., and M. P. Hoerling, 2000: Analysis of a conceptual model of seasonal climate variability and implications for seasonal prediction. *Bulletin of the American Meteorological Society*, **81 (2)**, 255–264.

Kwok, R., and D. A. Rothrock, 2009: Decline in Arctic sea ice thickness from submarine and ICESat records: 1958-2008. *Geophys. Res. Lett.*, **36 (L15501)**, doi:10.1029/2009GL039035.

Langland, R. H., M. A. Shapiro, and R. Gelaro, 2002: Initial condition sensitivity and error growth in forecasts of the 25 January 2000 East Coast snowstorm. *Monthly Weather Review*, **130 (4)**, 957–974.

Lawrence, H., N. Bormann, I. Sandu, J. Day, J. Farnan, and P. Bauer, 2019: Use and impact of Arctic observations in the ECMWF numerical weather prediction system. *Quarterly Journal of the Royal Meteorological Society*, **145 (725)**, 3432–3454.

Lee, J. A., J. P. Hacker, L. Delle Monache, B. Kosović, A. Clifton, F. Vandenberghe, and J. S. Rodrigo, 2017: Improving wind predictions in the marine atmospheric boundary layer through parameter estimation in a single-column model. *Monthly Weather Review*, **145 (1)**, 5–24.

Lee, S. H., P. D. Williams, and T. H. Frame, 2019: Increased shear in the North Atlantic upper-level jet stream over the past four decades. *Nature*, **572 (7771)**, 639–642.

Leith, C., 1974: Theoretical skill of monte carlo forecasts. *Monthly Weather Review*, **102 (6)**, 409–418.

Liberato, M. L., J. G. Pinto, I. F. Trigo, and R. M. Trigo, 2011: Klaus–an exceptional winter storm over northern Iberia and southern France. *Weather*, **66 (12)**, 330–334.

Lillo, S. P., and D. B. Parsons, 2017: Investigating the dynamics of error growth in ECMWF medium-range forecast busts. *Quart. J. Roy. Meteor. Soc.*, **143 (704)**, 1211–1226.

Ling, J., P. Bauer, P. Bechtold, A. Beljaars, R. Forbes, F. Vitart, M. Ulate, and C. Zhang, 2014: Global versus local MJO forecast skill of the ECMWF model during DYNAMO. *Monthly Weather Review*, **142 (6)**, 2228–2247.

Listowski, C., and T. Lachlan-Cope, 2017: The microphysics of clouds over the Antarctic Peninsula-Part 2: modelling aspects within Polar WRF. *Atmospheric Chemistry and Physics*, **17 (17)**, 10 195–10 221.

Little, E. M., 1968: Day length versus date graph at Arctic Circle is almost a sawtooth curve. *Journal of Geophysical Research*, **73 (2)**, 735–738.

Liu, J., J. A. Curry, H. Wang, M. Song, and R. M. Horton, 2012: Impact of declining Arctic sea ice on winter snowfall. *Proceedings of the National Academy of Sciences*, **109 (11)**, 4074–4079.

Lorenz, E. N., 1969: Atmospheric predictability as revealed by naturally occurring analogues. *J. Atmos. Sci.*, **26 (4)**, 636–646.

Lorenz, E. N., 1982: Atmospheric predictability experiments with a large numerical model. *Tellus*, **34 (6)**, 505–513.

Madonna, E., H. Wernli, H. Joos, and O. Martius, 2014: Warm conveyor belts in the ERA-Interim dataset (1979–2010). Part I: Climatology and potential vorticity evolution. *Journal of climate*, **27 (1)**, 3–26.

Magnusdottir, G., C. Deser, and R. Saravanan, 2004: The effects of North Atlantic SST and sea ice anomalies on the winter circulation in CCM3. Part I: Main features and storm track characteristics of the response. *Journal of Climate*, **17 (5)**, 857–876.

Martínez-Alvarado, O., E. Madonna, S. L. Gray, and H. Joos, 2016: A route to systematic error in forecasts of Rossby waves. *Quart. J. Roy. Meteor. Soc.*, **142 (694)**, 196–210.

Martius, O., and G. Rivière, 2016: *Rossby wave breaking: Climatology, interaction with low-frequency climate variability, and links to extreme weather events*, chap. 5, 69–78. Cambridge University Press.

Martius, O., C. Schwierz, and H. C. Davies, 2010: Tropopause-level waveguides. *J. Atmos. Sci.*, **67 (3)**, 866–879.

Mass, C. F., J. Baars, G. Wedam, E. Grimit, and R. Steed, 2008: Removal of systematic model bias on a model grid. *Weather and Forecasting*, **23 (3)**, 438–459.

Matsumura, S., X. Zhang, and K. Yamazaki, 2014: Summer Arctic atmospheric circulation response to spring Eurasian snow cover and its possible linkage to accelerated sea ice decrease. *Journal of Climate*, **27 (17)**, 6551–6558.

McInnes, K. L., and J. A. Curry, 1995: Modeling the mean and turbulent structure of the summertime Arctic cloudy boundary layer. *Boundary-layer meteorology*, **73**, 125–143.

Melhauser, C., and F. Zhang, 2012: Practical and intrinsic predictability of severe and convective weather at the mesoscales. *Journal of the Atmospheric Sciences*, **69 (11)**, 3350–3371.

Min, S.-K., X. Zhang, F. W. Zwiers, and G. C. Hegerl, 2011: Human contribution to more-intense precipitation extremes. *Nature*, **470 (7334)**, 378–381.

Mirocha, J., B. Kosović, and G. Kirkil, 2014: Resolved turbulence characteristics in large-eddy simulations nested within mesoscale simulations using the weather research and forecasting model. *Monthly Weather Review*, **142 (2)**, 806–831.

Morrison, H., J. Curry, and V. Khvorostyanov, 2005: A new double-moment microphysics parameterization for application in cloud and climate models. part i: Description. *Journal of the Atmospheric Sciences*, **62 (6)**, 1665–1677.

Morrison, H., G. de Boer, G. Feingold, J. Harrington, M. D. Shupe, and K. Sulia, 2012: Resilience of persistent arctic mixed-phase clouds. *Nature Geoscience*, **5 (1)**, 11–17.

Morrison, H., and J. Pinto, 2005: Mesoscale modeling of springtime arctic mixed-phase stratiform clouds using a new two-moment bulk microphysics scheme. *Journal of the Atmospheric Sciences*, **62 (10)**, 3683–3704.

Morrison, H., M. Shupe, and J. Curry, 2003: Modeling clouds observed at SHEBA using a bulk microphysics parameterization implemented into a single-column model. *Journal of Geophysical Research: Atmospheres*, **108 (D8)**.

Murphy, D. M., and T. Koop, 2005: Review of the vapour pressures of ice and supercooled water for atmospheric applications. *Quarterly Journal of the Royal Meteorological Society*, **131 (608)**, 1539–1565.

NCEP, 2020: NCEP ADP Global Upper Air and Surface Weather Observations (PREPBUFR format), May 1997 - Continuing. URL http://rda.ucar.edu/datasets/ds337.0/.

Nolin, A., R. Armstrong, and J. Maslanik, 1998: Near-Real-Time SSM/I-SSMIS EASE-Grid Daily Global Ice Concentration and Snow Extent. Version 4. *NASA DAAC at the National Snow and Ice Data Center, Boulder, Colorado*.

North, G. R., T. L. Bell, R. F. Cahalan, and F. J. Moeng, 1982: Sampling errors in the estimation of empirical orthogonal functions. *Monthly weather review*, **110 (7)**, 699–706.

Olsen, E. T., E. Manning, S. Licata, J. Blaisdell, L. Iredell, and J. Susskind, 2013: AIRS/AMSU/HSB Version 6 data release user guide. *Jet Propulsion Laboratory, California Institute of Technology, Pasadena, California*.

Overland, J. E., M. Wang, J. E. Walsh, and J. C. Stroeve, 2014: Future arctic climate changes: Adaptation and mitigation time scales. *Earth's Future*, **2 (2)**, 68–74.

Park, S. H., J. B. Klemp, and W. C. Skamarock, 2014: A comparison of mesh refinement in the global MPAS-A and WRF models using an idealized normal-mode baroclinic wave simulation. *Monthly Weather Review*, **142 (10)**, 3614–3634.

Parkinson, C. L., and D. J. Cavalieri, 1989: Arctic sea ice 1973–1987: Seasonal, regional, and interannual variability. *Journal of Geophysical Research: Oceans*, **94 (C10)**, 14 499–14 523.

Parsons, D. B., S. P. Lillo, C. P. Rattray, P. Bechtold, M. J. Rodwell, and C. M. Bruce, 2019: The role of continental mesoscale convective systems in forecast busts within global weather prediction systems. *Atmosphere*, **10 (11)**, 681.

Pedlosky, J., 1992: *Geophysical Fluid Dynamics*, Vol. 84. 2nd ed., Springer, 728 pp.

Petoukhov, V., S. Rahmstorf, S. Petri, and H. J. Schellnhuber, 2013: Quasiresonant amplification of planetary waves and recent Northern Hemisphere weather extremes. *Proceedings of the National Academy of Sciences*, **110 (14)**, 5336–5341.

Petoukhov, V., and V. A. Semenov, 2010: A link between reduced Barents-Kara sea ice and cold winter extremes over northern continents. *Journal of Geophysical Research: Atmospheres*, **115 (D21)**.

Pilon, R., C. Zhang, and J. Dudhia, 2016: Roles of deep and shallow convection and microphysics in the MJO simulated by the model for prediction across scales. *Journal of Geophysical Research: Atmospheres*, **121 (18)**, 10–575.

Pinto, J. O., 1998: Autumnal mixed-phase cloudy boundary layers in the arctic. *Journal of the Atmospheric Sciences*, **55 (11)**, 2016–2038.

Pithan, F., and Coauthors, 2016: Select strengths and biases of models in representing the Arctic winter boundary layer over sea ice: The Larcform 1 single column model intercomparison. *Journal of Advances in Modeling Earth Systems*, **8 (3)**, 1345–1357.

Pontius, R. G., O. Thontteh, and H. Chen, 2008: Components of information for multiple resolution comparison between maps that share a real variable. *Environmental and Ecological Statistics*, **15 (2)**, 111–142.

Porter, D. F., J. J. Cassano, and M. C. Serreze, 2011: Analysis of the Arctic atmospheric energy budget in WRF: A comparison with reanalyses and satellite observations. *Journal of Geophysical Research: Atmospheres*, **116 (D22)**.

Poterjoy, J., F. Zhang, and Y. Weng, 2014: The effects of sampling errors on the EnKF assimilation of inner-core hurricane observations. *Monthly Weather Review*, **142 (4)**, 1609–1630.

Purser, R., D. Parrish, and M. Masutani, 2000: Meteorological observational data compression; an alternative to conventional "super-obbing". *NOAA Office Note*, **(430)**.

Quinting, J. F., and S. C. Jones, 2016: On the impact of tropical cyclones on rossby wave packets: A climatological perspective. *Monthly Weather Review*, **144 (5)**, 2021–2048.

Raeder, K., J. L. Anderson, N. Collins, T. J. Hoar, J. E. Kay, P. H. Lauritzen, and R. Pincus, 2012: Dart/cam: An ensemble data assimilation system for cesm atmospheric models. *Journal of Climate*, **25 (18)**, 6304–6317.

Randall, D. A., and D. G. Cripe, 1999: Alternative methods for specification of observed forcing in single-column models and cloud system models. *Journal of Geophysical Research: Atmospheres*, **104 (D20)**, 24 527–24 545.

Richter-Menge, M. L. D., J., and E. M. Jeffries, 2019: Arctic report card 2019. URL https://www.arctic.noaa.gov/Report-Card.

Riedel, C., S. M. Cavallo, , and D. Parsons, 2019: Mesoscale prediction in the Antarctic using cycled ensemble data assimilation. *Monthly Weather Review*, In preparation.

Riemer, M., and S. C. Jones, 2010: The downstream impact of tropical cyclones on a developing baroclinic wave in idealized scenarios of extratropical transition. *Quarterly Journal of the Royal Meteorological Society: A journal of the atmospheric sciences, applied meteorology and physical oceanography*, **136 (648)**, 617–637.

Riemer, M., and S. C. Jones, 2014: Interaction of a tropical cyclone with a high-amplitude, midlatitude wave pattern: Waviness analysis, trough deformation and track bifurcation. *Quarterly Journal of the Royal Meteorological Society*, **140 (681)**, 1362–1376.

Ringler, T., L. Ju, and M. Gunzburger, 2008: A multiresolution method for climate system modeling: Application of spherical centroidal voronoi tessellations. *Ocean Dynamics*, **58 (5-6)**, 475–498.

Rodwell, M., and T. Palmer, 2007a: Using numerical weather prediction to assess climate models. *Quarterly Journal of the Royal Meteorological Society*, **133 (622)**, 129–146.

Rodwell, M. J., and T. Jung, 2008: Understanding the local and global impacts of model physics changes: An aerosol example. *Quart. J. Roy. Meteor. Soc.*, **134**, 1479–1497.

Rodwell, M. J., and T. N. Palmer, 2007b: Using numerical weather prediction to assess climate models. *Quart. J. Roy. Meteor. Soc.*, **133**, 129–146.

Rodwell, M. J., and Coauthors, 2013: Characteristics of occasional poor medium-range weather forecasts for Europe. *Bull. Amer. Meteor. Soc.*, **94 (9)**, 1393–1405.

Rossby, C., 1939: Planetary flow patterns in the atmosphere. *Quart. J. Roy. Met. Soc*, **66**, 68.

Rossby, C.-G., 1945: On the propagation of frequencies and energy in certain types of oceanic and atmospheric waves. *Journal of Meteorology*, **2 (4)**, 187–204.

Röthlisberger, M., O. Martius, and H. Wernli, 2016: An algorithm for identifying the initiation of synoptic-scale rossby waves on potential vorticity waveguides. *Quarterly Journal of the Royal Meteorological Society*, **142 (695)**, 889–900.

Röthlisberger, M., O. Martius, and H. Wernli, 2018: Northern Hemisphere Rossby wave initiation events on the extratropical jet—A climatological analysis. *Journal of Climate*, **31 (2)**, 743–760.

Sanders, F., and J. R. Gyakum, 1980: Synoptic-dynamic climatology of the "bomb". *Monthly Weather Review*, **108 (10)**, 1589–1606.

Sandu, I., A. Beljaars, P. Bechtold, T. Mauritsen, and G. Balsamo, 2013: Why is it so difficult to represent stably stratified conditions in numerical weather prediction (NWP) models? *Journal of Advances in Modeling Earth Systems*, **5 (2)**, 117–133.

Schäfler, A., and Coauthors, 2018: The North Atlantic waveguide and downstream impact experiment. *Bulletin of the American Meteorological Society*, **99 (8)**, 1607–1637.

Schwierz, C., M. Croci-Maspoli, and H. Davies, 2004a: Perspicacious indicators of atmospheric blocking. *Geophysical research letters*, **31 (6)**.

Schwierz, C., S. Dirren, and H. C. Davies, 2004b: Forced waves on a zonally aligned jet stream. *Journal of the atmospheric sciences*, **61 (1)**, 73–87.

Screen, J. A., C. Deser, and I. Simmonds, 2012: Local and remote controls on observed Arctic warming. *Geophysical Research Letters*, **39 (10)**.

Screen, J. A., and I. Simmonds, 2010a: The central role of diminishing sea ice in recent Arctic temperature amplification. *Nature*, **464 (7293)**, 1334–1337.

Screen, J. A., and I. Simmonds, 2010b: Increasing fall-winter energy loss from the Arctic Ocean and its role in Arctic temperature amplification. *Geophysical Research Letters*, **37 (16)**.

Screen, J. A., and I. Simmonds, 2014: Amplified mid-latitude planetary waves favour particular regional weather extremes. *Nature Climate Change*, **4 (8)**, 704.

Screen, J. A., I. Simmonds, C. Deser, and R. Tomas, 2013: The atmospheric response to three decades of observed Arctic sea ice loss. *Journal of Climate*, **26**, 1230–1248, doi:10.1175/JCLI-D-12-00063.1.

Semmler, T., T. Jung, M. A. Kasper, and S. Serrar, 2018: Using NWP to assess the influence of the Arctic atmosphere on midlatitude weather and climate. *Advances in Atmospheric Sciences*, **35 (1)**, 5–13.

Semmler, T., L. Stulic, T. Jung, N. Tilinina, C. Campos, S. Gulev, and D. Koracin, 2016: Seasonal atmospheric responses to reduced Arctic sea ice in an ensemble of coupled model simulations. *Journal of Climate*, **29 (16)**, 5893–5913.

Serreze, M. C., and R. G. Barry, 2011: Processes and impacts of Arctic amplification: A research synthesis. *Global and planetary change*, **77 (1-2)**, 85–96.

Serreze, M. C., and R. G. Barry, 2014: *The Arctic climate system*. Cambridge University Press, 404 pp.

Serreze, M. C., and J. A. Francis, 2006: The Arctic amplification debate. *Climatic change*, **76 (3-4)**, 241–264.

Shindell, D., and G. Faluvegi, 2009: Climate response to regional radiative forcing during the twentieth century. *Nature Geoscience*, **2 (4)**, 294.

Shupe, M. D., 2011: Clouds at Arctic atmospheric observatories. Part II: Thermodynamic phase characteristics. *J. Appl. Meteor. Climatol.*, **50 (3)**, 645–661.

Shupe, M. D., and J. M. Intrieri, 2004: Cloud radiative forcing of the Arctic surface: The influence of cloud properties, surface albedo, and solar zenith angle. *Journal of Climate*, **17 (3)**, 616–628.

Shupe, M. D., S. Y. Matrosov, and T. Uttal, 2006: Arctic mixed-phase cloud properties derived from surface-based sensors at SHEBA. *J. Atmos. Sci.*, **63 (2)**, 697–711.

Simmons, A. J., and B. J. Hoskins, 1979: The downstream and upstream development of unstable baroclinic waves. *J. Atmos. Sci.*, **36 (7)**, 1239–1254.

Skamarock, W., J. Klemp, J. Dudhia, D. Gill, and D. Barker, 2005: Coauthors, 2008: A description of the Advanced Research WRF version 3. NCAR Tech. Tech. rep., Note NCAR/TN-4751STR.

Skamarock, W. C., J. B. Klemp, M. G. Duda, L. Fowler, S. .-H. Park, and T. D. Ringler, 2012: A multi-scale nonhydrostatic atmospheric model using centroidal voronoi tesselations and C–grid staggering. *Monthly Weather Review*, **140**, 3090–3105.

Skamarock, W. C., C. Snyder, J. B. Klemp, and S.-H. Park, 2019: Vertical resolution requirements in atmospheric simulation. *Monthly Weather Review*, **147 (7)**, 2641–2656.

Smith, E. N., J. A. Gibbs, E. Fedorovich, and P. M. Klein, 2018: WRF Model study of the Great Plains low-level jet: Effects of grid spacing and boundary layer parameterization. *Journal of Applied Meteorology and Climatology*, **57 (10)**, 2375–2397.

Smithson, P., K. Addison, and K. Atkinson, 2013: *Fundamentals of the physical environment*. Routledge.

Snyder, C., 1999: Error growth in flows with finite-amplitude waves or coherent structures. *Journal of the atmospheric sciences*, **56 (4)**, 500–506.

Sotiropoulou, G., J. Sedlar, R. Forbes, and M. Tjernström, 2016: Summer Arctic clouds in the ECMWF forecast model: An evaluation of cloud parametrization schemes. *Quarterly Journal of the Royal Meteorological Society*, **142 (694)**, 387–400.

Souders, M. B., B. A. Colle, and E. K. Chang, 2014: The climatology and characteristics of Rossby wave packets using a feature-based tracking technique. *Monthly Weather Review*, **142 (10)**, 3528–3548.

Steele, M., W. Ermold, and J. Zhang, 2008: Arctic ocean surface warming trends over the past 100 years. *Geophysical Research Letters*, **35 (2)**.

Stensrud, D. J., 2013: Upscale effects of deep convection during the North American monsoon. *J. Atmos. Sci.*, **70 (9)**, 2681–2695.

Stroeve, J. C., J. Maslanik, M. C. Serreze, I. Rigor, W. Meier, and C. Fowler, 2011: Sea ice response to an extreme negative phase of the Arctic Oscillation during winter 2009/2010. *Geophysical Research Letters*, **38 (2)**.

Sun, Y. Q., and F. Zhang, 2016: Intrinsic versus practical limits of atmospheric predictability and the significance of the butterfly effect. *Journal of the Atmospheric Sciences*, **73 (3)**, 1419–1438.

Szapiro, N., and S. Cavallo, 2018: Tpvtrack v1. 0: a watershed segmentation and overlap correspondence method for tracking tropopause polar vortices. *Geoscientific Model Development*, **11 (12)**, 5173–5187.

Tanaka, H. L., and S. Seki, 2013: Development of a three-dimensional spectral linear baroclinic model and its application to the baroclinic instability associated with positive and negative arctic oscillation indices. *Journal of the Meteorological Society of Japan. Ser. II*, **91 (2)**, 193–213.

Teubler, F., and M. Riemer, 2016: Dynamics of rossby wave packets in a quantitative potential vorticity–potential temperature framework. *Journal of the Atmospheric Sciences*, **73 (3)**, 1063–1081.

Thompson, G., P. R. Field, R. M. Rasmussen, and W. D. Hall, 2008: Explicit forecasts of winter precipitation using an improved bulk microphysics scheme. part ii: Implementation of a new snow parameterization. *Monthly Weather Review*, **136 (12)**, 5095–5115.

Thorpe, A., and K. Emanuel, 1985: Frontogenesis in the presence of small stability to slantwise convection. *Journal of the atmospheric sciences*, **42 (17)**, 1809–1824.

Thuburn, J., T. D. Ringler, W. C. Skamarock, and J. B. Klemp, 2009: Numerical representation of geostrophic modes on arbitrarily structured c-grids. *Journal of Computational Physics*, **228 (22)**, 8321–8335.

Tippett, M. K., J. L. Anderson, C. H. Bishop, T. M. Hamill, and J. S. Whitaker, 2003: Ensemble square root filters. *Monthly Weather Review*, **131 (7)**.

Torn, R. D., 2010: Ensemble-based sensitivity analysis applied to African easterly waves. *Weather and forecasting*, **25 (1)**, 61–78.

Torn, R. D., and G. J. Hakim, 2008: Ensemble-based sensitivity analysis. *Monthly Weather Review*, **136 (2)**.

Torn, R. D., and G. J. Hakim, 2009: Initial condition sensitivity of western Pacific extratropical transitions determined using ensemble-based sensitivity analysis. *Monthly Weather Review*, **137**, 3388–3406.

Turner, D. D., M. D. Shupe, and A. B. Zwink, 2018: Characteristic atmospheric radiative heating rate profiles in Arctic clouds as observed at Barrow, Alaska. *J. Appl. Meteor. Climatol.*, **57 (4)**, 953–968.

Wallace, J. M., and D. S. Gutzler, 1981: Teleconnections in the geopotential height field during the Northern Hemisphere winter. *Monthly Weather Review*, **109 (4)**, 784–812.

Wallace, J. M., and P. V. Hobbs, 2006: *Atmospheric science: An introductory survey*, Vol. 92. Academic press, 483 pp.

Wang, J., T. Hock, S. A. Cohn, C. Martin, N. Potts, T. Reale, B. Sun, and F. Tilley, 2013a: Unprecedented upper-air dropsonde observations over antarctica from the 2010 concordiasi experiment: Validation of satellite-retrieved temperature profiles. *Geophysical research letters*, **40 (6)**, 1231–1236.

Wang, X., D. Parrish, D. Kleist, and J. Whitaker, 2013b: GSI 3DVar-based ensemble–variational hybrid data assimilation for NCEP Global Forecast System: Single-resolution experiments. *Monthly Weather Review*, **141 (11)**, 4098–4117.

Ware, R., and Coauthors, 1996: GPS sounding of the atmosphere from low earth orbit: Preliminary results. *Bulletin of the American Meteorological Society*, **77 (1)**, 19–40.

Waugh, D. W., A. H. Sobel, and L. M. Polvani, 2017: What is the polar vortex and how does it influence weather? *Bulletin of the American Meteorological Society*, **98 (1)**, 37–44.

Wedi, N., and S. Malardel, 2010: Non-hydrostatic modelling at ECMWF. *ECMWF Newsletter*, **125**, 17–21.

Wegener, A., 1911: *Thermodynamik der atmosphäre*. JA Barth.

Wernli, H., and H. C. Davies, 1997: A Lagrangian-based analysis of extratropical cyclones. I: The method and some applications. *Quart. J. Roy. Meteor. Soc.*, **123 (538)**, 467–489.

Wernli, H., S. Dirren, M. A. Liniger, and M. Zillig, 2002: Dynamical aspects of the life cycle of the winter storm 'Lothar' (24–26 December 1999). *Quart. J. Roy. Meteor. Soc.*, **128 (580)**, 405–429.

Westra, S., L. V. Alexander, and F. W. Zwiers, 2013: Global increasing trends in annual maximum daily precipitation. *Journal of climate*, **26 (11)**, 3904–3918.

Whitaker, J. S., G. P. Compo, and J. N. Thépaut, 2009: A comparison of variational and ensemble-based data assimilation systems for reanalysis of sparse observations. *Monthly Weather Review*, **137 (6)**, 1991–1999.

Whitaker, J. S., G. P. Compo, X. Wei, and T. M. Hamill, 2004: Reanalysis without radiosondes using ensemble data assimilation. *Monthly Weather Review*, **132 (5)**, 1190–1200.

Whitaker, J. S., and T. M. Hamill, 2002: Ensemble data assimilation without perturbed observations. *Monthly Weather Review*, **130 (7)**.

Wilks, D. S., 2011: *Statistical methods in the atmopsheric sciences*. 3rd ed., Academic Press, 676 pp.

Williams, K., and M. Brooks, 2008: Initial tendencies of cloud regimes in the Met Office Unified Model. *Journal of Climate*, **21 (4)**, 833–840.

Winters, A. C., and J. E. Martin, 2014: The role of a polar/subtropical jet superposition in the May 2010 Nashville flood. *Weather and forecasting*, **29 (4)**, 954–974.

Winters, A. C., and J. E. Martin, 2016: Synoptic and mesoscale processes supporting vertical superposition of the polar and subtropical jets in two contrasting cases. *Quarterly Journal of the Royal Meteorological Society*, **142 (695)**, 1133–1149.

Winton, M., 2006: Amplified arctic climate change: What does surface albedo feedback have to do with it? *Geophysical Research Letters*, **33 (3)**.

Wirth, V., M. Riemer, E. K. Chang, and O. Martius, 2018: Rossby wave packets on the midlatitude waveguide—a review. *Monthly Weather Review*, **146 (7)**, 1965–2001.

Wong, M., G. Romine, and C. Snyder, 2020: Model improvement via systematic investigation of physics tendencies. *Monthly Weather Review*, **148 (2)**, 671–688.

Wong, M., and W. C. Skamarock, 2016: Spectral characteristics of convective-scale precipitation observations and forecasts. *Monthly Weather Review*, **144 (11)**, 4183–4196.

Wood, K. R., J. E. Overland, S. A. Salo, N. A. Bond, W. J. Williams, and X. Dong, 2013: Is there a "new normal" climate in the beaufort sea? *Polar Research*, **32 (1)**, 19 552.

Woollings, T., and M. Blackburn, 2012: The North Atlantic jet stream under climate change and its relation to the NAO and EA patterns. *Journal of Climate*, **25 (3)**, 886–902.

Wu, A., W. W. Hsieh, G. J. Boer, and F. W. Zwiers, 2007: Changes in the Arctic Oscillation under increased atmospheric greenhouse gases. *Geophysical research letters*, **34 (12)**.

Xie, S., R. T. Cederwall, M. Zhang, and J. J. Yio, 2003: Comparison of SCM and CSRM forcing data derived from the ECMWF model and from objective analysis at the ARM SGP site. *Journal of Geophysical Research: Atmospheres*, **108 (D16)**.

Xie, S., S. A. Klein, J. J. Yio, A. C. Beljaars, C. N. Long, and M. Zhang, 2006: An assessment of ECMWF analyses and model forecasts over the North Slope of Alaska using observations from the ARM Mixed-Phase Arctic Cloud Experiment. *Journal of Geophysical Research: Atmospheres*, **111 (D5)**.

Yang, F., 2017: Review of GFS forecast skills in 2013. *National Centers for Environmental Prediction*, URL https://www.emc.ncep.noaa.gov/gmb/wx24fy/doc/GFS.performance.review.2017.pdf.

Zhang, C., Y. Wang, and K. Hamilton, 2011: Improved representation of boundary layer clouds over the southeast pacific in ARW-WRF using a modified Tiedtke cumulus parameterization scheme. *Monthly Weather Review*, **139 (11)**, doi:10.1175/MWR-D-10-05091.1.

Zhang, F., N. Bei, R. Rotunno, C. Snyder, and C. C. Epifanio, 2007: Mesoscale predictability of moist baroclinic waves: Convection-permitting experiments and multistage error growth dynamics. *Journal of the Atmospheric Sciences*, **64 (10)**, 3579–3594.

Zhang, F., C. Snyder, and R. Rotunno, 2003: Effects of moist convection on mesoscale predictability. *Journal of the Atmospheric Sciences*, **60 (9)**, 1173–1185.

Zhang, M., W. Perrie, and Z. Long, 2019: Dynamical downscaling of the Arctic climate with a focus on polar cyclone climatology. *Atmosphere-Ocean*, **57 (1)**, 41–60.

Zhang, M., R. C. Somerville, and S. Xie, 2016: The SCM concept and creation of ARM forcing datasets. *Meteorological Monographs*, **57**, 24–1.

Zhao, C., and Coauthors, 2019: Modeling extreme precipitation over East China with a global variable-resolution modeling framework (MPASv5. 2): impacts of resolution and physics. *Geoscientific Model Development*, **12 (7)**, 2707–2726.

Zheng, M., E. K. Chang, and B. A. Colle, 2013: Ensemble sensitivity tools for assessing extratropical cyclone intensity and track predictability. *Weather and forecasting*, **28 (5)**, 1133–1156.

Zhu, Y., J. Derber, A. Collard, D. Dee, R. Treadon, G. Gayno, and J. A. Jung, 2014: Enhanced radiance bias correction in the national centers for environmental prediction's gridpoint statistical interpolation data assimilation system. *Quarterly Journal of the Royal Meteorological Society*, **140 (682)**, 1479–1492.

Zierl, B., and V. Wirth, 1997: The influence of radiation on tropopause behavior and stratosphere-troposphere exchange in an upper tropospheric anticyclone. *Journal of Geophysical Research: Atmospheres*, **102 (D20)**, 23 883–23 894.